

Acoustofluidic Manipulation of Microparticles Using Surface Acoustic Wave Induced Streaming



Mercedes Stringer

A Thesis Submitted for The Degree of Doctor of Engineering

Cardiff University

June 2024

MUSL
Medical Ultrasound and
Sensors Laboratory

I. Abstract

Acoustofluidics enables contact-free manipulation of particles and fluids, offering transformative potential for biomedical applications. Recent advancements in acoustic streaming, driven by leaky surface acoustic waves (SAWs) generated through radio frequency signals applied interdigital transducers (IDTs) on piezoelectric substrates, have gained significant attention. This technique addresses challenges posed by low Reynolds numbers in micro- and nanoscale liquids, paving the way for applications such as isolating tumour cells, precise drug delivery, and tissue engineering.

This thesis extensively reviews the mechanisms and applications of acoustic streaming, revealing promising new avenues. The primary aim was to investigate innovative configurations for producing acoustic streaming with SAWs to enable versatile applications. A reconfigurable device utilizing a Hexagonal Flexible Printed Circuit Board (FPCB) IDTs was developed for rapid investigations beyond the limitations of conventional IDTs. This approach, combined with numerical analysis using COMSOL Multiphysics, allowed exploration of wave mode characteristics at different angles and their resulting acoustic streaming actuation.

Significant findings include enhanced acoustic streaming at 90° pseudo shear-horizontal-SAW (P-SH-SAW) compared to the conventional Rayleigh SAW (R-SAW at 0°) under identical power (30 dBm / 1 W) and fluid volume (100 μ L) conditions. The 90° P-SH-SAW at 34.4 MHz achieved an average area streaming velocity of 1.58 mm/s - approximately 15% higher than the R-SAW at 0° (1.35 mm/s at 19.8 MHz) - despite having a Z-displacement magnitude that was $\sim 40\%$ of the R-SAW. At a constant fluid viscosity (60:40 water:glycerol), P-SH-SAW consistently outperformed R-SAW by $\sim 50\%$ across all tested powers (20, 27, and 30 dBm). When varying viscosity, P-SH-SAW maintained higher streaming velocities, with over 50% improvement at low viscosity and a 55% drop at high viscosity, compared to a 42% drop for R-SAW. Streaming of a 1 mL fluid volume (25 mm diameter PDMS ring) was achieved within 2 seconds using pseudo-SH-SAW at 30 dBm, whereas R-SAW showed minimal displacement. Notably, P-SH-SAW induced streaming through a standard 96-well culture plate at 30 dBm, achieving velocities of ≈ 1.2 mm/s, whereas R-SAW failed to generate effective streaming under the same conditions. These

results highlight the potential of using combined wave modes and multidirectional SAW configurations on the 128° YX-cut LiNbO_3 substrate for enhanced fluid manipulation. These combined wave modes achieved enhanced particle concentration for $10\ \mu\text{m}$, $1\ \mu\text{m}$, and $500\ \text{nm}$ particles. For example, R-SAW plateaued early - often within the first 20% of the actuation time - while the combined wave modes continued to concentrate particles steadily throughout the duration, demonstrating superior performance for micro- and nanoparticle manipulation.

The development and characterization of the Hexagonal FPCB IDT expanded understanding of how anisotropic properties affect acoustic streaming. This insight improves device optimization by shifting focus from altering IDT designs to manipulating the wave mode selection. These findings address key challenges such as excessive damping of R-SAW and low-power acoustic streaming, optimizing device performance. The Hexagonal FPCB IDT supports multiple applications by utilizing different IDTs, providing the foundation for future research.

II. Acknowledgement

I would like to express my thanks to my supervisor, Dr. Chris Yang, for his role in my academic journey. I am also grateful to the members of my thesis committee for their constructive feedback and insightful comments.

Special thanks to my colleagues in the Medical Ultrasound and Sensors Laboratory for providing a collaborative environment. In particular, I would like to acknowledge Povilas Dumcius and Xiaoyan Zhang for their technical assistance and enlightening discussions.

I am appreciative of the funding and resources provided by Engineering and Physical Science Research Council (EPSRC) and Cardiff University. This research would not have been possible without their support.

On a personal note, I am incredibly fortunate to have supportive friends who have been with me throughout this journey. Thank you for your encouragement, support, and the much-needed breaks.

I am eternally grateful to my family for their unconditional love, financial support, and motivation. Their unwavering belief in me, especially during overwhelming times, helped me stay focused and positive.

Lastly, my heartfelt thanks go to my partner, whose patience, understanding, and generosity has been my anchor through the highs and lows of this journey. His thoughtfulness, from delicious home-cooked meals to constant laughter, has lifted my spirits and made all the difference.

III. Table Of Contents

I. Abstract.....	i
II. Acknowledgement.....	iii
III. Table Of Contents	iv
IV. List Of Figures.....	ix
V. List Of Tables.....	xxi
VI. List Of Abbreviations.....	xxii
VII. List Of Publications	xxiv
VIII. Conference Participation.....	xxv
Chapter 1 Introduction.....	1
1.1 Background.....	1
1.2 Aims and Objectives	2
1.3 Thesis Outline	3
1.4 Contribution to Knowledge.....	4
Chapter 2 Acoustic Streaming.....	5
2.1 Introduction	5
2.2 Fundamentals of Acoustofluidics	7
2.3 Governing Equations	10
2.4 Formation of Acoustic Streaming.....	15
2.5 Applications of Acoustic Streaming.....	20
2.5.1 TSAWs based streaming and acoustofluidics.....	21

2.5.2	SSAWs based streaming and acoustofluidics.....	39
2.6	Conclusion	44
Chapter 3	Acoustofluidic Devices	46
3.1	Introduction	46
3.2	Configuration of Acoustofluidic Devices.....	46
3.3	Basics of IDTs.....	48
3.3.1.	Design criteria.....	48
3.3.2.	Electrode materials	52
3.3.3.	Piezoelectric materials	53
3.3.4.	IDT Fabrication techniques	54
3.4	Advances of IDTs.....	55
3.4.1.	Conventional IDT structures	55
3.4.2.	Unconventional IDT structures.....	58
3.4.3.	IDTs embedded into multi-layer structures	61
3.5	Fluidic Vessel.....	62
3.5.1.	Vessel type	62
3.5.2.	Vessel materials	63
3.5.3.	Vessel fabrication techniques	64
3.6	Conclusion	67
Chapter 4	Development of Hexagonal FPCB IDT	68
4.1	Introduction	68

4.2	Motivation of a Hexagonal FPCB IDT	68
4.3	Overview of Hexagonal FPCB IDT	70
4.3.1	Piezoelectric Substrate	71
4.3.2	IDE Design.....	73
4.3.3	IDT Fabrication	74
4.3.4	Mechanical Housing and Assembly	76
4.3.5	Matching Network	79
4.3.6	Fluidic Vessel.....	81
4.4	Conclusion	83
Chapter 5	System Setup and Analysis Methods	84
5.1	Introduction	84
5.2	System Set-up	84
5.2.1	Device Operation	85
5.2.2	Electrical Characterisation	86
5.3	Experiment Process.....	87
5.3.1	Sample Preparation and Handling	87
5.3.2	Experimental Procedure	88
5.3.3	Data Collection and Analysis	89
Chapter 6	Numerical Studies.....	90
6.1	Introduction	90
6.2	Numerical Models	90

6.2.1	Model 1: Periodic Unit Cell IDT	92
6.2.2	Model 2: Basic 3D IDT	95
6.2.3	Model 3: Life scale 2D IDT.....	96
6.3	Numerical Analysis	98
6.3.1	IDE Design Validation.....	98
6.3.2	Rayleigh SAW Validation	98
6.3.3	Substrate Validation.....	103
6.3.4	Wave Modes.....	105
6.3.5	X-Rotation Angle Analysis	113
6.3.6	Optimal Wave Modes.....	132
6.3.7	Pseudo-SH-SAW	136
Chapter 7	Results and Discussion.....	139
7.1	Introduction	139
7.2	Experimental Findings	139
7.2.1	Device Characterisation.....	139
7.2.2	Acoustic Streaming Velocities.....	150
7.2.3	Acoustic Streaming Patterns.....	153
7.2.4	Damping Effects	154
7.3	Concentration of micro- and nano- particles	158
7.3.1	Numerical Analysis	158
7.3.2	Working Mechanism	160

7.3.3	Concentration Results.....	161
7.3.4	Additional Concentration Results.....	164
Chapter 8	Conclusion.....	167
8.1	Conclusion.....	167
8.2	Future Work.....	169
	Bibliography.....	174

IV. List Of Figures

Figure 1.1. Distribution displacements of (a) R-SAW and (b) SH-SAW. [Minor adaptation from [11].] 2

Figure 2.1. Acoustic streaming generation IDT-based acoustofluidic devices, methodologies (nebulisation, jetting, transport, rotation, mixing, separation), and their respective applications in drug delivery [54], bioprinting [55], pumping droplets [56], small organism phenotyping [52], chemical reactions [57], particle sorting/separation [25]). [Reproduced from “Stringer *et al.* Methodologies, technologies, and strategies for acoustic streaming-based acoustofluidics. Applied Physics Reviews 1 March 2023; 10 (1): 011315. <https://doi-org.abc.cardiff.ac.uk/10.1063/5.0134646>” [2], with the permission of AIP Publishing.]..... 7

Figure 2.2. Schematic illustrations of SAW devices [69] and types of wave propagation through the distribution of displacements [68]. (a) Top and side views of SAW generated by a single IDT, producing TSAW. (b) Top and side views of SAW generated by a pair of opposite IDTs, producing SSAW, demonstrating regions of PNs and ANs. (c) Rayleigh wave[70] (d) Lamb waves[71] (e) Shear horizontal waves and Love waves[64]. [Reproduced from “Stringer *et al.* Methodologies, technologies, and strategies for acoustic streaming-based acoustofluidics. Applied Physics Reviews 1 March 2023; 10 (1): 011315. <https://doi-org.abc.cardiff.ac.uk/10.1063/5.0134646>” [2], with the permission of AIP Publishing.] 10

Figure 2.3. Illustration of two-dimensional fundamental streaming patterns for (a-c) droplets and (d-f) channels, with varying positions of SAW propagation indicated by the blue arrows. In the droplet top view, SAW propagation enters from (a) the left, (b) laterally offset, and (c) both left and right (SSAW). In the channel top view, (d) and (e) streaming patterns, the SAW propagation enters from the left and bottom, respectively. In the front view, (f) streaming patterns with SAW propagation from both the left and right result in SSAW streaming. [Reproduced with minor adaption from “Stringer *et al.*; Methodologies, technologies, and strategies for acoustic streaming-based acoustofluidics. Applied Physics Reviews 1 March 2023; 10 (1): 011315. <https://doi-org.abc.cardiff.ac.uk/10.1063/5.0134646>” [2], with the permission of AIP Publishing.] 19

Figure 2.4. Examples of applications of TSAW streaming for digital acoustofluidic mixing. (a) Nanolitre order droplet mixing [Minor adaptation from [104]]. (b) Cell detachment for diagnostics [Reproduced from [118]]. (c) Nanoparticle formation via droplet fusion [Reproduced from [121]]. 23

Figure 2.5. Examples of applications of TSAW streaming for digital acoustofluidic concentration and separation. (a) Concentration of cancer cells [Minor adaptation from [124]]. (b) separation of malaria-infected RBCs [Minor adaptation from [128]]. (c) Drug loading and exosome encapsulation [Reproduced from [129]]. 25

Figure 2.6. Examples of applications of TSAW streaming for digital acoustofluidic splitting and merging. (a) Open platform droplet splitting and merging [Reproduced from [130]]. (b) On-demand droplet splitting [Minor adaptations from [131]]. 26

Figure 2.7. Examples of applications of TSAW streaming for digital acoustofluidic transportation. (a) Flexible/bendable droplet pumping [Reproduced from [56]] (b) Digital programmable droplet manipulation [Minor adaptation from [146]]. 28

Figure 2.8. Examples of applications of TSAW streaming for digital acoustofluidic jetting. (a) Vertical jetting induced by SH-SAW [Minor adaptation form [150]]. (b) Jetting along inclined surface [Minor adaptation from [144]]. (c) Focused acoustic beams to encapsulate single cells [Reproduced from [160]]. (d) Focused acoustic beams for printing tumour microenvironment [Minor adaptation from [165]]. 30

Figure 2.9. Examples of applications of TSAW streaming for digital acoustofluidic nebulisation. (a) SAW nebuliser for sample delivery and ionization demonstrating sensitive mass spectrometry [Reproduced from [171]]. (b) Prototype nebuliser employed for in vitro lung characterisation of aerosols [Reproduced from [54]]. 32

Figure 2.10. Examples of applications of TSAW streaming for channel/chamber acoustofluidic mixing. (a) Locally remove cells from culture surface to improve cell culture quality [Reproduced from [41]]. (b) Controllable mixing for fabrication of therapeutic nanoparticles [Reproduced from [174]]. (c) Acoustically accelerated neural differentiation of human embryonic stem cells [Reproduced from [210]]. (d) Acoustofection for intracellular delivery device [Minor adaptations from [211]]. 34

Figure 2.11. Examples of applications of TSAW streaming for channel/chamber acoustofluidic concentration and separation. (a) Sorting of tumour cells by a multi-stage SAW device [Reproduced from [216]]. (b) Particle separation using a detachable acoustofluidic system [Reproduced from [217]]. (c) Selective particle and cell capture in continuous flow [Minor adaptation from [219]]. (d) Hybrid spiral microfluidic platform for passive and active separation [Minor adaptations from [215]]. 36

Figure 2.12. Examples of applications of TSAW streaming for channel/chamber acoustofluidic rotation. (a) Tri-directional symmetrical acoustic tweezers for programmable trajectory manipulation [Reproduced from [222]]. (b) Controlled rotation on a lab-on-a-disc device [Reproduced from [225]]. (c) Rotational manipulation of zebrafish larvae, demonstrating multiple imaging of the rotation for 3D reconstruction of models [Minor adaptation from [52]]. 38

Figure 2.13. Examples of applications of TSAW streaming for channel/chamber acoustofluidic droplet manipulation. (a) Deterministic droplet coding of through dispensing of droplet volumes [Reproduced from [230]]. (b) Manipulation of 200 femtoliter droplets in nanofluidic channels [Reproduced from [232]]. 39

Figure 2.14. Examples of applications of SSAW streaming for digital acoustofluidics. (a) Growth of glycine crystals promoted by SSAW [Minor adaptations from [237]]. (b) Particle concentration and separation by SSAW through change in contact angle [Minor adaptations from [240]]. (c) Droplet transportation and merging with anisotropic ratchet conveyors control movement [Minor adaptations from [241]]. (d) SSAW induced stable jetting in capillary tubes [Minor adaptations from [243]]. 41

Figure 2.15. Examples of applications of SSAW streaming for channel/chamber acoustofluidics. (a) SSAW fluid mixing of deionized water and dye solution [Minor adaptations from [244]]. (b) Tilted-angle SSAW separation of red blood cells and bacteria [Minor adaptations from [250]]. (c) Isolating circulating exosomes from plasma samples device for early traumatic brain injury diagnostics [Minor adaptation from [213]]. (d) Dynamic and selective particle manipulation using harmonic acoustics [Minor adaptation from [270]]. 44

Figure 3.1. Typical configuration of a SAW acoustofluidic device. (a) Acoustofluidic experimental set-up. (b) SAW device consisting of a single conventional IDT on a piezoelectric substrate (c) Continuation of the TSAW from the IDT in (a) showing an example of fluidic mixing within a sessile droplet [283]. (d) Continuation of TSAW from (a) demonstrating particle separation within in microchannel [99]. (d) Continuation of TSAW from (a) causing vibrational stimulation of biological cells in a closed chamber [210]. 47

Figure 3.2. Conventional IDT and illustrations of example design considerations. (a) Schematic of conventional IDT with labelled parameters: period, finger spacing, aperture, and finger width. (b) A continuation of (a) illustrating the SAW wavefront propagation and associated heating effects. (c) Continuation of (a) showing the SAW wavefront during beam steering, highlighting the power flow angle. (d) Further continuation of (a) incorporating an opposing IDT configuration, demonstrating the triple transit and bidirectional effects of IDTs..... 52

Figure 3.3. Conventional IDT designs. (a) Standard bidirectional IDTs (b) Split IDTs (c) Single phase unidirectional transducer (d) Distributed acoustic reflecting transducer (e) Floating electrode unidirectional transducer (f) Apodised IDT (g) Focused or curved IDT (h) Chirped IDT or dispersive delay lines (i) Slanted finger IDT or tapered or tilted IDTs. [Reproduced with minor alterations from “Stringer *et al.* Methodologies, technologies, and strategies for acoustic streaming-based acoustofluidics. Applied Physics Reviews 1 March 2023; 10 (1): 011315. <https://doi-org.abc.cardiff.ac.uk/10.1063/5.0134646>” [2], with the permission of AIP Publishing.] 58

Figure 3.4. Unconventional IDT designs. (a) Circular or annular IDT (b) Swirling IDT (c) Electrode spiral angle IDT (d) Ring waveguide resonator IDT (e) Holographic IDT (f) Ball shaped IDT (g) Inter-digitated IDT (h) Tuneable IDT (i) Multiphase IDT. [Reproduced with minor alterations from “Stringer *et al.* Methodologies, technologies, and strategies for acoustic streaming-based acoustofluidics. Applied Physics Reviews 1 March 2023; 10 (1): 011315. <https://doi-org.abc.cardiff.ac.uk/10.1063/5.0134646>” [2], with the permission of AIP Publishing.] 61

Figure 3.5. Typical procedure for producing microfluidic vessels using two methods, 3D printing [210] and soft lithography, for a chamber and microchannel, respectively [377,382]. (1) Choice and design of fluidic vessel (2) Fabrication of the master mould, involving 3D printing the design or lithography mask process. (3) Vessel fabrication, including the PDMS preparation, casting, curing, peeling, bonding, and inserting inlets/outlets for channels..... 67

Figure 4.1. Abstract illustration overview of the Hexagonal FPCB IDT Device. (1) Piezoelectric substrate (128° YX-cut LiNbO₃ substrate) (2) IDE (3) FPCB (4) Mechanical Housing (5) Matching Network (6) Fluidic Vessel (PDMS Ring)..... 71

Figure 4.2. Schematic of Hexagonal IDT design (top view) (a) Entire IDT design showing the IDT fingers, busses, and the dimensions. (b) Zoomed in real image of IDT fingers section (highlighted in green)..... 74

Figure 4.3. Images of the Hexagonal Flexible PCB IDT (top view) showing the front (top) and back (bottom) images (a) Real-life image of the of the Hexagonal FPCB IDT. (b) Rigid PCB KiCad model displaying the design and silkscreen..... 76

Figure 4.4. Hexagonal FPCB IDT Mechanical housing and assembly. (a) Exploded view of the assembly. (b) Cross-sectional illustration of device. (c) Image of real-life model of device. 78

Figure 4.5. A schematic of a two-port network consisting of two IDTs and matching networks, demonstrating the S parameters and their ratio calculations. 79

Figure 4.6. Example of matching network process for R-SAW 0° (X-propagation) at 19. MHz where (a) the circuit diagram of matching network (b) Top view of PCB matching network design (top) and photo of example matching network (bottom) (c) smith chart process (c) S₁₁ with (blue) and without (red) a matching network..... 81

Figure 4.7. PDMS ring fabrication methods (a) 3D printing method. Step 1: Design ring mould using CAD software. Step 2: 3D prints designed mould on a glass slide. Step 3: Pour PDMS into mould and cure for 24 hours on a hot plate. Step 4: Bond cured PDMS ring to substrate. (b) Pipette method. Step 1: Dip pipette tip into PDMS, remove, and blow air into the opposite end of pipette tip to create aperture. Step 2: Place pipette

tip with the coated PDMS onto a glass slide and cure for 5 hours on a hot plate. Step 3: Carefully peel the cured PDMS ring off from pipette using tweezers. Step 4: Bond the peeled PDMS ring onto the substrate.....	83
Figure 5.1. Overall system set-up diagram.....	84
Figure 5.2. Circuit diagram for the device operation of a single IDT.....	85
Figure 5.3. Full system set-up and operation of the Hexagonal FPCB IDT.	86
Figure 5.4. Simplified flow chart illustration of the experimental procedure detailed.	89
Figure 6.1. Conceptual view of the unit cell IDT (Model 1) within the simplified 3D IDT (Model 2) and the life-scale 2D model (Model 3).....	91
Figure 6.2. Model 1: Periodic unit cell IDT. (a) Unit cell IDT dimensions. (b) Boundary labels. (c) “Fine” mesh. (d) Boundary parameter description. (e) Mesh convergence test.	93
Figure 6.3. Model 2: 3D Simplified IDT. (a) Dimensions. (b) Mesh. (c) Boundary condition parameters. (d) Boundary condition labels.	96
Figure 6.4. Model 3: Life-scale 2D Model. (a) Dimensions, with inset displaying 2 IDT fingers. (b) Simulated S_{11} readings at 0° X-rotation for 6 and 80 electrode fingers. (c) Mesh of a section, with an insert illustrating the boundary layer thickness of the viscous boundary layer (δ).	98
Figure 6.5. Simulation comparison of the displacement field for (a) rectangular and (b) trapezoidal IDT at 0° X rotation on 128° YX-cut LiNbO_3 substrate.	98
Figure 6.6. Eigenfrequency simulation results showing R-SAW Frequency at various angles, validated by equation (6.3) and experimental S_{11} measurements. Insert shows eigenfrequency wave mode shape of R-SAW at 0°	100
Figure 6.7. Eigenfrequency simulation results showing calculated R-SAW coupling coefficient and power flow angle at various X-rotation angles.....	101

Figure 6.8. Simulation of R-SAW displacement field for trapezoidal IDT for various X-rotation angles around the substrate (a) 15° (b) 30° (c) 45° (d) 60° (e) 75° (f) 90°. 103

Figure 6.9. Comparison of coupling coefficients in rotated Y-cut LiNbO₃ substrate orientations for R-SAW. The dependence of the in-plane X angle rotations (0°,30°,60°,90°) is shown with different curves. The orientations used in previous studies are marked..... 104

Figure 6.10. Admittance graph for 0.5 mm thick 128° YX-cut LiNbO₃. Demonstrating other wave modes to be investigated. The dependence of the in-plane X rotations of 0°, 30°, 60°, and 90° are shown with different curves. 105

Figure 6.11. Simulated wave modes with respect to in-plane x-rotation angles, with and without an IDT. 107

Figure 6.12. Simulated wave mode characteristics (phase velocity, coupling coefficient, and power flow angle) using the unit cell eigenfrequency results for 128° YX-cut LiNbO₃ substrate at X-rotation angles between 0° and 90°. The wave modes are corresponding to the wave modes phase velocities shown in Figure 6.11 (mode 0 to mode 19). 108

Figure 6.13. Continuation of simulated wave mode characteristics..... 110

Figure 6.14. Simulated wave modes shapes for modes 0 to 4 at 0°, 45°, and 90° X-rotation angle. 112

Figure 6.15. Graph of the relationship between various characteristics and frequency at 0°, illustrating the reflection coefficient (black), Z displacement (green), coupling coefficient (red), and power flow angle (blue)..... 114

Figure 6.16. Wave mode and wavefield of top 3 simulated S₁₁ results at 0° angle with respect to the X-direction where being (a) 19.6 MHz, (b) 35.9 MHz, and (c) 39.4 MHz. 116

Figure 6.17. Graph of the relationship between various characteristics and frequency at 15°, illustrating the reflection coefficient (black), Z displacement (green), coupling coefficient (red), and power flow angle (blue)..... 117

Figure 6.18. Wave mode and wavefield of top 3 simulated S_{11} results at 15° angle with respect to the X-direction where being (a) 19.4 MHz, (b) 35.8 MHz, and (c) 39.2 MHz. 119

Figure 6.19. Graph of the relationship between various characteristics and frequency at 30° , illustrating the reflection coefficient (black), Z displacement (green), coupling coefficient (red), and power flow angle (blue)..... 119

Figure 6.20. Wave mode and wavefield of top 3 simulated S_{11} results at 30° angle with respect to the X-direction where being (a) 18.5 MHz, (b) 19.5 MHz, and (c) 20.5 MHz. 121

Figure 6.21. Graph of the relationship between various characteristics and frequency at 45° , illustrating the reflection coefficient (black), Z displacement (green), coupling coefficient (red), and power flow angle (blue)..... 122

Figure 6.22. Wave mode and wavefield of top 3 simulated S_{11} results at 45° angle with respect to the X-direction where being (a) 17.5 MHz, (b) 20.4 MHz, and (c) 21.4 MHz. 124

Figure 6.23. Graph of the relationship between various characteristics and frequency at 60° , illustrating the reflection coefficient (black), Z displacement (green), coupling coefficient (red), and power flow angle (blue)..... 124

Figure 6.24. Wave mode and wavefield of top 3 simulated S_{11} results at 60° angle with respect to the X-direction where being (a) 20.5 MHz, (b) 31.7 MHz, and (c) 33.7 MHz. 126

Figure 6.25. Graph of the relationship between various characteristics and frequency at 75° , illustrating the reflection coefficient (black), Z displacement (green), coupling coefficient (red), and power flow angle (blue)..... 127

Figure 6.26. Wave mode and wavefield of top 3 simulated S_{11} results at 75° angle with respect to the X-direction where being (a) 30.7 MHz, (b) 33.4 MHz, and (c) 35.5 MHz. 129

Figure 6.27. Graph of the relationship between various characteristics and frequency at 90°, illustrating the reflection coefficient (black), Z displacement (green), coupling coefficient (red), and power flow angle (blue)..... 130

Figure 6.28. Wave mode and wavefield of top 3 simulated S_{11} results at 90° angle with respect to the X-direction where being (a) 30.3 MHz, (b) 33.4 MHz, and (c) 35.4 MHz. 132

Figure 6.29. Eigenmode shape for the key frequency at each angle (0°,15°,30°,45°,60°,75°,90°). Black arrows demonstrating displacement direction. 134

Figure 6.30. Displacement of (a) X and (b) Y at 0° (X-orientation) and 90° X-rotation (Y- orientation), observed from a specific point on the unit models surface with respect to the substrate’s axis, across the frequency range of 15 – 40 MHz. The model illustrates the orientations at 0° and 90° X-rotation for clarity on axis directions. ... 135

Figure 6.31. Illustration of the key wave modes around the 128° YX-cut LiNbO3 substrate. 136

Figure 6.32. Displacement pattern for (a) 2D side view R-SAW displacement (top) and P-SH-SAW (bottom). (b) Z displacement along the length (1000 μm) for both R-SAW (red) and P-SH-SAW (orange). 137

Figure 6.33. 2D side view demonstrating streaming mechanism for (a) R-SAW and (b) P-SH-SAW. The top images show the displacement and pressure distribution. The bottom images show displacement and laminar flow velocity. The white arrows indicate the streaming direction inside the droplet. 138

Figure 7.1. Three configurations (left) of the Hexagonal FPCB IDTs for experimental verification and the corresponding S_{11} values (right) for angles (a) 0° and 60°, (b) 15°, 45°, and 75° (c) 30° and 90°. 140

Figure 7.2. Comparison of experimental and simulated S_{11} results for 0° and 90°. 141

Figure 7.3. Comparison of experimental and simulated S_{11} results across different X-rotation angles with an air gap. (a) Schematic of unit cell model featuring the 0.5 μm air gap. S_{11} results at (b) 0°, (c) 15°, (d) 30°, (e) 45°, (f) 60°, (g) 75°, and (h) 90°. 142

Figure 7.4. Relationship between the clamping force, S_{11} and the droplet velocity on the rigid PCB-IDT [15]. [Reprinted from ‘Development and characterisation of acoustofluidic devices using detachable electrodes made from PCB’ by Mikhaylov *et al.*, Lab on a Chip, Volume 20, Issue 10, 2021, DOI: 10.1088/1361-6439/ac0515. Copyright The Royal Society of Chemistry.] 143

Figure 7.5. Comparison between the droplet velocities, which are driven by different input powers in the PCB-SAW device and CR-IDT [15]. [Reprinted from ‘Development and characterisation of acoustofluidic devices using detachable electrodes made from PCB’ by Mikhaylov *et al.*, Lab on a Chip, Volume 20, Issue 10, 2021, DOI: 10.1088/1361-6439/ac0515. Copyright The Royal Society of Chemistry.] 144

Figure 7.6. Relationship between the clamping force, S_{11} and R-SAW frequency on the FPCB-IDT [419]. [© 2021 IEEE. Reprinted, with permission, from Sun *et al.*, "Flexible Printed Circuit Board as Novel Electrodes for Acoustofluidic Devices," IEEE Transactions on Electron Devices, vol. 68, no. 1, pp. 393, January 2021.] 145

Figure 7.7. Comparison of the pumping velocity of a droplet between the FPCB-IDT and the rigid PCB-IDT device at different input powers (using matching networks) [419]. © 2021 IEEE. Reprinted with permission from Sun *et al.*, "Flexible Printed Circuit Board as Novel Electrodes for Acoustofluidic Devices,". IEEE Transactions on Electron Devices, vol. 68, no. 1, pp. 393, 2021. 146

Figure 7.8. The reproducibility in the (a) R-SAW mode frequency and (b) the minimum S_{11} of the reassembly of a FPCB-IDT device with and without the matching network [419]. [© 2021 IEEE. Reprinted with permission from Sun *et al.*, "Flexible Printed Circuit Board as Novel Electrodes for Acoustofluidic Devices," IEEE Transactions on Electron Devices. vol. 68, no. 1, pp. 393, 2021.] 147

Figure 7.9. FPCB IDT rotation test for investigating the use of the VNWA to register the alignment of the IDTs. The transmitting IDT being rotated around its central point, while the receiving IDT is held fixed. [14]. [Reprinted from ‘A reconfigurable and portable acoustofluidic system based on flexible printed circuit board for the manipulation of microspheres’ by Mikhaylov *et al.*, Journal of Micromechanics and Microengineering, Volume 31, Number 7, 2021, DOI: 10.1088/1361-6439/ac0515.

This figure is licensed under a Creative Commons Attribution 4.0 International License.]..... 148

Figure 7.10. FPCB IDT device S-parameter results for different rotation angles of the IDT where (a) S_{11} (b) S_{21} [14]. [Reprinted from ‘A reconfigurable and portable acoustofluidic system based on flexible printed circuit board for the manipulation of microspheres’ by Mikhaylov *et al.*, Journal of Micromechanics and Microengineering, Volume 31, Number 7, 2021, DOI: 10.1088/1361-6439/ac0515. This figure is licensed under a Creative Commons Attribution 4.0 International License.] 149

Figure 7.11. S_{11} minima for a specific configuration (0° and 60°) of the Hexagonal FPCB IDT showcasing inter-device variability where (a) $0^\circ = 180^\circ$, (b) $60^\circ = 120^\circ = 240^\circ = 300^\circ$ 150

Figure 7.12. Measured average area velocity magnitude for the largest three S_{11} minima frequencies for each configuration. (a) 0° and 60° ($n = 6$), (a) 15° , 45° and 75° ($n = 3$), (c) 30° and 90° ($n = 6$). The absolute S_{11} of the corresponding angle is shown shaded in the same colour. 153

Figure 7.13. Corresponding streaming patterns for optimal frequencies / wave modes (0° at 19.8 MHz, 15° at 19.5 MHz, 30° at 18.6 MHz, 45° at 20.6 MHz, 60° at 32.2 MHz, 75° at 34.2 MHz, and 90° at 34.4 MHz.). The 100 μ l fluid (50:50, water: glycerol) within a PDMS ring was actuated at 30 dBm (1 W). 154

Figure 7.14. Average area velocity magnitude for 0° R-SAW and 90° P-SH-SAW for different (a) viscosity fluids (water: glycerol ratio) (b) IDT power (20 dBm (0.1W), 27 dBm (0.5W), and 30 dBm (1 W)) 155

Figure 7.15. Macro-streaming using 0° R-SAW and 90° P-SH-SAW for a 1 ml fluid volume (PDMS ring diameter 25 mm) showing at $t = 0$ and $t = 2$ seconds. 156

Figure 7.16. Streaming in a culture plate coupled with glycerol. (a) 2D device set-up with a glycerol layer coupling a single 96-well culture plate. (b) Average area velocity magnitude for 0° R-SAW and 90° P-SH-SAW inside a culture plate at different powers. (c) PIVLab image of the streaming velocity magnitude for 90° P-SH-SAW inside a culture plate at 30 dBm. Scale represents 0.25 mm. 157

Figure 7.17. Illustration of concentration test configurations (left) and corresponding numerical analysis (right). (a) R-SAW configuration with 0° X-rotation and PDMS ring offset. (b) D-SAW configuration with 60° X-rotation and PDMS ring offset [12]. (c) P-SH-SAW configuration with 90° X-rotation and PDMS ring offset. 160

Figure 7.18. Concentration results, at 32 dBm power, for different configurations at three different size PS beads (a) 10 µm, (b) 1 µm (c) 500 nm. The three configurations are R-SAW (red), D-SAW (green), and P-SH-SAW (yellow). 163

Figure 7.19. 60° X-rotation D-SAW configurations for concentration, with the PDMS ring placed centrally directly opposite the IDTs. (a) single IDT. (b) pair of opposite IDTs..... 164

Figure 7.20. Concentration results using 60° X-rotation D-SAW single and pair configuration with no offset for (a) 10 µm, (b) 1 µm, and (c) 500 nm sized particles. The red dashed line shows R-SAW concentration for comparison. 166

Figure 8.1. Preliminary cell detachment results. (a) GFP cells with no SAW. (b) GFP cells after SAW has been applied for 1 minute at 4 W (36 dBm). (c) Percentage of green fluorescence and (d) percentage viability with no SAW applied, and after SAW applied (n = 2). 171

Figure 8.2. Preliminary concentration and separation results demonstrating colour cross-over using the microscope (GX Vision Ltd, GXM-L2800). 172

V. List Of Tables

Table 6.1. Parameters for numerical and analytical analysis.	90
Table 6.2. Fitting parameters and values for Taylor series expansion (Equation 6.3) to three significant figures [336].	99

VI. List Of Abbreviations

SAW	Surface Acoustic Wave
TSAW	Travelling Surface Acoustic Wave
SSAW	Standing Surface Acoustic Wave
R-SAW	Rayleigh Surface Acoustic Wave
SH-SAW	Shear Horizontal Surface Acoustic Wave
L-SAW	Leaky Surface Acoustic Wave
P-SH-SAW	Pseudo Shear Horizontal Surface Acoustic Wave
D-SAW	Dual Surface Acoustic Wave
BAW	Bulk Acoustic Wave
IDT	Interdigital Transducer
CR-IDT	Cleanroom Interdigital Transducer
IDE	Interdigital Electrode
FPCB	Flexible Printed Circuit Board
PCB	Printed Circuit Board
LiNbO ₃	Lithium Niobate
LiTaO ₃	Lithium Tantalate
PDMS	Polydimethylsiloxane
PN	Pressure Node

AN	Antinode
PIVLab	Particle Image Velocimetry Lab
CAD	Computer Aided Design
VNWA	Vector Network Analyzer
RF	Radio Frequency
GFP	Green Fluorescent Protein
PS	Polystyrene
CTC	Circulating Tumour Cell
RBC	Red Blood Cell
IPA	Isopropanol Alcohol
RMS	Root Mean Square

VII. List Of Publications

Stringer, M., Zeng, Z., Zhang, X., Chai, Y., Wen, L., Zhang, J., Ong, H., Liang, D., Dong, J., Li, Y., Fu, Y., Yang, X. (2023). Methodologies, technologies, and strategies for acoustic streaming-based acoustofluidics. *Applied Physics Reviews*, 10, 011315.

Mikhaylov, R., **Stringer, M.**, Dumcius, P., Wang, H., Wu, F., Zhang, X., Akhimien, V., Sun, C., Clayton, A., & Fu, Y. (2021). A reconfigurable and portable acoustofluidic system based on flexible printed circuit board for the manipulation of microspheres. *Journal of Micromechanics and Microengineering*, 31(7), 074003.

Dumcius, P., Mikhaylov, R., Zhang, X., Bareford, M., **Stringer, M.**, Errington, R., Sun, C., Gonzalez, E., Krukovski, T., Falcon-Perex, J., Liang, D., Fu, Y., Clayton, A., Yang, X. (2023). Dual-wave acoustofluidic centrifuge for ultrafast concentration of nanoparticles and extracellular vesicles. *Small*, 19, 2300390.

Wang, Q., Maramizonouz, S., **Stringer, M.**, Zhang, J., Ong, H., Liu, Q., Yang, X., Rahmati, M., Torun, H., Pang, W., Wu, Q., Binns, R., Fu, Y. (2024). Acoustofluidic patterning in glass capillaries using travelling acoustic waves based on thin film flexible platform. *Ultrasonics*, 136, 107149.

Sun, C., Dong, Y., Wei, J., Cai, M., Liang, D., Fu, Y., Zhou, Z., Sui, Y., Wu, F., Mikhaylov, R., Wang, H., Fan, F., Xie, Z., **Stringer, M.**, Yang, Z., Wu, Z., Tian, L. & Yang, X. (2022). Acoustically accelerated neural differentiation of human embryonic stem cells. *Acta Biomaterialia*, 151, 333-345.

Zhang, X., Dumcius, P., Mikhaylov, R., Qi, J., **Stringer, M.**, Sun, C., Nguyen, V., Zhou, Y., Sun, X., Liang, D., Liu, D., Yan, B., Feng, X., Mei, C., Xu, C., Feng, M., Fu, Y., Clayton, A., Zhi, R., Dong, Z., Yang, X. Multi-view acoustofluidic rotation cytometry for cytopathology (MARC2). (Submitted with revisions to *Advanced Science*)

VIII. Conference Participation

Stringer, M. Device Demonstration. Reconfigurable Hexagonal FPCB IDT for concentration of micro- and nano- particles. Acoustofluidics 2023.

Dumcius, P., Mikhaylov, R., **Stringer, M.**, et al. A Flexible Printed Circuit Board Based SAW Device for Effective Concentration of Micro-particles. Acoustofluidics 2022.

Mikhaylov, R., **Stringer, M.**, Dumcius, P., et al. An Easy and Accessible Manufacturing Method for Reconfigurable SAW Devices. Acoustofluidics 2021.

1.1 Background

Acoustofluidics use acoustic waves to manipulate fluids and particles within fluids, all in a contact-free and biocompatible manner [1]. Among the techniques in this field, surface acoustic wave (SAW) technology has driven significant advancements in particle manipulation and bio-sensing [1–3]. SAWs have gained extensive interest due to their ability to generate multiple functions on a single platform [3–5]. However, each functionality often requires a specific acoustic mode, necessitating different or multiple geometries and devices, which presents a significant challenge for integration into a single lab-on-a-chip [4].

SAWs can be characterised by two main acoustic wave modes in non-layered SAW devices [5] (shown in Figure 1.1): Rayleigh SAWs (R-SAWs) and Shear Horizontal SAWs (SH-SAWs). R-SAWs involve acoustic propagation near the surface of an elastic medium, creating elliptical particle motion. SH-SAWs involve oscillatory shearing motion along the longitudinal direction. Traditionally, R-SAW has been favoured for acoustofluidic actuation due to its effective energy transfer to fluids [6]. R-SAW mode has been found to support a wide range of fluidic functions through the mechanism of acoustic streaming, which can be used for mixing, pumping, and ejection of sessile droplets [2,7,8]. Whereas, SH-SAWs have been used as an effective fluid biosensor due to its minimal damping or attenuation in fluid, making them less effective for fluid actuation [4,9,10].

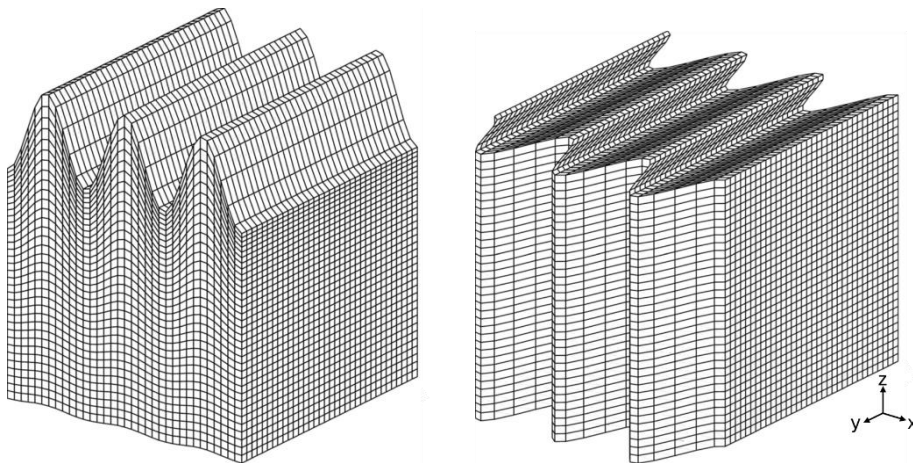


Figure 1.1. Distribution displacements of (a) R-SAW and (b) SH-SAW. [Minor adaptation from [11].]

Pseudo-SAW modes combine characteristics of different wave modes. They can be generated by methods such as actuating SAWs in various directions and frequencies on an anisotropic substrate [12], or by varying the thickness of an anisotropic substrate [4,13]. These combined modes could enhance acoustofluidic actuation through improved acoustic streaming, leveraging the beneficial properties of each wave mode [12]. A multidirectional device using different wave modes could create multifunctional SAW devices for single lab-on-a-chip devices. Therefore, understanding SAW phenomena, particularly when oriented at various angles on anisotropic substrates, is critical for optimizing acoustofluidic effects.

Comprehensive investigations into pseudo-SAW modes and their effects on acoustic streaming remain limited [12]. This limitation is due to the fixed nature of cleanroom fabricated SAW devices, which cannot be adjusted once constructed [14,15]. Investigating various angles would require producing numerous devices, which is prohibitively expensive. Research into different wave modes and their fluid interactions can lead to the development of multidirectional and multifunctional SAW devices, enhancing their acoustofluidic applications.

1.2 Aims and Objectives

The main aim of this research is to investigate innovative configurations for producing acoustic streaming with SAWs to enable microparticle manipulation for versatile biomedical applications.

The objectives of the research include:

- Review the mechanisms and applications of acoustic streaming.
- Develop a reconfigurable device that enables rapid investigation.
- Explore different angles and wave modes, and evaluate how they affect acoustic streaming.
- Simulate and characterise wave modes at different angles.

- Evaluate fluid manipulation capabilities of acoustic streaming produced by different wave modes.
- Evaluate particle manipulation capabilities of acoustic streaming produced by different wave modes.

1.3 Thesis Outline

This thesis is structured into seven chapters, described as follows:

Chapter 1 provides a brief introduction to the thesis and outlines the main aims and objectives.

Chapter 2 reviews the fundamentals of acoustic streaming, the governing equations, and discusses current applications in this field. This chapter includes content published in Stringer *et al.* Methodologies, technologies, and strategies for acoustic streaming-based acoustofluidics. Applied Physics Reviews 1 March 2023; 10 (1): 011315. <https://doi-org.abc.cardiff.ac.uk/10.1063/5.0134646> [2], with the permission of AIP Publishing.

Chapter 3 details the construction of both the active components (SAW devices) and passive components (channel/chamber) of acoustofluidic devices which can perform the streaming applications discussed in Chapter 2. This chapter includes content published in Stringer *et al.* Methodologies, technologies, and strategies for acoustic streaming-based acoustofluidics. Applied Physics Reviews 1 March 2023; 10 (1): 011315. <https://doi-org.abc.cardiff.ac.uk/10.1063/5.0134646> [2], with the permission of AIP Publishing.

Chapter 4 provides comprehensive information about the motivation, rationale, and pathway in the design and development of the Hexagonal Flexible Printed Circuit Board (FPCB) Interdigital Transducer (IDT).

Chapter 5 describes the assembly of the system and experimental platform. This includes the system set-up, and the experimental procedure.

Chapter 6 presents the numerical models and numerical analysis results. This covers numerical analysis of different wave modes at various angles, further numerical analysis of P-SH-SAW.

Chapter 7 presents and discusses the experimental results. This chapter characterises the Hexagonal FPCB IDT explores the experimental investigation of acoustic streaming by different wave modes, the damping effects of P-SH-SAWs, and the concentration capabilities of different wave modes on micro- and nanoparticles.

Chapter 8 summarises the results with reference to the objectives outlined in Chapter 1, draws the main conclusion from the work, and outlines potential future work based on the findings in this thesis.

1.4 Contribution to Knowledge

1. Authored a comprehensive review on acoustic streaming-based acoustofluidics, which was featured on the homepage of a highly reputable journal (impact factor = 15) [2]. This review serves as an invaluable reference in an important and emerging topic for both newcomers and experts in acoustofluidics.
2. Developed an innovative Hexagonal FPCB IDT device that simplifies the acoustofluidic prototyping process, facilitating research and exploration of unique applications.
3. Conducted an in-depth investigation of the anisotropic behaviour, providing a valuable resource and tool for researchers in the field.
4. Discovered a promising wave mode, P-SH-SAW, offering practical benefits for acoustofluidics, including:
 - Enabling macro-scale manipulation ideal for clinical samples sizes.
 - Facilitating cost-effective reuse of single SAW device using disposable and standardised superstrates, such as multi-well culture plates.
5. Explored various concentration configurations, achieving rapid and efficient concentration of micro- and nano- particles

2.1 Introduction

The interaction between acoustic and fluids has ancient roots, illustrated by practices like the Chinese resonance bowl promoting healing [16]. This bowl generates standing waves by inducing vibrations from rubbing the handles, leading to the ejection of water droplets with intriguing patterns [17]. However, it was not until 1866 that research on acoustic streaming began with the design of the Kundt's tube experiment, which aimed to measure the speed of sound in a fluid medium [18]. The experimental setup involved rubbing a resonating rod in a fluid-filled tube, which formed standing waves leading to particle clusters at the nodes [18]. Subsequently, Dvorak, in 1876, first reported acoustic streaming in Kundt's tube, observing airflow from nodes to antinodes and inversely along the wall [19]. Rayleigh's 1884 theoretical model was built on these findings [20]. Scientists such as Schlichting (1932) [21], Westervelt (1953) [22] and Nyborg (1953) [23] expanded the study to incompressible and compressible fluids.

Acoustic streaming induces fluid recirculation and pressure gradients in fluids, offering the potential for particle manipulation, including patterning [24], concentration [25,26], and separation [27,28]. Particle manipulation aims to control particle dynamics precisely and can be realised by various passive methods, such as deterministic lateral displacement, hydrodynamic filtration, and inertial microfluidics [29]. While these methods offer advantages such as simplicity and low costs, they do not always provide precise and on-demand control in comparison to many active ways involving external forces or fields, such as magnetic [30], electrical [31–33], optical [34,35], and ultrasonics or acoustic wave forces. Acoustic waves excel in manipulating various bioparticles, from nanometre-sized extracellular vesicles to micrometre-sized circulating tumour cells (CTCs), with considerable throughputs and high compatibility [36–40]. These non-invasive, label-free tools integrate well with other systems for multifunctionality [3,10,39]. Despite being a studied phenomenon, acoustic streaming has only recently gained traction in microfluidics applications as it overcomes challenges posed by low Reynolds numbers of micro- or nanoscale liquids, whether in sessile droplets or a continuous fluid within microchannels/chambers [41–44].

Acoustic streaming also generates acoustic pressure or force for operations such as deformation, transportation and manipulation of bulk fluid, namely jetting [45,46], nebulisation or atomisation [47–50], microscale streaming [51], object rotation [52,53]. Figure 2.1 summarises the acoustic streaming-based acoustofluidics topic, emphasising biological applications and methodologies (Chapter 2.5) using IDTs based devices (Chapter 3). It illustrates applications (drug delivery [54], bioprinting [55], pumping droplets [56], small organism phenotyping [52], chemical reactions [57], particle sorting/separation [25]) and their respective methodology (nebulisation, jetting, transport, rotation, mixing, separation, trapping). A handful of popular IDT designs (bidirectional IDT, chirped IDT, slanted-finger IDT, and focused IDT) are shown in the centre. Overall, Figure 2.1 displays a glimpse of the potential that acoustic streaming-based acoustofluidics holds.

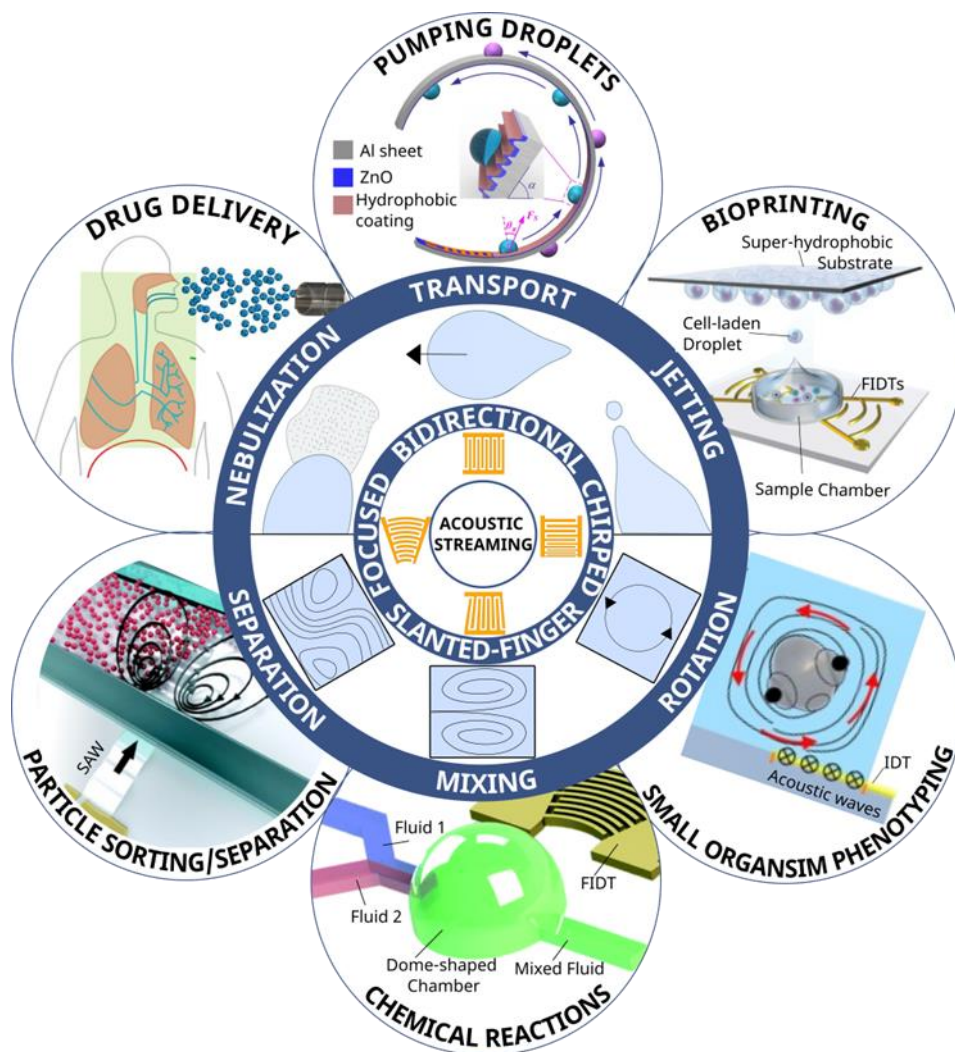


Figure 2.1. Acoustic streaming generation IDT-based acoustofluidic devices, methodologies (nebulisation, jetting, transport, rotation, mixing, separation), and their respective applications in drug delivery [54], bioprinting [55], pumping droplets [56], small organism phenotyping [52], chemical reactions [57], particle sorting/separation [25]). [Reproduced from “Stringer *et al.* Methodologies, technologies, and strategies for acoustic streaming-based acoustofluidics. Applied Physics Reviews 1 March 2023; 10 (1): 011315. <https://doi-org.abc.cardiff.ac.uk/10.1063/5.0134646>” [2], with the permission of AIP Publishing.]

The following chapter focuses on the fundamentals of Acoustofluidics, providing qualitative and quantitative descriptions of its mechanisms and the formation of Acoustic Streaming. Finally, key biomedical applications are discussed, highlighting the importance of Acoustic Streaming in Acoustofluidics.

2.2 Fundamentals of Acoustofluidics

Acoustofluidics refers to manipulating particles in fluids, or the actuation of the fluid itself, through applying acoustic waves. These waves are mechanical, propagating energy through the movements of atoms and molecules and can span infrasonic, audible, and ultrasonic ranges. In Acoustofluidics, ultrasonic waves are particularly favoured as they offer a versatile and powerful toolset for manipulating and controlling fluids and particles. The higher energy levels and frequencies associated with ultrasonic waves enable them to penetrate fluids effectively, facilitating precise manipulation of fluids and particles. This level of high-frequency control proves especially valuable in microfluidic systems, where even small alterations can significantly impact the outcomes.

Ultrasonic waves can be generated using a transducer – a device that converts one form of energy to another. The most popular type of ultrasonic transducer in this field is an electromechanical transducer featuring a piezoelectric crystal. This piezoelectric crystal possesses a remarkable material property known as piezoelectricity, wherein an oscillating electric field is converted into a mechanical vibration. It should be noted that piezoelectric materials exhibit anisotropic properties, implying that they do not possess uniform characteristics across all axes. Anisotropy depends on factors such as crystal symmetry and orientation, which directly influence the type of wave

generated [3]. Further information on this aspect is presented in Chapter 3.3.3, Piezoelectric Substrates, as it constitutes a critical component in the design of acoustofluidic devices.

The acoustic waves generated from the piezoelectric effect can be generally classified into two types [58]: bulk acoustic waves (BAW), where the acoustic wave propagates perpendicular to the material's surface into the bulk medium, and SAW, which propagate along the surface of the material. BAW is produced by applying an alternating current across the two sides of the piezoelectric material. As a result, the acoustic wave propagates throughout the entire thickness, forming a stationary wave at specific frequencies [58]. Depending on the crystalline orientation, the piezoelectric material can expand and contract perpendicularly to the surface [58]. On the other hand, SAW is typically produced using metallic electrodes that consist of two interlocking comb-shaped arrays called interdigital electrodes (IDEs). These IDEs are patterned onto a piezoelectric substrate to produce the IDTs. Further information on the design of these IDTs for Acoustofluidic Devices is discussed in Chapter 3. When a radio frequency (RF) voltage is applied to the IDTs, it causes alternating regions of tensile and compressive strains between the fingers of the electrode, thus producing mechanical waves that can propagate on the surface. While IDTs have been extensively researched in the past fifty years for applications in RF communications, filter applications [59,60], and RF identification [59,61,62], their potential in acoustofluidic applications remains a relatively new and intriguing area for exploration[60,63].

Note that this thesis predominantly centres around SAW-based acoustofluidic devices for acoustic streaming. The choice is attributed to the versatile design adaptability of SAWs, allowing for generating diverse acoustic wave modes, miniaturisation, low power consumption, and precise manipulation capabilities. Hence, BAW-based streaming information is presented briefly, focusing on fundamental details. The inclusion of BAW-based applications could extend the thesis beyond its intended focus.

SAW's capability to offer a wide range of surface wave modes benefits various applications [10]. Among these, Rayleigh waves are generated by most acoustofluidic

SAW devices due to their strong interaction with liquids and particles. Rayleigh waves propagate along the surface of the substrate with both longitudinal and vertical shear components. In Rayleigh waves, particles on the surfaces have elliptical trajectories and show a rapid decay of particle oscillation with depth [64]. The waves' velocity depends on the substrate's material and the crystals' orientation. A conventional Rayleigh SAW device comprises an IDT that produces travelling SAW (TSAWs), as shown in Figure 2.2(a). When two identical IDTs face each other (Figure 2.2(b)), they generate two oppositely propagating TSAWs that interfere, leading to a standing SAW (SSAW) with pressure nodes (PNs) and antinodes (ANs), which are often used for particle manipulation [65,66].

In addition to the fundamental Rayleigh waves (depicted in Figure 2.2(c)), SAWs can produce wave modes. For example, high wave modes in a layered device known as Sezawa waves primarily propagate through boundaries or interlayers at velocities greater than the top layer [64]. Lamb waves (Figure 2.2(d)), generated in a thin plate or membranes, share similarities to Rayleigh waves; however, they travel along the whole plate structure (i.e., along both upper and lower surfaces), resulting in two free surfaces as guiding boundaries instead of just one [67]. Shear horizontal SAWs (SH-SAWs, Figure 2.2(e)) propagate on the substrate surface and various piezoelectric thin films with in-plane crystal textures [68]. Love waves arise in SH-SAWs (Figure 2.2(e)) when the surface is covered with a thin waveguide layer. The SH-SAWs and Love mode waves are predominantly employed for biosensing rather than microfluidic applications due to their limited damping effects or weak coupling with the liquid compared to Rayleigh waves [64]. It should be noted that in practice, these wave modes can often exhibit a blend of different components.

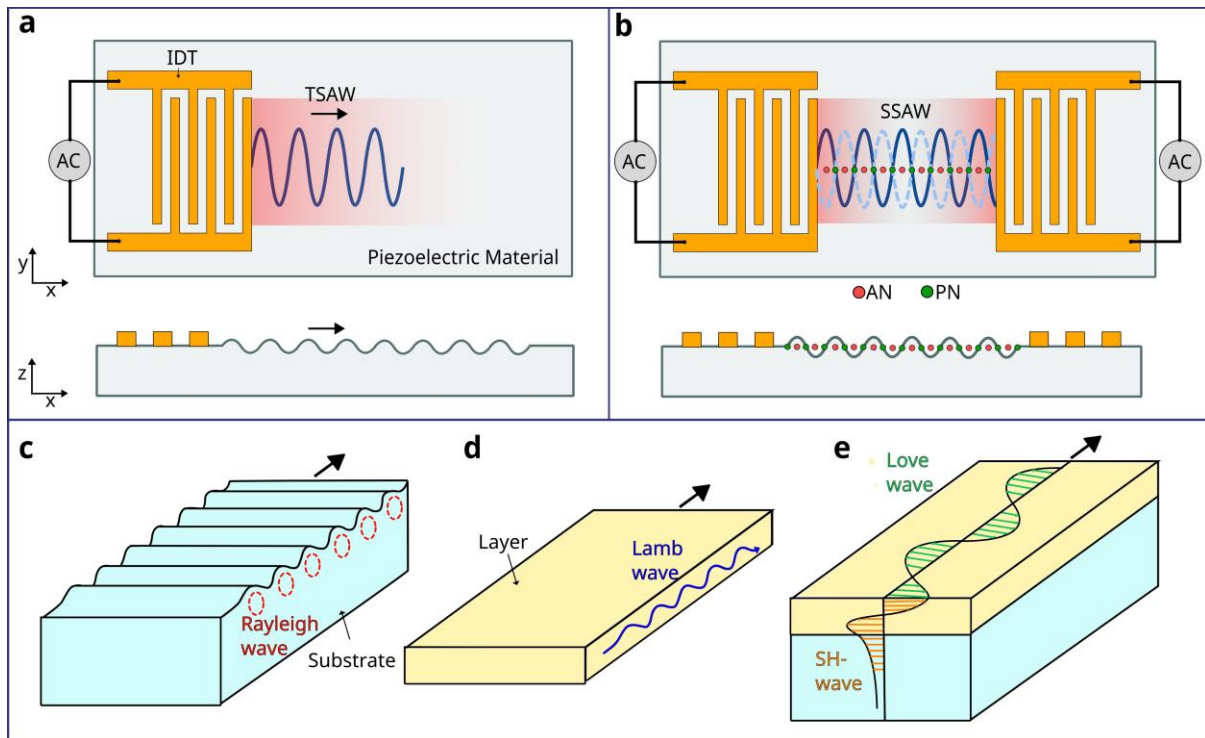


Figure 2.2. Schematic illustrations of SAW devices [69] and types of wave propagation through the distribution of displacements [68]. (a) Top and side views of SAW generated by a single IDT, producing TSAW. (b) Top and side views of SAW generated by a pair of opposite IDTs, producing SSAW, demonstrating regions of PNs and ANs. (c) Rayleigh wave[70] (d) Lamb waves[71] (e) Shear horizontal waves and Love waves[64]. [Reproduced from “Stringer *et al.* Methodologies, technologies, and strategies for acoustic streaming-based acoustofluidics. *Applied Physics Reviews* 1 March 2023; 10 (1): 011315. <https://doi-org.abc.cardiff.ac.uk/10.1063/5.0134646>” [2], with the permission of AIP Publishing.]

2.3 Governing Equations

Fluid dynamics enables the study of the behaviour of fluids under the influence of external forces such as acoustic forces. This section delves into the fundamental fluid dynamics equations and explores the forces specific to Acoustofluidics.

Fluid Dynamics

The fundamental equations governing fluid dynamics are the Continuity and Navier-Stokes equations, which describe how the velocity and pressure of a fluid change in

response to external and internal properties. Acoustofluidics is analysed quantitatively using this continuity (conservation of mass) and Navier-Stokes (conservation of momentum) equations. In the general form for compressible fluids, respectively, these equations are, [17]

$$\frac{\partial \rho}{\partial t} + \nabla \cdot (\rho \mathbf{v}) = 0 \quad (2.1a)$$

$$\rho \left(\frac{\partial \mathbf{v}}{\partial t} + (\mathbf{v} \cdot \nabla) \mathbf{v} \right) = -\nabla p + \mu \nabla^2 \mathbf{v} + \left(\mu_b + \frac{\mu}{3} \right) \nabla (\nabla \cdot \mathbf{v}) + \mathbf{F}_{SAW} \quad (2.1b)$$

The continuity equation (Equation 2.1a) states that the rate of change of mass density (ρ) with respect to time (t), plus the divergence of mass flux density ($\rho \mathbf{v}$, where \mathbf{v} is the velocity vector) must be zero. In basic terms, it means that the mass is conserved, and the change in density is due to fluid flow.

The Navier-Stokes equation (Equation 2.1b) describes how the velocity of the fluid changes over time and space due to pressure gradients, viscous forces, and external forces. Here, ρ is the fluid density, \mathbf{v} is the velocity vector, p is the pressure, μ is the dynamic shear viscosity of the fluid, μ_b represents the bulk or dilatational viscosity. The term \mathbf{F}_{SAW} is the SAW action force, defined as the energy transferred by SAW to the fluid medium [72],

$$\mathbf{F}_{SAW} = -\rho(1 + \alpha_1^2)^{\frac{3}{2}} A^2 \omega^2 k \exp(2[kx + \alpha_1 kz]) \quad (2.2)$$

where $\alpha_1 = -j(\sqrt{1 - (v_s/v_l)^2})$ is the attenuation coefficient, A the wave amplitude, ω the wave frequency and k the SAW wave number, which can be calculated by a linear function of the wave frequency [72].

The left-hand side of the Navier-Stokes equation is the inertia force per unit volume of fluid. The first term is unsteady acceleration, which represents the acceleration of the fluid particles. The second term is convective acceleration, which accounts for the advection of momentum associated with Reynolds stress [17]. The net forces per unit volume on the right side include pressure gradient (first term) and viscosity gradients (second and third term) [73]. For incompressible fluids ($(\nabla \cdot \mathbf{v}) = 0$) the third term may be neglected. All external fields, such as gravity, buoyance, and electromagnetism,

have not been considered for simplicity. The heat transfer equation is normally not required as only the isothermal case has been considered in many cases [74]. These equations can be used with the boundary conditions and the linear relationship between pressure p and mass density ρ to predict the motion of the fluid and, hence, acoustic streaming [75].

$$p = c_0^2 \rho \quad (2.3)$$

where c_0 is the speed of sound in the fluid. Nonetheless, solving these equations analytically presents considerable challenges. The concept with a well-established basis is perturbation theory, which only applies to slow streaming scenarios and not fast streaming [3,7].

Reynolds number (R_e) serves as a parameter characterising the fluid flow. It represents the ratio of inertia to viscous terms. The flow is laminar when the viscous force dominates or turbulent when the inertia forces dominate. In the context of slow streaming, the effect of inertia on the streaming motion is negligible compared to viscous effects, leading to laminar flow. In contrast, fast streaming occurs when the effect of inertia cannot be disregarded, indicating that $R_e > 1$. Reynolds number depends on the flow velocity and the fluid mechanical system [76]. It is defined as,

$$R_e \equiv \rho U_0 \mathcal{L} / \mu \quad (2.4)$$

where \mathcal{L} is the characteristic length, $U_0 \equiv |\mathbf{U}|$ is the characteristic flow velocity, which includes the velocity of the fluid \mathbf{v}_0 and the effect of the acoustic propagation $|\mathbf{U}| = \mathbf{v}_0 + \langle \rho_1 \mathbf{v}_1 \rangle / \rho_0$. Reynolds number for each streaming form uses a different length scale: Schlichting $\mathcal{L} = \delta_v$, Rayleigh $\mathcal{L} = \lambda$ and Eckart $\mathcal{L} = L$. δ_v is viscous penetration depth, and L is a characteristic length scale much larger than the acoustic wavelength λ [17].

Due to their small dimensions, the R_e tends to be low in most microfluidic systems. As a result, the flow is typically laminar, and no turbulence occurs. For slow streaming, perturbation theory provides a reliable linear model to predict the behaviour. However, in cases of fast streaming, where R_e can become considerably high, and the flow becomes unstable, the nonlinear term needs to be considered in the analysis [17,75].

Perturbation theory is a method to find approximate solutions for the continuity and Navier-Stokes equations, represented by Equation 2.1. By considering minor disturbances in density, pressure, and velocity, a linearised form of these equations can be derived,

$$p = p_0 + \varepsilon p_1 + \varepsilon p_2 + \dots \quad (2.5a)$$

$$\rho = \rho_0 + \varepsilon \rho_1 + \varepsilon \rho_2 + \dots \quad (2.5b)$$

$$\mathbf{v} = \mathbf{v}_0 + \varepsilon \mathbf{v}_1 + \varepsilon \mathbf{v}_2 + \dots \quad (2.5c)$$

where subscripts 0, 1, and 2 denote static (absence of sound), first-order, and second-order quantities, respectively. In the absence of sound, the undisturbed state, \mathbf{v}_0 , is 0 as the fluid is quiescent. To quantify the smallness perturbations, the Mach number $\varepsilon = v_1/c_0$ is used [17], where v_1 is the fluid velocity, and c_0 is the speed of sound. The perturbation method relies on the assumption that successive approximations converge. Consequently, ε must be sufficiently small, making the method applicable only for slow streaming analysis [17]. The successive approximations do not converge for fast streaming, rendering the perturbation approach unsuitable for such cases.

By incorporating perturbation expansions, the continuity and Navier-Stokes equations can be solved for each order component of the acoustic field. The first-order acoustic field solution describes acoustic wave motions in the system, encompassing oscillatory motions characterised by \mathbf{v}_1 , the acoustic velocity, and p_1 , the acoustic pressure field. The first order acoustic field solution is

$$\frac{\partial \rho_1}{\partial t} + \nabla \cdot (\rho_0 \mathbf{v}_1) = 0 \quad (2.6a)$$

$$\rho_0 \frac{\partial \mathbf{v}_1}{\partial t} = -\nabla p_1 - \mu \nabla^2 \mathbf{v}_1 + \left(\mu_b + \frac{\mu}{3} \right) \nabla \nabla \cdot \mathbf{v}_1 \quad (2.6b)$$

This first-order solution is substituted into second-order equations and time-averaged to find the solution for acoustic streaming $\langle \mathbf{v}_2 \rangle$ [17].

$$\left\langle \frac{\partial \rho_2}{\partial t} \right\rangle + \nabla \cdot \langle \rho_1 \mathbf{v}_1 \rangle + \rho_0 \nabla \cdot \langle \mathbf{v}_2 \rangle = 0 \quad (2.7a)$$

$$\rho_0 \left\langle \frac{\partial v_2}{\partial t} \right\rangle + \langle \rho_1 \frac{\partial v_1}{\partial t} \rangle + \rho_0 \langle (\mathbf{v}_1 \cdot \nabla) \mathbf{v}_1 \rangle = -\nabla \langle \rho_2 \rangle + \mu \nabla^2 \langle \mathbf{v}_2 \rangle + \left(\mu_b + \frac{\mu}{3} \right) \nabla \nabla \cdot \langle \mathbf{v}_2 \rangle \quad (2.7b)$$

This streaming consists of both harmonic and steady components [3]. Physically, the second-order time-averaged velocity $\langle \mathbf{v}_2 \rangle$ is the acoustic streaming, and the second-order time-averaged pressure $\langle p_2 \rangle$ produces the acoustic radiation force that occurs when the acoustic waves are scattered on the particles, causing them to move [74].

Zaremba [77] proposed an alternative approach that overcomes the limitations of the perturbation method, enabling the calculation of acoustic streaming velocities exceeding particle velocities, such as the case for fast streaming. This approach involves decomposing the dependent variables in the fluid into a time-averaged streaming flow component and an instantaneous first-order component. The streaming motion can be solved by substituting the variables into the continuity and Navier-Stokes equations and performing time averaging over the exception period [17]. By employing this method, it is possible to study cases of fast streaming and obtain results for acoustic streaming velocities.

Acoustofluidic Forces

Particles in a fluid experience various forces when exposed to an acoustic wave. These forces can be categorised into two main types: the net acoustic radiation force \mathbf{F}^{ARF} and the SAW acoustic streaming-induced Stokes drag force \mathbf{F}^{drag} [78]. The dominance of either force depends on the size of the particles, particularly larger than a certain threshold size, which is primarily influenced by acoustic radiation force [3]. This threshold size is influenced by actuation frequency, acoustic contrast factor, and kinematic viscosity [79].

The net acoustic radiation force comprises two components: primary acoustic radiation pressure and secondary acoustic radiation pressure. Primary acoustic radiation pressure represents the force exerted on an individual particle in a fluid due to the direct irradiation by the acoustic field [3]. In comparison, secondary acoustic radiation pressure is the force that arises from the acoustic interactions between particles in the fluid [3]. The particle moves towards either the PNs or ANs depending on its

mechanical properties, with its destination determined by the acoustic contrast factor [3,80].

To quantify \mathbf{F}^{ARF} , a surface integral of the time-averaged second-order pressure p_2 and momentum flux tensor $\rho_0 \langle \mathbf{v}_1 \mathbf{v}_1 \rangle$ at a fixed surface just beyond the oscillating sphere is employed [81,82]. Hence, the generalised equation can be written as:

$$\mathbf{F}^{ARF} = - \int_{\partial\Omega} da \{ \langle p_2 \rangle \mathbf{n} + \rho_0 \langle (\mathbf{n} \cdot \mathbf{v}_1) \mathbf{v}_1 \rangle \} \quad (2.8)$$

where \mathbf{n} is the unit normal vector of the particle surface directed into the fluid.

Additionally, particles in a fluid experience the Stokes drag force (\mathbf{F}^{drag}) resulting from acoustic streaming induced by the SAW. \mathbf{F}^{drag} depends on particle size and shape, the fluid flow field, and viscosity [83]. For a spherical particle of radius r , with medium viscosity η and relative velocity v , \mathbf{F}^{drag} it is given by [83,84]

$$\mathbf{F}^{drag} = 6\pi\eta r v \quad (2.9)$$

It is important to note that microfluidics introduces a range of significant forces at small scales, such as surface tension and viscosity. In contrast, at a larger scale, forces like gravity become more influential [17]. Moreover, particle-particle interaction forces, like *van der Waals* interactions, electrostatic interactions and hydrophobic/hydrophilic effects, also play a role [8].

2.4 Formation of Acoustic Streaming

Acoustic streaming exhibits diverse forms and is sensitive to varying geometries and boundary conditions. It is observed in Newtonian fluids, superfluids, and non-Newtonian viscoelastic fluids, hence finding wide-ranging applications [85]. This section aims to provide an overview of acoustic streaming, starting with its fundamental concepts and then delving into its generation mechanisms and classifications.

Acoustic streaming arises as a liquid flow phenomenon, resulting from forces originating from the gradient in time-averaged acoustic momentum flux in a fluid [8,86]. Put simply, it is the fluid flow generated by the attenuation of an acoustic wave in the

fluid. It can be classified into two common types: boundary-driven and bulk-driven streaming (Eckart streaming or quartz wind) [8].

Boundary-driven streaming is characterised by the attenuation of the acoustic wave at the container walls, forming inner (Schlichting streaming) and outer boundary streaming (Rayleigh streaming) vortices. When an acoustic wave propagates parallel to a solid boundary, the non-slip boundary creates a high-velocity gradient perpendicular to the surface. The high-velocity gradient is what causes the generation of a steady inner boundary layer vorticity confined within the thin viscous boundary layer (referred to as the shear-wave layer or Stokes layer) of thickness given by $\delta_v = \sqrt{2\nu/\omega}$, where ν is the kinematic viscosity, and ω is the angular frequency of the acoustic wave [75]. The resulting strong inner boundary streaming induces counter-rotating vortices within the fluid, the outer boundary streaming [75]. Examples include wave propagation in waveguides, standing waves in resonant chambers, or waves scattering off solid objects [75]. This streaming predominantly occurs in smaller acoustofluidic channels, where the characteristic length scale of the fluid chamber (h) is much smaller than the acoustofluidic wavelength (λ), expressed as $\lambda \gg h \gg \delta_v$.

In contrast, bulk-driven streaming, also known as Eckart streaming, originates from the viscous attenuation within the bulk of the fluid [8]. As described by Stoke's Law, the dissipation rate of sound energy leads to a steady momentum flow, generating a fluid jet along the direction of acoustic propagation. This fluid jet, in turn, creates a vortex-like flow due to the fluid replacement and pressure difference from the sides of the chamber [87]. Bulk-driven streaming becomes more pronounced in larger devices, where the length of the fluid chamber (L_E) exceeds the acoustic wavelength, expressed as $L_E \gg \lambda$ [88].

It should be noted that the driving mechanism for streaming significantly varies between BAW and SAW systems. In BAW systems, streaming is mainly driven by boundary layer effects (Schlichting streaming and Rayleigh streaming). In contrast, in SAW systems, it is primarily due to the velocity gradient resulting from the attenuation within the fluid (bulk-driven streaming) [89–91]. The angle of sound propagation plays a crucial role; for BAW systems, the sound propagation is parallel to the edge of the fluid chamber, giving rise to strong boundary effects, whilst these effects are lessened

in a SAW system where the sound propagates at an angle to the boundary [89]. Nevertheless, inner boundary streaming may arise in SAW systems due to the transmission of shear from the substrate to the fluid [90]. Consequently, this can induce outer boundary streaming in the bulk of the fluid. However, it is important to note that boundary layer streaming is not commonly reported in SAWs [92] and often remains negligible compared to bulk streaming, particularly if the fluid container size and SAW attenuation length greatly exceed the SAW wavelength [93].

Understanding these driving mechanisms and their impact on fluid interactions provides valuable insights into the formation of streaming patterns when the wave contacts a liquid. For example, when SAW contacts a liquid, a portion of the SAW refracts into the liquid as a longitudinal wave at an angle known as the Rayleigh angle θ_R [3,94], given by,

$$\theta_R = \sin^{-1} \frac{v_l}{v_s} \quad (2.10)$$

where v_s is the SAW velocity on the surface material, and v_l is the acoustic velocity in the liquid [95]. For example, a Rayleigh angle of about 22° is obtained when using a 128° YX-cut lithium niobate (LiNbO_3) piezoelectric substrate at room temperature, where the SAW velocity is about 3,990 m/s, and the speed of sound in water is 1,490 m/s [3]. This value can be as large as 41° for a ZnO/Al plate SAW-based device, as the SAW velocity in the aluminium substrate is about 1,835 m/s [96]. Consequently, the SAW undergoes a mode change into a leaky SAW within the fluid, with its intensity attenuating exponentially as it propagates through the medium due to viscosity [97]. This decay length is the attenuation length, α^{-1} [98]:

$$\alpha^{-1} = \frac{\rho_s v_s^2}{f \rho_l v_l} \quad (2.11)$$

where ρ_l and ρ_s are the densities of the fluid and the solid, respectively. On the other hand, SAW propagates within the liquid medium following the Rayleigh angle, exhibiting a significantly greater attenuation length, β^{-1} [86]:

$$\beta^{-1} = \frac{\rho_1 v_1^3}{4\pi^2 f^2 (\frac{4}{3}\mu + \mu')} \quad (2.12)$$

where μ and μ' are the shear and bulk viscosities of the fluid, respectively.

Nonetheless, the streaming pattern induced by SAW exhibits a significant variation depending on the shape of the confined liquid. Two primary categories of acoustofluidics have been established to address this: digital acoustofluidics and continuous flow acoustofluidics. Typical SAW streaming patterns that may occur for digital and continuous acoustofluidics are displayed in Figure 2.3. Figure 2.3(a-c) and Figure 2.3(d-e) illustrate streaming patterns in droplets and channels, respectively, demonstrating the varying streaming patterns with different SAW propagation positions and directions (blue arrow).

Digital acoustofluidics involves sessile droplets subjected to an acoustic field. These droplets serve as sample carriers, enabling systematic sorting, trapping, micing, pipetting, and splitting. This approach offers numerous advantages, such as reduced sample consumption, high throughput, flexible manipulation, the elimination of cross-contamination, and the need for complex channel fabrication [99]. The specific parameters of the droplets, such as their shape, volume, contact angle, and evaporation rate, play a crucial role in determining the resulting acoustic streaming patterns, which subsequently influence the behaviour of particles [100,101]. Figure 2.3(a) illustrates an example of a droplet streaming pattern with SAW propagation entering from the left, forming two vortexes. Figure 2.3(b) showcases streaming when the SAW propagates laterally offset to the droplet, creating a single vortex. Additionally, Figure 2.3(c) displays SSAW propagation, generating four vortexes. The applications of these streaming types, which include mixing, concentration, and pumping, are further explored in Sections 2.5.1.1, 2.5.1.2 and 2.5.2.1.

Continuous flow acoustofluidics involves the liquid within microchannels or chambers interacting with acoustic waves. Channels and chambers offer distinct advantages, including containing larger liquid volumes, accommodating flow, and modifying boundary conditions for versatile applications. It is important to note that the boundary of a channel or chamber significantly impacts its applications. This boundary can be

composed of different materials (e.g., glass capillary, polydimethylsiloxane (PDMS)), interfaces (e.g., liquid-air, liquid-glass) or geometries (e.g., different dimension/shape tubes or chambers). Figure 2.3(d) and Figure 2.3(e) illustrate continuous flow acoustofluidic patterns, where the fluid is driven by propagating SAWs originating from the left and the bottom of the channel, respectively. These SAWs create two distinct vortex-like flows, one at the top and bottom, and the other at the left and right sides of the channel. These streaming patterns offer versatile applications, including mixing, concentration, and rotation, as outlined in Section 2.5.1.3. Furthermore, Figure 2.3(f) illustrates SSAW streaming from a front-view perspective, revealing the presence of two vortices [102]. These applications of SSAW streaming are discussed in Section 2.5.2.2.

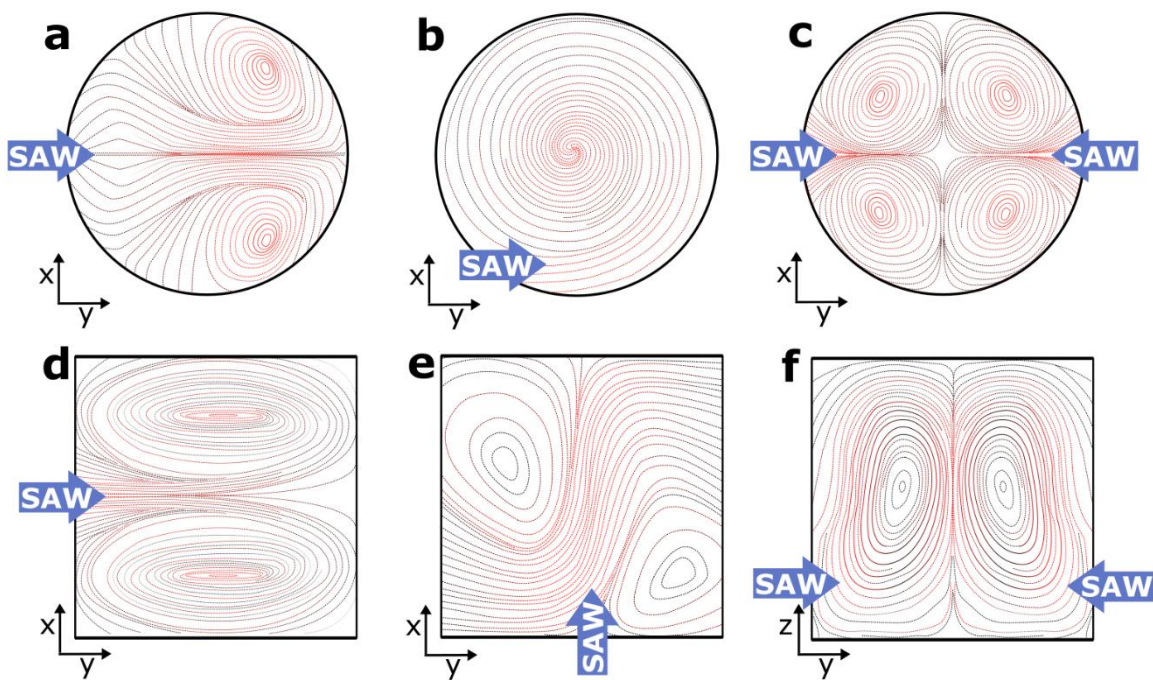


Figure 2.3. Illustration of two-dimensional fundamental streaming patterns for (a-c) droplets and (d-f) channels, with varying positions of SAW propagation indicated by the blue arrows. In the droplet top view, SAW propagation enters from (a) the left, (b) laterally offset, and (c) both left and right (SSAW). In the channel top view, (d) and (e) streaming patterns, the SAW propagation enters from the left and bottom, respectively. In the front view, (f) streaming patterns with SAW propagation from both the left and right result in SSAW streaming. [Reproduced with minor adaption from “Stringer *et al.*; Methodologies, technologies, and strategies for acoustic streaming-based

acoustofluidics. Applied Physics Reviews 1 March 2023; 10 (1): 011315. <https://doi-org.abc.cardiff.ac.uk/10.1063/5.0134646> [2], with the permission of AIP Publishing.]

It is important to acknowledge that the SAW-induced streaming patterns in digital and continuous flow acoustofluidics exhibit significant variation influenced by various factors. For instance, the input power applied to a transducer for actuating a droplet can considerably vary the streaming patterns. At low input powers (in the order of mW), preliminary acoustic streaming on the free surface is generated, which can be used for vibration, mixing and driving applications. Higher input power (e.g., above a few watts) leads to a breakup of the stabilising interface and allows for techniques such as jetting, atomisation or nebulisation [100]. Other aspects include the type of configuration used to actuate the acoustic signal (e.g., the IDT design), the incident position, the angle, and the operating frequency [3]. A comprehensive exploration of these aspects is presented and discussed in detail in Chapter 3. Acoustofluidic Devices. The following section will delve into the applications of acoustic streaming, building upon the streaming patterns discussed in this section.

2.5 Applications of Acoustic Streaming

Acoustofluidic devices are increasingly used in biomedical applications as they are non-invasive, label-free, and meet most point-of-care requirements. Acoustic streaming-based acoustofluidics is versatile and tuneable, providing flexibility and adaptability for various tasks. These advantages make acoustic streaming an attractive and valuable tool in various biomedical applications, supporting research, diagnostics, and potential personalised medicine and healthcare advancements.

This thesis section will be organised by first categorising applications based on whether they utilise TSAWs or SSAWs-based acoustic streaming technique. Applications will be further classified within each technique based on whether they involve digital or continuous acoustofluidic systems. Subsequently, the methodologies employed within each category, such as mixing, concentration, and pumping, will be discussed.

2.5.1 TSAWs based streaming and acoustofluidics

2.5.1.1 Mixing, concentration, and splitting of sessile droplets in digital acoustofluidics

Mixing

Microfluidic applications involving sessile droplets encounter challenges due to diffusion-limited mixing linked to their small dimensions. SAW devices offer a solution by acting as effective mixers. The implementation of TSAW-induced streaming proves successful for mixing sessile droplets [103] and nanolitre order droplets [104], as shown in Figure 2.4(a). The ability to manipulate droplets is promising for micro-total-analysis systems, especially in portable healthcare.

Microfluidic functionality can be enhanced with the addition of other techniques. For instance, an electric field can increase the streaming velocity in a droplet by a factor of about 2-3 [105]. Moreover, employing a focused SAW [106] significantly elevates the streaming force by 480% compared to conventional SAW [107]. Additionally, other technologies can be combined, such as metal-enhanced fluorescence [108], electrowetting on dielectric [109], or surface plasmon resonance system [51] to improve mass transfer through mixing. Such mixing and mass transfer capabilities are valuable for biological sensors, for example, cleaning biosensors and removing fouling caused by nonspecific binding proteins on the surface, for more accurate determination and reuse of the devices [110]. A demonstration is found in a study that employs this method to shorten SARS-COV-2 antibody immunoassay from 20 min to 40 s, enabling rapid detection and minimising sample waste [111].

As a result of the mixing and, hence, inhomogeneous acoustic streaming in a droplet, cells within the liquid droplet will experience a shear force [112]. This shear force may interact with cells through biological pathways, including the cell membrane, extracellular matrix, and cytoskeleton, instead of simply displacing cells [113]. The shear forces can induce action potentials [114] and calcium responses [115] in neurons. This has significant implications for neuroscience research and the treatment of neurological disorders. Notably, SAW-based techniques offer advantages over traditional ultrasound methods for neuron stimulation, such as generating less self-

heating, less cavitation, and physically smaller [113]. Furthermore, mixing-induced shear forces can affect cell adhesion and survival rate in cell culture [112,116–118]. Investigating and evaluating cell properties is instrumental in better understanding biological processes. Cell adhesion is important for wound healing, cell growth and immune response. For example, a SAW device has been used for the characterisation of adhesive properties of red blood cells (RBCs) in a 9 μm droplet within just 30 s [116]. Similarly, the detachment and sorting of human embryonic kidney 293 cells from A7r5 cells, displayed in Figure 2.4(b), were based on differences in adhesion strength within minutes [118]. This showcases rapid diagnostics and disease monitoring in a small fluid volume, preventing the need for external rising agents such as trypsin, typically used for cell detachment from the solid substrate. The shear force produced through TSAW-induced mixing can also aid in gentle and controllable cell lysis. For example, the collision between cells and magnetic Ag-nanowires in a droplet can lead to 97% lysis efficiency with a power of just 1 Watt [119]. Cell lysis is vital for detecting intracellular secrets for biochemical detection, biomechanical analysis, and biophysics [119].

Acoustic streaming-based droplet mixing also holds significance for particle manipulation techniques. One application is a particle sampling device for collecting airborne micro-particles [120], which is important given the increasing risk of bioterrorism and the emergence of antibiotic-resistant bacteria. Moreover, TSAW mixing enables size-tuneable nanoparticle fabrication using droplet fusion [121] (Figure 2.4(c)), which is beneficial for treating cancer and genetic diseases.

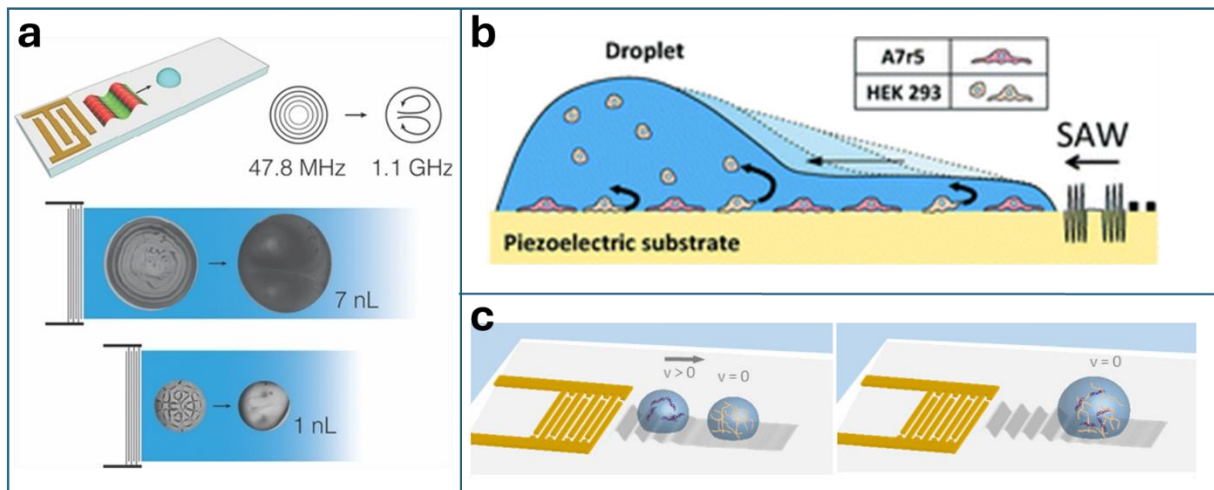


Figure 2.4. Examples of applications of TSAW streaming for digital acoustofluidic mixing. (a) Nanolitre order droplet mixing [Minor adaptation from [104]]. (b) Cell detachment for diagnostics [Reproduced from [118]]. (c) Nanoparticle formation via droplet fusion [Reproduced from [121]].

Concentration and Separation

The key to concentration within a droplet lies in the asymmetric SAW radiation distribution along the droplet width [122]. This method can concentrate polystyrene microspheres (1 to 45 μm) and living yeast cells (10-20 μm) at low powers from 120 to 510 mW [122]. The particle enrichment enhances analyte detection sensitivity, overcomes diffusion limits without particle damage, and broadens sensor applications. Particle concentration is controlled by factors such as particle diameter, SAW frequency, acoustic wave field (travelling or standing), acoustic waves' attenuation length, droplet volume [26] and the contact angle [123]. One study shows four distinct regimes (R1-R4) [26]: concentrated particles at the centre (R1), particle ring around the periphery (R2), particles at the side of the droplet (R3), and smaller ring of particles near the centre (R4) [26]. Additionally, adjusting the contact angle allows label-free, noncontact concentration of cancer cells as shown in Figure 2.5(a). Such concentration can mimic a primary tumour site, serving as a valuable cancer cell model for advancing cancer therapy [124].

The concentration process may be augmented by employing different forms of SAW. For instance, circular and elliptical SAWs, can rapidly concentrate particles in under 1 s due to their increased wave intensity and asymmetry, – this is several orders of

magnitude faster than conventional microscale devices [106]. Amplitude modulation can further improve the speed of particle concentration by up to 70% and reduce droplet temperature [125].

Combining acoustic radiation force and acoustic streaming can efficiently concentrate and separate microparticles of different sizes within a droplet [126,127]. For example, SAW actuations can separate malaria-infected RBCs (shown in Figure 2.5(b)) based on density differences in less than 3 s while maintaining the capability to detect infection levels as low as 0.0005% [128]. This rapid separation demonstrates the potential for point-of-care diagnosis, especially at low infection levels. Moreover, this technology can be employed with finger-prick blood samples [128], further enhancing accessibility.

Despite challenges in nanoscale manipulation due to dominant acoustic streaming and insufficient radiation force, acoustic centrifuge motion offers a biocompatible and versatile solution [28]. This method is important for gene/drug delivery, precision bioassays, cancer diagnosis, and catalysing reactions. This system facilitates differential concentration and separation, notably exosome separation (<100nm size range), transport, drug loading and encapsulation [28,129] (displayed in Figure 2.5(c)). Nevertheless, the extraction process of the separated species is often challenging. An omnidirectional spiral SAW configuration can extract size-based particles and cells [27]. This can be used for platelets from mouse blood for further integrated point-of-care diagnostics.

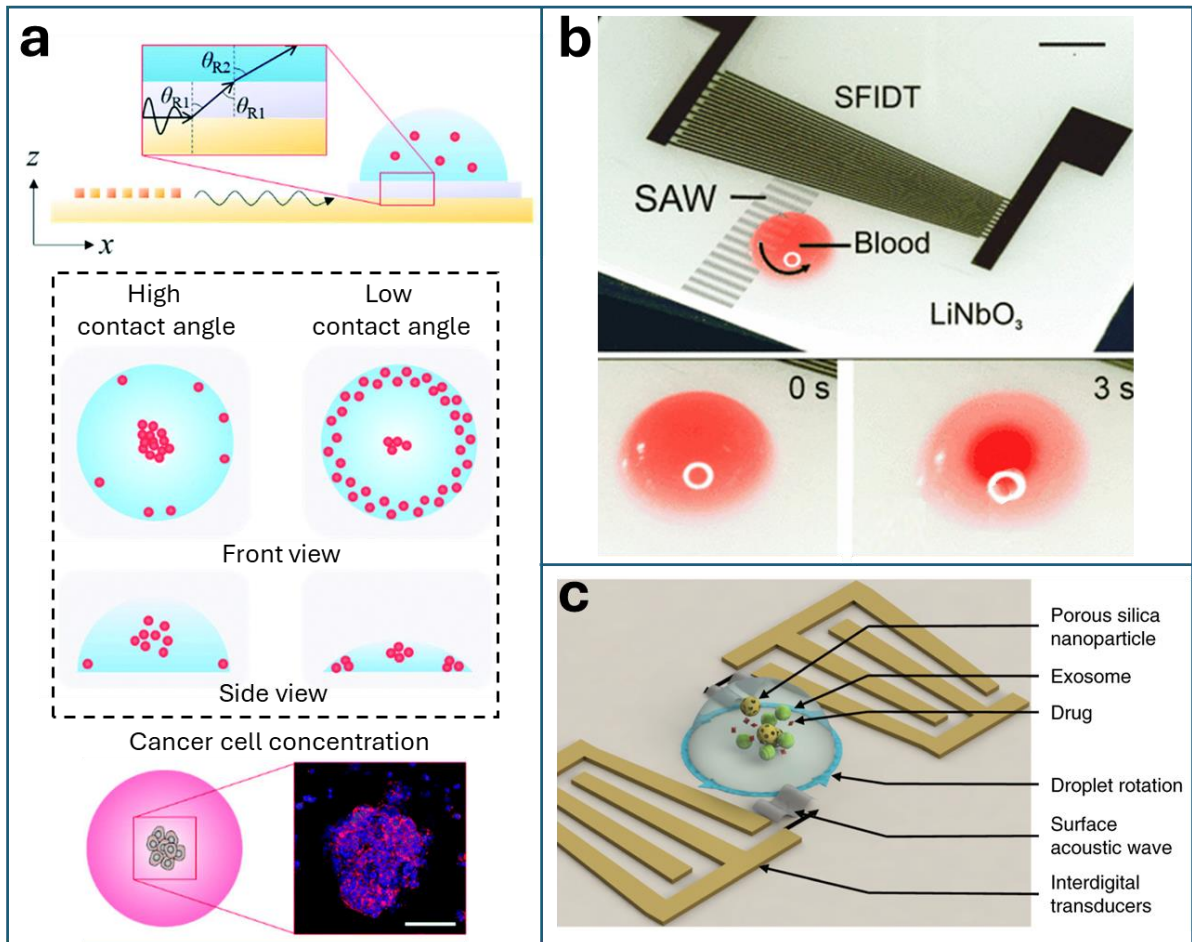


Figure 2.5. Examples of applications of TSAW streaming for digital acoustofluidic concentration and separation. (a) Concentration of cancer cells [Minor adaptation from [124]]. (b) separation of malaria-infected RBCs [Minor adaptation from [128]]. (c) Drug loading and exosome encapsulation [Reproduced from [129]].

Splitting

SAW technology not only focuses on particle concentration and object separation within droplets but also enables merging and splitting of droplets [130] as shown in Figure 2.6(a). This methodology increases throughput, reduces volumes, washes samples, and produces identical droplets [130,131]. A simple SAW device can achieve on-demand size tuneable droplet splitting (Figure 2.6(b)), unlike electrowetting, which requires multiple devices [131]. Additionally, SAW can separate different fluids, such as water from a microliter oil/water drop, highlighting its potential for separating immiscible liquids [132].

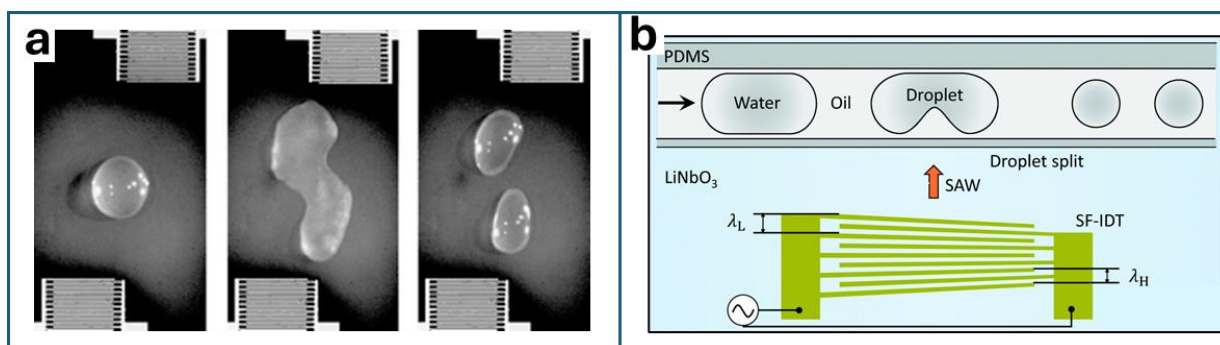


Figure 2.6. Examples of applications of TSAW streaming for digital acoustofluidic splitting and merging. (a) Open platform droplet splitting and merging [Reproduced from [130]]. (b) On-demand droplet splitting [Minor adaptations from [131]].

2.5.1.2 Pumping, jetting, nebulisation/atomisation, and droplet generation in digital acoustofluidics

Transportation

Droplet pumping uses SAW power above a threshold to induce streaming and deformation, propelling the droplet. In microfluidics, the challenge is to pump droplets without increasing temperature or causing evaporation, which is crucial for protecting biological activities and low-power lab-on-chip systems. Various strategies are employed to mitigate these challenges, including utilising low power levels [133,134], encapsulating the droplet within an oil medium [44,135,136] introducing a steel ball medium [137], preventing direct radiation of SAWs onto the substrate, or converting microdroplets into a continuous flow [138]. Another example is with SAW Rayleigh-Lamb inertia-capillary modes, which uses higher amplitude oscillations, enabling droplet movement at a speed of 5 mm/s with reduced power by a factor of 3 [134]. Moreover, alternative SAW configurations can also be used. For instance, a focused SAW can propel a droplet approximately five times faster than conventional SAW methods [139]. SAW-induced droplet transportation and temperature control via thin film heaters have proven effective in biological analysis chips enabling highly sensitive, rapid, and specific PCR reactions even with volumes as low as 200 nL [135]. This device has successfully identified single nucleotide polymorphisms (SNPs) associated with Leiden Factor V syndrome in human blood [135]. Droplet pumping promising applications in diagnostics, drug testing, automated reactions, and sample processing.

The substrates surface properties also influence the velocity of the droplet pumping. Optimising the hydrophobic film can reduce the necessary power by 50 to 75% [133], minimizing temperature increase and evaporation. For example, by implementing a hydrophobic self-assembled monolayer of octadecyl trichlorosilane (OTS) [140], pumping of 5 μl droplets at approximately 1.4 cm/s has been achieved. Alternatively, a slippery layer of lubricating oil-filled hydrophobic surface can significantly reduce (up to 85%) the threshold power to pump the droplet on a ZnO/Si SAW device [141]. The surface behaviour of droplet manipulation in microfluidics has been discussed in detail by Wu *et al.* [142].

Typically, droplet acoustofluidic devices need a flat surface to operate correctly. Nevertheless, alterations in surface treatment and the adoption of thin-film SAW devices, such as ZnO/Si, ZnO/glass, AlN/Si or ZnO/Al, can achieve droplet transportation [143,144]. These approaches enable effective droplet transport across various substrates and diverse geometries, as shown in Figure 2.7(a), including inclined, curved, vertical, inverted, and laterally positioned surfaces [56,143]. This capability is promising for next generation microfluidic systems and biosensors, such as wearable, flexible multilayered or 3D devices.

Chemical modifications to the chip surface can create pathways for programmable microfluidic processing. This enables droplet transport along predetermined trajectories for actions like splitting, merging, mixing, and processing [145]. Alternatively, acoustic streaming-induced hydrodynamic traps offer contactless droplet transport and manipulation, maintaining a contamination-free environment (diffusion into the fluorinate carrier is lower than 10-10%) and high biocompatibility (with 99.2% cell viability) [146]. Such a system, demonstrated in Figure 2.7(b) used an array of IDTs for streaming-based pumping in vertical directions [146]. Such re-programmable platform can achieve various droplet manipulations (transport, merge, mix and split) and scale to perform massive interaction matrices within a single device [136]. Electrical control of multitone signals provides fluidic functions such as routing and gating droplets, minimizing cross-contamination and extending to fluidic processors akin to transistor arrays [44]. These techniques are promising for biomedical and biochemical applications such as on-chip bioassays, high throughput compound

screening, biochemical synthesis, and droplet processing strategies that follow digital logic rules.

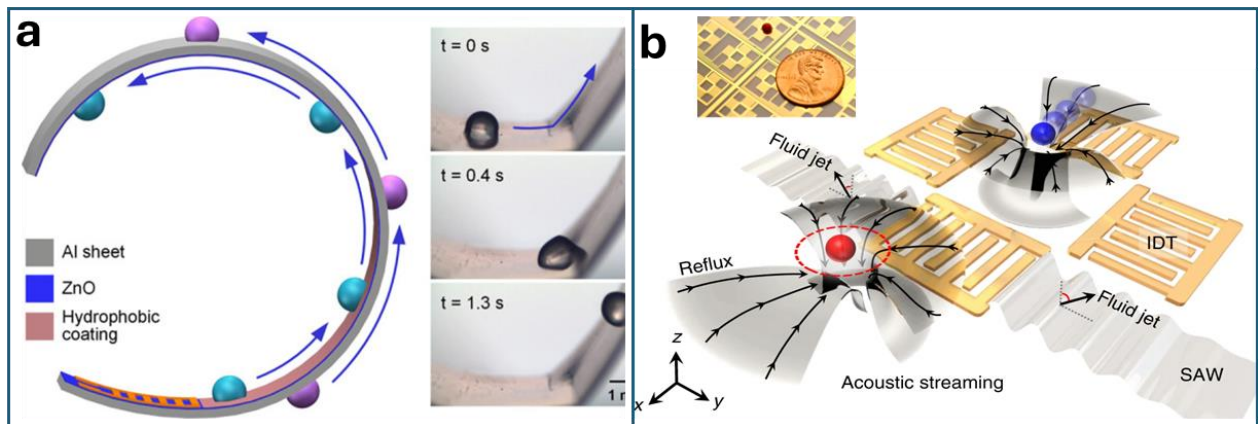


Figure 2.7. Examples of applications of TSAW streaming for digital acoustofluidic transportation. (a) Flexible/bendable droplet pumping [Reproduced from [56]] (b) Digital programmable droplet manipulation [Minor adaptation from [146]].

Jetting

Generating jetting phenomena involves concentrating wave energy into a confined region to optimise mechanical displacement within sessile droplets. SAW offers a nozzle-free, contact-free approach that minimises cell damage, benefitting applications like 2D and 3D bioprinting, needle-free fluid injection, and single-molecule detection. This method is cost-effective, easy to manufacture, and suitable for miniaturisation. Jetting can be achieved using standard SAW devices on hydrophobically-treated 128° Y-X LiNbO_3 substrate [147]. Focused SAW implementations can amplify droplet jetting and ejection [45], enhanced by adjusting the substrates wettability [148]. However, focused SAW devices can increase temperature in water environments, posing risks to biological tissues and cells [149].

Different materials and wave modes yield various jetting phenomena. For example, droplets are generally ejected along the Rayleigh angle (e.g., 23° on a 128° Y-X LiNbO_3 substrate), while SH-SAW devices on a 36° Y-X lithium tantalate (LiTaO_3) substrate in Figure 2.8(a) induce vertical jetting [9,150]. Surface reflected bulk waves on 128° Y-X LiNbO_3 substrate can obtain improved nebulization efficiency without added device complexity or cost, suitable for large-scale nanoparticle synthesis,

therapeutic encapsulation, and crystallization [151]. This specially designed droplet ejection technique protects the device by preventing direct liquid contact with electronics, offering a modular, reconfigurable platform for use in 96-well plates [152]. Nonetheless, it is essential to consider the anisotropic characteristics of such piezoelectric materials. In some instances, designs may mitigate the differences in acoustic velocities, enabling efficient or focused effects. However, this introduces complexities in terms of modelling and mask design [153].

Thin-film SAW devices, like those using ZnO or AlN [154], present advantages for jetting phenomena. Beyond their isotropic wave velocities, these devices exhibit superior power-handling capabilities. In-plane isotropic ZnO/Si circular SAW devices can produce controlled, concentrated vertical droplet jetting, superior to 128° Y-X LiNbO₃ substrate [46]. However, ZnO SAW devices have lower electromechanical coupling coefficient, potentially weakening jetting [155]. Integrating an ultra-smooth nanocrystalline diamond (UNCD) interlayer into a ZnO/Si device enhances efficiency by increasing SAW energy transfer to the liquid [156]. Furthermore, thin-film materials, such as the AlN/Si SAW device displayed in Figure 2.8(b), can enable jetting along inclined or curved surfaces [144].

SAW-generated jetting serves various biomedical applications, including droplet suspension a liquid bridge formation, useful for studying fluid dynamics in biological systems [157]. Moreover, the jetting phenomenon can repetitively eject individual droplets into the air, from the continuous resupply of a parent drop reservoir. The droplet size can be adjusted by the pulse width duration [158,159]. Such technique is used for encapsulation of single cells (Figure 2.8(c)) [160], single CTCs [161–163] and rare cryopreserved cells [164]. Additionally, it supports acoustic droplet-based printing of tumour organoids [55] and tumour microenvironment [165] as shown in Figure 2.8(d), facilitating single-cell analysis and cell-based diagnostics.

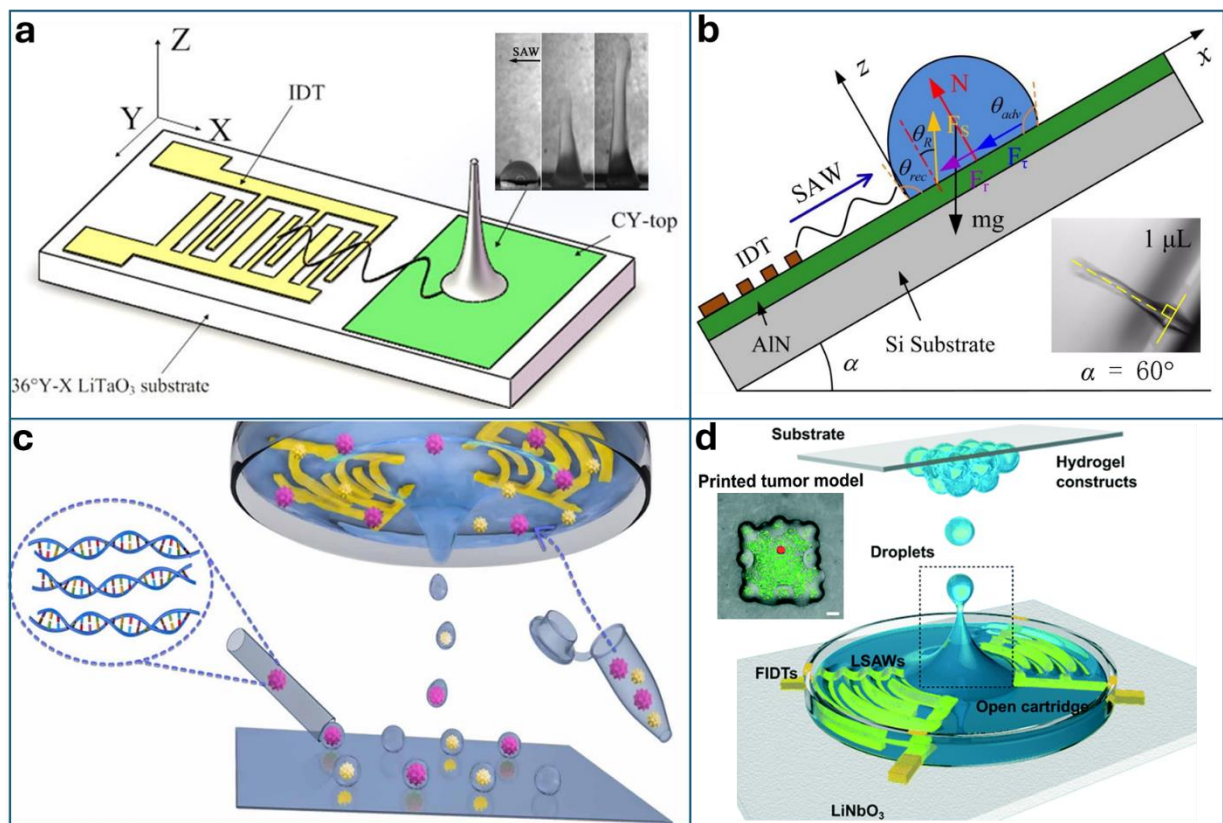


Figure 2.8. Examples of applications of TSAW streaming for digital acoustofluidic jetting. (a) Vertical jetting induced by SH-SAW [Minor adaptation form [150]]. (b) Jetting along inclined surface [Minor adaptation from [144]]. (c) Focused acoustic beams to encapsulate single cells [Reproduced from [160]]. (d) Focused acoustic beams for printing tumour microenvironment [Minor adaptation from [165]].

Nebulisation

Atomisation and nebulisation techniques generate finely dispersed aerosol droplets for applications requiring precise, uniform droplet sizes, such as spray cooling, inhalation therapy for drug delivery, mass spectrometry, and bioprinting. SAW technology excels in creating monodispersed microdroplets, mitigating shear and cavitation effects through high frequencies and low powers, minimising biomolecule damage [166]. Droplet size in the atomised mist can be controlled by adjusting the liquid properties, frequency, and input power [47,50]. Thin-film liquid geometries enhance atomisation efficacy due to their capacity for higher frequencies and concentrated effects on the surfaces [47]. For instance, a thin graphene film deposited on 128° Y-X LiNbO₃ can boost fluid atomisation rates by up to 55% [167]. Atomisation

performance can also be improved with focused SAW to enhance concentration [50] or amplitude modulation to reduce power requirements [168]. Additionally, tapered SAW designs enables selective local cooling by changing the excitation frequency without repositioning the device [169]. These advancements lead to practical, handheld, battery-powered nebulisation devices.

A SAW nebulising device has successfully nebulised epidermal growth factor receptor monoclonal antibodies into a fine aerosol mist for pulmonary delivery, particularly relevant in lung cancer treatment [48]. This versatile SAW setup can also deliver drugs through the pulmonary route for treating various diseases [170], including chronic obstructive pulmonary diseases and respiratory infections. Integrating additional devices enhances functionality; for example, coupling with an ionization device, as shown in Figure 2.9(a), allows detection of nanomolar drug concentrations in blood and plasma and heavy metals in tap water [171]. An acoustofluidic nebulisation device can also use surface reflected bulk waves for increased output and efficacy. This wave propagates along and through the substrate, drawing the solution through the substrate-contacting needle and then nebulising the liquid [172]. This method has achieved *in vitro* pulmonary delivery of antibiotic alternatives that can be successfully achieved against *Staphylococcus aureus* (prototype illustrated in Figure 2.9(b)) [54] and *in vivo* human lung deposition [172].

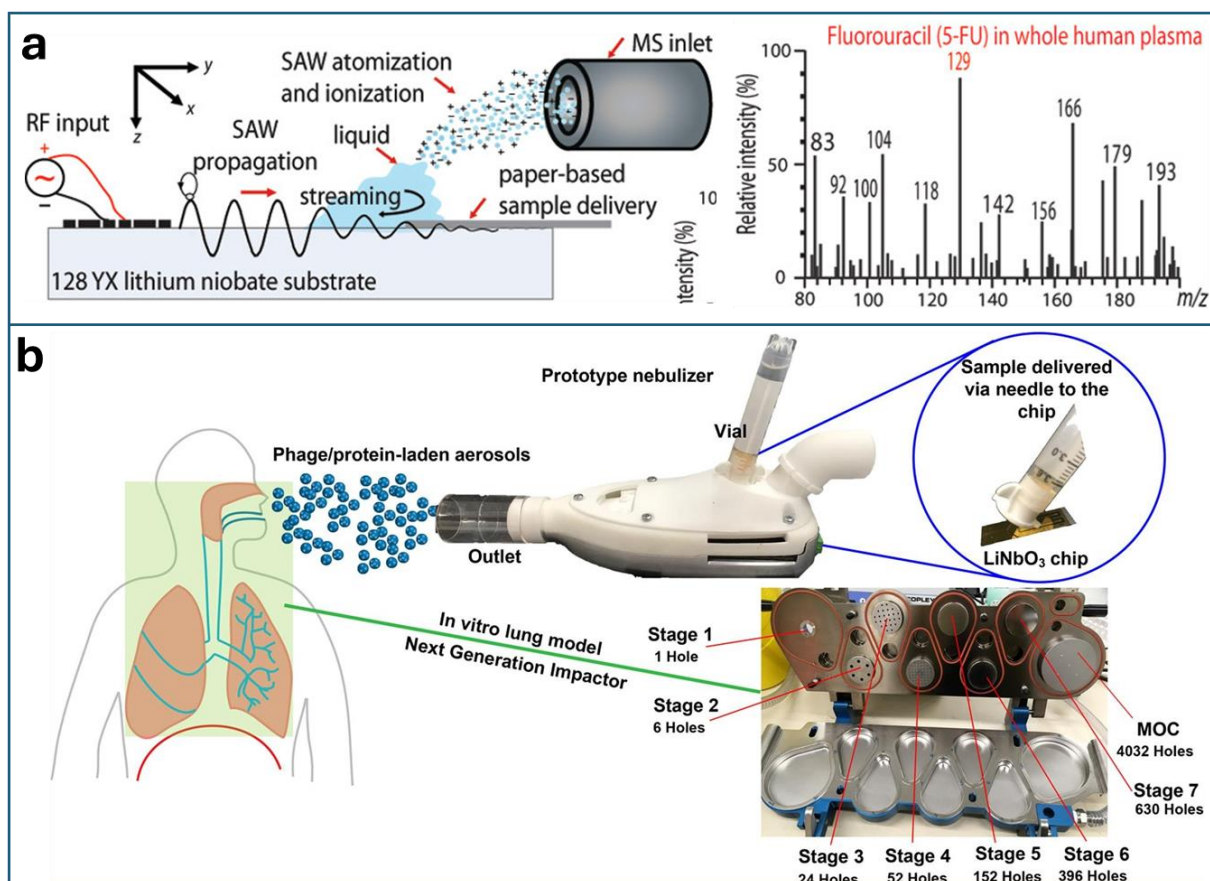


Figure 2.9. Examples of applications of TSAW streaming for digital acoustofluidic nebulisation. (a) SAW nebuliser for sample delivery and ionization demonstrating sensitive mass spectrometry [Reproduced from [171]]. (b) Prototype nebuliser employed for in vitro lung characterisation of aerosols [Reproduced from [54]].

2.5.1.3 Mixing, concentration, and rotation of liquid in chamber/channel for continuous acoustofluidics

Mixing

Microchannel or chamber mixing predominately relies on diffusion-based mechanisms, but efficiency is limited due to the low Reynolds number. SAW-based methods provide a low-power, non-invasive, and effective solution to enhance mixing by overcoming diffusion constraints. This is significant in chemical and biochemical assays and miniaturised total analysis systems. Microchannel or chamber mixing holds significant biomedical potential; increasing reaction yield in biosensing [173], removing cells to improve cell culture quality (Figure 2.10(a)) [41], and supporting nanoparticle production for nanomedicine (Figure 2.10(b)) [174]. Integrating SAW-

mixing with a surface plasmon resonance microfluidic sensor enhances functionalization efficiency by up to 5 times with respect to instances without SAW [175].

Acoustic streaming-based mixing in microchannels is controlled by parameters such as SAW power, fluid viscosity, and flow rate [176]. Additionally, altering the SAW device setup, such as using focused [177] or tapered SAWs [178], can achieve rapid and uniform mixing in microchannels. However, substantial channel thickness attenuates acoustic waves. Directly coupling SAWs and fluids in micromixers increases throughput (e.g. total flow rate of 50 $\mu\text{l}/\text{min}$) while reducing power consumption (e.g., 12 V) compared to standard SAW-based counterparts [179]. While sessile droplet systems avoid such challenges, they encounter instability at high power. Adopting a dome-shaped chamber addresses this, offering flexibility in contact angle (e.g., 68°) and reflection angle ($\sim 22^\circ$) to enhance mixing (mixing indices > 0.9 at 300 $\mu\text{l}/\text{min}$ with 20 V) [57]. Other methods involve employing three-dimensional dual SAWs from the top and bottom substrates, inducing internal swirling for high efficiency (100% at 50 $\mu\text{l}/\text{min}$ flow rate with 14 V) [180]. Conductive liquid-based electrodes can also achieve high mixing efficiency (97% at 80 $\mu\text{L}/\text{min}$ with 21 V) [181].

Introducing bubbles within channels can amplify the mixing effects [182–186]. Resonating acoustic waves activate these bubbles, inducing streaming and disrupting laminar flow, rapidly mixing viscous fluids in about 50 milliseconds [184]. Challenges with bubble stability, heat generation, and the intricacies of bubble trapping must be considered. Additionally, channel geometry significantly influences the acoustic streaming vortices and mixing. Sharp edges [187–196] generates a substantial Reynolds body force compared to using a non-sharp edge [187]. This characteristic has proven effective in mixing [194], cell lysis [197], pumping [198] and rotation [199,200]. The potential of enhancing acoustic streaming is not confined to sharp edges; other microstructures [201,202] such as microcylinders [203–205], micro square pillars [206], and micro parallelepipeds [202,207] offer viable alternatives.

Vibrational mixing with high-frequency and low-power continuous SAW signals is advantageous for applications requiring mechanical stimulation without cavitation or heat. This method can be used for vibration-enhanced cell growth [208] and for

investigating ultrasound-induced mechano-transduction at the single-cell level, such as inducing intracellular calcium responses in human embryonic kidney 293T [209]. Additionally, successful acceleration of neural differentiation in human embryonic stem cells has been achieved, (Figure 2.10(c)) highlighting a potential avenue for regulating stem cell differentiation in therapeutic contexts [210]. This approach, as shown in Figure 2.10(d), enhances uptake in difficult-to-transfect nonadherent cell lines like suspension T cells within 10 minutes, maintaining high cell viability (>91%) and outperforming methods like conventional nucleofection (76%) [211]. These findings highlight the diverse applications of SAW-induced acoustic streaming-based mixing.

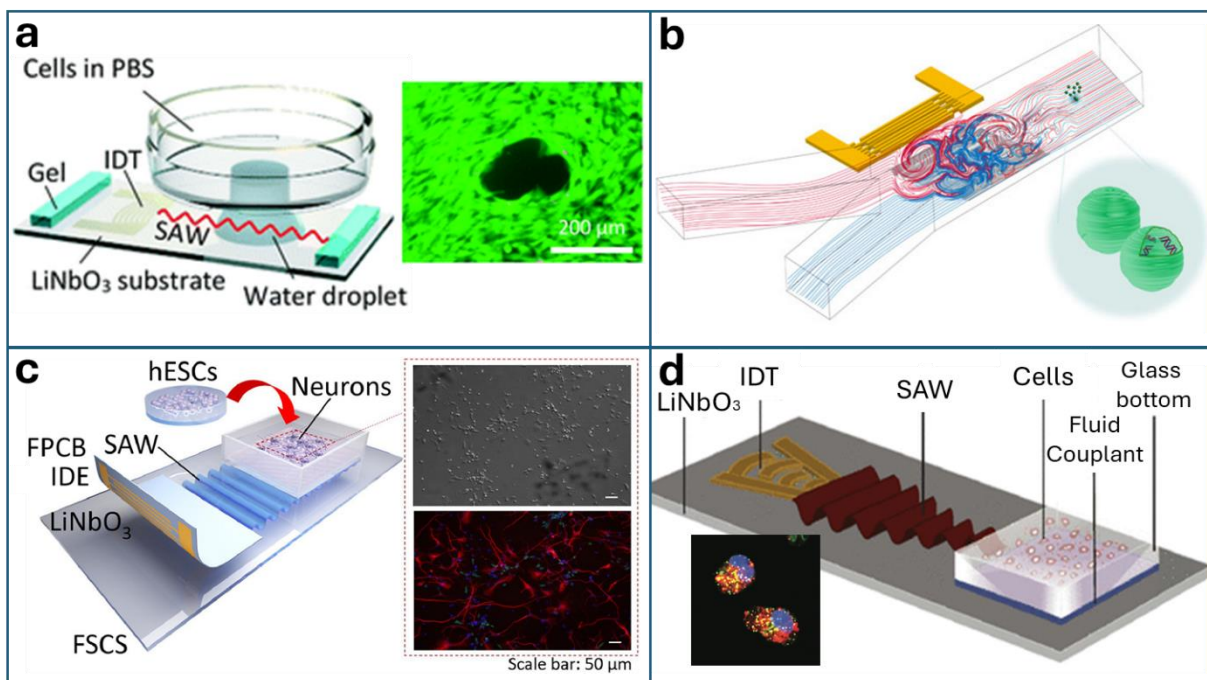


Figure 2.10. Examples of applications of TSAW streaming for channel/chamber acoustofluidic mixing. (a) Locally remove cells from culture surface to improve cell culture quality [Reproduced from [41]]. (b) Controllable mixing for fabrication of therapeutic nanoparticles [Reproduced from [174]]. (c) Acoustically accelerated neural differentiation of human embryonic stem cells [Reproduced from [210]]. (d) Acoustofection for intracellular delivery device [Minor adaptations from [211]].

Concentration and separation

The concentration and subsequent separation of particles and cells within a channel have traditionally relied on acoustic radiation forces [99], utilising SSAW to drive

objects toward minimum PNs or ANs. This method is significant for concentrating and isolating extracellular vesicles [212,213] and CTCs [214,215], which are pivotal in diagnostic and treatment decisions.

Incorporating both SSAW and TSAW can enhance separation performance in multistage devices. For example, as shown in Figure 2.11(a), the initial SSAW stage concentrates CTCs and RBC at pressure nodes, while a subsequent TSAW stage uses acoustic streaming forces to separate CTCs from RBCs, achieving approximately 94.2% particle separation efficiency for 2 μm and 5 μm polystyrene particles [216]. A single TSAW can independently achieve the separation of 10 and 15 μm particles in a detachable microchannel with separation efficiency surpassing 98%, displayed in Figure 2.11(b) [217]. The disposability and assembly convenience of this system enable the practical application of noncontact, disposable particle manipulation techniques in biomedical sample preparation.

Further strategies involve employing two counterpropagating TSAWs at different frequencies to laterally migrate 5 μm particles across the fluid flow to precise locations with a ± 10 μm accuracy [218]. This approach facilitates longer-range force fields, driving particle concentration to a single trapping site [218]. Moreover, high amplitude and frequency focused SAWs induce robust acoustic streaming, leading to fluid streamlines and vortices (Figure 2.11(c)) [219]. This method underpins the selective capture of 2 μm particles from mixed suspensions of 1 μm particles in a continuous flow [219], size-selective aggregation down to 300 nm in enclosed channels [220], and consistent differential focusing of nanometre particles with continuous channels [25].

Integrating configurations with passive microfluidic cell sorting techniques offers promising solutions for increased performance. Techniques like reverse wavy [221] or spiral [215] microchannels ((as shown in Figure 2.11(d)) are used for inertial cell enrichment, alongside active TSAW single cell sorting. For instance, this approach achieves at least a 2500-fold purity enrichment of MCF-7 breast cancer cells spiked in diluted whole blood samples with cell viability maintained at $91 \pm 1\%$ (compared to $94 \pm 2\%$ before sorting) [221]. SAW holds the potential for high-throughput and precise isolation of rare cell populations in practical biomedical applications.

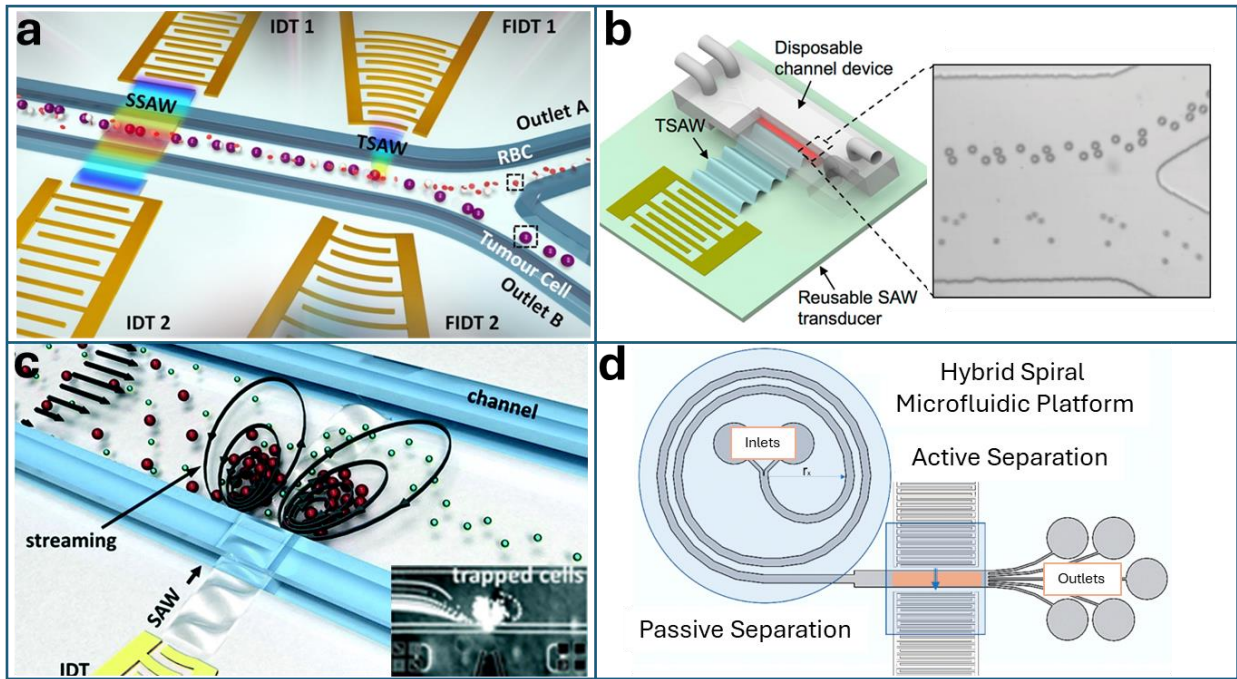


Figure 2.11. Examples of applications of TSAW streaming for channel/chamber acoustofluidic concentration and separation. (a) Sorting of tumour cells by a multi-stage SAW device [Reproduced from [216]]. (b) Particle separation using a detachable acoustofluidic system [Reproduced from [217]]. (c) Selective particle and cell capture in continuous flow [Minor adaptation from [219]]. (d) Hybrid spiral microfluidic platform for passive and active separation [Minor adaptations from [215]].

Rotation

Accurate and noncontact rotation and manipulation of physical and biological objects are highly desirable in nanofabrication, micro and nano-robotics, drug delivery, and cell and tissue engineering applications. Acoustic tweezers have rapidly emerged as a versatile platform enabling precise manipulation across a broad object size range. Typically, acoustic tweezers rely on SSAW, yet a different approach employs TSAW to leverage streaming fluid flows. This indirect handling of particles in fluids through streaming vortices simplifies operation but may compromise spatial resolution due to the challenging control of nonlinear streaming [9].

A tri-directional symmetrical acoustic tweezer (Figure 2.12(a)) generates TSAW to control microparticle movements precisely. By switching excitation combinations, programmable motion control is achieved, facilitating linear, clockwise, and

anticlockwise trajectories [222]. For increased precision in 2D fluid and particle manipulation, an array of transducers generating swirling acoustic forces offer a more refined approach [223]. Moreover, using an array of transducer plates creates stable and symmetrical pairs of vortices, establishing hydrodynamic traps [9]. These versatile transducer plates function as acoustic wave generators and boundaries to shape 3D streaming-based acoustic tweezers [9]. 3D tweezers can be achieved without a complex transducer array by combining SSAW to manipulate in two directions with TSAW streaming vortex for levitation in the third dimension [224].

The devised rotational mechanisms manipulate and propel objects, as demonstrated by their application in a centrifugal microfluidic platform. For example, a miniaturised lab-on-a-disc (miniLOAD) SAW device (Figure 2.12(b)) [225] is designed to harness acoustic streaming for the steering rotation of thin millimetre-scale discs resting atop a fluid coupling layer. Adjusting the power and input frequency to the device allows the rotational velocity and direction of the disc to be controlled [226]. Disposable microchannels can be fabricated on the discs to achieve self-contained and portable centrifugal functionalities.

Utilising the same methodology, whereby TSAW generates an acoustic streaming vortex within a channel, enables noncontact rotation of small veritable models [53,199]. This rotational manipulation opens avenues for high-speed, 3D multispectral imaging and digital reconstruction, culminating in accurate 3D models that facilitate quantitative evaluation of morphological characteristics and advanced combinations metrics. This basis proves valuable for small organism phenotyping, screening, and microsurgery. For example, controlled rotation of *Caenorhabditis elegans* can be achieved using alternate counterpropagating TSAWs for clockwise or anticlockwise motion in a continuous or stepwise manner [53]. However, the vortex size confines its suitability to larger organisms, such as millimetre-scale zebrafish larvae, commonly used in rapid drug screening and disease evaluation. Consequently, it is vital to develop functional platforms that provide clear visualisation and precise analysis, essential for high-throughput phenotypic evaluations. Addressing this need, a robust, stable, and consistent unidirectional polarised vortex pattern, as shown in Figure 2.12(c), has been developed for quantification and 3D reconstruction of zebrafish larvae [52]. Collectively, such systems hold promise across diverse biomedical

domains, including accelerating drug discovery and simplifying testing of personalised therapies in animal models.

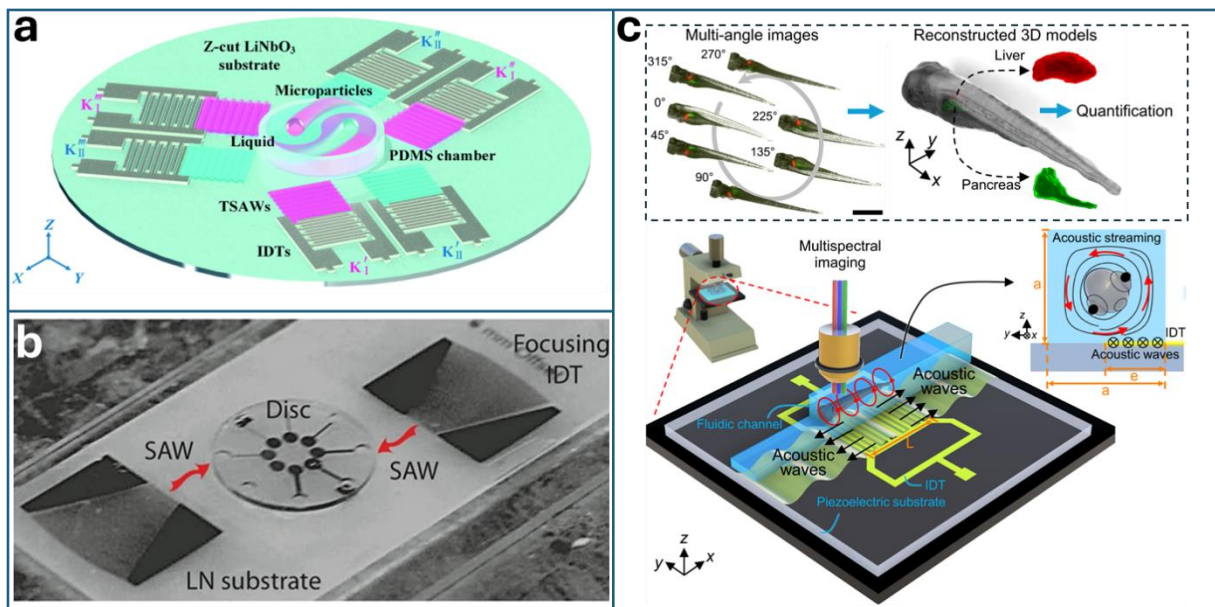


Figure 2.12. Examples of applications of TSAW streaming for channel/chamber acoustofluidic rotation. (a) Tri-directional symmetrical acoustic tweezers for programmable trajectory manipulation [Reproduced from [222]]. (b) Controlled rotation on a lab-on-a-disc device [Reproduced from [225]]. (c) Rotational manipulation of zebrafish larvae, demonstrating multiple imaging of the rotation for 3D reconstruction of models [Minor adaptation from [52]].

Droplet manipulation

Confining droplets within microchannels presents a versatile strategy for fluid control [42], establishing discrete microenvironments to prevent cross-contamination [227]. This capability benefits various biological applications, including complex micro-total analysis systems or high throughput single-cell screening in large cell populations. Notably, the selective merging of droplets has been demonstrated to initiate biochemical reactions [227,228], facilitate encapsulate samples [229], and enable precise dispensing based on droplet volumes (Figure 2.13(a)) [230]. Additionally, the use of TSAW-based streaming allows for precise manipulation of 200 fl [231] and 10 fl (Figure 2.13(b)) [232] droplets within nanofluidic channels, overcoming challenges inherent to nanoscale manipulation governed by surface and viscous forces [231,232]. Manipulating nano-droplets within these nanostructures can increase the sensitivity of

analytical tools for applications such as medical diagnostics and personalised treatments.

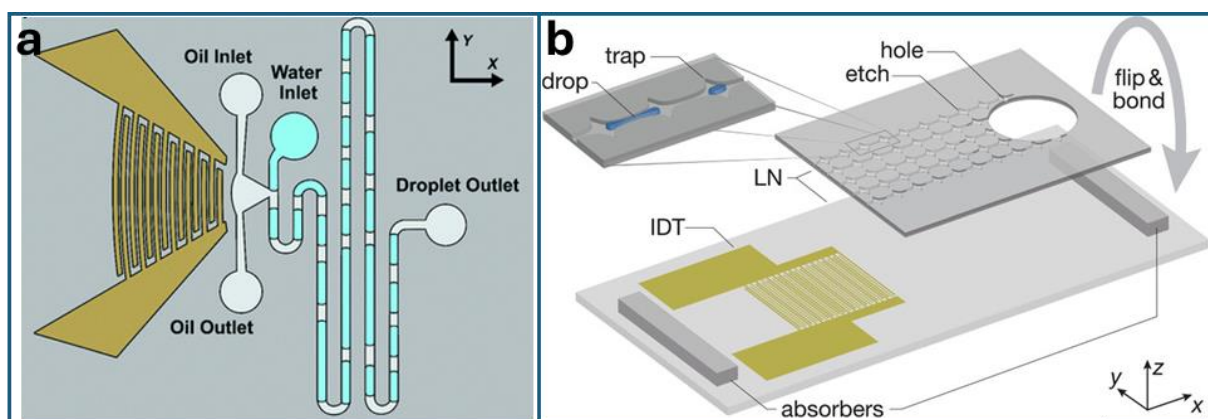


Figure 2.13. Examples of applications of TSAW streaming for channel/chamber acoustofluidic droplet manipulation. (a) Deterministic droplet coding of through dispensing of droplet volumes [Reproduced from [230]]. (b) Manipulation of 200 femtoliter droplets in nanofluidic channels [Reproduced from [232]].

2.5.2 SSAWs based streaming and acoustofluidics

2.5.2.1 SSAW induced droplet streaming in digital acoustofluidics

Mixing

When a pair of IDTs generate SSAWs to actuate a sessile droplet, it initiates symmetrical acoustic wave propagation, inducing strong acoustic streaming forces within the droplet, even if its movement is not easily observed. Consequently, SSAW-induced streaming proves advantageous for the stable mixing of sessile droplets. For example, SSAW-induced mixing finds applications in dynamic cell culture [233], labelling of nanoparticles [234], or lowering the detection limit for biomarkers [235]. Moreover, SSAW mixing enhances the kinetic impact on the recrystallisation process of metal-organic frameworks, as illustrated in Figure 2.14(a). For example, this is achieved with HKUST-1 crystals [236] and variously sized glycine crystals [237] within droplets, as well as the isolation of sodium chloride crystals [238] within evaporated droplets. This mixing holds promising potential for drug delivery and release applications within the pharmaceutical industry.

Concentration and Separation

The SSAW field can be modified using nickel pillar-type crystals to introduce scattered SSAW and consequently induce strong acoustic streaming localised in the half of a droplet. Such a mechanism has been utilised for concentrating and separating 2 and 20 μm polystyrene (PS) particles within a microliter droplet [239]. Furthermore, concentration and separation within a sessile droplet via SSAWs can be achieved by adjusting the droplet's contact angle [240], as presented in Figure 2.14(b).

Transportation

While SSAWs do not inherently contribute to droplet transport, coupling SSAW-induced streaming with anisotropic ratchet conveyors achieves this by utilising hydrophilic patterns on the substrate to control droplet movement direction [241]. For example, Figure 2.14(c) shows this technique for transporting and merging droplets [241]. Another method uses a combination of TSAW and SSAW, where the velocity and direction are controlled by adjusting the temporal phase shift of SAW in exciter-exciter modes [242]. The simplicity of this device can improve the convenience and programmability of lab-on-chip applications.

Jetting and Nebulization

The stability of SSAWs actuating a droplet enables controlled jetting. When SSAW is generated through a small aperture in a vertical capillary tube, as demonstrated in Figure 2.14(d), it can produce controlled and stable jetting [243]. This configuration harnesses the benefits of higher energy density output performance and enhanced driving capability, resulting in focused energy concentration and more uniform wave paths [243]. Moreover, adding anisotropic ratchet conveyors can aid droplet confinement for nebulisation [241].

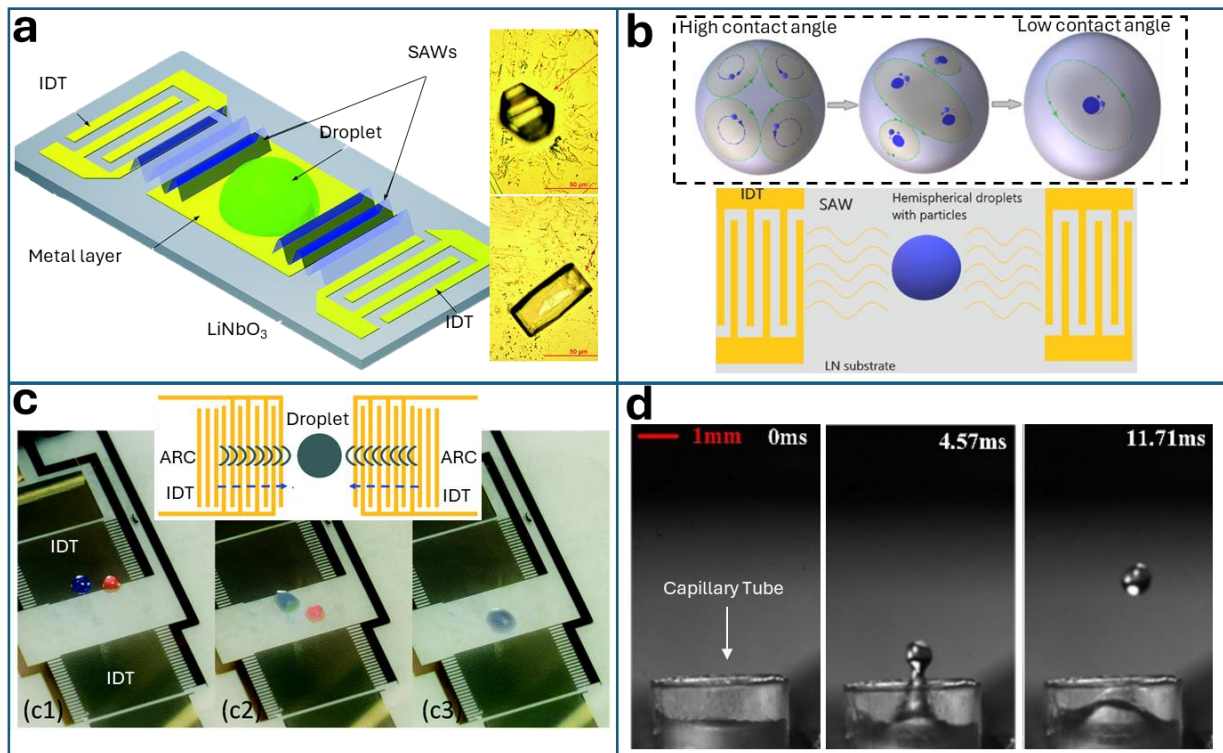


Figure 2.14. Examples of applications of SSAW streaming for digital acoustofluidics. (a) Growth of glycine crystals promoted by SSAW [Minor adaptations from [237]]. (b) Particle concentration and separation by SSAW through change in contact angle [Minor adaptations from [240]]. (c) Droplet transportation and merging with anisotropic ratchet conveyors control movement [Minor adaptations from [241]]. (d) SSAW induced stable jetting in capillary tubes [Minor adaptations from [243]].

2.5.2.2 SSAW induced streaming in a microchannel in continuous acoustofluidics

Mixing

SSAWs are typically recognised for generating ANs and PNs to manipulate particles; however, they also influence fluid streaming within a chamber. Notably, SSAWs mixing (shown in Figure 2.15(a)) has been demonstrated to outperform TSAWs with a mixing performance of 96.7% compared to TSAWs 69.8% under the same applied voltages ($85 V_{p-p}$) and flow rates ($10 \mu\text{l}/\text{min}$) [244]. The mixing behaviour induced by SSAW acoustic streaming proves to be advantageous, offering prevention of particle deposition within a microchannel [245] or facilitating microextraction functions for applications in biochemical analysis [246,247].

Concentration and Separation

As discussed in Section 2.2, the interaction of two counterpropagating TSAWs generates SSAW, establishing a time-averaged pattern of nodal and antipodal positions across the channel [248]. Consequently, SSAWs readily form one-dimensional nodal lines within channels or chambers, allowing particle and cell patterning for concentration and separation applications [249]. For example, Figure 2.15(b) demonstrates the separation of red blood cells and bacteria using a tilted-angle SSAW device [250]. This approach can seamlessly integrate into a straightforward multistage device [251–253], enhancing efficiency and throughput. For example, SSAW particle/cell sorting in the first stage is followed by TSAW particle/cell deflection in the second [216,254,255]. To further enhance effectiveness, alternative strategies can be employed, such as phase modulation to align particles at various moving pressure nodes without needing an increase in channel width [256–258] or the application of nanosecond-scale pulses to generate localised time-averaged patterning regions for selective trapping [259].

SSAW has proven effective in sorting cell-encapsulating beads according to bead density, a pivotal parameter in evaluating encapsulated cells' biocompatibility and immune response, notably in cell therapy [260]. Furthermore, SSAW-based sorting has been applied to separate different size constituents in whole blood samples [261,262], which holds significance for whole blood analysis and antigen-based cell diagnostics. This sorting capability extends to the isolation of circulating tumour cells within whole blood samples, offering early-stage cancer diagnosis potential [214,215,249,263]. SSAW methods also facilitate exosome separation in whole blood samples, which is crucial for exosome-related health monitoring, disease diagnosis, and therapeutic research [264]. The separation of exosomes and lipoproteins in blood [212] is particularly significant given the challenge of isolating submicron-scale components with overlapping size distributions. This separation is beneficial as both components are valuable for diagnostics biomarkers and therapeutics. By engineering the acoustic field pattern and channel dimensions, distinct groups can be directed towards different outlets based on their acoustic contrast factor. Moreover, SSAW-based separation has already shown its potential in early traumatic brain injury diagnosis by successfully isolating circulating exosomes from plasma samples, as

demonstrated in Figure 2.15(c) [213]. Overall, SSAW-based approaches offer high sensitivity, efficiency, throughput, and rapid processing advantages for total analysis and diagnosis applications. Their label-free, contact-free nature ensures biocompatible control, preserving the structural, characteristic, and functional attributes of particles and cells.

Tweezers

Acoustic tweezers can be realised through two orthogonal SSAWs [3,265], forming a 2D pattern of nodes and antinodes for particle manipulation [266–268]. This straightforward approach offers rapid, precise, and noncontact control over particles and cells. The compact nature of SSAW-based tweezers allows seamless integration with microfluidic systems, enabling versatile lab-on-a-chip tools [36]. For example, 2D SSAW single-cell patterning has been used to examine *Plasmodium falciparum*-infected red blood cells [266], paving the way for investigations into cell-to-cell, cell-to-bacterium, and organism-to-bacterium interactions [36]. Furthermore, extending the capabilities, 3D SSAW acoustic tweezers can be achieved by manipulating acoustic parameters such as phase shifts [269], frequency, or amplitude modulation (as illustrated in Figure 2.15(d) [270,271]). These techniques enable dynamic reconfiguration of tweezer patterns without complex electronics [271]. For instance, 3D SSAW approaches have been employed for single-cell manipulation [269] and controlled rotation and translation of spherical particles or living cells in a 3D format [272]. Additionally, bio-acoustic methods can be incorporated through an extracellular matrix-based hydrogel, like gelatine methacryloyl [273]. Furthermore, SSAWs enable the patterning of particles and cells into 3D spatial lines [274], crystal-lattice-like matrix patterns in chambers with millimetre height [275] (suitable for whole organism manipulation such as *Caenorhabditis elegans*) [276], or the formation of multicellular spheroids [277,278]. The 3D spatial distribution of cells maintains their viability and functionality, making them valuable for diverse biomedical applications, including tissue engineering, in vitro cell studies, or the creation of 3D biometric tissue structures.

In summary, acoustic tweezers, with patterning and particle manipulation capabilities through SSAWs, have emerged as a prominent research area in the acoustofluidic

field. This field has been comprehensively reviewed in many papers [36,38,279–282]. However, as the primary focus of this thesis centres on acoustic streaming techniques, further exploration of acoustic tweezers will not be addressed within this work. Interested readers should refer to the above or other review papers for more information.

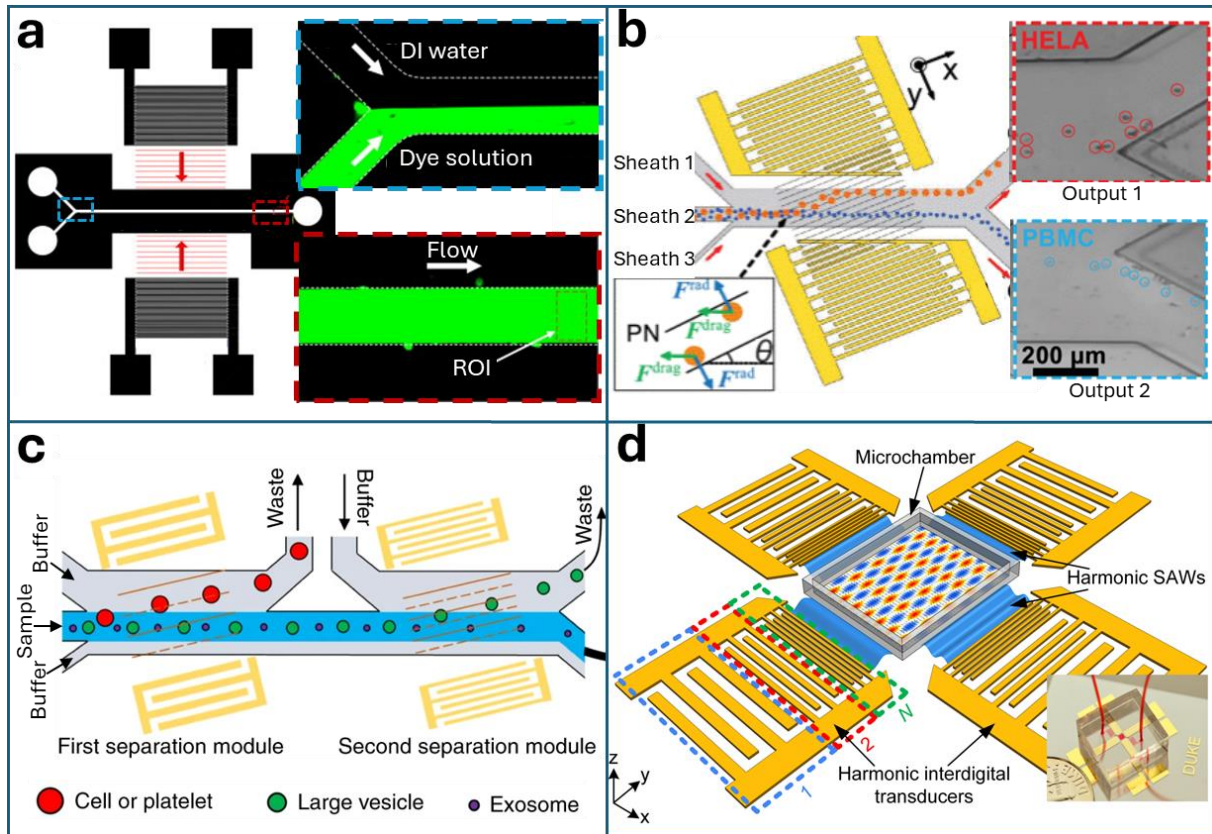


Figure 2.15. Examples of applications of SSAW streaming for channel/chamber acoustofluidics. (a) SSAW fluid mixing of deionized water and dye solution [Minor adaptations from [244]]. (b) Tilted-angle SSAW separation of red blood cells and bacteria [Minor adaptations from [250]]. (c) Isolating circulating exosomes from plasma samples device for early traumatic brain injury diagnostics [Minor adaptation from [213]]. (d) Dynamic and selective particle manipulation using harmonic acoustics [Minor adaptation from [270]].

2.6 Conclusion

This chapter provides a comprehensive overview of acoustic streaming, exploring its mechanisms, applications, and recent developments. Its role in various fields, from

biomedical research to clinical applications, highlights its valuable contribution to modern science and technology.

3.1 Introduction

Recent studies have investigated electrode designs and patterning for lab-on-a-chip applications, including bio-sample functions, precise sensing, and, more importantly, improved microfluidic functions [60,63]. However, current IDT designs are primarily tailored for RF communication and sensing applications rather than optimising their designs for acoustofluidic functions [39]. Therefore, this chapter delves into the intricacies of designing and constructing the active and passive components of acoustofluidic devices, specifically for acoustic streaming-based acoustofluidic applications explored in Chapter 2. The methodology provides a detailed overview of the active components, including Acoustofluidic Device Configuration and IDTs. It covers design criteria, transducer materials, fabrication techniques, and IDT advancements. Additionally, passive components such as fluidic vessels are discussed. By offering a comprehensive guide to constructing streaming-capable acoustofluidic devices, this chapter equips researchers to advance their work in Acoustic Streaming-based Acoustofluidic applications. It plays a pivotal role within the broader thesis, exploring the multifaceted capabilities of SAW acoustofluidic devices for acoustic streaming. Furthermore, this chapter sets the stage for subsequent chapters, particularly Chapter 4, which discusses the novel Hexagonal FPCB acoustofluidic device.

3.2 Configuration of Acoustofluidic Devices

An Acoustofluidic system contains three main components: the experimental set-up, the acoustofluidic device, and the data collection/analysis methods. To briefly describe these components, the experiment includes a function generator connected to the acoustofluidic device to generate acoustic waves. Optionally, an amplifier can be integrated to enhance power, and a power meter for power measurement, as depicted in Figure 3.1(a). The operation of the acoustofluidic device is typically observed through a benchtop microscope equipped with an objective lens and a camera. The acoustofluidic device comprises the piezoelectric substrate, the IDT, and the fluidic vessel. The fluidic vessel can take various forms, such as a sessile droplet, a

microchannel, or a chamber, illustrated in Figure 3.1(b-d). The acoustofluidic device generates acoustic waves to manipulate particles and fluids within the adjacent fluidic vessel. Data collection is facilitated through the microscope's camera, and subsequent analysis is conducted using software tools like ImageJ. The specific parameters subjected to analysis may vary depending on the application; examples encompass time, speed, and fluorescence intensity. Chapter 5 delves into the details of the experimental set-up and data collection/analysis techniques, focusing on the Hexagonal FPCB IDT, as discussed in Chapter 4.

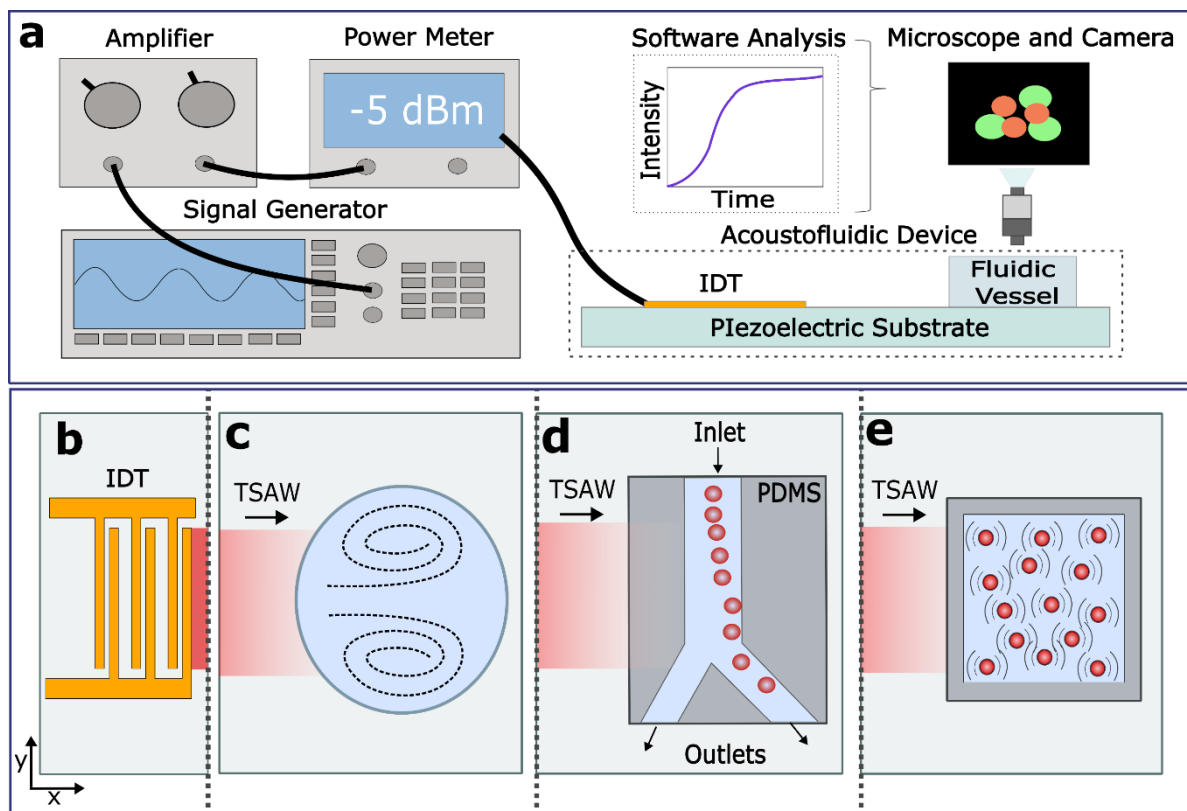


Figure 3.1. Typical configuration of a SAW acoustofluidic device. (a) Acoustofluidic experimental set-up. (b) SAW device consisting of a single conventional IDT on a piezoelectric substrate (c) Continuation of the TSAW from the IDT in (a) showing an example of fluidic mixing within a sessile droplet [283]. (d) Continuation of TSAW from (a) demonstrating particle separation within in microchannel [99]. (e) Continuation of TSAW from (a) causing vibrational stimulation of biological cells in a closed chamber [210].

A typical SAW IDT, using a SAW resonator as an example, consists of several key elements: electrode fingers, bus bars, electrode pad, and, sometimes, reflectors. In

applications related to biosensing, these SAW devices necessitate specific characteristics, including higher SAW frequencies, larger amplitude, reduced width (leading to higher quality factor), minimised noise levels, and precise IDT dimensions. Researchers have extensively reported these types of SAW devices [71,284–286]. Conversely, SAW devices are tailored to perform multiple microfluidic functions in microfluidic applications. These applications often demand higher power outputs, increased vibration amplitudes, various wave modes, and occasionally a broader range of frequencies, spanning from low frequencies in the MHz range to several hundred MHz. Some SAW devices operating at high frequencies, in the range of several hundred megahertz, have been explored for tasks such as manipulating nanoscale droplets, single cells or sub-micron particles [287,288], as discussed in Chapter 2. Acoustic streaming applications.

The design of SAW IDTs involves considering several critical factors, which will be delved into in the following section. Briefly, these factors encompass aspects such as geometry and thickness, electrode materials selection, mass loading, metallisation patterns, electrical regeneration and geometric discontinuity, piezoelectric shorting and strength of electromechanical coupling constant [289,290]. However, as already mentioned, most existing IDT designs primarily serve for RF communications and sensing applications. Consequently, there is a challenge in designing IDTs that are specifically tailored for optimal acoustofluidic performance [39]. The following sections will cover various IDT topics relevant to acoustofluidics, separated into active and passive components. The active components include the IDT design, transducer materials, fabrication techniques, and advances in IDT for acoustic streaming and acoustofluidics applications. The passive components involve the fluidic vessel types, materials, and fabrication.

3.3 Basics of IDTs

3.3.1. Design criteria

Designing effective IDTs for SAWs involves considering multiple key considerations. These parameters encompass [147] frequency (centre (or resonant) frequency, frequency spectrum and bandwidth), power and efficiency (power output density, insertion loss, reflection/transmission functions and resistance), electrode (electrode

materials, types, positions, shape/dimensions (including thickness), number of reflective electrodes, phase, delay effect, electrode length and aperture), substrate (substrate materials and isotropic/anisotropic properties), and wave characteristics (dispersion and wave direction/directivity (e.g., bidirectionality or unidirectionality)).

The primary objectives when enhancing electrode designs for acoustofluidics are to (i) increase the generation efficiency of acoustic waves, (ii) improve spurious signal suppressions, (iii) reduce insertion loss, and (iv) minimise signal distortion [64]. A labelled schematic of a conventional IDT is shown in Figure 3.2(a).

Depending on the specific applications (e.g., biosensing or acoustofluidics), the critical design factors and issues concerning IDT designs that need to be considered are: [291]

(1) Phase velocity: The propagation velocity of a single plane wave [6]. Phase velocity is a function of propagation direction; hence, the frequency applied to the IDT would change with its placement angle for a particular IDT design. Additionally, distinct wave modes will have different phase velocities. The phase velocity can be calculated with the simple wave velocity equation,

$$v_n(\theta) = f\lambda \quad (3.1)$$

Where f is the eigenfrequency of the acoustic mode, and λ is length of the acoustic mode, i.e., the wavelength/pitch of the IDT.

(2) Numbers of fingers (N) [70,292]: The number of fingers in an IDT. This number directly impacts its bandwidth, with an increase narrowing the bandwidth and improving the quality factor of resonant peaks. Bandwidth is inversely proportional to the number of fingers, calculated by,

$$BW = \frac{2f}{N} \quad (3.2)$$

Increasing the finger number can minimise spurious responses. However, too many finger numbers will result in mass loading and scattering effects from the electrodes, performance degradation, and increased electrode size or area.

(3) Acoustic aperture [293]: The overlapping length of the electrode. Precise design of the acoustic aperture is essential to prevent acoustic beam diffraction. A narrow aperture can result in beam steering and increased wave spreading during propagation. The impedance of the IDT is also influenced by this aperture size, typically requiring it to be at least 50 times the wavelength to ensure effective functionality.

(4) Heating effect [64]: Consequence of propagating waves generating atomic vibrations, leading to heat generation (Figure 3.2(b)). Factors such as defects, degradation, device malfunction causing internal energy dissipations, or reflections from the power supply can worsen this effect.

(5) Electromechanical coupling coefficient [294]: The numerical measure of conversion efficiency between electrical and acoustic energy in a piezoelectric material. The electromechanical coefficient of the mode is calculated by,

$$K^2 = 2 \frac{v_f - v_m}{v_f} \quad (3.3)$$

where v_f and v_m are the SAW phase velocities, calculated for free and electrically short-circuits surface, respectively [295]. Due to the phase velocity being a function of propagation direction, it also causes an orientation-dependent coupling coefficient. The coefficient will also change depending on the wave mode, electrode, and substrate materials. For example, 128° YX- LiNbO₃ has a maximum R-SAW coupling coefficient $K^2 = 5.4\%$ for propagation along the X-axis ($\theta = 0$) [296].

(6) Beam divergence or wave diffraction [70]: Deviation from the perfectly normal wavefront propagation direction [70], illustrated in Figure 3.2(c). This deviation is due to beam steering effects or the anisotropic behaviour of piezoelectric materials. The beam divergence also has orientation and frequency dependency for the same reason as the coupling coefficient. The slowness curve can reveal the beam direction by demonstrating the curve that deviates from a circular shape [6]. Hence, if the slowness curve is not circular, the beam direction is generally no longer parallel to the propagation direction [6]. This slowness curve is defined by,

$$k = \frac{\omega}{v_n(\theta)} \quad (3.4)$$

where \mathbf{k} is the wave vector, and ω is the angular frequency of the wave mode. Additionally, the power flow angle (ψ_n), which is the angle between the wave vector (defining the propagation direction) and the beam direction (given by the power flow) is also used to calculate the beam divergence. Unique wave modes and orientation angles will have distinct power flow angles that may need to be considered [295]. The power flow angle (Figure 3.2(c)) is calculated by:

$$\psi_n = \text{arctg} \frac{1}{v_n} \frac{dv_n}{d\theta} \quad (3.5)$$

where dv_n is the change in mode velocity caused by a change in $d\theta$ (radians) in its propagation direction on a plate face, and ψ_n (radians) is an angle between a mode beam and a propagation direction [295].

(7) Impedance matching[70,297]: Ensuring the impedance at the input and output impedance are the same, preventing acoustic energy from being dissipated within the IDTs. Electrical dissipation in other forms should be avoided, such as electrical shielding and conductive short connections. Solutions include using matching networks or adjusting the IDT designs. This is one of the key factors in the complexity of SAW fields used for microfluidic applications [297].

(8) Bragg reflection [293]: The wave reflections due to the electrode interactions lead to in-phase scattering waves with significantly stronger reflections. This occurs when the wavelength (λ) equals the periodicity (P). Alternative electrode designs, such as double electrode or split electrode IDTs, are discussed in the following section as potential solutions.

(9) Triple transit signals [293]: This phenomenon, also referred to as triple-transit-interference (TTI) or multiple-paths effects, is generated by the non-matched output of IDTs, leading to periodic ripples in frequency responses. This interference is attributed to reflected waves produced by output IDTs, undergoing multiple reflections, including reflections from the opposite IDTs and a secondary reflection by the input IDTs (shown in Figure 3.2(d)).

(10) Bidirectional effect [70]: Conventional IDTs simultaneously propagate waves in two directions (Figure 3.2(d)), potentially wasting wave energy if one direction is unused. This can be resolved using alternative designs, such as a single-phase unidirectional transducer, discussed later.

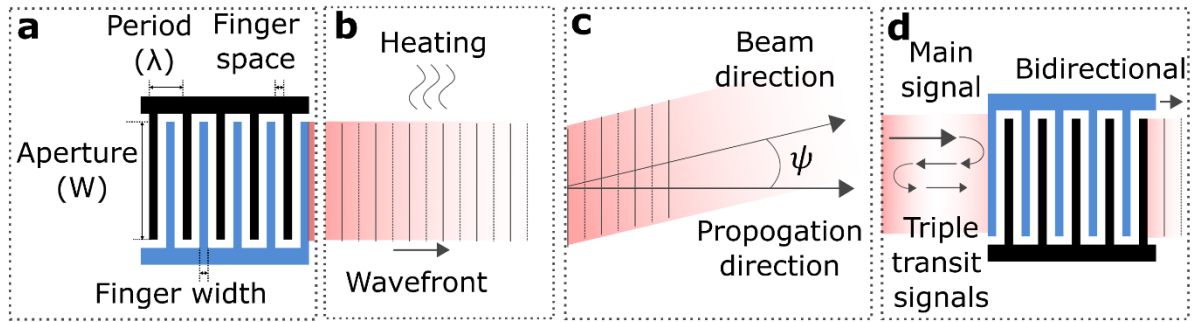


Figure 3.2. Conventional IDT and illustrations of example design considerations. (a) Schematic of conventional IDT with labelled parameters: period, finger spacing, aperture, and finger width. (b) A continuation of (a) illustrating the SAW wavefront propagation and associated heating effects. (c) Continuation of (a) showing the SAW wavefront during beam steering, highlighting the power flow angle. (d) Further continuation of (a) incorporating an opposing IDT configuration, demonstrating the triple transit and bidirectional effects of IDTs.

3.3.2. Electrode materials

The choice of materials for the IDT electrodes influences the SAW devices' performance and electromechanical coupling coefficient [298–300]. IDTs are typically required to possess specific characteristics to optimise their functionality. These include low mass to minimise damping, high acoustic impedance to confine acoustic waves within the piezoelectric layer, and high conductivity to reduce series resistance during the transmission of excitation signals. Different electrode materials have been examined by Fu et al. [64], primarily considering their acoustic impedances ($Z = \rho \cdot v$, with ρ and v being the material density and wave velocity) and resistivity (ξ) of the materials.

In the fabrication of SAW devices, the most used electrode materials are aluminium (Al) and gold/chromium Au/Cr (or gold/titanium; Au/Ti). Aluminium stands out due to its advantages, including its abundance, low cost, low resistivity, low acoustic impedance, and high Q factor, making it suitable for SAW IDTs. Nonetheless, it does have critical drawbacks, such as low mechanical strength, a low melting point, and poor resistance to electro-corrosion. Typically, it requires enough thickness (commonly 100 to 200 nm) to achieve low electrical resistance while avoiding issues related to mass loading and excessive acoustic impedance. Gold electrodes excel at

high-power applications, liquid environments, or corrosive settings. However, gold IDTs show large mechanical losses at higher frequencies, relatively high mass loading, and reflection. In contrast, aluminium IDTs display high reflection coefficients and Q factors at higher frequencies [301].

Other materials, including conductive and transparent oxides, such as aluminium-doped zinc oxide and indium tin oxide, have applications as electrode materials in transparent SAW devices [302,303]. Additionally, Graphene [304,305] and its derivatives, known for their exceptional conductivity and minimal mass loading [306] due to their thin and lightweight nature, have been employed as IDTs for SAW devices [307,308]. Multilayer graphene with a sheet resistance in the tens of Ω/sq has been explored to enhance transmission properties [309].

3.3.3. Piezoelectric materials

Various factors should be considered when selecting the substrate materials to place the IDTs on. These factors include cost, temperature dependence, attenuation, and propagation velocity. It is important to recognise that piezoelectric materials exhibit anisotropy, meaning their properties vary across axes. Moreover, the ratio of plate thickness (h) to wavelength (λ) within the substrate can influence the anisotropy [295]. This anisotropy will impact the phase velocities, types of waves generated [3], electromechanical coupling coefficient and the power flow angle at different orientation angles and cuts [6]. Therefore, the layout and orientation of IDTs on the substrate and choice of substrate cut play a pivotal role in determining the efficiency of electrical energy transduction from SAWs [148], especially for desired optimum acoustofluidic effects. For example, the coupling coefficient may be increased 10 times or decreased to zero by changing the plate thickness [295]. The total modes detected in one substrate may be as large as ~ 100 [295]. Nevertheless, some modes may have small electromechanical coupling coefficients and/or larger power flow angles. These wave modes include SH-SAWs, leaky SAW, or pseudo-SAW [3].

For SAW fabrication in microfluidics, R-SAW on 128° YX-cut LiNbO_3 is typically used due to the large surface normal displacement component, which produces the transfer of momentum to the fluid [6]. To harness R-SAW on this particular substrate, an IDT is placed perpendicular to the X-axis, exploiting its exceptional electromechanical

coupling coefficient in this orientation [292]. However, this configuration is limited to acoustofluidic manipulation only in the X-direction. Alternative piezoelectric materials can address this limitation and achieve multidirectional SAW propagation. Among them, 152° Y-cut LiNbO₃ has demonstrated optimal performance, offering minimal anisotropic effects while maximising electromechanical properties [294]. Nevertheless, it's worth noting that 128° YX-cut LiNbO₃ remains the most widely adopted for R-SAW due to its outstanding electromechanical coupling, ensuring optimum acoustofluidic manipulation performance. Nonetheless, the inherent rigidity, brittleness, and anisotropic characteristics of LiNbO₃ have led to exploring various alternative substrates. Piezoelectric thin films, including zinc oxide (ZnO) [310–312] and aluminium nitride (AlN), can be deposited onto various substrates such as silicon (Si), glass, ceramics, diamond, quartz, glass, and more recently also polymer, metallic foils and bendable glass/silicon for making flexible devices [64,311]. Piezoelectric films would allow for integrated, disposable, or bendable device fabrication. Due to the isotropic nature of thin film materials deposited onto a planar substrate, flexible designs of electrodes or IDTs, such as focused, curved, circular/annular, or randomly shaped patterns, are readily achievable on thin film acoustic wave devices [64]. Furthermore, a bulk ceramic substrate such as LiNbO₃ has a low thermal conductivity and poor fracture toughness, which becomes a challenge when high power is needed. In contrast, thin films such as aluminium nitride or gallium nitride (GaN) could present novel piezoelectric films that, although piezoelectric performance is compromised, offer higher input power and superior thermal stability [313,314].

3.3.4. IDT Fabrication techniques

Cleanroom manufacturing techniques, including photolithography, evaporation, sputtering, lift-off and etching, allow the fabrication of high-efficiency, small-scale, precise, and reproducible IDTs. The two main standard patterning methods are subtractive and additive. Subtractive patterning involves deposition, lithography, and etching (wet or dry), starting with wafer cleaning, followed by IDE material deposition using methods like sputtering, thermal evaporation, or chemical vapour deposition. Lithography patterns photoresist with ultraviolet light exposure to create a positive IDE image, then etching techniques are used to remove the IDE material, and the photoresist is finally removed. In contrast, additive patterning employs lithography to

create a negative IDE image, deposits the IDT material on the patterned photoresist and utilises a lift-off process to remove both.

Advanced techniques like electron beam lithography, focused ion beam milling, or nanoimprinting enable the creation of sub-micron wavelengths for super-high frequency SAW devices. For instance, the e-beam lithography method has produced SAW devices with frequencies from 20 to 44 GHz based on LiNbO_3 , $\text{ZnO}/\text{SiO}_2/\text{Si}$, or $\text{LiNbO}_3/\text{SiO}_2/\text{SiC}$ heterostructures [315–317].

Cleanroom techniques can be expensive, and brittle substrates like LiNbO_3 pose challenges in modification and repair. An alternative approach involves manufacturing IDEs separately from the piezoelectric material. For example, the IDEs can be made onto printed circuit boards (PCBs) and pressed onto piezoelectric substrates, especially for prototyping. This method involves mechanically clamping electrodes made using PCB or even flexible PCB with a piezoelectric substrate [14,15,318]; hence, the waves can be generated by simply applying RF frequency to the pressed IDEs on the piezoelectric substrates.

Other electrode manufacturing methods include pouring low-melting-point metal into a mould by PDMS [319], stacking aluminium foil strings onto substrate [320] and using superstrates on conventional SAW devices for reuse in different applications [321]. 3D printing can produce various shapes of electrodes and electrode arrays with specially designed reflectivity and directionally (e.g., bidirectionality/unidirectionality) and varied frequency spectra. However, the IDTs' resolution may not match lithography produced ones.

3.4 Advances of IDTs

3.4.1. Conventional IDT structures

The **standard bidirectional IDTs**, discussed in Section 3.3.1, have a simple design (Figure 3.3(a)). The design comprises two electrode fingers, bus bars, and an electrode pad. However, it has issues such as internal mechanical edge reflections and loss of wave energy due to half the energy being wasted in one direction. Alternative designs to address these issues have been explored, including straight or curved (focused or plane waves) IDT types, standing waves versus propagating

waves, and aligned or shifted waves. While some IDTs are designed for sensing purposes, they may not be optimally suited for acoustic streaming applications.

(1) Split IDTs (Figure 3.3(b)) [64]. These IDTs reflect some waves, reducing reflections and minimising spurious responses caused by finger reflections.

(2) Single phase unidirectional transducer (Figure 3.3(c)) [64]. These are commonly used to reflect or cancel regenerated waves through internally tuned reflectors within the IDTs, enabling unidirectional SAW propagation. They are effective in minimising the triple transmission effect, reducing noise/insertion loss, and decreasing passband ripples [322,323]. Various designs exist: (1) Split finger pair using $1/16 \lambda$, in which all the gaps equal $1/8 \lambda$. (2) Fixed split finger pair or different-width split finger (varied widths to obtain a required directivity) [324], (3) Triple electrode section, with specific gaps and finger sizes of $3\lambda/8$, which will generate a third harmonic response stronger than its fundamental response. (4) Special designs include finger widths of $1/5$, $2/5$, $1/5$, and $1/5 \lambda$. However, these may limit the fabrication of super high-frequency devices, resulting in reduced SAW energy efficiency and higher insertion loss.

(3) Distributed acoustic reflecting transducer (Figure 3.3(d)) [64,325]. These consist of a sequence of identical cells with a length equal to wavelength λ . Each cell has two electrodes with a width of $1/8 \lambda$, and one with a width of $1/4 \lambda$, separated by an inter-electrode space of $1/8 \lambda$. This design enables variable reflection to cancel net reflection and transmission effects. Segmenting the reflecting electrodes provides design flexibility, beneficial for SAW microfluidics and sensors as it enhances performance while maintaining optimal operating conditions.

(4) Floating electrode unidirectional transducers (Figure 3.3(e)) [64,326]. One or more electrodes are not connected to others (floating). These shorted or open electrode configurations change the transducer/reflector interactions and promote forward transmissions.

(5) Apodised IDTs (Figure 3.3(f)) [64]. Apodised IDTs achieve non-uniform beam profiles by varying or setting the lengths and positions of the IDTs. Varying the electrode overlaps along the transducer length produces a specific frequency response. This generates impulse response/pre-pattered pulse waves. Apodisation techniques involve designing the top electrode with non-parallel edges to increase the

resonant path and attenuate spurious lateral modes. This pattern is used for wave shaping, frequency response manipulation, minimising heating effects, avoiding bulk wave interferences, diffraction, and IDT end-effects, or optimising the output signal profile.

(6) Focused or curved IDTs (Figure 3.3(g)). Focused IDTs generate concentrated acoustic force or energy, enhancing pumping and mixing efficiency in acoustofluidics [327] and improving sensitivity and resolution in sensing applications. However, modification of IDTs into a concentric elliptical shape is recommended for anisotropic crystal cuts of bulk piezoelectric materials, ensuring that the curvature aligns with that of the waves surface [327,328].

(7) Chirped IDTs or dispersive delay lines (Figure 3.3(h)). Chirped IDTs control wave modes and reflectivity by varying the width and frequency of the IDTs, enabling linear modulation of wave pitch/frequency. These IDTs have a relatively large bandwidth and can gradually change frequency by altering the electrode spacing. These can be designed as expanders (large width to smaller width) or compressors (small width to larger width). Chirped IDTs are valuable for creating focused acoustic energy by tuning the frequency, manipulating droplets in different directions, and manipulating single microparticles, cells and organisms [276,329,330].

(8) Slanted finger IDTs or tapered or tilted IDTs (Figure 3.3(i)). [178,331] Slanted finger IDTs feature varying frequencies in the IDT section achieved by altering the electrodes periodicity. These IDTs have broad bandwidths and can change the moving direction of a droplet by continuously adjusting the operating frequency [3,332,333].

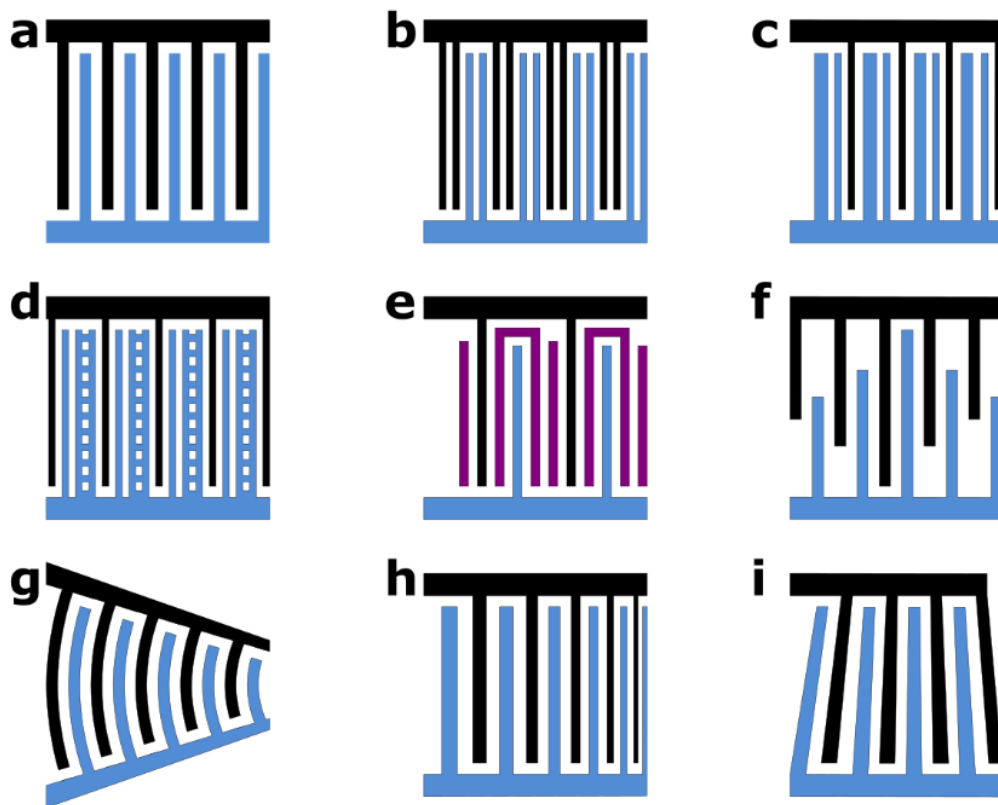


Figure 3.3. Conventional IDT designs. (a) Standard bidirectional IDTs (b) Split IDTs (c) Single phase unidirectional transducer (d) Distributed acoustic reflecting transducer (e) Floating electrode unidirectional transducer (f) Apodised IDT (g) Focused or curved IDT (h) Chirped IDT or dispersive delay lines (i) Slanted finger IDT or tapered or tilted IDTs. [Reproduced with minor alterations from “Stringer *et al.* Methodologies, technologies, and strategies for acoustic streaming-based acoustofluidics. *Applied Physics Reviews* 1 March 2023; 10 (1): 011315. <https://doi.org/abc.cardiff.ac.uk/10.1063/5.0134646>” [2], with the permission of AIP Publishing.]

3.4.2. Unconventional IDT structures

Many uncommonly used IDT patterns exist besides the commonly used IDT structures.

(1) Circular or annular IDT (Figure 3.4(a)) [334,335]. Circular IDTs, an extension of focused IDTs, offer a large focused acoustic force or energy and find applications in improved pumping, mixing and droplet jetting. However, like focused IDTs, they

encounter issues related to the anisotropic properties of substrates. This can be addressed by designing a slowness curve-adjusted device (deviating from the circular shape) or using a concentric elliptical shape, shifting the beam direction away from a parallel propagation direction [336]. These issues are often less significant for piezoelectric thin film-based SAW devices due to the isotropic wave propagation on the planar surfaces [64].

(2) Spiral IDT designs [271,337] or anisotropic swirling SAWs (see Figure 3.4(b) to Figure 3.4(d)). The three types main types of Spiral IDTs are: (1) Swirling IDT designs (Figure 3.4(b)), which enable varied acoustic wave fields by adjusting the applied signals; (2) Constant electrode spiral angle (Figure 3.4(c)), which provides a uniform spiral angle for electric field but varied intensity [27,337]; (3) Constant pitch (distance) between adjacent electrodes (Figure 3.4(d)), which provides a uniform intensity of electrode fields but various spiral angles, allowing for in-plane torsional displacement and vibrations [338,339]. This design, also known as Ring waveguide resonator IDTs [340], is suitable for sensor applications due to its high-quality factor and absence of sidelobes in electrical admittance. Additionally, circular slanted finger IDTs with angularly varying finger widths and spacing can introduce frequency-multiplexing [341]. These complex wave fields generated using spiral SAW acoustical vortices can be used for particle tweezing, liquid twisting, and swirling on a single functional platform. This design can generate focused waves which are varied constantly by adjusting different focusing points in arbitrary positions [223,342]. This has been used for various biological applications, including 3D manipulation, droplet transportation, separation, fusion, and nebulisation [223,342]. However, spiral IDTs can be difficult to design when considering anisotropic substrates.

(3) Holographic IDTs (Figure 3.4(e)) [343,344]. Holographic IDTs create waves using specially designed metallic electrodes that form equi-phase lines of the targeted wavefield on the surface of the piezoelectric substrates. This results in laterally-focused (cylindrical) and 3D-focused (spherical) acoustical vortices. These IDTs [343,344] offer advantages such as high working frequency (resolutions down to micrometric scales), ease of fabrication with standard lithography techniques, and seamless integration with standard microscopes, as they are flat, transparent and miniaturised [343,344].

- (4) **Ball shaped IDTs** (Figure 3.4(f)). In these IDTs, waves propagate around the equator of a large sphere in multiple roundtrips. The number of SAW circulations around the ball is the SAW propagation length. This configuration is beneficial for sensors and acoustofluidic devices on spherical surfaces, as it minimises energy loss from diffraction and allows for longer propagation paths, enhancing sensitivity [345].
- (5) **Inter-digitated IDT** (Figure 3.4(g)) [346]. These IDTs utilise interweaved input and output transducers to eliminate the inner transducers' bidirectional insertion losses and suppress spectral sidelobes.
- (6) **Tuneable IDT** (Figure 3.4(h) and **multiphase IDTs** (Figure 3.4(i)). Tuneable IDTs are a series of densely distributed electrodes [347]. Different wavelengths can be formed by connecting them in various configurations without changing the electrode layout. Other tuneable IDTs could consist of several IDTs arranged in an in-line configuration with different centre frequencies and bandwidths [348].
- (7) **Embedded IDTs**. In these IDTs, the fingers are embedded within the substrates, mitigating reflection and scattering effects [349]. However, this approach requires additional fabrication steps, such as etching into substrates and post-polishing [349]. Embedded IDTs are particularly important for focused IDTs as they minimise finger grating effects on the angular dependence of phase velocity [350]. This process is simplified for thin film-based SAW devices as the IDTs can be deposited onto the surface or filled into the grooves to eliminate technological imperfections [351,352].

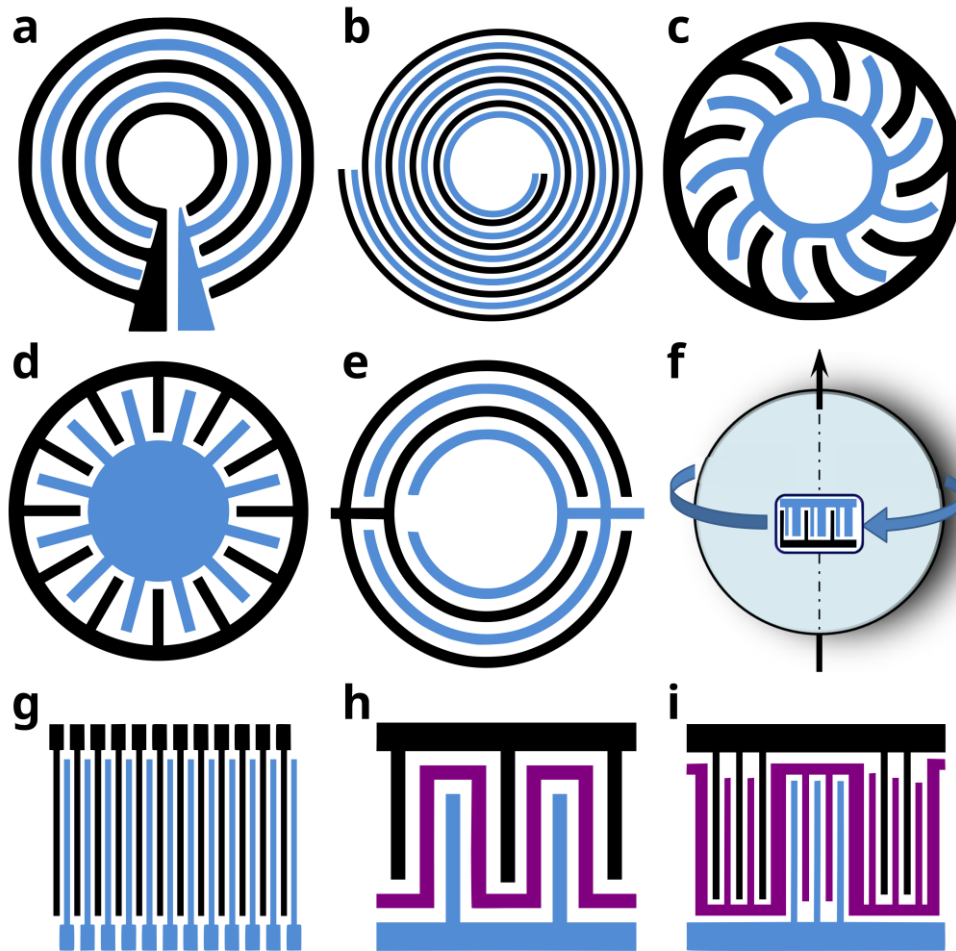


Figure 3.4. Unconventional IDT designs. (a) Circular or annular IDT (b) Swirling IDT (c) Electrode spiral angle IDT (d) Ring waveguide resonator IDT (e) Holographic IDT (f) Ball shaped IDT (g) Inter-digitated IDT (h) Tuneable IDT (i) Multiphase IDT. [Reproduced with minor alterations from “Stringer *et al.* Methodologies, technologies, and strategies for acoustic streaming-based acoustofluidics. *Applied Physics Reviews* 1 March 2023; 10 (1): 011315. <https://doi-org.abc.cardiff.ac.uk/10.1063/5.0134646>” [2], with the permission of AIP Publishing.]

3.4.3. IDTs embedded into multi-layer structures

As previously discussed, the isotropic nature of thin-film materials deposited onto a planar substrate enables flexible electrode designs of IDT designs, including focused, curved, circular/annular, or randomly shaped patterns, on thin-film acoustic wave devices [148]. Furthermore, the thin film deposition process offers flexibility in the placement of the IDTs relative to the piezoelectric materials.

IDTs do not always need to reside on top of piezoelectric materials. For instance, a “liquid needle” was demonstrated using a circular self-focused bulk wave acoustic transducer with circular IDTs on the top and bottom of the thin-film piezoelectric material. This configuration generated a focused acoustic wave, resulting in a needle-shaped liquid column on the free liquid surface [353–355]. In thin-film acoustic wave devices, various layers have been employed to enhance temperature stability, phase velocity, and electromechanical coupling coefficient, leading to different IDT placement options [356]. These designs include placing IDTs on top of the substrate or intermediate layer, incorporating piezoelectric or insulating layers, and configuring short-circuiting planes [64].

The position of the IDT can vary, whether on the piezoelectric layer or beneath it, to generate acoustic waves. The addition of a piezoelectric layer or dielectric layer with high permittivity above the IDTs enhances electromechanical coupling. This allows for the fabrication of devices with reduced insertion loss or smaller dimensions [357]. In some cases, a hard insulating top layer can shield the IDTs, piezoelectric film, sub-layers, and the substrate from harsh environments or liquids, thereby improving the long-term stability of the devices [358].

3.5 Fluidic Vessel

3.5.1. Vessel type

The fluidic vessel used in microfluidics is typically split into two types: digital or continuous. Digital normally refers to droplet-based, which has the benefits of high mobility, reduced cross-contamination, flexibility, sample isolation and elimination of channel fabrication. However, droplets have a limited volume and may be more complex to handle, especially due to their droplet instability and inconsistent formation. Parameters, including the droplet's shape, volume, contact angle, and evaporation, determine acoustic streaming patterns that lead to various particle manipulations. Additionally, the vessel's position can be adjusted concerning the IDT to create different functions; for example, a droplet offset to an IDT can create concentration [359].

Continuous microfluidics is the liquid within microchannels or chambers. This includes open chambers (exposed to air), closed chambers (entirely closed and sealed from the surrounding environment) and microfluidic channels (open or closed chambers with micron-sized dimensions that fluid can flow through). Incorporating a chamber provides stability and control for larger volumes of liquid. Additionally, a chamber can mimic a droplet, such as a dome chamber [57] or a PDMS ring [12,360] which enables consistent droplet sizes. Channels offer a steady flow and higher throughput. Nevertheless, channels and chambers have limited mobility and may be susceptible to cross-contamination and sample loss within the channel/chamber. It is important to note that the channel/chamber boundary significantly impacts the streaming patterns, which allow for versatile applications. The boundary could consist of different geometries (e.g., dimensions/thicknesses or shape, tubes or chambers), interfaces (e.g., liquid–air, liquid–glass) or materials (e.g., glass capillary, PDMS). For example, boundary shapes can be manipulated to create sharp edges or microstructures for improved streaming [361].

The choice between using droplets or channels in acoustofluidics depends on the specific requirements of the application. Researchers need to carefully consider their experimental goals and constraints when selecting the appropriate approach.

3.5.2. Vessel materials

Acoustofluidic manipulation functionality and performance are significantly impacted by the material used for the channel/chamber. These materials typically fall into three categories: hard, soft, or hybrid, each with advantages and drawbacks in acoustofluidics.

Hard materials offer precise control over channel geometry, high chemical compatibility, transparency, thermal stability, and durability [362]. However, these materials are primarily used in BAW devices due to their low attenuation and high acoustic reflection properties. Examples of hard materials include polymethylmethacrylate, polycarbonate [362], silicon/glass slides [363], or steel sheets [364]. These materials are typically not used for SAW due to the high reflection rate, which prevents SAW from interacting with the sample [365]. Additionally, hard materials tend to be brittle and involve complex fabrication processes [366].

Soft materials have reduced acoustic reflection, flexibility, and biocompatibility. They are easy to fabricate, cost-effective, disposable, and transparent for observation [367,368]. These are made with plastics and elastomers, with PDMS being the most common choice [362,366,368]. Nonetheless, soft materials have higher permeability to specific chemicals and require more precise temperature control, limiting their suitability. They may also undergo dimensional changes over time, potentially impacting device performance [366].

Hybrid materials offer a middle ground, enhancing functionality for complex device designs, structural integrity, and flexibility. Customisation options allow users to tailor materials to specific application requirements, considering biocompatibility, precision, and cost. Examples include using PDMS with a reflective layer such as PDMS/glass slides [369,370], PDMS/hard PDMS thin film [371] or PDMS/aluminium [372]. In such cases, users benefit from the soft properties of PDMS while enhancing reflective properties, which change the acoustofluidic manipulation. For example, this can be used to increase the critical particle diameter that a device can actuate, increase the channel throughput [373], or change the position of the nodal lines [372]. However, designing and fabricating hybrid materials are more complex, especially with limited laboratory resources [362].

In summary, microfluidic vessels encompass a range of materials, a comprehensive review of which can be found in references [366,368,374]. PDMS is a popular choice for acoustofluidic applications due to its biocompatibility, ease of fabrication, flexibility, low cost, transparency, reduced acoustic reflection, and the ability to integrate with electronics. It suits various biological and biomedical applications, preserving sample integrity and precise control. Nevertheless, material selection should align with specific application requirements.

3.5.3. Vessel fabrication techniques

The choice of fabrication technique depends on the material, channel complexity, required precision, and the available equipment in the research/manufacturing facility. These techniques can be categorised into material removal and depositional processes [374].

For hard materials, which demand precision and can endure aggressive techniques, some options include photolithography, wet or dry etching, and laser ablation. Photolithography (250 nm resolution) selectively removes material from a wafer, typically using SU-8 negative photoresist [375] (due to its high resolution, mould durability and capacity for high aspect ratios[376]) and ultraviolet light exposure. Other photolithography techniques can include nanoimprint lithography (15 nm), x-ray lithography (15 nm) or electron beam lithography (10 nm); however, these methods are primarily used in large-scale manufacturing facilities [377]. Wet or dry etching [378] can remove material through dissolved chemical solution or ionised gas, respectively. Laser ablation vaporises or removes material through high-energy beams [377]. These methods offer high precision and fast manufacturing; however, they have complex procedures and often need expensive cleanroom procedures.

Soft materials may require different material removal/deposition techniques. Soft lithography is like photolithography but tailored to soft materials like PDMS, using their elastomeric properties [379]. This technique is often the standard fabrication method of microfluidic devices due to their high-resolution replicas and 3D geometries. However, there are issues with pattern deformation and damage. Hot embossing is ideal for soft materials like PDMS, which can deform as a patterned template is pressed into uncured PDMS, which is then cured to replicate the pattern for the microfluidic channel [376]. For the same reason, PDMS also works with injection moulding, where uncured PDMS is injected into a cavity, cooled, and removed from the mould [376]. Injection moulding and hot embossing are more popular in commercial microfluidic devices due to their mass production capability [380]; however, their initial costs limit them for microfluidic researchers [376]. Low-cost manufacturing methods include micro-milling (25 μm), laser cutting (25 μm), and 3D printing (5-100 μm) [377]. Micromilling and laser cutting use mechanical drills or lasers to cut and engrave layers to create channel structures. 3D printing involves creating the channel layer-by-layer, which is useful for microfluidic researchers and can be easily used for prototyping [376]. An alternative approach consists of utilising a 3D-printed master mould on a smooth glass slide [381], enabling the creation of a PDMS channel using off-the-shelf components. A straightforward cleaning procedure with isopropanol alcohol (IPA) alone ensures adequate adhesion of the PDMS channel to the substrate [12], making it highly suitable for prototyping. Alternatively, adding a thin

layer of PDMS gel or using a mechanical clamp can further strengthen the bonding [210,381]. Notably, this technique relies solely on suction or mechanical pressure and eliminates the need for clean room facilities, such as plasma treatment [381]. While most materials require bonding to the substrate, the specific bonding method can vary, such as clean room methods (e.g., plasma treatment), thermal techniques, a mechanical pressor, suction, or adhesive materials (e.g., a thin gel).

A demonstration of the vessel fabrication procedure is presented in Figure 3.5. Initially, the selection of the appropriate fluidic vessel type, be it droplet, chamber, or channel, is determined based on the specific application requirements. In the case of chambers or channels, computer-aided design (CAD) software is used to create the corresponding mask design. Subsequently, a chosen fabrication method is applied to create the master mould, exemplified by 3D printing for a chamber and soft lithography for microchannels. Following the mould fabrication, a PDMS mixture is prepared by combining PDMS elastomer with a curing agent (10:1 ratio). Vacuuming is then used to eliminate any trapped air bubbles within the PDMS mixture. The PDMS mixture is poured into the prepared mask and allowed to cure. Once solidified, the mask can be gently removed and bonded to the substrate using one of several bonding techniques, such as mechanical pressor or plasma treatment. In the case of microchannels, it is necessary to incorporate inlets and outlets, which can be achieved by perforating the PDMS material.

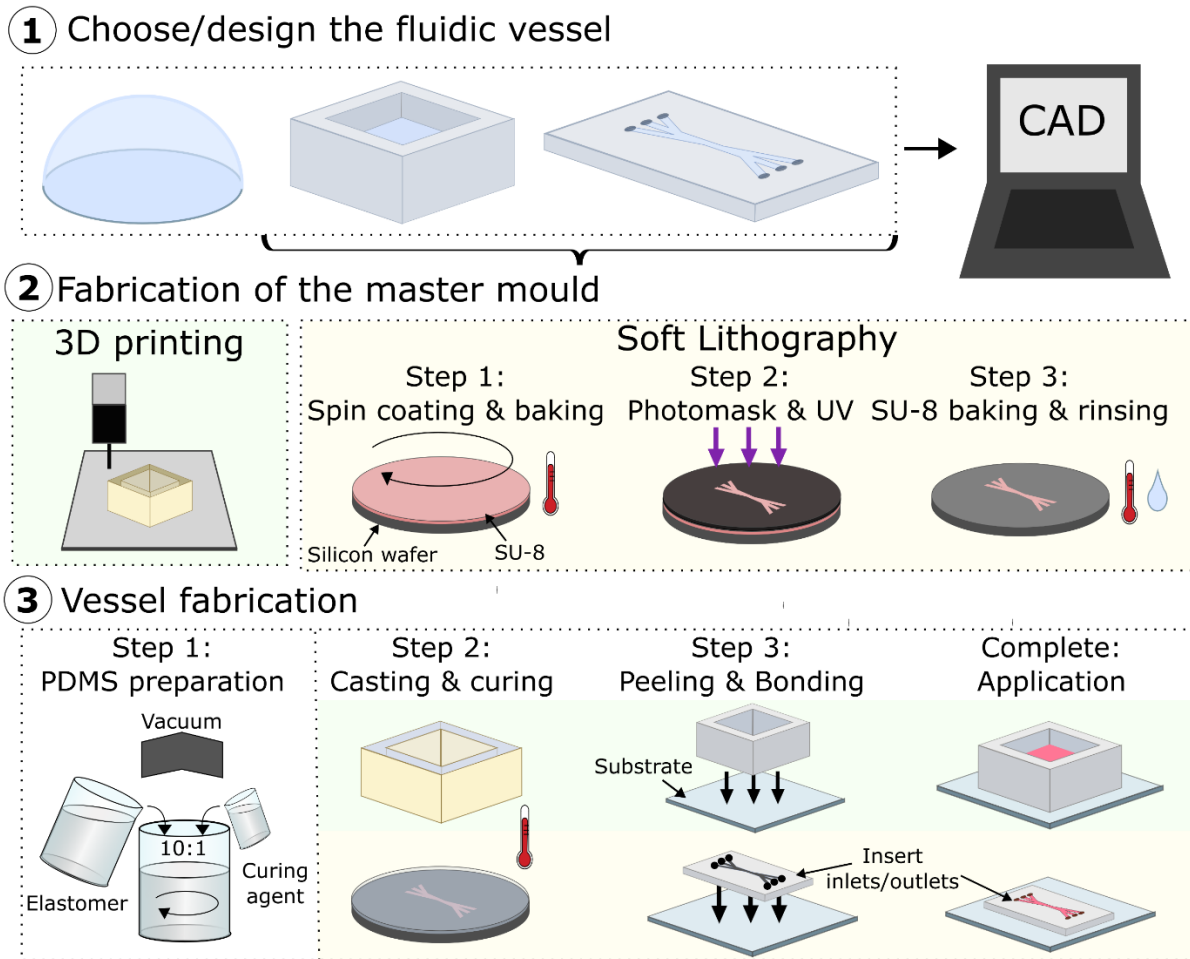


Figure 3.5. Typical procedure for producing microfluidic vessels using two methods, 3D printing [210] and soft lithography, for a chamber and microchannel, respectively [377,382]. (1) Choice and design of fluidic vessel (2) Fabrication of the master mould, involving 3D printing the design or lithography mask process. (3) Vessel fabrication, including the PDMS preparation, casting, curing, peeling, bonding, and inserting inlets/outlets for channels.

3.6 Conclusion

In brief, IDT and the fluidic vessel designs and fabrications are critical in generating streaming patterns using SAW devices. Different designs and configurations can generate a variety of sensing functions and distinct streaming patterns. Adjusting the IDT design, configuration, and input parameters (such as applied power, amplitude, and frequency) makes improving sensitivity or manipulating acoustic streaming patterns for the desired applications possible, as discussed in Chapter 2.

4.1 Introduction

Chapter 4 of this thesis delves into the foundation, development, and specifics of the Hexagonal FPCB IDT. As previously discussed in Chapter 2 [2], SAW-based acoustic streaming generated by IDTs has found diverse biomedical applications. Chapter 3 reviews the strategies by which one can complete these acoustofluidic applications. This includes varying IDT designs, piezoelectric substrates, wave modes, and the fluidic vessel [5,39,60,70,71,284]. This chapter offers a thorough insight into the rationale and the developmental pathway, based on the knowledge covered in Chapter 3, of a novel Hexagonal FPCB IDT suitable for rapid prototyping and investigations for acoustic streaming based acoustofluidic applications.

4.2 Motivation of a Hexagonal FPCB IDT

Typically, acoustofluidic functions were generated using R-SAW on 128° YX-cut LiNbO_3 substrate. This choice is attributed to its substantial surface normal displacement, facilitating efficient energy/momentum transfer to the fluid [6]. Therefore, they have been extensively applied to generate functions such as mixing, pumping, concentrating, and jetting [2]. The 128° YX-cut LiNbO_3 substrate is optimal for generating R-SAW along the X-axis, however, this orientation limits acoustofluidic manipulation along a single axis, restricting its use in applications that benefit from diverse configurations.

The ability to generate various types of waves in a multidirectional manner offers substantial advantages in acoustofluidics [294]. For instance, the use of multidirectional SAWs for acoustic tweezers, such as two orthogonal symmetric SSAWs [3,265], enables the creation of intricate 2D patterns of nodes and antinodes for precise manipulation of particles/cells [266–268]. Additionally, incorporation of TSAWs for levitation in a third direction allows for the realization of three-dimensional (3D) acoustic tweezers [224]. Another acoustic tweezer configuration using symmetrical tri-directional IDTs generates TSAWs to achieve programmable control of microparticle movements [222]. These straightforward approaches offer rapid, precise, and noncontact control over particles and cells [36], making it suitable for

diverse biomedical applications including tissue engineering, in vitro cell studies, or 3D biometric structures. Understanding SAW phenomena, particularly when the IDTs are oriented at different angles on anisotropic substrates, is crucial for determining subsequent acoustofluidic effects [6]. Research effort has been made to explore R-SAW phenomena under various setups, shedding light on practical considerations for optimal transducer designs [6]. This understanding becomes paramount when considering the interaction of SAWs with the fluidic environment, as it enables the mitigation of adverse effects and optimization of acoustic streaming for enhanced micro- and nanoparticle manipulation [294,336].

Moreover, simultaneous excitation of multiple wave modes, such as SH-SAWs and R-SAWs, has shown promise in enhancing biosensor sensitivity [383] and overcoming diffusion limitations without causing particle damage [384]. Such SH-SAW biosensors hold significant potential for the detection of [385], DNA [386] and proteins [387] in liquid environments. Although both fluidic and sensing functions have been realised effectively on various crystal cuts, the integration of SH-SAW for acoustofluidic actuation applications remains relatively unexplored [9,388], mainly due to its reduced damping effects or weakened coupling with the liquid. The promising result of dominant SH-SAWs on alternative crystal cuts, such as 36° YX-cut LiTaO₃ substrate, underscore its suitability for acoustofluidic applications requiring mixing, pumping, and jetting [9,388]. For instance, SH-SAW generated on 36° YX-cut LiTaO₃ achieved streaming velocities of 5 mm/s, exceeding those of R-SAW on the same substrate, which produced 2 mm/s for 2 µl water droplet at 15 dBm [9]. Additionally, SH-SAWs have also demonstrated vertical jetting [388]. This technique presents valuable tools for applications such as 2D and 3D bioprinting, needle-free fluid injection, and single-molecule detection. However, it is noteworthy that the SH-SAW streaming velocity on 36° YX-cut LiTaO₃ is comparable in magnitude to that observed on standard R-SAW produced on the 128° YX-cut LiNbO₃ substrate with a similar size and power [9,389].

Despite advancements with multidirectional wavefields and wave modes, a comprehensive investigation of wave modes and angles remains largely unexplored. Understanding these complex wavefields and wave modes is crucial for optimizing acoustofluidic devices as it determines all subsequent acoustofluidic effects [6,294,336,390]. This knowledge can shift the focus from altering IDT designs to

manipulating wave mode selection, enhancing device performance by enabling multiple acoustofluidic effects within a single device. For example, our team demonstrated that alternating the X-rotation angle on the 128° YX-cut LiNbO₃ substrate enabled a synergistic blend of R-SAW and SH-SAW mechanisms for rapid exosome concentration [12]. Utilizing COMSOL studies and the Hexagonal FPCB IDT, we can uncover novel wave modes on the 128° YX-cut LiNbO₃ substrate with promising use in acoustofluidics.

This thesis introduces using hexagonal FPCB IDT to enable the study of multidirectional wavefields, which offers a reconfigurable platform for rapid investigations beyond the constraints of those conventional IDTs. This opens new possibilities for multidirectional SAW applications, providing unprecedented variability and control in manipulation techniques. To our knowledge, the utilisation of Hexagonal IDTs [391] has previously been used only for simultaneous surface manipulation and sensing in a biosensor [392,393]. This research opens new possibilities for enhanced manipulation and sensing in diverse fields such as biomedicine and industrial processes.

4.3 Overview of Hexagonal FPCB IDT

The schematic illustration of the Hexagonal FPCB-SAW device is shown in Figure 4.1. The subsequent sections provide a comprehensive explanation of each component of this device, along with the detailed rationale:

1. Piezoelectric Substrate (Section 4.3.1)
2. IDE Design (Section 4.3.2)
3. IDE Fabrication Technique (Section 4.3.3)
4. Mechanical Housing and Assembly (Section 4.3.4)
5. Matching Network (Section 4.3.5)
6. Fluidic Vessel (Section 4.3.6)

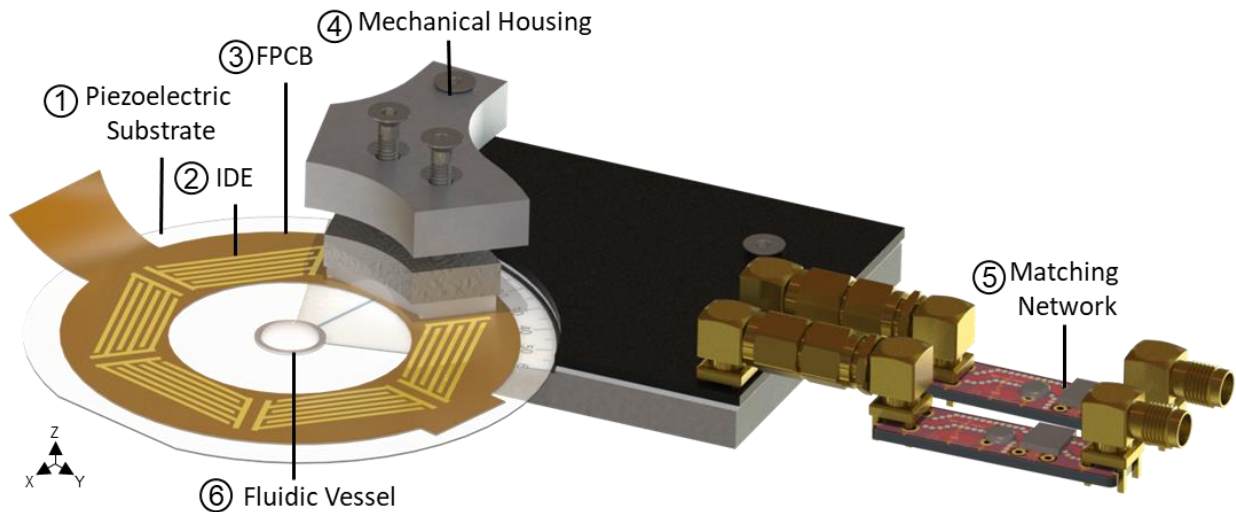


Figure 4.1. Abstract illustration overview of the Hexagonal FPCB IDT Device. (1) Piezoelectric substrate (128° YX-cut LiNbO_3 substrate) (2) IDE (3) FPCB (4) Mechanical Housing (5) Matching Network (6) Fluidic Vessel (PDMS Ring).

4.3.1 Piezoelectric Substrate

When selecting the appropriate piezoelectric substrate for multidirectional acoustofluidic device, several critical factors were considered, including material choice, crystal orientation, electromechanical properties, thickness, acoustic wave mode, cost, availability. The considerations are elucidated as follows:

Firstly, the substrate material choice was a vital decision due to the range of properties associated with different materials, as discussed in Chapter 3. For instance, thin films like ZnO or AlN exhibit isotropic in-plane behaviour allows greater flexibility in electrode design for generation and propagation [5,394]. However, they generally possess lower electromechanical coupling coefficients in comparison to LiNbO_3 [294]. LiNbO_3 stands out for acoustofluidic devices due to its large coupling coefficient relative to other single-crystalline materials for SAW and other wave modes [294]. Furthermore, it offers the advantage of being free from hysteresis and heating issues associated with in polycrystalline piezoelectrical materials [395], along with the convenience of use when compared with thin-film piezoelectric materials [294].

Nonetheless, the specific cut of the LiNbO_3 also influences its properties. For example, the 131° Y-cut LiNbO_3 has previously demonstrated the highest electromechanical coupling coefficient and insertion loss [396,397]. However, this cut comes with the

drawback of generating numerous parasitic bulk waves [294]. On the other hand, 128° YX-cut LiNbO₃ is optimal for generating R-SAW along a single x-axis. Nevertheless, at other angles, beam steering and a reduction in electromechanical coupling occurs. For example, SAWs along the x-axis exhibit double the vibration displacement and particle velocity compared to those along the y-axis [294,398]. Studies employing multidirectional circular IDTs have often favoured the use of X-cut LiNbO₃ rather than 128° YX-cut LiNbO₃ [271] [341] due to its capacity to support a broader range of directions with relatively high-energy SAWs. Additionally, a study has found that 152° Y-cut LiNbO₃ is the most optimal in achieving both minimal anisotropic effects and maximum electromechanical properties [294], rendering it suitable for multidirectional SAW.

For the acoustofluidic device under discussion, the choice of substrate ultimately fell upon the 128° YX-cut LiNbO₃. The decision was primarily influenced by factors such as ease of availability, particularly during the constraints posed by the COVID pandemic, the cost, and the substrates status as one of the most widely used materials in the field of acoustofluidics. The use of multiple IDTs on this substrate allows leveraging the high electromechanical coupling in the X direction [6] and provides room for exploration in other angles and wave modes. Despite the potential of other waves modes, their characterisation for 128° YX-cut LiNbO₃ have received limited attention in the field of acoustofluidics. Nevertheless, the reconfigurability of this device, further discussed in Section 4.3.3, allows for easy adjustment and investigation of the orientation of the 128° YX-cut LiNbO₃ using all six IDTs. Additionally, the reconfigurability offers the flexibility to swap the substrate, and hence the choice of substrate in the initial design phase was not as critical compared to devices where such flexibility is not an option.

Furthermore, the substrates thickness can impact the performance. For example, changing the plate thickness can lead to a wave mode's velocity shifting, the coupling coefficient being increased 10 times or decreased to zero, or an acoustic beam direction changing [295]. Therefore, the available 128° YX-cut LiNbO₃ substrate of constant thickness of 0.5 mm (resulting in a plate thickness of $h/\lambda = 2.5$), was chosen and maintained throughout experiments. Additionally, a circular-shaped substrate with a diameter of 10 cm was selected to provide adequate space for the IDEs, the fluidic

vessel, and for observation. However, this size choice introduces a degree of brittleness, which prompted the design of the mechanical housing to account for this (Section 4.3.4).

4.3.2 IDE Design

The decision to produce a multi-IDT acoustofluidic device was to explore acoustic streaming effects and potential applications in directions other than the X-axis on 128° YX-cut LiNbO₃ substrate. An even number of IDTs, placed opposite to each other, was chosen due to the substrates inherent two lines of symmetry so that it can also facilitate investigation of SSAW at various angles. While four IDTs have been extensively investigated for acoustofluidic tweezers, the exploration of six IDTs or more is not often studied. Although more than six IDTs are intriguing, this device was constrained by factors such as power supply and signal generator resources. Consequently, a multidirectional SAW device was devised, featuring six IDTs, striking a balance between research possibilities and resource limitations, to investigate acoustic streaming manipulation.

To mitigate potential anisotropy-related challenges, straight IDTs were developed. Furthermore, the hexagonal configurations of 6 IDTs allowed for the option of either rectangular or trapezium-shaped straight IDTs, which would maximize the use of the available space.

The Hexagonal FPCB IDT design is illustrated in Figure 4.2(a), with the inset (b) displaying an image of the IDT fingers. The six IDEs were designed to be 60° apart in a hexagonal configuration. With the substrate measuring 10 cm in diameter, the inner diameter of the IDTs was set to 4 cm (measured from the centre of one IDTs to another). This adjustment allowed for adequate space for placing a fluidic vessel and for observation purposes. Each IDE was a trapezoidal shape, with dimensions of 2.7 cm for the back and 1.7 cm for the front (aperture). It is noteworthy that the acoustic aperture should exceed 1 cm, as discussed in Chapter 3, to satisfy the requirement of being at least 50 times the wavelength for optimal impedance and effective performance [293]. The bus bars thickness ranges from 1.3 mm to 1.8 mm, where they are thicker closer to the IDTs. A minimum 0.5 mm spacing between each bus bar (clearance) was implemented to prevent electrical shorts and crosstalk. The chosen

pitch size was set at $200\ \mu\text{m}$, the smallest feasible for the manufacturer, ensuring a high-frequency output. This pitch size consisted of an IDE width of $50\ \mu\text{m}$ and IDE gap of $50\ \mu\text{m}$. A total of 40 pairs of fingers (80 individual) were used to achieve a narrow bandwidth.

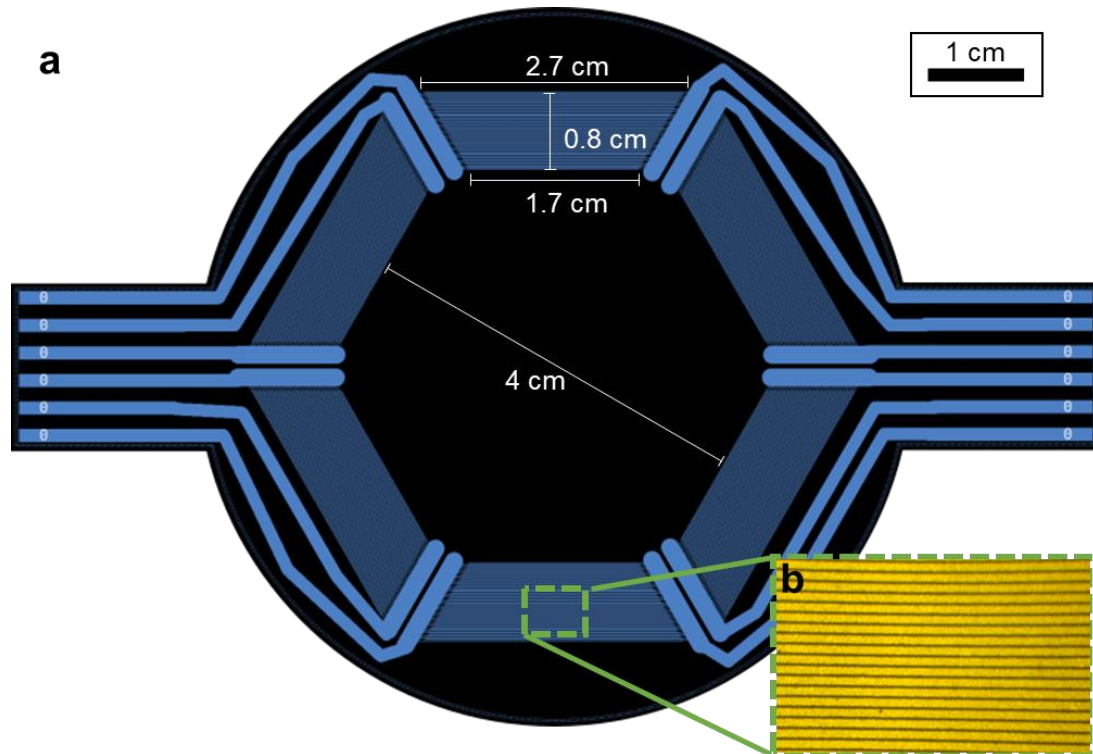


Figure 4.2. Schematic of Hexagonal IDT design (top view) (a) Entire IDT design showing the IDT fingers, busses, and the dimensions. (b) Zoomed in real image of IDT fingers section (highlighted in green).

4.3.3 IDT Fabrication

The IDT fabrication consists of two components: (1) the flexible PCB IDT for the IDEs, and (2) the rigid PCB IDT for the wiring and connectors.

Firstly, the FPCB-based IDTs designed on AutoCAD (Autodesk, US) and files were transferred to Eagle software (Autodesk, US). The design was converted to GERBER files and was sent to be manufactured externally (circuitfly.com), using a standard PCB manufacturing process. The IDEs were made of metal bilayers Au/Ni, $30\ \text{nm}/2\ \mu\text{m}$) patterned on a $70\ \mu\text{m}$ thick polyester laminate [399]. Figure 4.3(a) shows the front and back image of the final manufactured FPCB, respectively. The FPCB-based IDTs are highly versatile as they can be easily replaced, redesigned, or utilized with different

substrate materials and therefore it is ideal for prototype testing and research. For example, their flexible ability enables “lifting” up an IDT if not used to ensure no reflections. Additionally, if some electrode fingers have inconsistent dimensions, then the flexibility allows all the fingers to still contact the substrate. Compared to cleanroom made IDTs, FPCB-based IDTs save manufacturing effort and cost. They also offer the advantages of dynamic flexing, less weight, and better heat dissipation. PCB- and FPCB-based IDTs have been characterized in a previous study [399], proving they are suitable for generating SAWs. Our team has previously demonstrated droplet streaming, standing waves, and particle alignment using R-SAW [14,400]. Additionally, the use of a PCB-based approach enabled incorporation of a silkscreen design to assist in experiments. For example, the FPCB’s silkscreen features a centrally outlined line by the IDT, allowing for precise positioning and alignment of the IDT with the paper template.

A rigid PCB (Figure 4.3(b)), designed on KiCad, was used for the wiring and connectors, and helped align the IDT with the substrate-holding base plate. Its shape matched that of the base plate, with four corner holes for secure fastening and additional holes for attachment of the pressor. This PCB optimized the devices compactness and minimized wiring; a valuable feature particularly given there were six IDTs. Neatly positioned SMA connectors were soldered for external connections, and a helpful silkscreen aided in identifying each IDT, simplifying diagnostics and repairs. The central opening on the PCB was reserved for the FPCB IDT and the fluidic channel. The FPCB IDT was soldered to the relevant PCB solder pads. The design incorporated thick, equal-length yet direct traces, with adequate clearance maintained between traces to prevent crosstalk. A separate ground return was established with a reduced ground loop area, a consideration when separate IDTs were driven at different frequencies. Stitching vias were used for their higher current-carrying capacity and heat dissipation capabilities, ensuring reliable functionality.

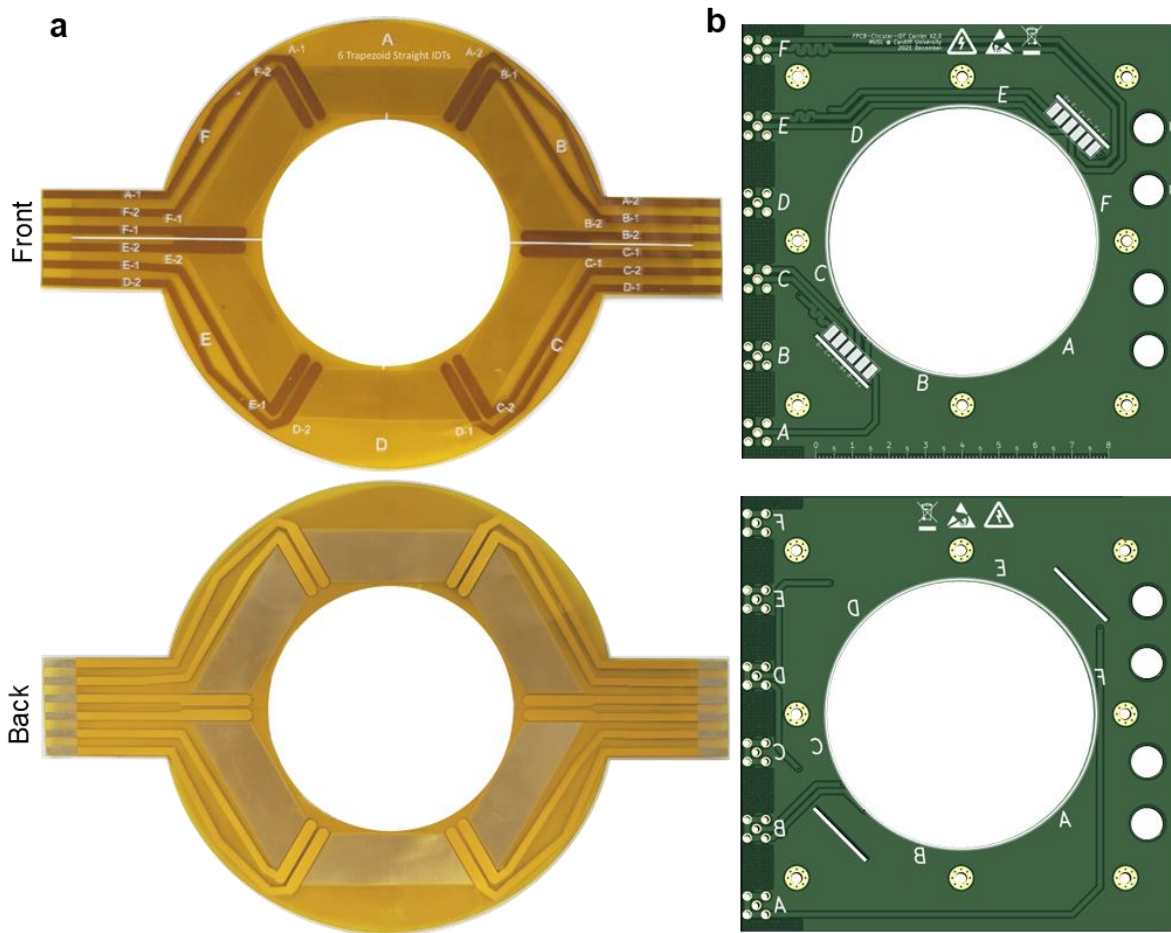


Figure 4.3. Images of the Hexagonal Flexible PCB IDT (top view) showing the front (top) and back (bottom) images (a) Real-life image of the of the Hexagonal FPCB IDT. (b) Rigid PCB KiCad model displaying the design and silkscreen.

4.3.4 Mechanical Housing and Assembly

The assembly of the Hexagonal FPCB device was a straightforward process, involving a purpose-built mechanical housing to establish contact between the FPCB IDEs and the substrate. An exploded view of the SolidWorks assembly is shown in Figure 4.4(a), followed by a cross-section schematic in Figure 4.4(b), and a fully assembled real-life model in Figure 4.4(c).

The foundation component was the aluminium base plate, selected for its heat dissipation and sturdiness properties. The base plate features a circular incision designed to securely hold the substrate in place. Within this incision, a precisely cut circular paper template was positioned and secured with double sided tape. This paper served a dual purpose – firstly it acted as a template for consistent fluidic vessel

location and displayed the angles offering alignment options. Secondly, it ensured a smooth surface for the placement of the LiNbO_3 to avoid cracking due to an uneven or rough surface when pressure was applied. Both the base plate and the paper template incorporated observation windows, permitting light to pass through for microscopes.

At the core of the assembly was the 128° YX-cut LiNbO_3 wafer, carefully cleaned with IPA, and positioned centrally on the base plate, directly on top of the paper template. The LiNbO_3 wafer had a distinct reference flat edge, served as a visual guide for determining the X propagation direction. A permanent marker was used to draw a line on the bottom surface, defining the centre of the flat reference. This line was carefully aligned with the paper templates angles, allowing for the adjustment of the substrates angle. For example, aligning the flat edge line with 0 degrees on the paper template ensures that the clamped IDT will conform to that specific angle.

The rigid PCB was aligned to the base plate and securely fastened using four M5 screws located at the corners. Four 3D printed pillars were used to ensure the screws are fastened at the same height and with uniform distribution of pressure to effectively hold the structure. The FPCB IDT was cleaned with IPA before assembly and soldered onto the rigid PCB designated pads. The FPCB was pressed against the LiNbO_3 wafer using localized pressers and silicon pads which was securely held by an aluminium ring clamp. The aluminium ring clamp was firmly affixed to the plate using four M5 screws, with the added support of eight 3D printed pillars – four of which were identical in height to those used for the rigid PCB, while the remaining four were situated above the PCB, ensuring the height exceeds the silicon pressure pads. Adjusting the screws altered the pressure applied to the localized pressers, and the silicon pads evenly distributed the clamping force. When the FPCB IDEs and substrate were coupled, an RF signal was applied to the IDTs to produce SAWs. Finally, the addition of a fluidic vessel (discussed in section 4.3.6) completed the assembly process.

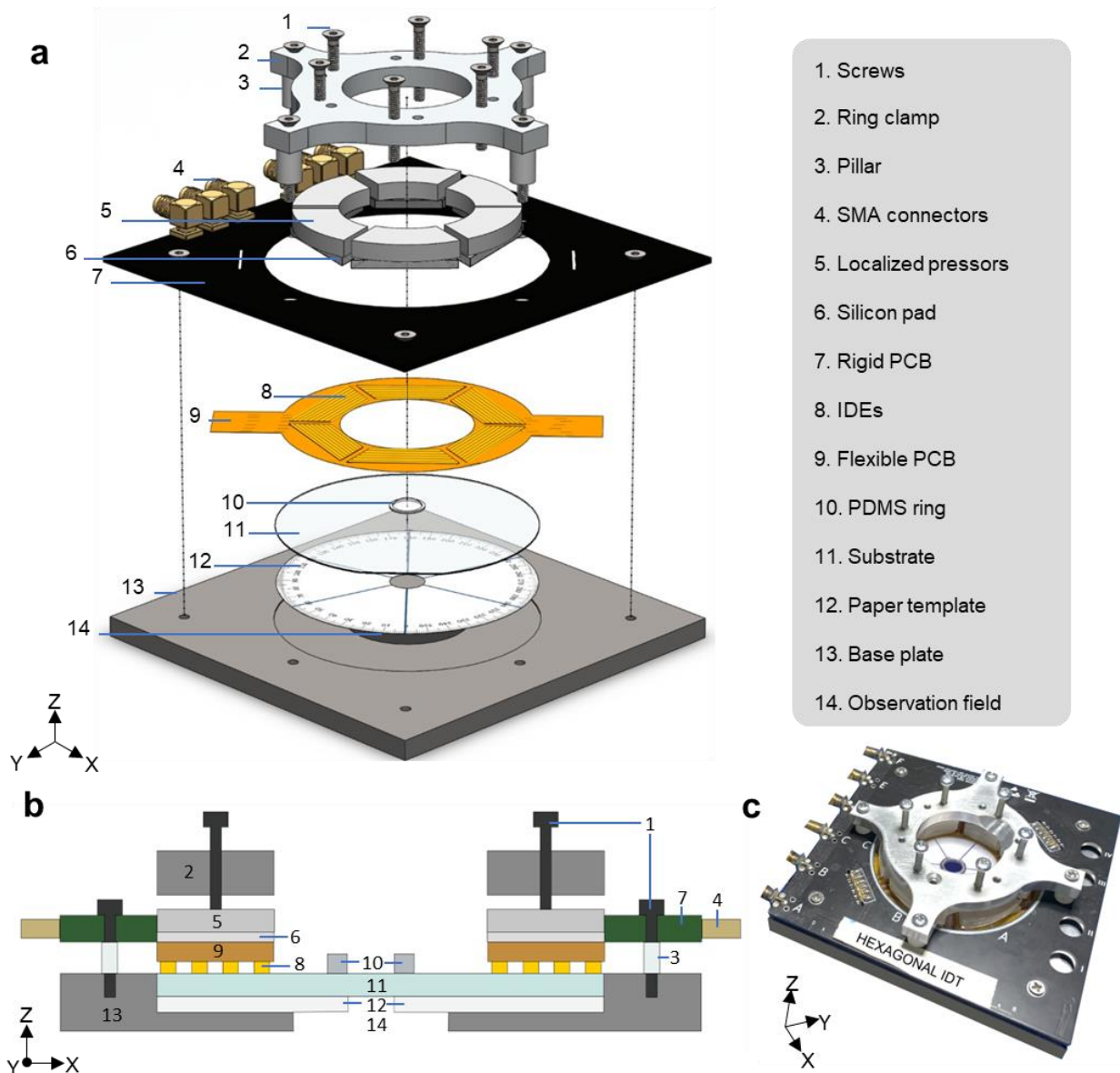


Figure 4.4. Hexagonal FPCB IDT Mechanical housing and assembly. (a) Exploded view of the assembly. (b) Cross-sectional illustration of device. (c) Image of real-life model of device.

The manufacturing of the aluminium base plate and aluminium ring clamp was achieved using a computer numerical control (CNC) router. The manufacturing of the FPCB and rigid PCB were discussed in the previous section. The pillars were manufactured internally using a 3D printer (Ultimaker 2+ extended, Netherlands), designed using Solidworks (Autodesk, USA) and translated into g-code, for 3D printing, using Cura (Ultimaker, Netherlands). They components were printed using polylactic acid (2.85 mm, Ultimaker) [14,400].

4.3.5 Matching Network

The electrical characterization of the device was conducted using S-parameters. These parameters describe the relationship between various ports within a network. In the context of a one-port network, hence just one IDT, there is just one S-parameter, S_{11} , which represents the input port voltage reflection coefficient. A two-port network (shown in Figure 4.5) with two IDTs, has S_{11} , but also S_{12} reverse voltage gain, S_{21} the forward voltage gain, and S_{22} the output port voltage reflection coefficient. In other words, S_{11} and S_{22} are the reflection coefficients which describe the impedance match between input and output, respectively. S_{21} and S_{12} are the transmission coefficients that describe the gain/loss and reverse isolation. These parameters are measured using a vector network analyser (VNA) which ratio the power observed at each port (ratios shown in the equations in Figure 4.5). The minima of the S_{11} parameter correspond to the frequency range at which the device reflects the least amount of power. Ideally, a substantial negative reflection coefficient at the required frequency is desired, as it signifies optimal power transfer.

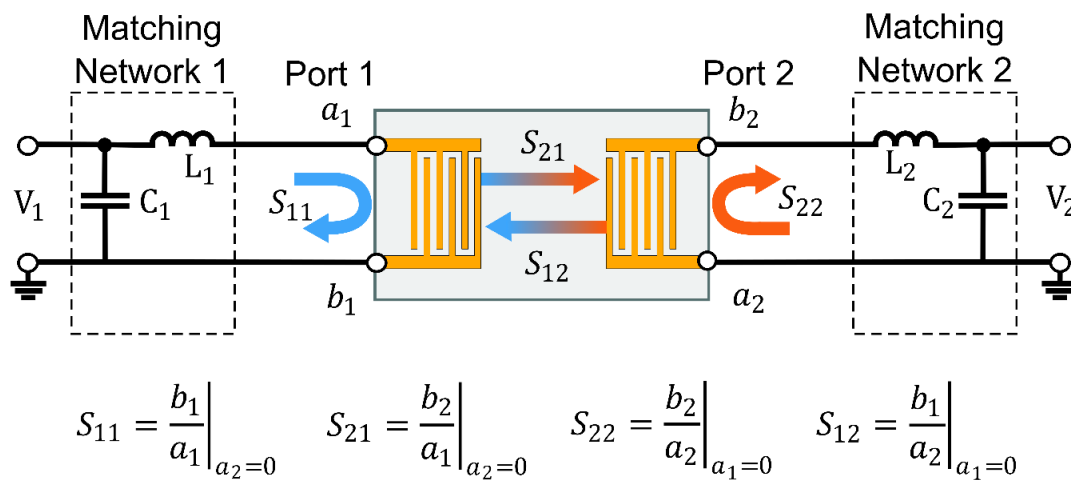


Figure 4.5. A schematic of a two-port network consisting of two IDTs and matching networks, demonstrating the S parameters and their ratio calculations.

A matching network (illustrated in Figure 4.5, and specific example shown in Figure 4.6) is an electronic circuit designed to improve the electrical power efficiency transferred to the IDTs. Its integration leads to an increase in the S_{11} minima, signifying enhanced power efficiency through reduced reflection. While matching networks are

typically unnecessary for clean room IDTs, it is advisable to use them in FPCB IDTs due to the mechanical clamping mechanism used for the substrate coupling causing less efficient power transmission. The matching network operates by matching the impedance between the source and the load, typically taking the form of a straightforward yet widely used combination of inductors and capacitors. The design of this network can be initially theoretical, using the measured impedance values of the VNWA and a Smith Chart. The goal is to shift the impedance value toward the origin of the Smith Chart for 50-ohm impedance match. Subsequently, the capacitance and inductance values can be empirically fine-tuned from the theoretical values using the VNWA. It is important to note that for the initial testing involving different angles and frequencies (Chapter 7), a matching network was not used as its construction depends on the specific frequency and, consequently, the position or angle of the IDT. As such, a matching network must be individually constructed for each IDT when specific frequency and angle is determined.

For instance, Figure 4.6(a-d) demonstrates an example of an IDT's matching network when working at 19.9 MHz and propagating at 0° X-direction. Figure 4.6(a) shows the circuit diagram of the matching network created, where the impedance seen at the load (IDT) is $Z_1 = 34 - j44 \Omega$ and an LC circuit with a 540 nH inductor in series and 110 pF capacitor in parallel was needed to achieve a near 50-Ohm impedance match. A PCB matching network guide was used for simplified manufacturing of the matching networks. Figure 4.6(b) shows the design (top), and real example (bottom) of these PCB matching networks, which were useful as they are clear, systematic and allow interchangeability of the type of network (e.g., LC or CL). Figure 4.6(c) shows the smith chart procedure for finding the inductor and capacitor values to match the impedance. Lastly, Figure 4.6(d) shows the result of S_{11} , where the minima only reached - 5.7 dB without a matching network, and - 46.8 dB with a matching network, demonstrating the increased reflection dip and hence improved power transfer.

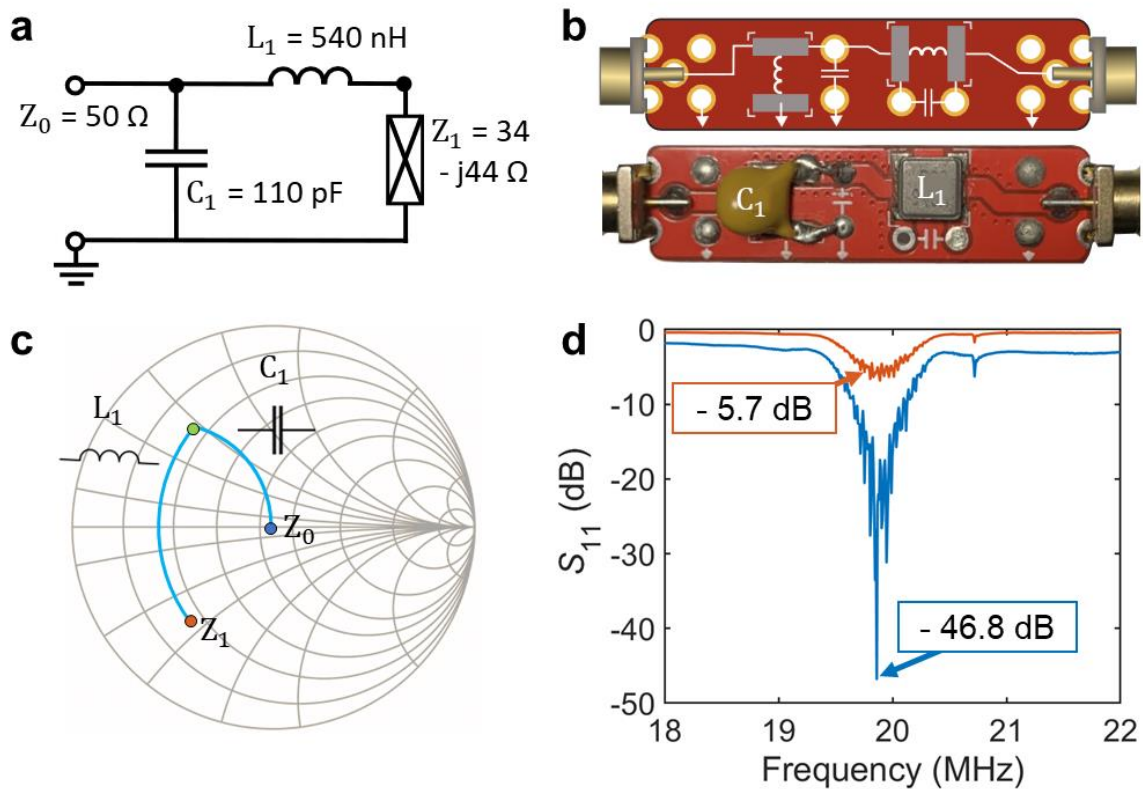


Figure 4.6. Example of matching network process for R-SAW 0° (X-propagation) at 19. MHz where (a) the circuit diagram of matching network (b) Top view of PCB matching network design (top) and photo of example matching network (bottom) (c) smith chart process (d) S_{11} with (blue) and without (red) a matching network.

4.3.6 Fluidic Vessel

A PDMS ring was selected as the fluidic vessel for this device for several reasons. Firstly, it can be fabricated using readily available laboratory materials, in a cost-effective and time-efficient manner, avoiding the need for cleanroom facilities. Furthermore, PDMS rings can be adhered to the substrate surface through a simple cleaning process with IPA and suction, eliminating the necessity for additional mechanical pressors that overcrowd the working area. Additionally, PDMS rings offer advantages such as increased volume capacity, consistent boundary conditions, and enhanced stability compared to conventional droplets.

Two methods of PDMS ring fabrication are described in Figure 4.7. One method, Figure 4.7(a) involved creating a 3D-printed mould. This mould, designed in SolidWorks, had inner and outer circles with a small separation, where the gap

determined the thickness of the PDMS ring. A glass slide (measuring 76 mm in width, 26 mm in length, and 1 mm in thickness) was placed on the 3D printer surface and secured using masking tape. The mould was directly 3D-printed onto the glass slide using a 0.25 mm nozzle and polylactic acid filament. Following cooling, the glass slide with the mould was detached and placed in a petri dish. PDMS, composed of a silicon elastomer (DowSil, Sylgard 184) and curing agent (DowSil, RT Cure) mixed at a 10:1 ratio, was prepared by and in a vacuum treatment to remove air bubbles. The PDMS (Sylgard 184, Farnell UK) mixture was poured into the petri dish containing the mould and undertook additional vacuum treatment if residual air bubbles persist. The PDMS naturally cures at room temperature over 48 hours, but it can also be cured on a hotplate (SD160, Colepalmer) at 45 °C for 24 hours, a temperature below the polylactic acid melting point of 60 °C. After curing and cooling, the 3D-printed mould was carefully peeled away from the PDMS. To bond the PDMS ring to the substrate, it was cleaned with IPA and secured using suction. Alternatively, for added security, a thin layer of PDMS can be spread on the bottom surface and allowed to cure at room temperature. This approach simplifies mould creation, eliminating the need for cleanroom facilities, and enhanced accessibility and efficiency.

Nevertheless, this is method required over 24 hours to complete, which may not be ideal if there is a need to replace PDMS rings regularly to prevent contamination. Consequently, a simpler and faster procedure was introduced involving the base of a pipette tip as the mould (Figure 4.7(b)). Initially, a small quantity of PDMS was poured into a petri dish. A pipette tip was meticulously inserted into the PDMS and subsequently removed. An air pump was blown through the tip of the pipette to create an aperture, allowing the PDMS to envelop the outer neck of the pipette. Careful attention that no air bubbles were trapped inside the pipette was ensured. The pipette was gently positioned onto a glass slide, which was cured for just 5 hours at 70°C. The PDMS solidified and adopted the shape of the pipette tip. Once cured and cooled, the pipette was extracted from the glass slide and tweezers were used to slowly peel off the PDMS ring from the base of the pipette, leaving behind the PDMS ring with diameter corresponding to the dimension of the pipette base. This method demands attention to detail, and its repeatability is dependent on the user's skill. It can be challenging to ensure no air bubbles and no damage to the PDMS ring. Nonetheless, it was a straightforward and time saving method. Additionally, this technique yields

PDMS rings with thinner walls, which is advantageous for minimizing SAW damping. The thinner walls exhibit enhanced adherence to the substrate, reducing likelihood of leakage.

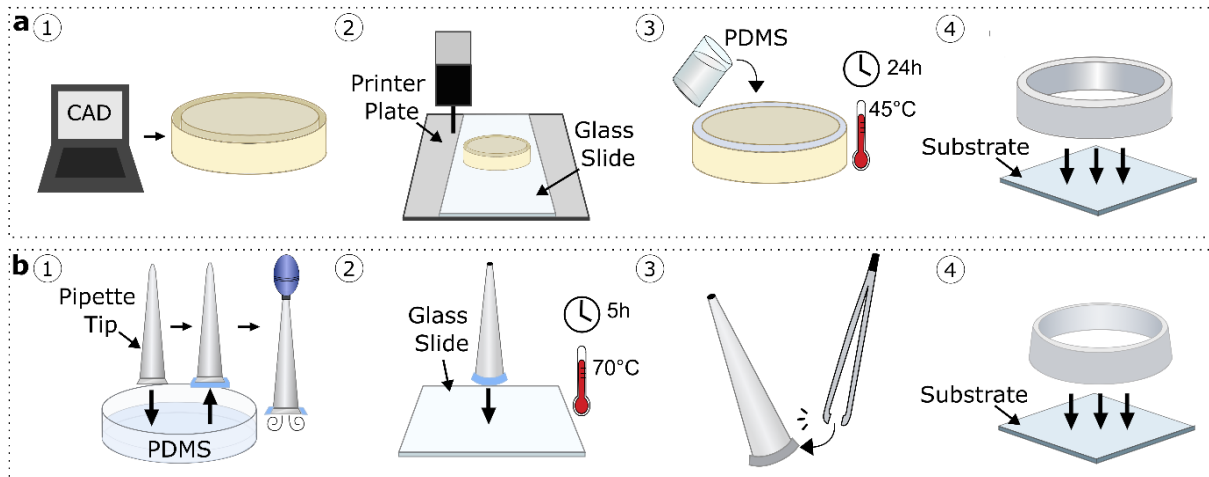


Figure 4.7. PDMS ring fabrication methods (a) 3D printing method. Step 1: Design ring mould using CAD software. Step 2: 3D prints designed mould on a glass slide. Step 3: Pour PDMS into mould and cure for 24 hours on a hot plate. Step 4: Bond cured PDMS ring to substrate. (b) Pipette method. Step 1: Dip pipette tip into PDMS, remove, and blow air into the opposite end of pipette tip to create aperture. Step 2: Place pipette tip with the coated PDMS onto a glass slide and cure for 5 hours on a hot plate. Step 3: Carefully peel the cured PDMS ring off from pipette using tweezers. Step 4: Bond the peeled PDMS ring onto the substrate.

4.4 Conclusion

This chapter introduced a novel Hexagonal FPCB device designed to investigate acoustic streaming effects and applications at various angles and/or wave modes on piezoelectric substrates. The rational and the developmental of each component was discussed. Techniques for manufacturing SAW IDTs and fluidic vessels without the need for cleanroom facilities were demonstrated. The flexibility of the Hexagonal FPCB allows for easy reconfiguration of the device, while the number of IDTs reduces the configurations required for testing different angles. Overall, this device streamlines the acoustofluidic prototyping process, enabling investigations for unique applications.

5.1 Introduction

This chapter serves as the materials and methods section for the whole thesis. It is divided into two parts – System Set-up (Section 5.2), and Experiment Procedure (Section 5.3). Section 5.2 explains how to construct a system platform and the device operation of the Hexagonal FPCB IDT (discussed in Chapter 4) to collect the data presented in Chapter 7. The system platform includes mechanical, electrical, and software components. Section 5.3 describes the particle manipulation experiment procedure, including the data collection and analysis methods. Overall, this chapter provides a clear and detailed account of the conducted research methodology.

5.2 System Set-up

Alongside the Hexagonal FPCB IDT configuration described in Chapter 4, the device has a system platform to operate the particle manipulation experiments. The overall system set-up diagram is shown in Figure 5.1. This is divided into the systems control, acoustofluidic platform, and data collection and analysis. The systems control includes the RF signal for the IDTs, amplifier, and power monitoring. The acoustofluidic platforms includes sample collection. Data collection and analysis includes the microscope, camera, and analysis software.

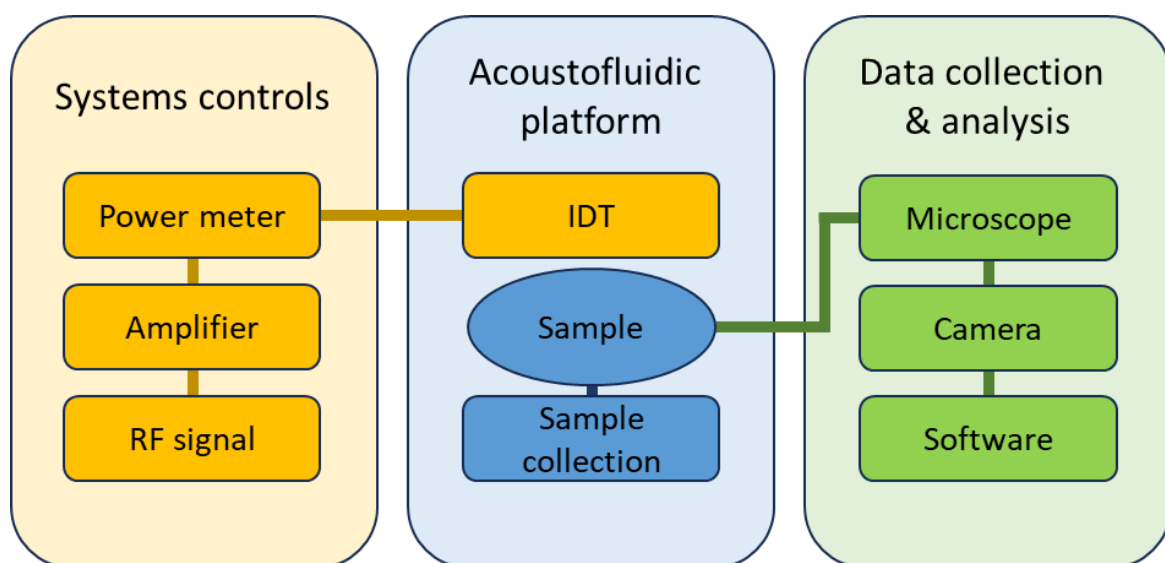


Figure 5.1. Overall system set-up diagram.

5.2.1 Device Operation

The circuit diagram for the device operation of a single IDT is displayed in Figure 5.2. An IDT was actuated by applying an RF signals. The RF signal was generated using signal generators (RS Pro, RSDG 5162) and amplified with a power amplifier (Mini circuit, LZY-22+), powered by direct-current power supplies (Tenma, 72-295). Power meters were used to monitor the input signals to the IDT. The signal monitoring components can help to calculate the real-time efficiency of the electrical input power of the IDT. The forward power and reverse power were shown by the two power meters (Keysight 8990B) connected to a coupler (Mini-circuit, ZFBDC20-62HP-S+). The difference between the forward and reverse power could be calculated to determine the input power. An abnormal efficiency indicates that a systematic check needs to be implemented before further operation to avoid damaging the system. Matching networks were designed (using method in Chapter 4) to improve the electrical power efficiency transferred to the IDTs.

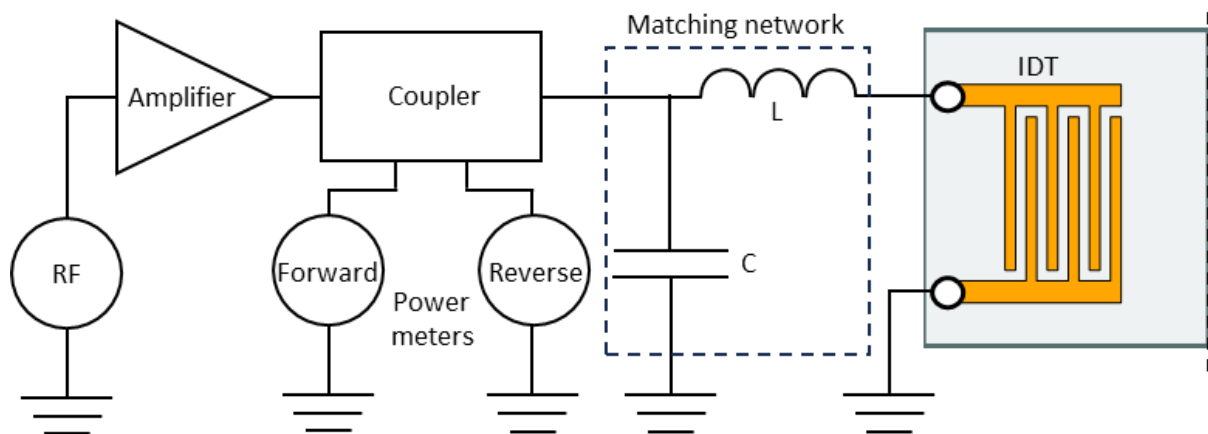


Figure 5.2. Circuit diagram for the device operation of a single IDT.

The Hexagonal FPCB is capable of actuating six IDTs simultaneously. The complete system operation is illustrated in Figure 5.3. This setup involved three signal generators, amplifiers, and power meters. Power splitters were used to distribute the signal to two opposite IDTs at the same frequency and power, eliminating the need for additional equipment. If each IDT is to be used with separate frequencies or power levels, six signal generators, amplifier, and power meters would be required. Each power splitter was connected to the matching networks designed for each IDT. The acoustofluidic platform was placed under the microscope (GX Vision Ltd, GXM-

L2800), where an overhead camera took videos or images which was analysed with computer software.

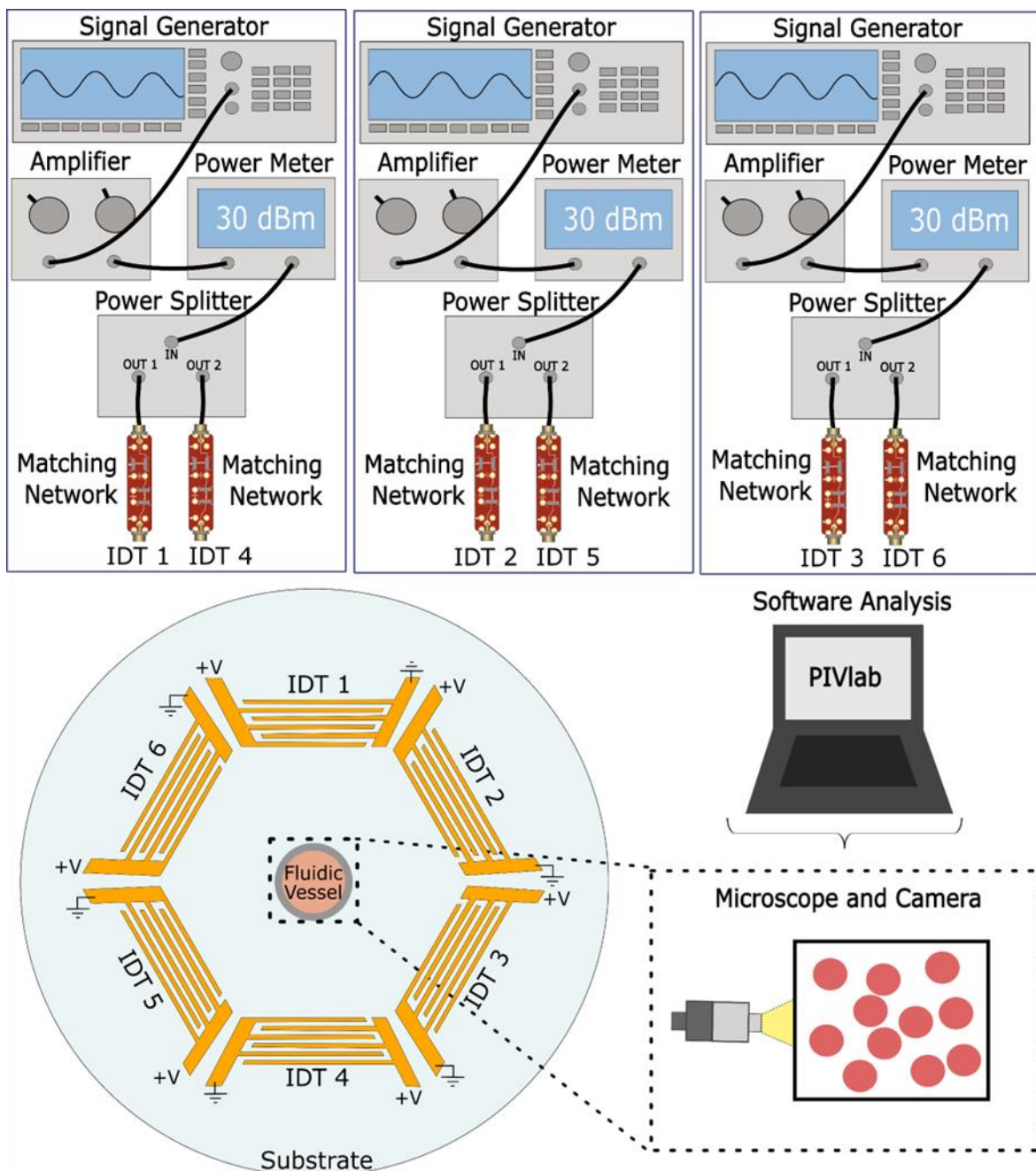


Figure 5.3. Full system set-up and operation of the Hexagonal FPCB IDT.

5.2.2 Electrical Characterisation

The electrical impedance of the IDT was identified by a VNWA (DG8SAWQ) (VNA, E5061B ENA, Keysight Technologies, U.K.). The Hexagonal FPCB IDT was setup by connecting it to the VNWA via the SMA connectors, and the S_{11} dip is monitored when

fastening the screws to ensure an adequate dip without breaking the substrate. The electrical characterisation of the 128° XY-cut LiNbO₃ consisted of using the VNWA and the Hexagonal FPCB IDT (without a matching network) to measure the S₁₁ dips (wave mode frequencies) at varying angles from 0° to 90° in 15° increments. The VNWA was set to visualise 15 – 40 MHz to observe the other harmonic frequencies. The 128° XY-cut LiNbO₃ was rotated to align to a paper template with the angles placed under the IDT to get the correct angles. This was repeated 5 times to ensure correct angles and frequencies.

When using the Hexagonal FPCB for application purposes rather than experimental, a matching network was designed to enable optimal power transfer (discussed in Chapter 4). Its integration leads to an increase in the S₁₁ minima, signifying enhanced power efficiency through reduced reflection. While matching networks are typically unnecessary for clean room IDTs, it is advisable to use them in this PCB IDTs due to the mechanical clamping mechanism used for the substrate coupling causing less efficient power transmission. It is important to note that for the initial testing involving different angles and frequencies a matching network was not used as its construction depends on the specific frequency and, consequently, the position or angle of the IDT. As such, a matching network must be individually constructed for each IDT when specific frequency and angle is determined.

5.3 Experiment Process

5.3.1 Sample Preparation and Handling

The sample preparation differed for each experiment. Firstly, red 10 µm polystyrene particles (Sigma Aldrich, USA) were used to visualise the acoustic streaming flow fields. These particles were prepared by diluting them into various glycerol and water ratios. The PDMS ring was filled with a sample size of 100 µl. Initially, for the angle-frequency experiments a ratio of 1:100:100 of particles, water and glycerol, respectively, was chosen as proof of concept for ease of viewing and analysis the acoustic streaming patterns using computer software [93]. The water and glycerol ratios were varied in the viscosity experiments, whereby the least viscous was 100:0 (water: glycerol), following by 80:20, and lastly 60:40 to mimic the viscosity of blood at room temperature [401]. The power and 1 ml volume experiments were also used

60:40 ratio to mimic the viscosity of blood. The single 96-well culture plate used experiments used the same particle ratio, with 300 μ l water.

The micro-scale concentration experiments consisted of using a sample size of 100 μ l, containing 400:5 mixture of water and PS microspheres. Red 10 μ m (Sigma Aldrich, USA), green 1 μ m (BaseLine Chromtech, China), and red 500 nm (Sigma Aldrich, USA) PS particles were used as these cover a wide range of biological cell/particle sizes, such as cells, bacteria, and extracellular vesicles respectively.

5.3.2 Experimental Procedure

A step-by-step procedure for the experiments is described below and illustrated in Figure 5.4. The same experimental procedure is used for all experiments, with variations in device configurations and power, as discussed in each relevant chapter. Once each experiment was completed, repetitions could be performed by repeating steps 4 to 6 with the same assembly.

1. Create and Set PDMS Rings: Follow the method described in Chapter 4 to create PDMS rings. Allow time for the PDMS rings to set.
2. Clean and Assemble the Device: Clean the unassembled device using IPA and distilled water. Assemble the cleaned device, positioning it at the correct angle with respect to the flat edge of the substrate. Loosely fasten the device using screws on top of the aluminium ring.
3. Connect the VNWA and Set up RF System: Connect the VNWA to the device and properly fasten the IDT, ensuring suitable S_{11} minima. Set up the RF system with the correct power and frequency.
4. Place PDMS Ring and Pipette Sample: Use tweezers to carefully place the PDMS ring on the substrate at the indicated position on the paper template. Prepare the same and pipette into the PDMS ring.
5. Activate Systems and Initiate Fluid Actuation: Connect the acoustofluidic system and RF system. Turn on the camera at the microscope and activate the RF system to initiate fluid actuation.
6. Complete Experiment and Analyse Data: Once fluid actuation is complete, turn off the RF system and remove the sample. Clean the assembled device after

each experiment. Collect videos from the camera on the microscope and analyse them using computer software.

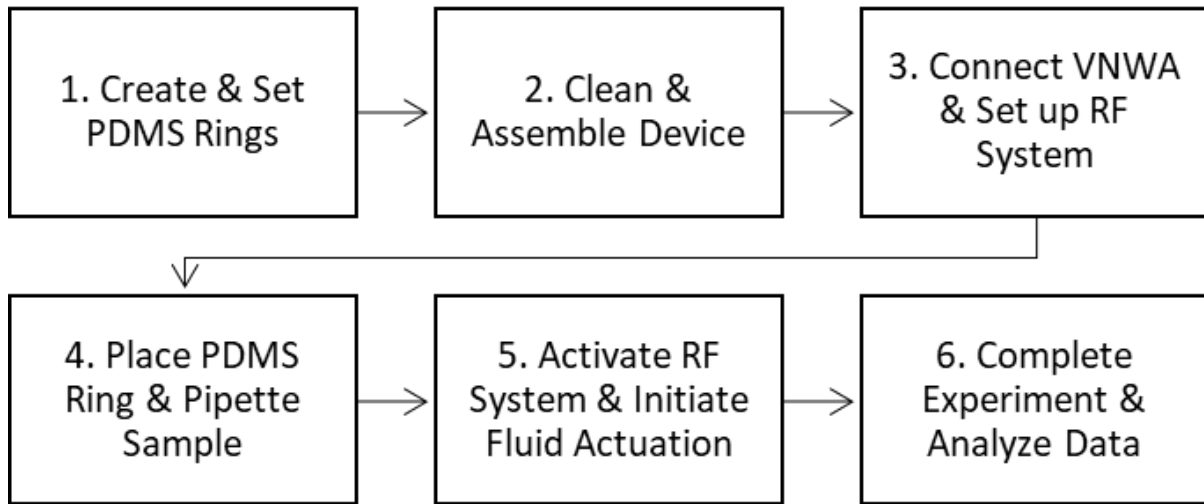


Figure 5.4. Simplified flow chart illustration of the experimental procedure detailed.

5.3.3 Data Collection and Analysis

The mathematical software MATLAB supplies a particle image velocimetry tool (PIVlab) [402,403], which is adopted to analyse the velocity field for relevant experiments. This non-invasive technique calculates the flow field information based on moving images recorded from the microscope on the overhead camera. The calibration was set to 1060 pixels for the 8 mm diameter of the PDMS ring for all videos.

ImageJ (National Institutes of Health) was used to quantify the concentration and separation. For concentration, the image was set to grey scale and a 1 mm diameter circle was drawn in the middle. The greyscale intensity was measured over time in the centre circle to quantify the speed at which the particles concentrated.

6.1 Introduction

This chapter presents numerical simulations performed using COMSOL Multiphysics to support the design and analysis of the Hexagonal FPCB IDT developed in Chapter 4. A periodic unit cell model was used to efficiently calculate wave mode characteristics and coupling coefficients; a simplified 3D model was developed to visualise displacement fields and substrate-fluid interactions across multiple orientations; and a life-scale 2D model provided detailed analysis of frequency responses and fluid behaviour under two orientations. These simulations were used to validate R-SAW behaviour, quantify anisotropy, and explore the emergence of hybrid modes. These results provide insights into multidirectional SAW performance for acoustofluidic applications and complement the experimental findings presented in later chapters.

6.2 Numerical Models

Numerical studies are conducted to explore, visualise, and calculate wave mode data generated at different angles and frequencies. Three finite element models using COMSOL Multiphysics (v.5.5) were created for this thesis: a unit cell IDT, a simplified 3D IDT and life-scale 2D IDT. Figure 6.1 shows a conceptual view of the unit cell IDT as part of the Basic IDT model. Note that the key parameters for numerical and analytical analysis is shown in the appendix, Table 6.1.

Table 6.1. Parameters for numerical and analytical analysis.

Parameter	Symbol	Value (Unit)
Fluid density	ρ_f	997 (kg/m ³)
Fluid compressibility	β_f	4.48E-10 (m ² /N)
Fluid thermal expansion	α_f	2.75E-4 (1/K)
Fluid heat capacity	Cp_f	4180 (J/kg.K)
Fluid ratio of specific heats	γ_f	1.012

Fluid dynamic viscosity	μ_f	8.9E-4 (Pa.s)
Fluid bulk viscosity	μB_f	24.7E-4 (Pa.s)
Fluid shear viscosity	η_f	1 (cP)
Fluid thermal conduction	k_{condf}	0.6 (W/(m.K))
Fluid sound velocity	c_f	1500 (m/s)
Substrate density	ρ_s	4647 kg/m ³

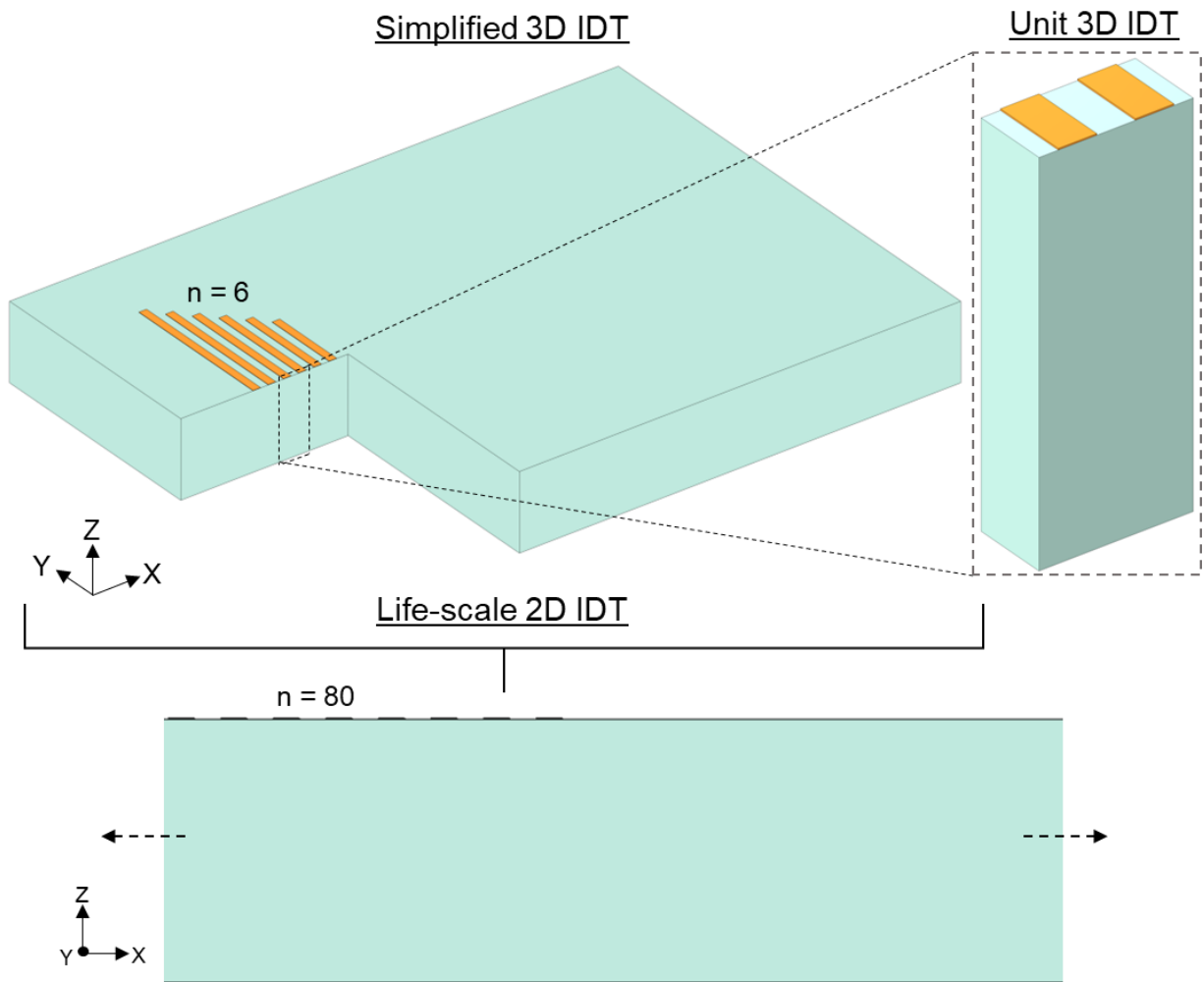


Figure 6.1. Conceptual view of the unit cell IDT (Model 1) within the simplified 3D IDT (Model 2) and the life-scale 2D model (Model 3).

6.2.1 Model 1: Periodic Unit Cell IDT

The periodic unit cell model simulation can be used to reduce the model geometry of an IDT [404]. The Figure 6.2 displays the period unit cell model, including its (a) dimensions, (b) boundary condition labels and (c) the mesh used. This model consisted of using one three-dimensional (3D) straight IDT finger pair measuring λ in X direction, $\lambda/2$ in Y direction and 0.5 mm (substrate thickness) in the Z direction. Figure 6.2(d) describes the boundary condition parameters. As a 128° XY-cut LiNbO_3 wafer was used, periodic boundary conditions were applied in ZX and ZY faces to mimic the x-direction propagating SAW wave. The model was set up using the predefined piezoelectric materials interface. The bottom boundary was fixed in the model, which enforces a zero structural displacement but does not contribute to any significant reflection from the lower boundary back into the bulk of the substrate [404]. The left and right electrode finger was set to ground and an electric potential, with zero surface charge accumulation [404]. Note that this model was also used without electrodes to calculate the free surface eigenfrequency results. All other boundaries are Free for Solid Mechanics interface and Zero Charge for the electrostatics interface, respectively [404]. Figure 6.2(e) shows a convergence test through an Eigenfrequency study to find R-SAW resonance frequency at 0° . Note that an extremely fine mesh could not convergence. A “fine” mesh was chosen to balance accuracy and computational time. The fine mesh consisted of a uniform mesh, keeping identical mesh for the periodic boundary conditions [404].

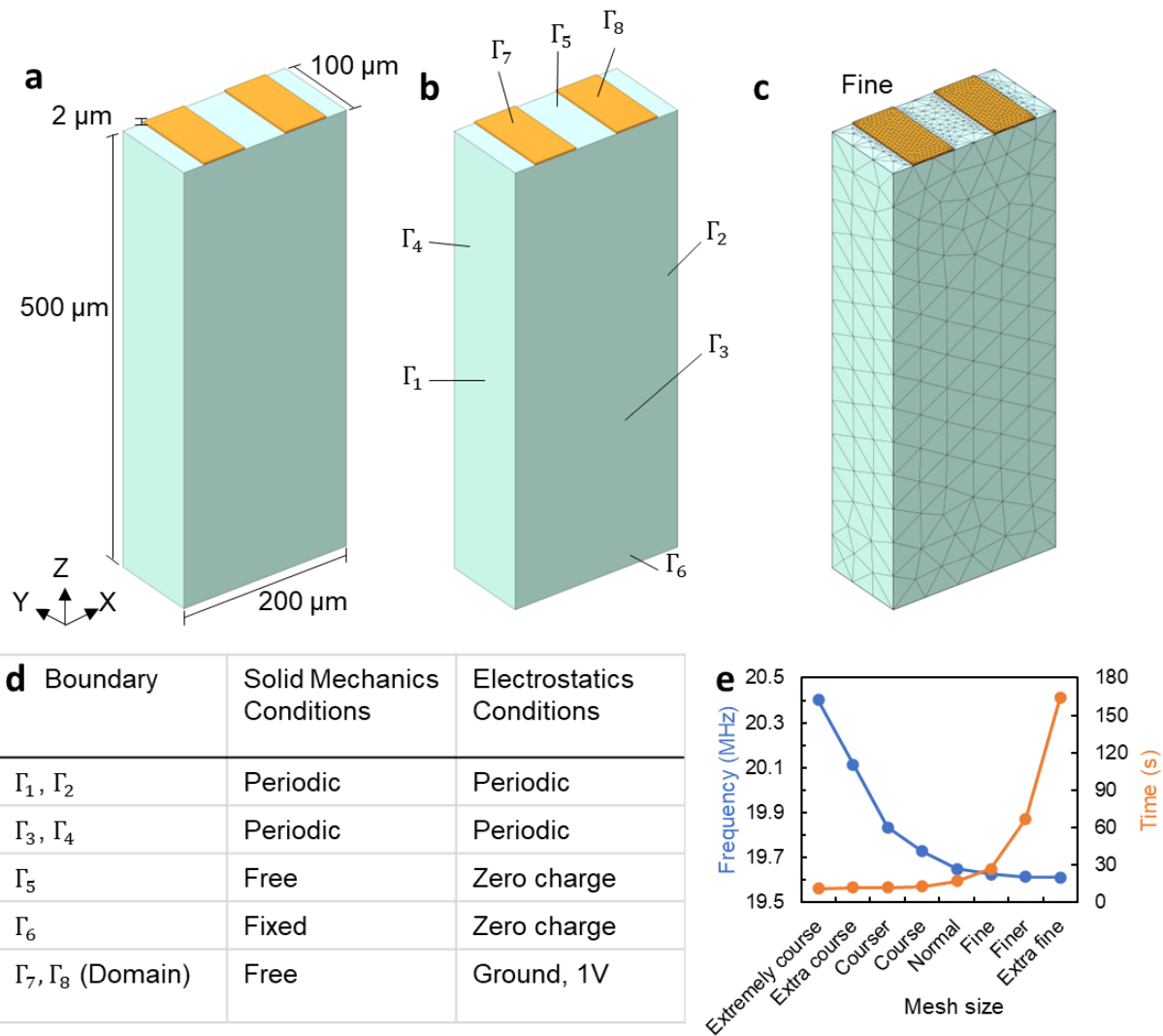


Figure 6.2. Model 1: Periodic unit cell IDT. (a) Unit cell IDT dimensions. (b) Boundary labels. (c) “Fine” mesh. (d) Boundary parameter description. (e) Mesh convergence test.

The piezoelectric materials physical characteristics were established using a trigonal crystal system consisting of six elastic stiffness, four piezoelectric tensors, and two dielectric coefficients. The piezoelectric coefficient values reported in Refs. [405] and [406] were used to produce a complete definition of the LiNbO₃ as presented in Voigt notation:

$$[c_{ij}] = \begin{bmatrix} 199.5 & 55.27 & 67.67 & 8.7 & 0 & 0 \\ 55.27 & 199.5 & 67.67 & -8.7 & 0 & 0 \\ 67.67 & 67.67 & 235.2 & 0 & 0 & 0 \\ 8.7 & -8.7 & 0 & 59.48 & 0 & 0 \\ 0 & 0 & 0 & 0 & 59.48 & 8.7 \\ 0 & 0 & 0 & 0 & 8.7 & 72.2 \end{bmatrix} (GPa) \quad (6.1a)$$

$$[e_{ij}] = \begin{bmatrix} 0 & 0 & 0 & 0 & 3.65 & -2.39 \\ -2.39 & 2.39 & 0 & 3.65 & 0 & 0 \\ 0.31 & 0.31 & 1.72 & 0 & 0 & 0 \end{bmatrix} \left(\frac{C}{m^2}\right) \quad (6.1b)$$

$$[k_{ij}] = \begin{bmatrix} 45.05 & 0 & 0 \\ 0 & 45.05 & 0 \\ 0 & 0 & 26.2 \end{bmatrix} \quad (6.1c)$$

The crystal and IDT coordinate systems were defined as (α, β, γ) and (x, y, z) , respectively. Initially, the LiNbO₃ crystal and geometry coordinates were set to $(0, 0, 0)$. A Euler angle coordinate transformation of $(\alpha + 0^\circ, \beta - 38^\circ, \gamma + 0^\circ)$ was performed to describe the 128° XY-cut LiNbO₃ substrate crystal cut angle. For calculations of varying Y-cut LiNbO₃ β is rotated. Whereas the rotation of the IDT about the X in-plane axis was simulated by rotating the substrate along α for different angles

Eigenfrequency studies were used on this model (Figure 6.2) to visualise the type and shape of the wave mode occurring at different angles and frequencies. Note that an eigenfrequency analysis can only provide shape of the mode, and not the amplitude of any physical vibration [407]. Only angles between X-rotation angles 0° to 90° were needed due to the 128° Y-cut LiNbO₃ substrate symmetry. Frequencies between 15-45 MHz were chosen to limit computation time. With the acquired frequency knowledge of each eigenmode, with and without electrodes, the phase velocity, coupling coefficient and power flow angle could be calculated for different wave modes at varying angles. This model (Figure 6.2) was also used in a frequency sweep study to determine information on the electrical and mechanical interactions, admittance, resonance frequencies, and material properties. An isotropic loss factor of 0.02 was considered for simulating the S-parameters. The loss factor was determined by $1/Q$,

where Q is the quality factor which was calculated from the experimental S_{11} results [408] and was suitable compared to theory [409].

6.2.2 Model 2: Basic 3D IDT

The vibration pattern on the device surface was further studied using a second 3D COMSOL numerical simulation. This simulation consisted of a simplified 3D IDT model, with only 6 electrodes and scaled down in length by 10 to reduce computation time.

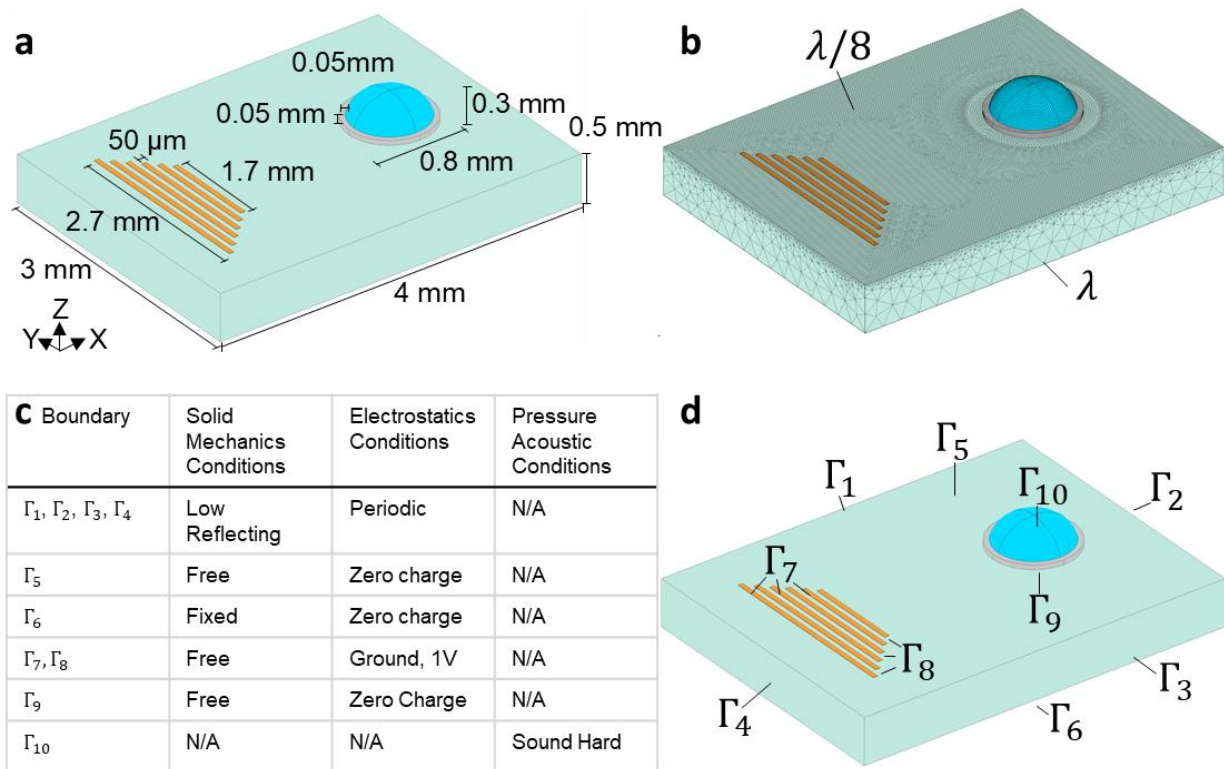


Figure 6.3 displays the model consisting of (a) the measurements, (b) the mesh, (c) boundary condition parameters, and (d) boundary condition labels.

A 3D rectangle of measurements 4 x 3 x 0.5 mm was used for the 128° Y-cut LiNbO₃ substrate. The electrode fingers were 50 μm width and 2 μm height. The length of the electrode figures depended on the shape of the IDT being studied - rectangular IDT (1.7 mm) or trapezoidal IDTs (2.7 mm to 1.7 mm, in 0.2 mm increments). These measurements matched the Hexagonal FPCB IDT lengths but were scaled down. A PDMS ring of height and thickness 0.05 mm, surrounded a droplet of 0.4 mm in radius and 0.3 mm height. A uniform mesh of $\lambda/8$ was used for the top surface, the PDMS

ring and the fluid domain as this is enough for this simulation [410]. A larger mesh of λ was used for the remaining boundaries to save computational time.

The predefined piezoelectric materials interface used, with a fixed bottom boundary and low reflecting boundaries along the sides. The piezoelectric coefficient values in equations 6.2 were used, with the same Euler angle coordinate transformation of $(0^\circ, -38^\circ, 0^\circ)$. The COMSOL “Solid Mechanics” and the “Electrostatics” interface are used to calculate the stress, strain, electrical displacement field, and the electric field of the piezoelectric crystal. This is obtained by solving the following equations [410].

$$\mathbf{T}_{ij} = \mathbf{C}_{ijkl}^E \cdot \mathbf{S}_{kl} - e_{ijk}^T \cdot \mathbf{E}_k \quad (6.2a)$$

$$\mathbf{D}_i = e_{ikl} \cdot \mathbf{S}_{kl} - \varepsilon_{ij}^S \cdot \mathbf{E}_k \quad (6.2b)$$

Where \mathbf{T}_{ij} is the stress vector, \mathbf{C}_{ijkl}^E is the elasticity matrix (N/m^2), \mathbf{S}_{kl} is the strain vector, e_{ijk}^T is the piezoelectric matrix (C/m^2), \mathbf{E}_k is the electric field, \mathbf{D}_i is the electrical displacement, and ε_{ij}^S is the permittivity matrix (F/m). A “Frequency Domain” solver was used to solve the physics together at the driving frequencies. The waveforms produced could visually verify the coupling coefficient and power flow angles calculated from the Model 1 eigenfrequency study. Model 2 can also be used to study the interaction of the vibration pattern with the droplet. A 3D semi-sphere was added to the model. The acoustic pressure and velocity distribution are computed inside the droplet using the "Pressure Acoustics" module. For the first-order pressure field calculation, the velocity at the bottom is derived from the displacement variation of the substrate [410].

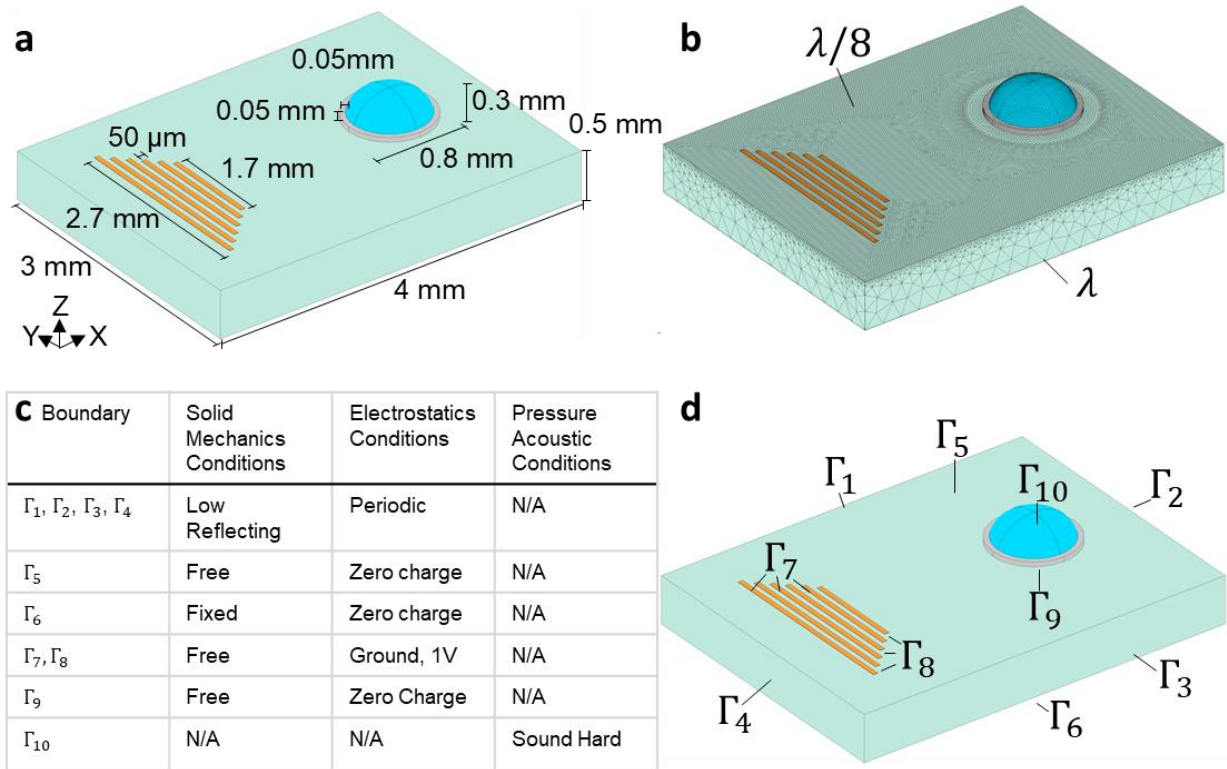


Figure 6.3. Model 2: 3D Simplified IDT. (a) Dimensions. (b) Mesh. (c) Boundary condition parameters. (d) Boundary condition labels.

6.2.3 Model 3: Life scale 2D IDT

Lastly, a life-scale 2D (side-view) model (Model 3) was created to further analyse the wave modes, specifically at 0° and 90° angles. The life-scale 2D model (with 90 IDT fingers) is shown in Figure 6.4(a), where the inset displays two of the IDT fingers on the substrate. This model provides an accurate representation ensuring precise analysis of the frequencies and wave modes. Figure 6.4(b) shows the simulated S_{11} readings at 0° X-rotation angles for 6 and 80 IDT fingers. Increasing finger count reduces bandwidth leading to improved S_{11} readings. Conversely, with only 6 fingers, akin to the simplified 3D model, the bandwidth is broad, hindering frequency and wave mode distinction. Therefore, a life-scale 2D model proves valuable for IDT simulation, given the computational constraints of a life-scale 3D model. A 2D model allowed more detailed studies using finer meshes ($\lambda/10$) throughout, as shown in Figure 6.4(c). Implementing a boundary layer mesh provided results that included the viscous boundary layer (δ), illustrated by the inset in Figure 6.4(c). The same crystal matrix was used as in Model 1 and Model 2; however, the coordinate system was set to XZ

for 0° and YZ for 90° . Other X-rotation angles in between (30° and 60°) were not achievable using Euler angles in 2D as this involved a 3D rotation. This model employed the same “Frequency Domain” solver to solve “Solid Mechanics” and “Electrostatics” physics as Model 1 and 2. Rather than “Pressure Acoustics”, the “Thermoviscous Acoustics” interface was integrated via the “Acoustic-Structure Boundary” Multiphysics method to analyse more detailed thermoviscous pressure and velocity distributions. Additionally, the “Laminar Flow” physics addressed acoustic streaming. Mass and force source terms were imposed by adding “weak contribution” and “volume force” conditions, respectively [411,412]. This physics was solved via a “Stationary” solver by using the solution from the mentioned “Frequency Domain” Solver.

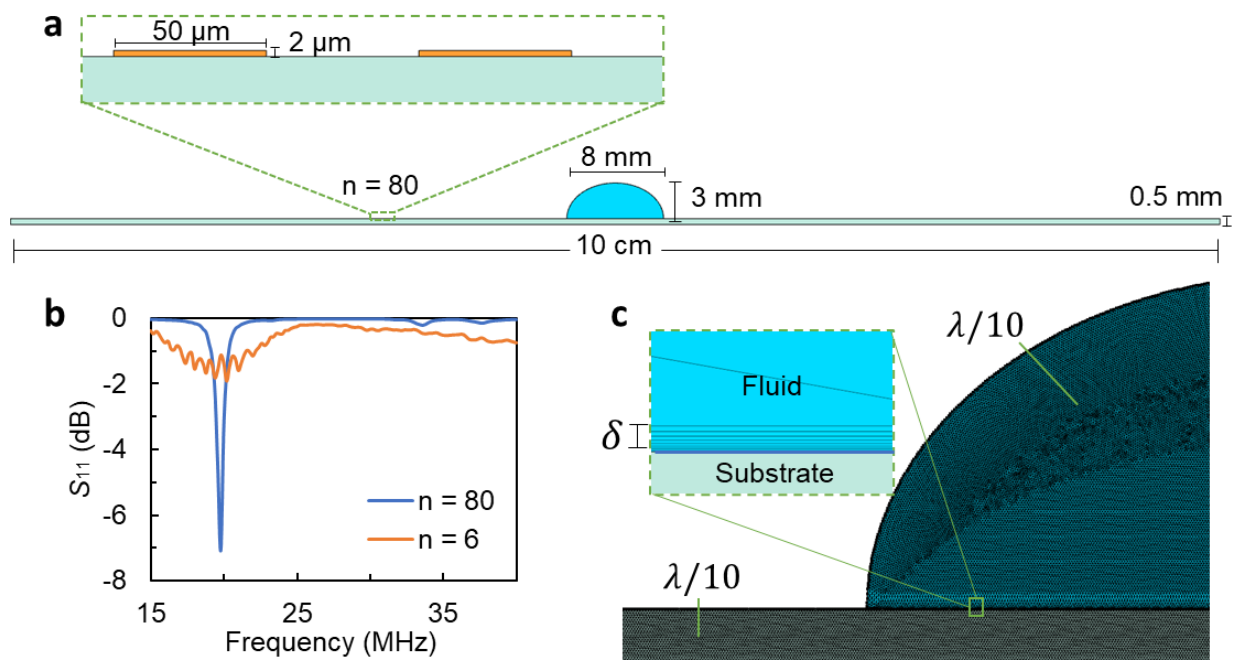


Figure 6.4. Model 3: Life-scale 2D Model. (a) Dimensions, with inset displaying 2 IDT fingers. (b) Simulated S_{11} readings at 0° X-rotation for 6 and 80 electrode fingers. (c) Mesh of a section, with an insert illustrating the boundary layer thickness of the viscous boundary layer (δ).

6.3 Numerical Analysis

6.3.1 IDE Design Validation

First, the simplified 3D model was used to understand the performance difference between a conventional rectangular IDE and a trapezoidal IDE that was designed. Numerical simulation (Figure 6.5) demonstrated that the inclusion of trapezium-shaped IDTs could potentially enhance the acoustic beam width, thereby enabling the manipulation of larger fluidic vessels. Additionally, the trapezoidal IDTs have less dispersion effect when compared to the straight IDTs, which can facilitate uniform wavefields.

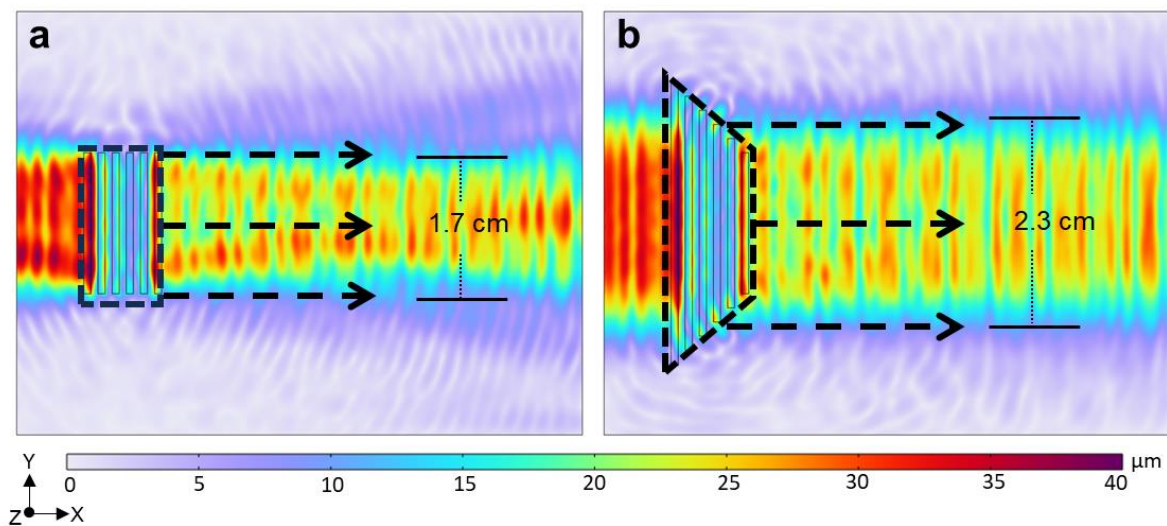


Figure 6.5. Simulation comparison of the displacement field for (a) rectangular and (b) trapezoidal IDT at 0° X rotation on 128° YX-cut LiNbO_3 substrate.

6.3.2 Rayleigh SAW Validation

Secondly, numerical studies of a single unit IDT was performed to provide and validate fundamental information on the excitation of SAW for different orientations with respect to the X-direction on the 128° YX-cut LiNbO_3 . Figure 6.6 shows the simulated eigenfrequency results for R-SAW at varying angles around the X-direction. The image insert shows the R-SAW wave mode shape at 0° , clearly demonstrating the surface wave component. The frequency shows the resonant behaviour due to the periodicity of IDT electrodes and the wavelength-to-frequency relationship $v = \lambda \cdot f$. The SAW

wavelength is defined by the IDT electrode periodicity whereas the phase velocity is given by the substrate's material and propagation orientation.

The values are consistent with experimental readings of the R-SAW from the frequency-dependent reflection coefficient (S_{11}) minima and the following continuous fourth-order Fourier series and the fitted parameters are given in Table 6.2 [336]:

$$v(\theta) = a_0 + \sum_{n=1}^{n=4} a_n \cos(n\omega\theta) + b_n \sin(n\omega\theta) \quad (6.3)$$

Table 6.2. Fitting parameters and values for Taylor series expansion (Equation 6.3) to three significant figures [336].

Parameter	Value
a0	3710
a1	174
a2	126
a3	-4.66
a4	-14.7
b1	0.116
b2	0.169
b3	-0.009
b4	-0.039
ω	0.035

It should be noted that the simulated eigenfrequency values were lower with IDTs placed on top of the substrate compared to with no IDTs. The difference is caused by the resonance frequency not being equivalent to the synchronous frequency of the IDT because internal reflections at the electrodes cause an asymmetry of resonance

peaks of the reflection coefficient. Hence, the resonance frequency is slightly lower in these cases than the synchronous frequency [6]. Additionally, the difference between the simulated frequency values and experimental values is caused by differing phase velocities since the phase velocity within the IDT differs from that of uncoated LiNbO_3 due to the presence of electrode metallisation [6]. In general, the correlation observed between the unit cell simulated and experimental findings of R-SAW phase velocities validates the use of simulation outcomes as a foundation basis for exploring various angles and wave modes in further investigations.

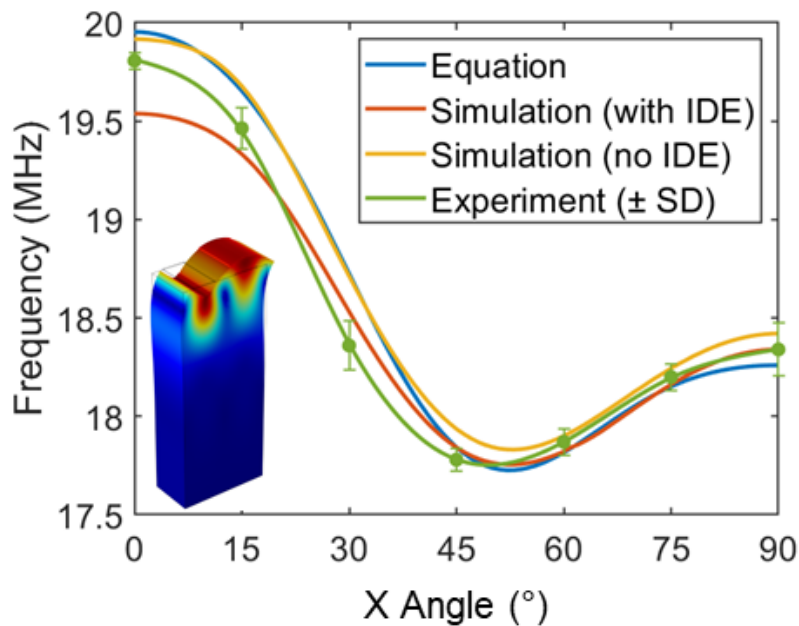


Figure 6.6. Eigenfrequency simulation results showing R-SAW Frequency at various angles, validated by equation (6.3) and experimental S_{11} measurements. Insert shows eigenfrequency wave mode shape of R-SAW at 0° .

The simulated eigenfrequency values were used to find the R-SAW phase velocities for free and electrically short-circuited surfaces. These phase velocities could calculate the coupling coefficient and power flow angles using equations 3.3 and 3.5 (from Chapter 3), respectively. The calculated coupling coefficient and power flow angle at R-SAW with different in-plane X-rotations are shown in Figure 6.7, demonstrating excellent agreement with the literature [6,294,336]. This further validates the use of the unit cell simulation to explore various angles and wave modes. For example, it demonstrates the coupling coefficient of 5.5% for propagation along the X-axis ($\theta = 0^\circ$) [296] and the two lines of symmetry at $\theta = 0^\circ$ and $\theta = 90^\circ$. Although the coupling

coefficient decreases, and the power flow angle varies, this presents opportunities for experimentation, such as using $\sim 30^\circ$ X-rotation R-SAW, which has a moderate coupling coefficient of 3.2% while introducing a significant variation in power flow angle of -12.1° . However, it also shows invaluable R-SAW frequencies, such as at $\sim 60^\circ$ X-rotation with a poor coupling coefficient of 1%.

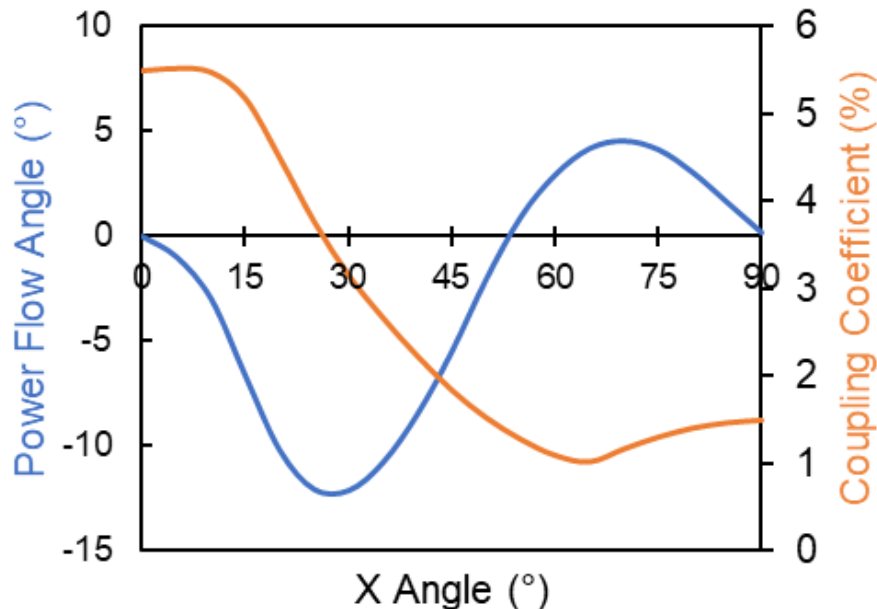


Figure 6.7. Eigenfrequency simulation results showing calculated R-SAW coupling coefficient and power flow angle at various X-rotation angles.

Moreover, the simplified 3D model can be used to visualise the power flow angles. In the case of R-SAW propagating at angles of 15° , 30° , 45° , 60° , 75° , and 90° from the X-direction, the simulated displacement response at each angle and frequency correspond well to the power flow angle and coupling coefficient shown in Figure 6.7. Note that R-SAW for angle 0° was previously shown in Chapter 4 (Figure 6.5), demonstrating 0° power flow angle. Figure 6.8(a) demonstrates at 15° X-rotation excited at 19.2 MHz, a power flow angle of $\sim -7^\circ$ with high displacements indicating high coupling coefficient ($\sim 5\%$). By 30° X-rotation the coupling coefficient is still adequate ($\sim 3\%$), demonstrated by the comparable displacement magnitudes to 15° rotation. Meanwhile the power flow angle increases to $\sim -12^\circ$, which is shown by the movement of the beam direction (+Y direction in Figure 6.8(b)). As the X-rotation angle increases the displacement decreases, becoming similar between 60° to 90° . By 60° X-rotation, the beam direction opposes that of the beam directions between 15° and

45°, from +Y to -Y as shown in Figure 6.8(d). When at 90° X-rotation the beam direction returns to 0° (X direction). Overall, the results validate the R-SAW frequencies and power flow angles from the unit cell simulations, highlighting the potential of the simplified 3D model to also investigate other angles and wave modes.

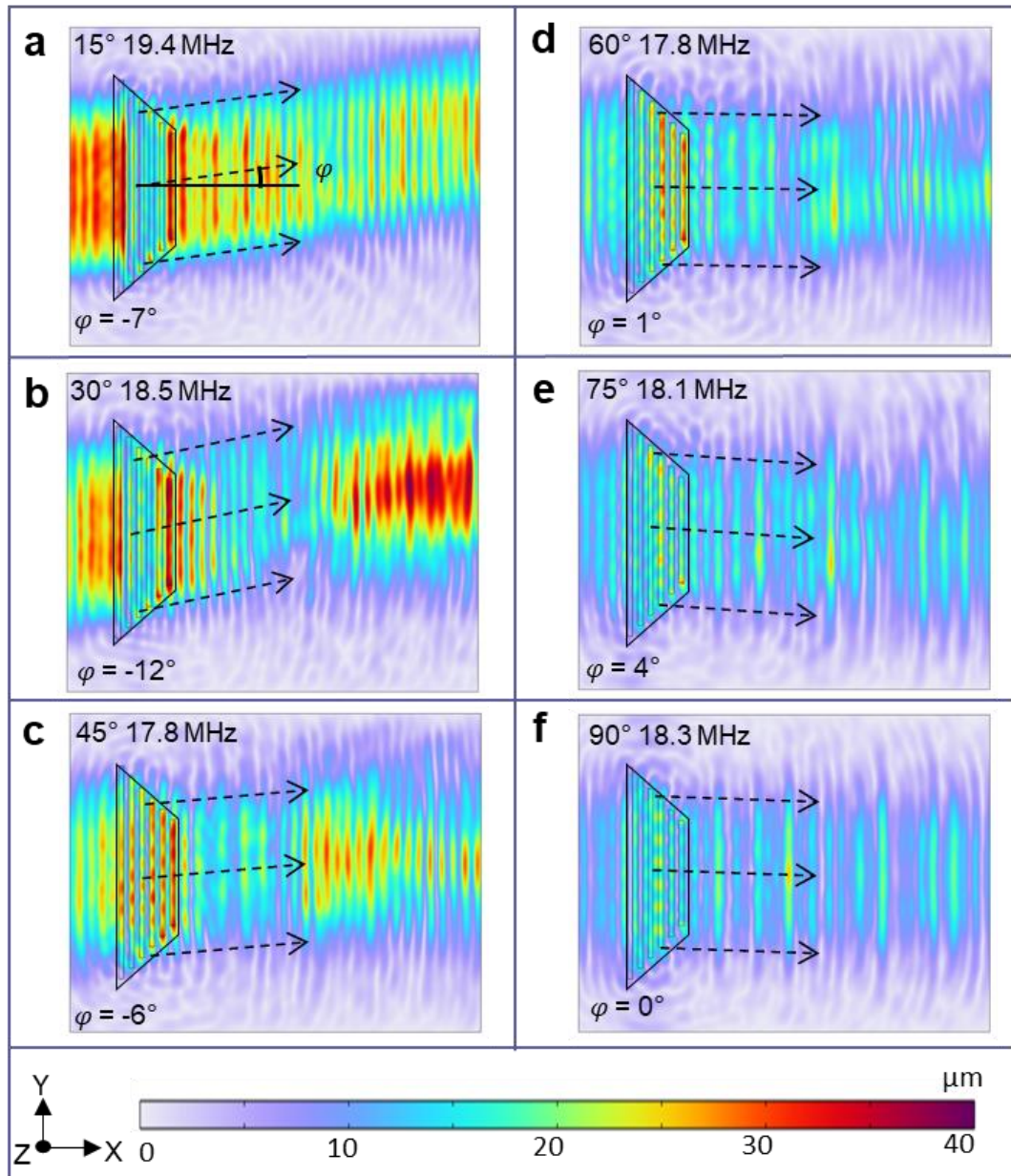


Figure 6.8. Simulation of R-SAW displacement field for trapezoidal IDT for various X-rotation angles around the substrate (a) 15° (b) 30° (c) 45° (d) 60° (e) 75° (f) 90°.

6.3.3 Substrate Validation

To demonstrate the rationale behind substrate selection and to quantify the anisotropic effects on R-SAW performance, a simulation was performed to evaluate the electromechanical coupling coefficients of rotated Y-cut LiNbO₃ substrates. This simulation explores how coupling efficiency varies with different Y-cut angles and in-plane IDT orientations (0°, 30°, 60°, and 90°).

The results, shown in Figure 6.9, reveal the significant directional dependence of R-SAW generation. For example, coupling coefficient is maximised at specific cuts and orientations, such as 128° YX-cut at 0°, and declines as the IDT is rotated away from this axis. This angular sensitivity reflects the anisotropic nature of LiNbO₃ and shows the challenge of achieving consistent SAW performance across multiple directions, which is critical when designing multidirectional acoustofluidic devices and selecting an appropriate substrate.

These findings agree with the material considerations discussed in Chapter 4.3.1, where previous reports [294,396,397] of Y-cut angles were examined. The key crystal cuts reported in literature [294,396,397] are marked in the figure for reference. This simulation illustrates why 128° YX-cut was chosen for the current device - offering strong R-SAW coupling along the X-direction - while also motivating the exploration of alternate wave modes to improve performance at other angles.

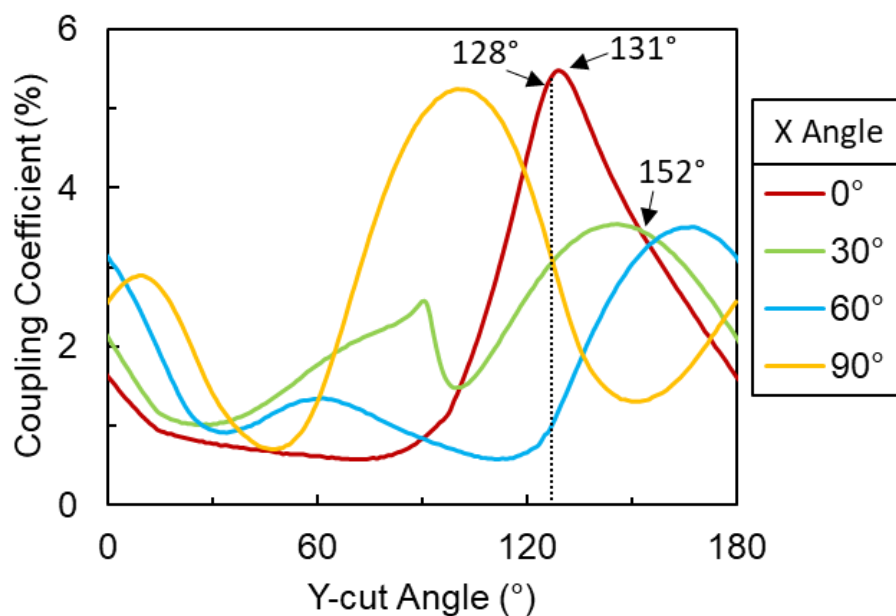


Figure 6.9. Comparison of coupling coefficients in rotated Y-cut LiNbO₃ substrate orientations for R-SAW. The dependence of the in-plane X angle rotations (0°,30°,60°,90°) is shown with different curves. The orientations used in previous studies are marked.

Figure 6.10 shows the admittance graphs of 128° YX-cut LiNbO₃ with a 200 μm wavelength IDT, at various in-plane X rotations of the IDT at 0°, 30°, 60°, and 90° (shown with different curves). The admittance demonstrates the number of modes detected. The total amount of modes detected in one substrate may be as large as ~100 [295], however some modes may have small coupling coefficients and/or large power flow angles. This observation highlights the existence of potentially valuable, underexplored modes within acoustofluidic manipulation devices. For instance, various wave modes have been investigated revealing possibilities to alter the power flow angle and coupling coefficient [295] to enhance the performance of acoustic liquid sensors [296]. Consequently, employing a 128° YX-cut LiNbO₃, while not optimized for multidirectional SAW, remains a practical and relevant choice.

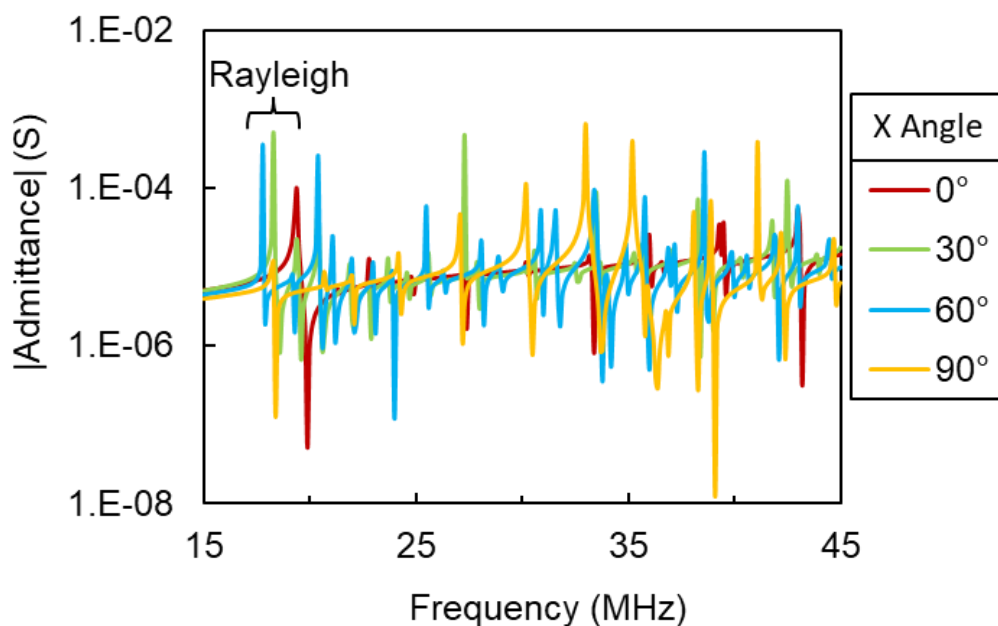


Figure 6.10. Admittance graph for 0.5 mm thick 128° YX-cut LiNbO₃. Demonstrating other wave modes to be investigated. The dependence of the in-plane X rotations of 0°, 30°, 60°, and 90° are shown with different curves.

6.3.4 Wave Modes

The following section investigates alternative wave modes at different angles given the limitations observed in R-SAW's performance at angles other than 0° X-rotation, on the 128° YX-cut LiNbO_3 . The inadequacy of R-SAW beyond 0° X-rotation highlights the necessity to explore alternative wave modes for different angles, a step towards enhancing the versatility and effectiveness of SAW-based technologies.

All the simulated wave mode's phase velocity between 15 MHz and 40 MHz are plotted with respect to the X-rotation, as shown in Figure 6.11. This figure shows the simulated wave modes including an IDT on the surface and without for calculation of coupling coefficient and power flow angle. The greater the change in phase velocity between the phase velocity with and without the IDT, the larger the coupling coefficient. Whereas the power flow angle is related to the change in phase velocity with change in x-rotation angle. The coupling coefficient and power flow angle were calculated for each wave mode, as shown in Figure 6.12, and is further discussed per X-rotation angle in the subsequent section. Although these graphs look visibly similar, the phase velocity for each wave mode has shifted slightly. An obvious difference in phase velocities can be seen in wave mode 15, 16 and 17, where they show relatively different shaped curves.

Note that this is a simplified view of the wave modes – longitudinal waves that do not have surface wave components and did not change phase velocity were not displayed to prevent overcrowding of the figure. The Mode 0 (red) exhibits the R-SAW wave mode, and the other wave modes are excited at higher frequencies. The wave modes are numbered in order of low to high phase velocity from 0° .

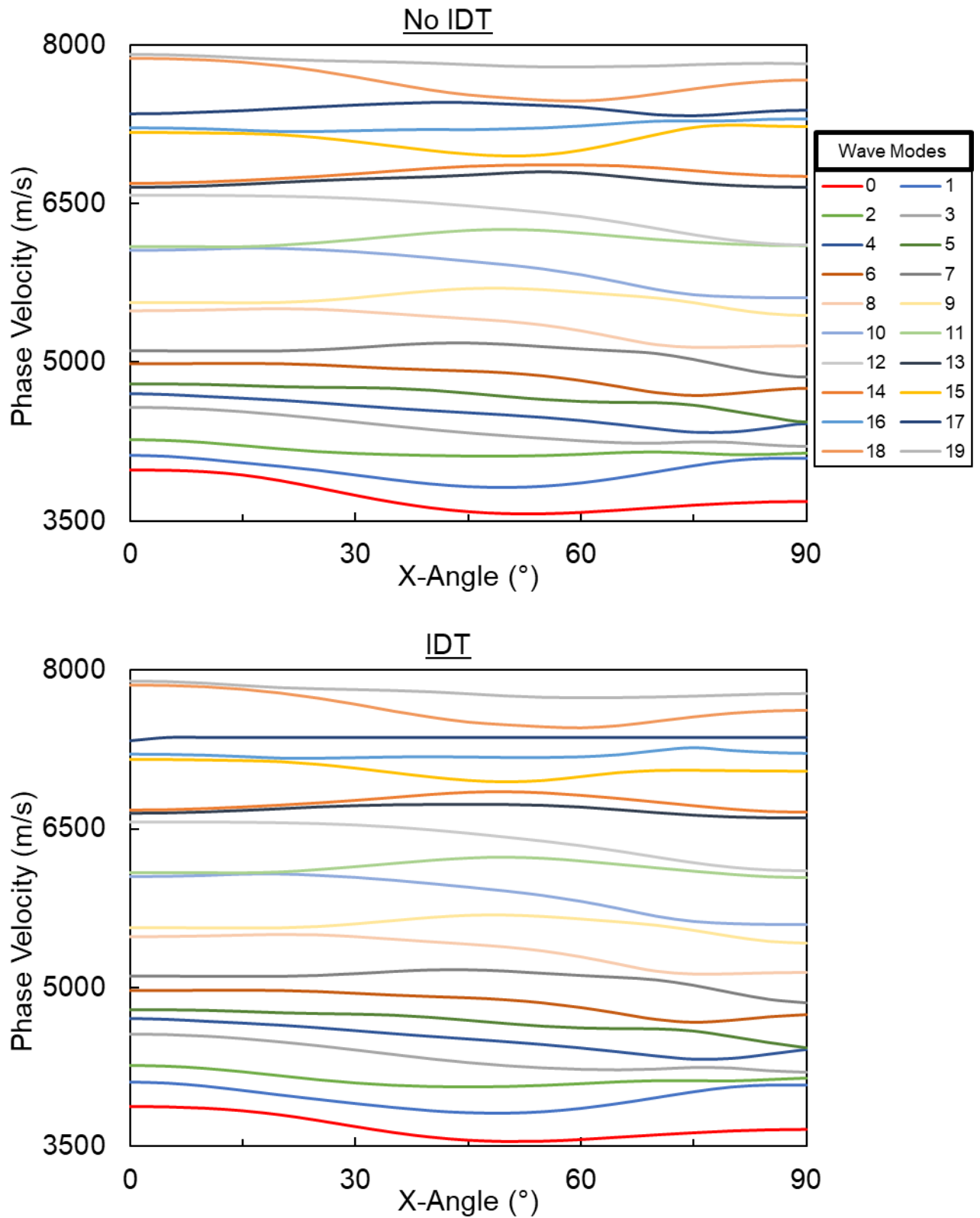


Figure 6.11. Simulated wave modes with respect to in-plane x-rotation angles, with and without an IDT.

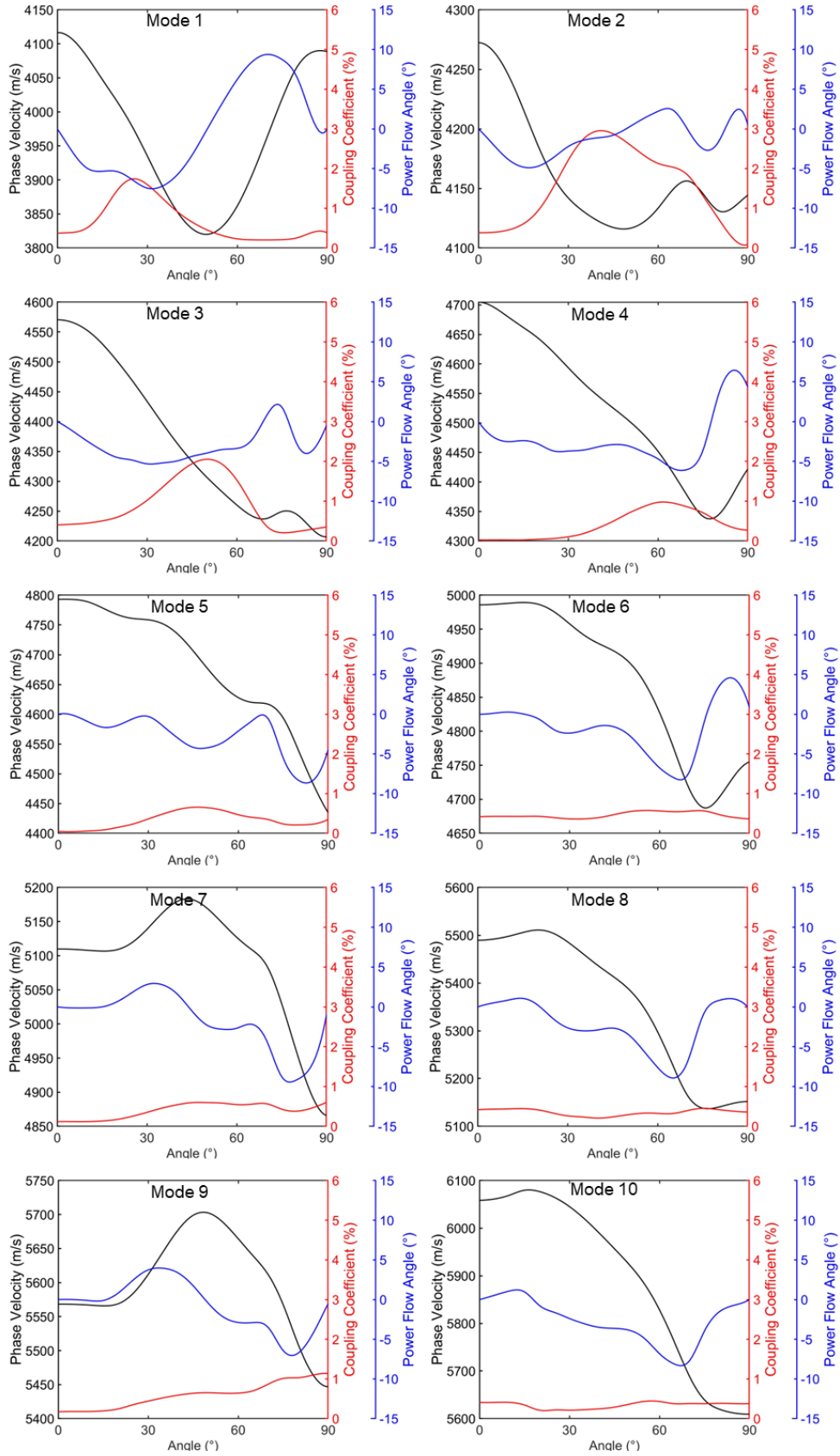


Figure 6.12. Simulated wave mode characteristics (phase velocity, coupling coefficient, and power flow angle) using the unit cell eigenfrequency results for 128°

YX-cut LiNbO₃ substrate at X-rotation angles between 0° and 90°. The wave modes are corresponding to the wave modes phase velocities shown in Figure 6.11 (mode 0 to mode 19).

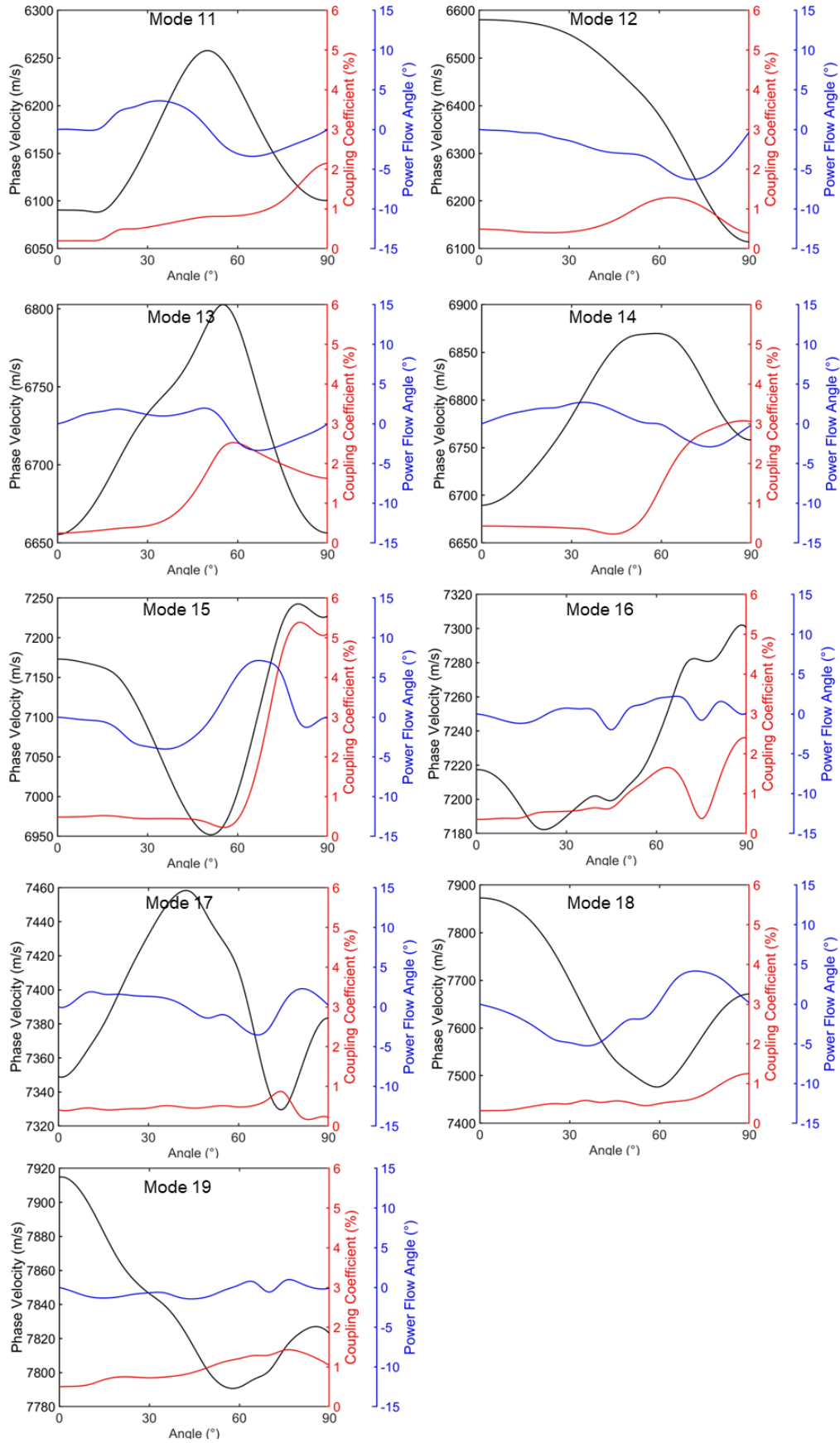


Figure 6.13. Continuation of simulated wave mode characteristics.

A broad spectrum of wave modes, totalling over 20, is shown within a 25 MHz bandwidth, with many of these modes exhibiting harmonics of a fundamental wave. For instance, as depicted in Figure 6.14, each wave mode has a combination of surface, shear-horizontal and bulk components. Note that Eigenmode studies cannot be used to measure the displacement amplitude [407]; hence, the colours are shown for visual demonstration of the shape and are not to a particular scale. These surface waves have three mechanical displacement components, comprising two shear and one longitudinal displacement [413]. Each wave mode has a mixture of each component, with different ratios, which can also change at different angles. The numerical analysis accounts for all three physical features of wave propagation in anisotropic crystals [413].

Mode 0 distinctly shows the surface wave component of R-SAW, while Mode 1 (Leaky-SAW; L-SAW) demonstrates the penetration of the surface wave component into the substrate bulk. Mode 2 and 3 both encompass shear-horizontal and bulk components, whereas Mode 4 predominantly embodies an acoustic wave component in the bulk. Upon altering the X-rotation angle, such as 45° and 90° as shown in Figure 6.14, significant alterations in the wave mode shape occur. At 90° X-rotation, minimal changes in wave mode shapes are observed compared to the 0° X-rotation, albeit with a visible slight shift. Conversely, at 45° X-rotation, substantial variations in wave mode shapes are evident, exhibiting a seemingly disorganised and less structured appearance, despite some resemblance to the original wave mode shapes. Notably, the L-SAW mode appears to demonstrate a combination of SH-SAW characteristics. This observation suggests that within the range of X-rotation angles 0° and 90°, wave modes exhibit hybrid characteristics, offering potential advantages for exploitation.

Further exploration of key wave modes is undertaken in the subsequent section, which focuses on individual X-rotation angles to facilitate a comprehensive investigation spanning angles 0°, 15°, 30°, 45°, 60°, 75°, and 90°.

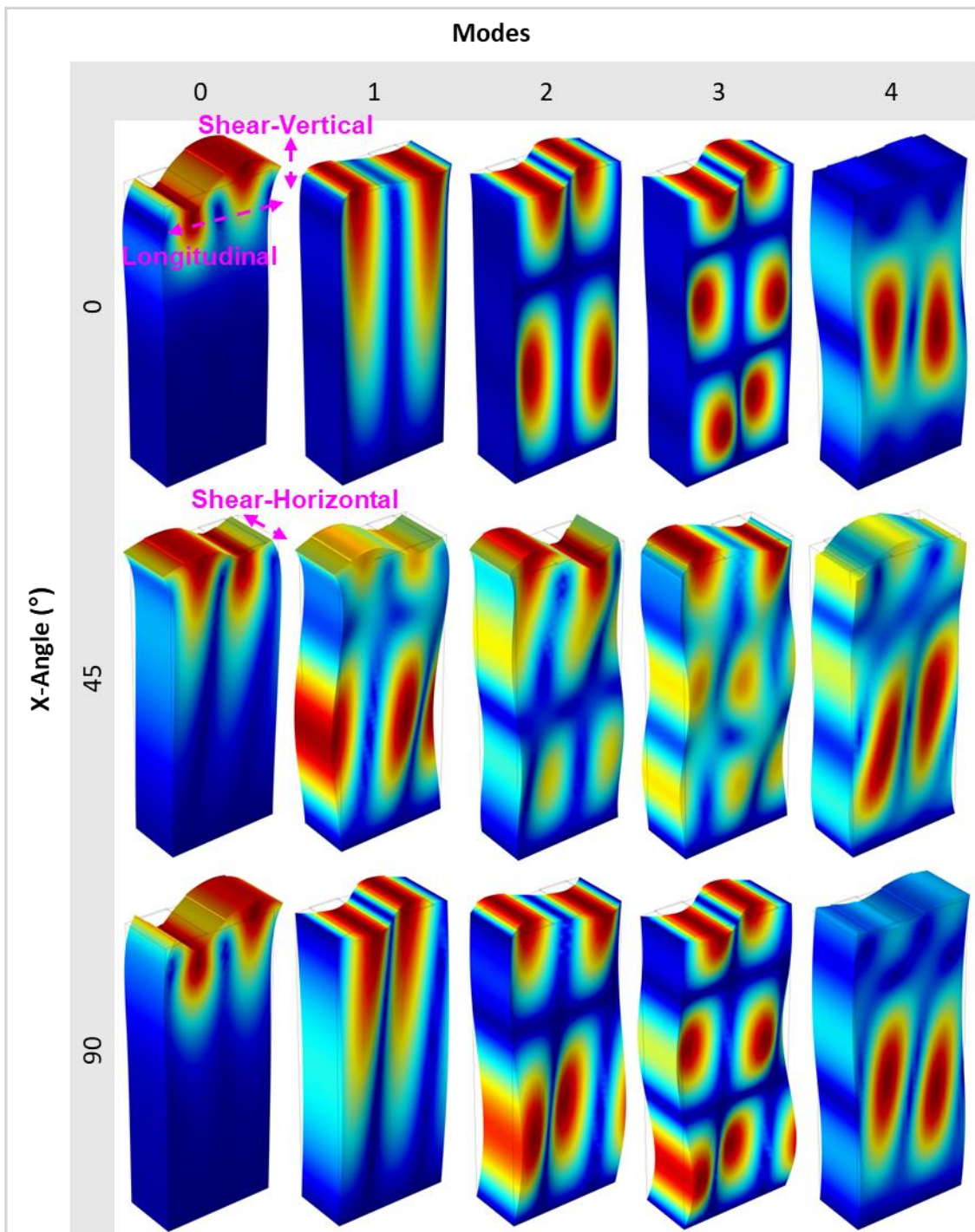


Figure 6.14. Simulated wave modes shapes for modes 0 to 4 at 0°, 45°, and 90° X-rotation angle.

6.3.5 X-Rotation Angle Analysis

Numerical analysis was used to analyse the relationship between different characteristics and frequencies (ranging from 15 MHz – 40 MHz) at individual X-rotation angles (0°, 15°, 30°, 45°, 60°, 75°, and 90°). This enables a thorough investigation of the anisotropic behaviour of the wave modes on the 128° YX-cut LiNbO₃. The characteristics involved the reflection coefficient (S_{11}), Z displacement, coupling coefficient, and power flow angle.

The S_{11} is a useful measure of the conversion between electrical to acoustic energy. The lower the minimum value of electrical reflection, the less electric energy is reflected from the IDT towards the signal generator. Hence, more electric energy is reflected and no longer available for SAW excitation. A higher S_{11} minimum is caused by a large impedance mismatch. The Z displacement is the vertical displacement of the wave mode, which is used as an indication on whether the wave mode can actuate the fluid. The coupling coefficient is the ratio between the converted energy and the supplied energy, a useful measurement for the transduction efficiency of the material [414]. The power flow angle is the angle between propagation direction of wave and power flow, which is an important parameter for the development of SAW devices as the ability to control the SAW is vital [415].

Eigenfrequency study was used to comprehend the wave mode shape for the key frequencies per angle, this gives a clear idea on what wave mode was in use and its properties. A simplified 3D simulation was also used to visualize the wavefield and the fluids interaction. This simulation can help visualise the Z displacement, coupling coefficient, power flow angle, and see how they could impact the acoustofluidic effect. However, its essential to acknowledge that this simplified 3D model incorporates only 6 IDT fingers, significantly fewer than the 80 fingers. As demonstrated in Chapter 6, this limitation results in an inaccurate representation, due to the broader bandwidth, which complicates ensuring the correct wave mode and frequency selection. Additionally, the 3D model is scaled down significantly with numerous physical assumptions, hence the wavefields interaction pattern with the fluid is not comparable. Therefore, the results should be interpreted with caution, and it is used to simply

determine fluid interaction and not the fluid interaction pattern. Despite its limitations, this model still contributes to the comprehension of wavefields and fluid interactions.

6.3.5.1 0 degrees

Figure 6.15 displays the simulated Z displacement, S_{11} , coupling coefficient and power flow angle with respect to frequency (range of 15-40 MHz) at an orientation angle of 0° relating to the X-rotation. Figure 6.15 demonstrates the simulated S_{11} values showing a good correlation to the coupling coefficient. Additionally, the Z displacement seems to closely match the S_{11} minima. This shows the potential of using the S_{11} minima as a guideline for utilizing other harmonics. Moreover, the power flow angle is close to zero which corresponds well with theory [295]. Although R-SAW at 19.6 MHz has clearly got the largest S_{11} minima, other minima's can be observed at 35.9 MHz, and 39.4 MHz which could indicate beneficial wave modes that may offer distinct acoustofluidic effect. Despite the S_{11} minima, the coupling coefficients and Z displacements are low and hence is unlikely to induce effective acoustofluidic streaming.

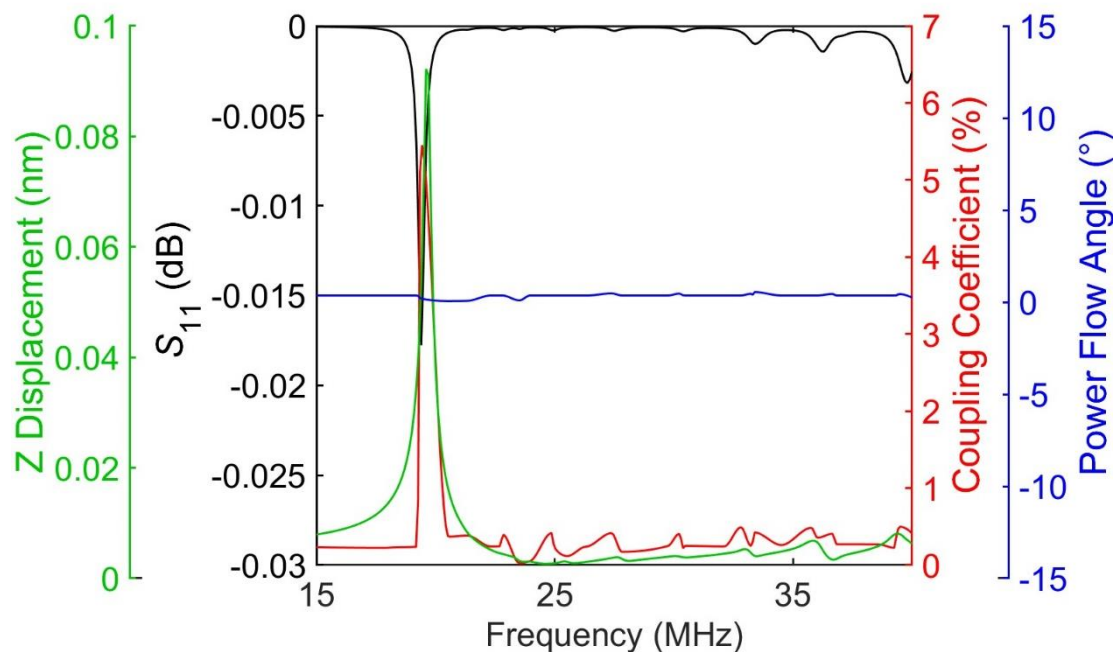


Figure 6.15. Graph of the relationship between various characteristics and frequency at 0° , illustrating the reflection coefficient (black), Z displacement (green), coupling coefficient (red), and power flow angle (blue).

Figure 6.16(left) displays the wave mode shape for the top three wave modes at an orientation angle of 0° with respect to the X-rotation. The frequency at the largest S_{11} minima being (a) 19.6 MHz, (b) 35.9 MHz, and (c) 39.4 MHz. These frequencies correspond to the wave modes 0, mode 15, and mode 18, respectively, as shown in Figure 6.11. Figure 6.16(right) reveals the simulated wavefield in front of a single trapezoidal IDT oriented at 0° angle with respect to the X-direction and demonstrates the wavefields interaction with the fluid displaying the root mean squared (RMS) acoustic velocity (mm/s). The displacement amplitudes (with a unit of nm) show how characteristic behaviours changed from the different propagation directions and frequencies. Note that the displacement and RMS acoustic velocity scale is the same and capped for all the following wavefield simulations for comparison purposes.

Figure 6.16(a) clearly illustrates the distinct surface component and vertical displacement of the R-SAW wave mode shape. The R-SAW characteristic is also presented through the wavefield propagation pattern, shown by peaks and troughs of the displacement. Conversely, Figure 6.16(b) and (c) shows similar wave mode shapes with both components in the surface and the bulk. The wavefield demonstrates beam profile distortion at the higher frequencies indicating bulk waves were excited in the substrate, thus interfering with the surface waves [6]. Additionally, Schulmeyer *et al.* observed corresponding wavefield patterns using Laser-Doppler-Vibrometer wavefield measurements for R-SAW and SH-SAW modes [383]. The maximum displacement amplitudes of wavefields occur at the same frequencies of the coupling coefficient calculations with the largest S_{11} minima, where 19.6 MHz presents the largest (5.5% and -0.018 dB, respectively), followed by 39.4 MHz (0.5% and -0.003 dB, respectively). The wavefield droplet interaction shows minimal acoustic velocity at the higher frequency wave mode, this also corresponds with the low coupling coefficient calculations with the S_{11} minima, as well as having a small Z displacement amplitude (< 0.01 nm) when compared to R-SAW (~ 0.09 nm) as shown in Figure 6.15.

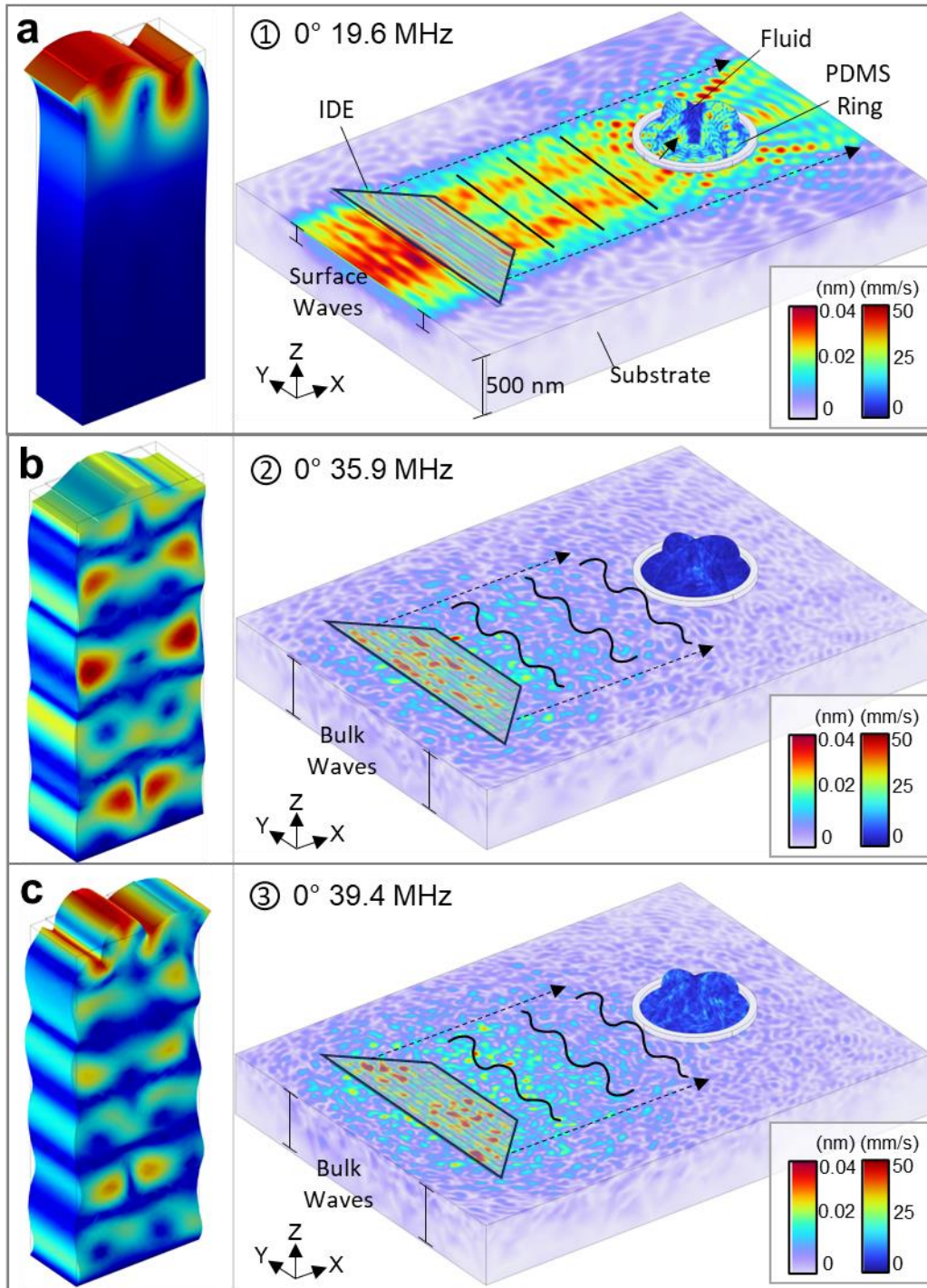


Figure 6.16. Wave mode and wavefield of top 3 simulated S_{11} results at 0° angle with respect to the X-direction where being (a) 19.6 MHz, (b) 35.9 MHz, and (c) 39.4 MHz.

6.3.5.2 15 degrees

Figure 6.17 presents the simulated characteristics (Z displacement, S_{11} , coupling coefficient and power flow angle) at an orientation angle of 15° with respect to the X-

rotation. The top three S_{11} minima (19.4 MHz, 35.8 MHz, and 39.2 MHz) are similar to that at 0° X-rotation in Figure 6.15, also corresponding to mode 0, mode 15, and mode 18, respectively, however the frequencies show a slight decrease shift and a reduction in magnitude. The frequency shift correlates to the wave mode phase velocities shown in Figure 6.11, where the wave modes phase velocities at mode 0, 15, and 18, decrease marginally at 15° X-rotation. The coupling coefficient and Z displacement also correlate well with the S_{11} minima. The key difference is that the power flow angle varies with frequency. At lower frequency modes, the power flow angle exhibits greater variation, exceeding -5° , whereas at high frequencies, the variation is more limited, within a range of $\sim \pm 1^\circ$.

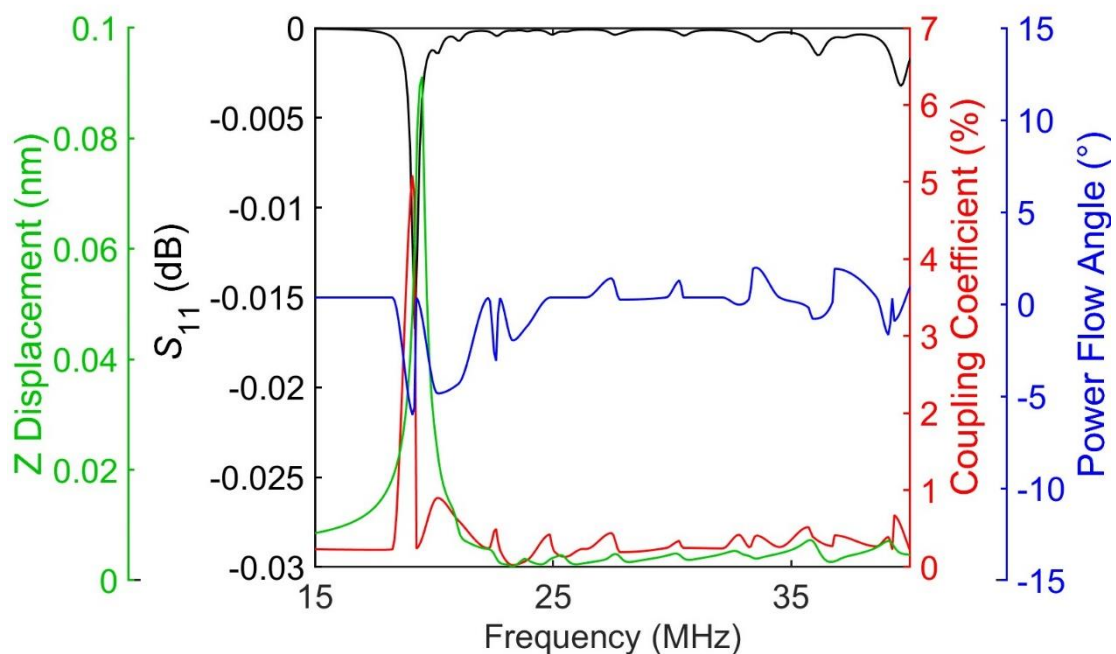


Figure 6.17. Graph of the relationship between various characteristics and frequency at 15° , illustrating the reflection coefficient (black), Z displacement (green), coupling coefficient (red), and power flow angle (blue).

Figure 6.18(a), for 15° X-rotation, parallels the observations from Figure 6.16(a), displaying distinct surface features and vertical displacements characteristic of R-SAW wave mode. The propagation pattern of R-SAW in the wavefield remains evident. Figure 6.18(b) and (c) similarly demonstrate wave mode shapes indicative of both surface and bulk components, accompanied by beam profile distortion wavefield patterns. The maximum displacements amplitude and acoustic velocities aligns with

the frequencies corresponding to the largest S_{11} minima, highest coupling coefficient and Z displacements. Moreover, the simulated wavefield displacement in the XY plane confirms the calculated power flow angles. For R-SAW, the wavefield demonstrates the beam steering ($\sim 6.6^\circ$), as also shown in Figure 6.17. Beam steering is evident in the higher frequency wavefield, observed through their asymmetry, albeit challenging to quantify due to the distorted nature of the wavefield.

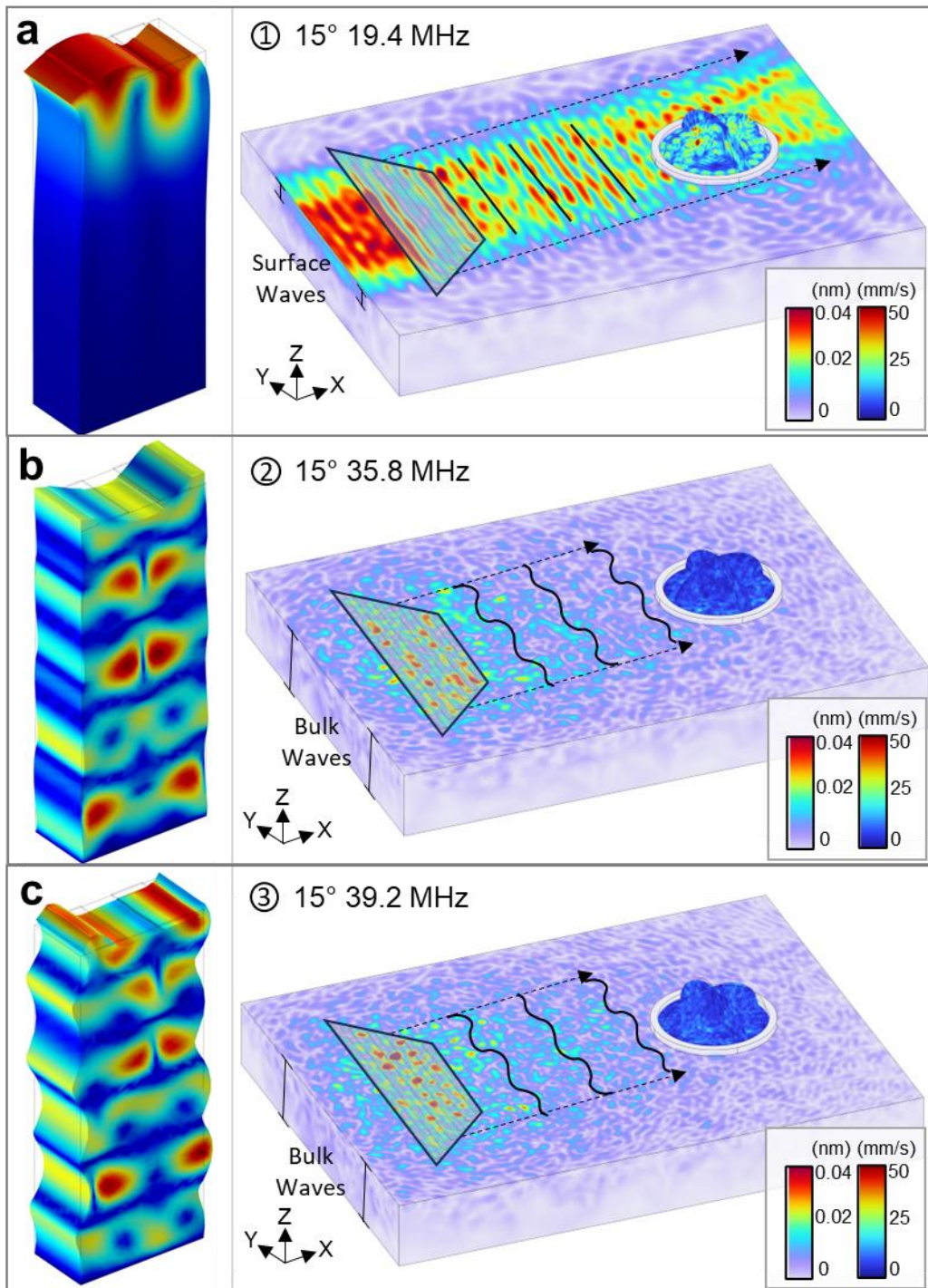


Figure 6.18. Wave mode and wavefield of top 3 simulated S_{11} results at 15° angle with respect to the X-direction where being (a) 19.4 MHz, (b) 35.8 MHz, and (c) 39.2 MHz.

6.3.5.3 30 degrees

Figure 6.19 shows the simulated characteristics at an orientation angle of 30° with respect to the X-rotation. The top three S_{11} minima are 18.5 MHz, 19.5 MHz, and 20.5 MHz, corresponding to mode 0, mode 1, and mode 2, respectively. Higher coupling coefficient ($\sim 3.2\%$), S_{11} (~ -0.009 dB) and Z displacements are observed at lower frequencies. The S_{11} minima and coupling coefficient correlate well, with a similar trend for the Z displacement. However, there are relatively lower Z displacement values for 19.5 MHz and 20.5 MHz (0.01 nm and 0.03 nm respectively, compared to 0.07 nm at 18.5 MHz R-SAW). The power flow angle has large variations with frequency compared to 0° and 15° X-rotation. For example, at 18.5 MHz, 19.5 MHz and 20.5 MHz, the power flow angle is $\sim -12.1^\circ$, -7.5° , and -2.2° , respectively.

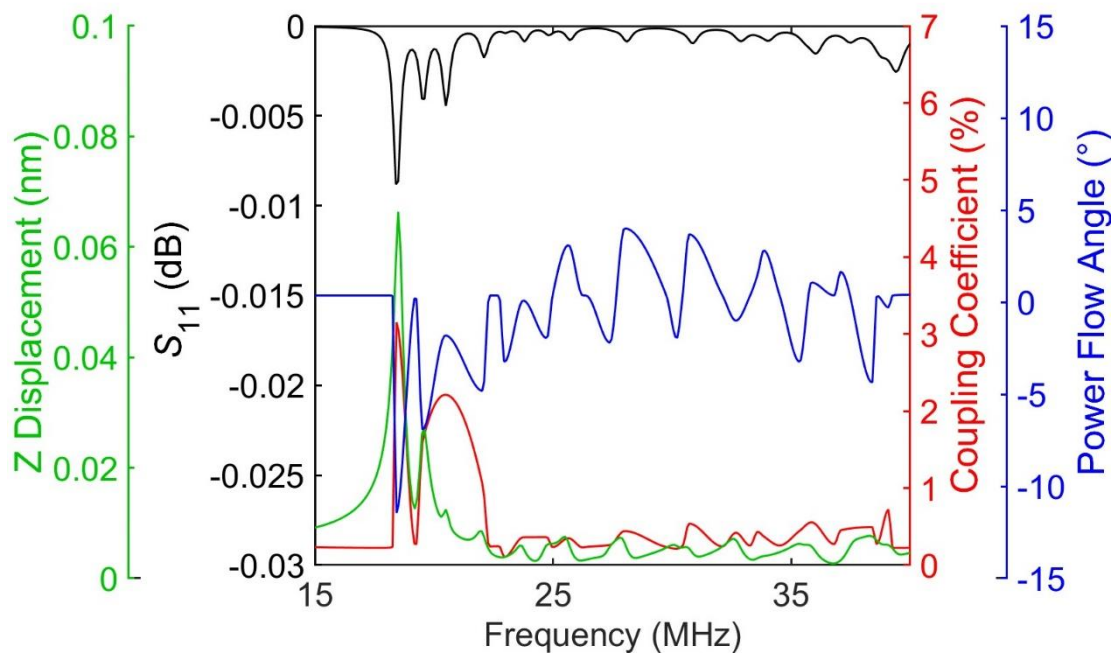


Figure 6.19. Graph of the relationship between various characteristics and frequency at 30° , illustrating the reflection coefficient (black), Z displacement (green), coupling coefficient (red), and power flow angle (blue).

The wave modes with the largest S_{11} minima at 30° X-rotation, shown in Figure 6.20, each exhibit predominantly surface features and vertical displacements characteristic

of R-SAW wave mode. However, the wave modes at (b) 19.5 MHz and (c) 20.5 MHz also show L-SAW component with the penetration of the surface wave component into the substrate bulk. The propagation pattern of the R-SAW component in the wavefield is evident for each frequency.

Notably, the maximum displacements amplitude aligns with the frequencies corresponding to the largest S_{11} minima and the highest coupling coefficient, where R-SAW at 18.5 MHz demonstrates highest displacement magnitude. Although it does not correlate with the simulated Z displacements, the wavefields show the displacement magnitude and hence not limited to the Z direction only. This indicates that the wave modes at 19.5 MHz and 20.5 MHz have displacements in the X or Y direction. Furthermore, the wavefield displacement in the XY plane confirms the calculated power flow angles. For 18.5 MHz R-SAW, the wavefield demonstrates the large beam steering ($\sim 12.1^\circ$), whereas, for 19.5 MHz and 20.5 MHz the power flow angle is -7.5° and -2.2° , respectively. Nevertheless, the beam profiles indicate a slight focusing effect, i.e. the width of the SAW beam profile decreases with increasing distance from the IDT. This is probably caused by diffraction effects due to the limited aperture of the IDTs [6]. The wavefield droplet interaction shows increased acoustic velocity at 18.5 MHz R-SAW when compared to the 19.5 MHz and 20.5 MHz at 30° X-rotation; however, this acoustic velocity is reduced when compared to R-SAW at 0° and 15° X-rotation. Interestingly, 20.5 MHz at 30° X-rotation demonstrates relatively increased RMS acoustic velocity when compared to 19.5 MHz, even though it has a reduced Z displacement, as well as a comparable S_{11} minima and coupling coefficient. This indicates that the bulk component exhibits a different displacement direction (X or Y) which could aid fluid actuation.

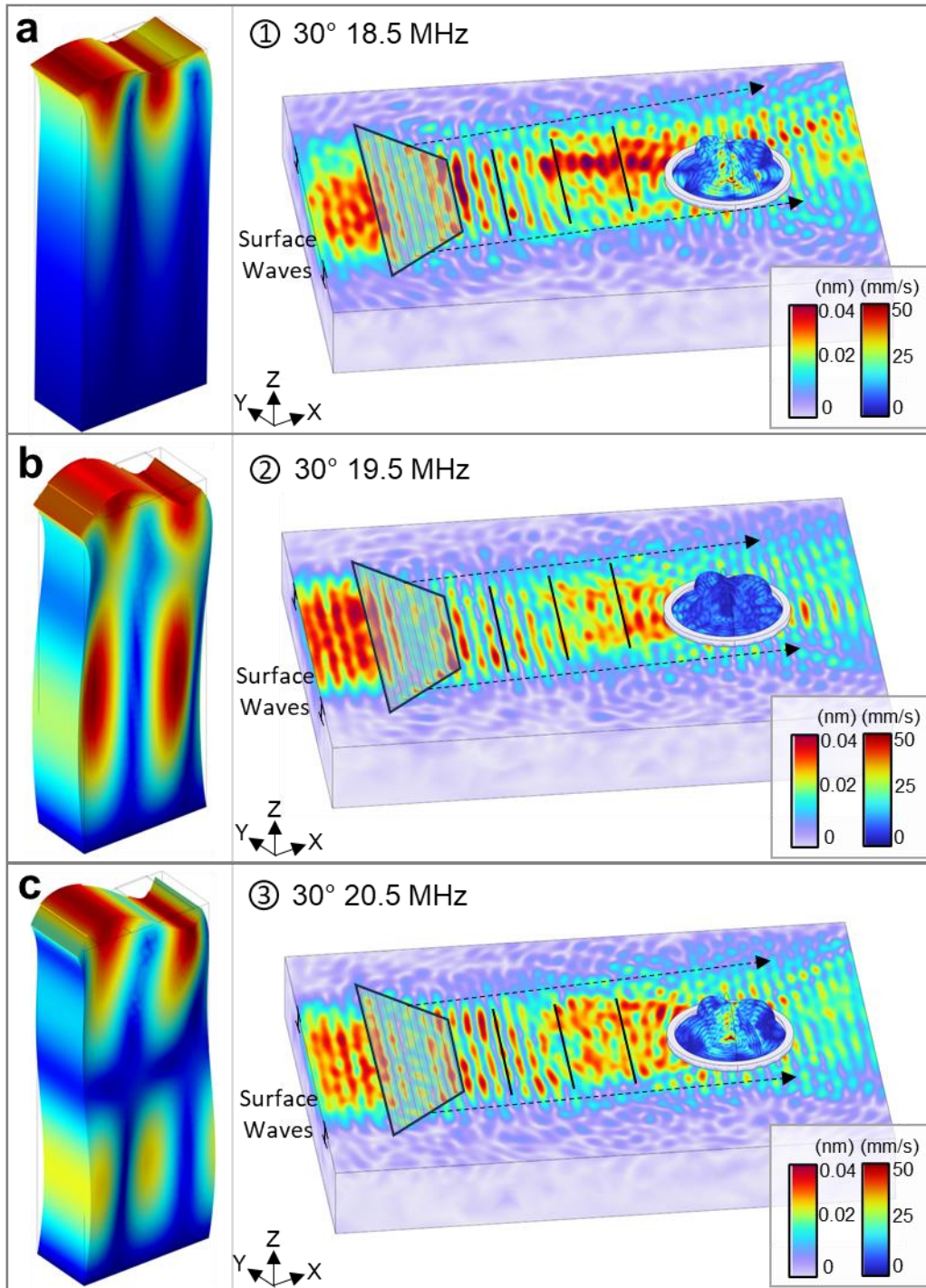


Figure 6.20. Wave mode and wavefield of top 3 simulated S_{11} results at 30° angle with respect to the X-direction where being (a) 18.5 MHz, (b) 19.5 MHz, and (c) 20.5 MHz.

6.3.5.4 45 degrees

The simulated characteristics at an orientation angle of 45° with respect to the X-rotation is shown in Figure 6.21. Similar to earlier findings, there is a strong correlation

between the S_{11} minima values and the coupling coefficient. The dominant three frequencies are at 17.8 MHz, 20.4 MHz, and 21.4 MHz, corresponding to mode 0, mode 2, and mode 3, from Figure 6.11, respectively. Additionally, the power flow angle varies with frequency, where for the largest three S_{11} minima the power flow angle is -5.5° , -0.8° , and -4.4° respectively. The Z displacement is highest at 17.8 MHz R-SAW (~ 0.03 nm), when compared to 20.4 MHz (~ 0.02 nm) and 21.4 MHz (~ 0.01 nm). Nevertheless, the S_{11} , coupling coefficients and Z displacements are relatively smaller in comparison to 0° , 15° , and 30° X-rotation.

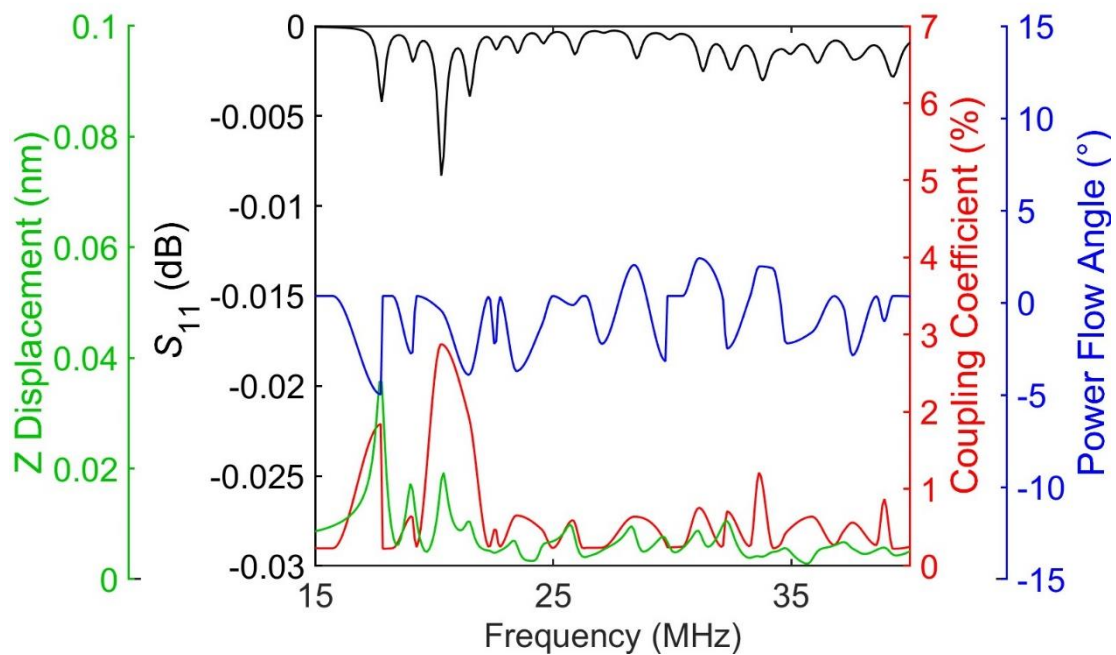


Figure 6.21. Graph of the relationship between various characteristics and frequency at 45° , illustrating the reflection coefficient (black), Z displacement (green), coupling coefficient (red), and power flow angle (blue).

The wave modes and wavefield interactions at largest three frequencies ((a) 17.8 MHz, (b) 20.4 MHz, and (c) 21.4 MHz) for 45° X-rotation are shown in Figure 6.22. The wave modes are similar to the wave modes observed at 30° X-rotation, where they show predominantly surface features and vertical displacements characteristic of R-SAW wave mode, and the latter wave modes (20.4 MHz and 21.4 MHz) also show L-SAW component. The maximum displacements amplitudes for each of the wavefield are comparable, even though R-SAW at 17.8 MHz has the largest Z displacement. This is likely due to the same reason as for the maximum displacements at 30° X-

rotation frequencies. The propagation pattern of the R-SAW component in the wavefield is apparent for each frequency. The wavefield droplet interaction shows increased acoustic velocity at 20.4 MHz and 21.4 MHz compared to 17.8 MHz. Although the higher frequencies have a reduced Z displacement, the coupling coefficients are greater. However, it should be noted that at each of these frequencies the RMS acoustic velocity is minimal compared to the prior X-rotation angles analysed.

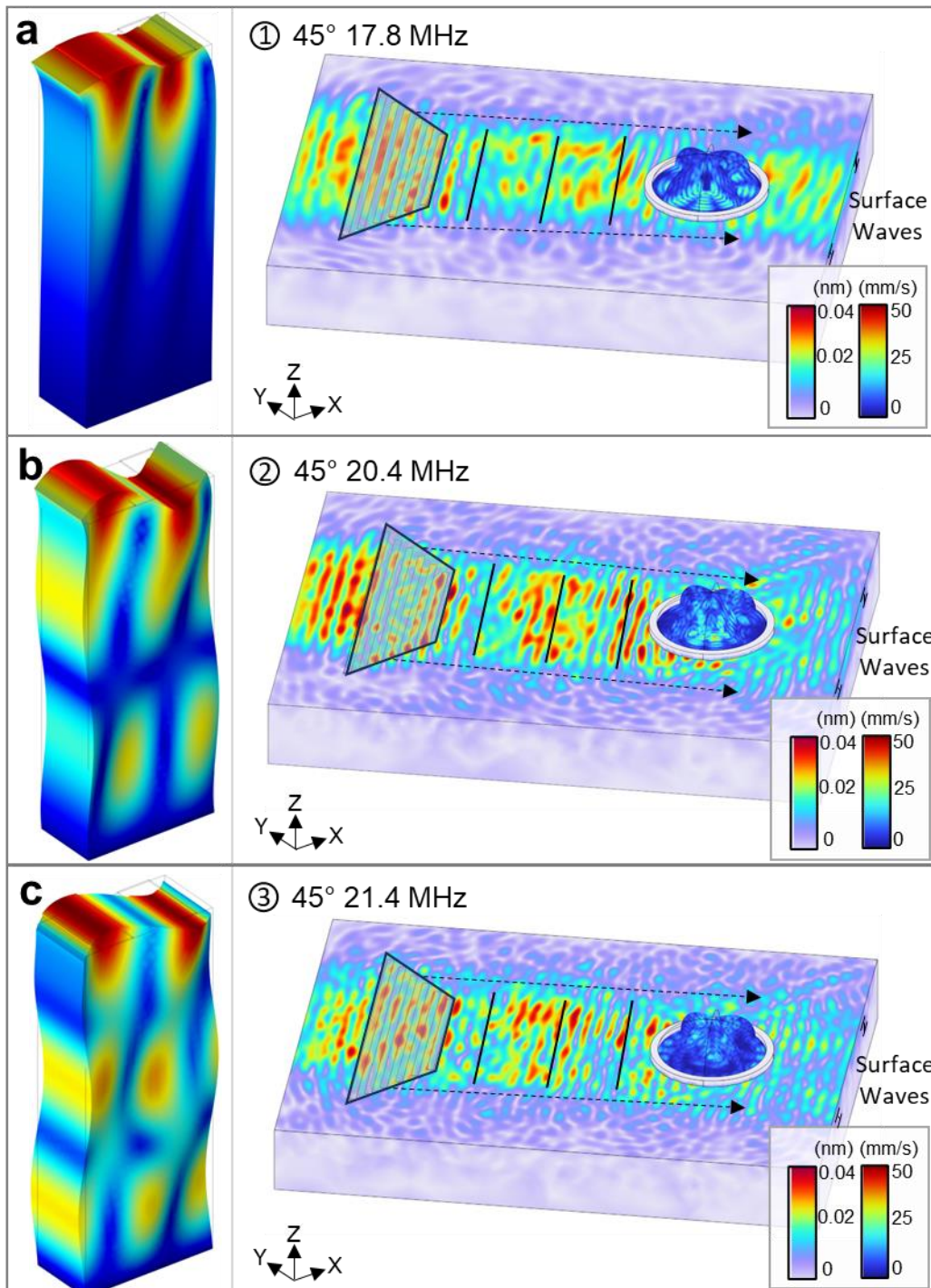


Figure 6.22. Wave mode and wavefield of top 3 simulated S_{11} results at 45° angle with respect to the X-direction where being (a) 17.5 MHz, (b) 20.4 MHz, and (c) 21.4 MHz.

6.3.5.5 60 degrees

The simulated characteristics (Z displacement, S_{11} , coupling coefficient and power flow angle) at an orientation angle of 60° with respect to the X-rotation are depicted Figure 6.23. Consistent with prior observations, a notable correlation between the S_{11} minima values and the coupling coefficient exist. The largest three frequencies are at 20.5 MHz, 31.7 MHz, and 33.7 MHz, corresponding to mode 2, mode 12, and mode 13, respectively. Compared to the previous angles, 60° X-rotation display frequencies with good characteristics (moderate S_{11} and coupling coefficient) across a range of lower and higher frequencies. The power flow angle exhibits variation with frequency, where for the largest three S_{11} minima the power flow angle is 2.2° , -4.4° , and -2.2° respectively. The Z displacement is no longer highest for R-SAW, instead demonstrating comparable displacement of ~ 0.01 nm for each frequency.

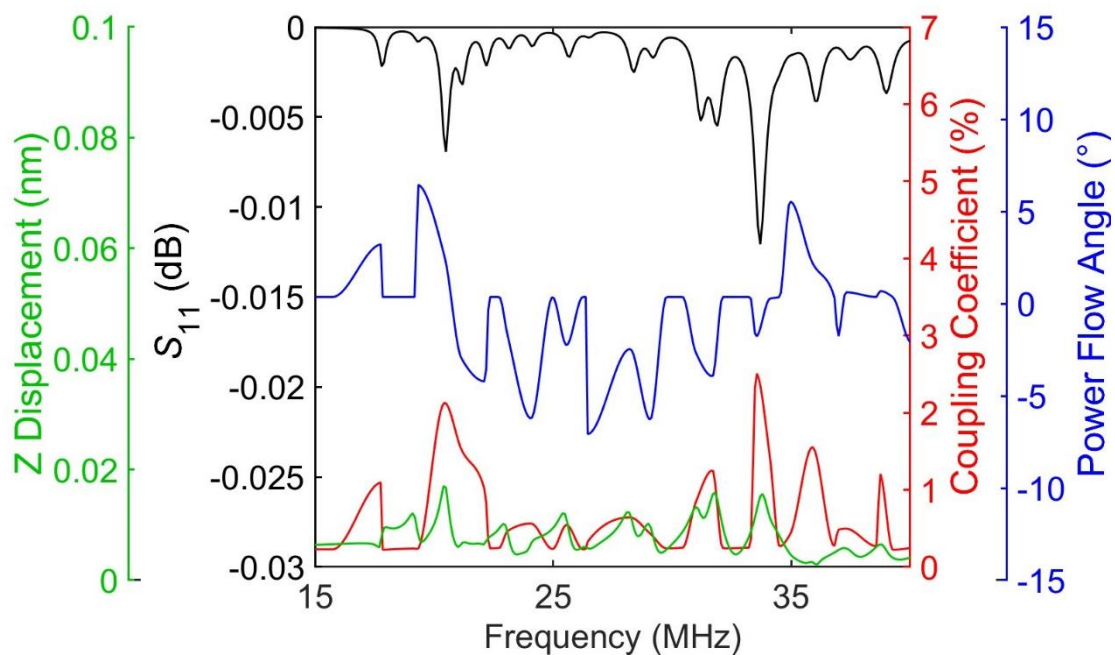


Figure 6.23. Graph of the relationship between various characteristics and frequency at 60° , illustrating the reflection coefficient (black), Z displacement (green), coupling coefficient (red), and power flow angle (blue).

The wave modes and wavefield interactions at largest three frequencies ((a) 20.5 MHz, (b) 31.7 MHz, and (c) 33.7 MHz) for 60° X-rotation are shown in Figure 6.24. Figure 6.24(a) displays similar a wave mode observed at 30° and 45° X-rotation with R-SAW and L-SAW component. Figure 6.24(b) and (c) both show a combination of wave mode components, demonstrating surface and bulk components in various directions. The wavefield propagation for 20.5 MHz displays the R-SAW propagation characteristic as seen for previous angles. The wavefield observed also validates the calculated power flow angle of 2.2° at 20.5 MHz. On the other hand, the wavefields at the higher frequencies (31.7 MHz and 33.7 MHz) demonstrates the beam profile distortion indicating bulk waves were excited and interfering the surface waves. Similar to the higher frequency wavefields at other angles, a beam steering can be observed due to the asymmetry. Although each frequency has comparable Z displacements, the maximum displacement amplitudes are larger for the higher frequencies at 31.7 MHz and 33.7 MHz, suggesting the bulk modes have displacements in other directions. The wavefield droplet interaction shows comparable RMS acoustic velocities at each frequency.

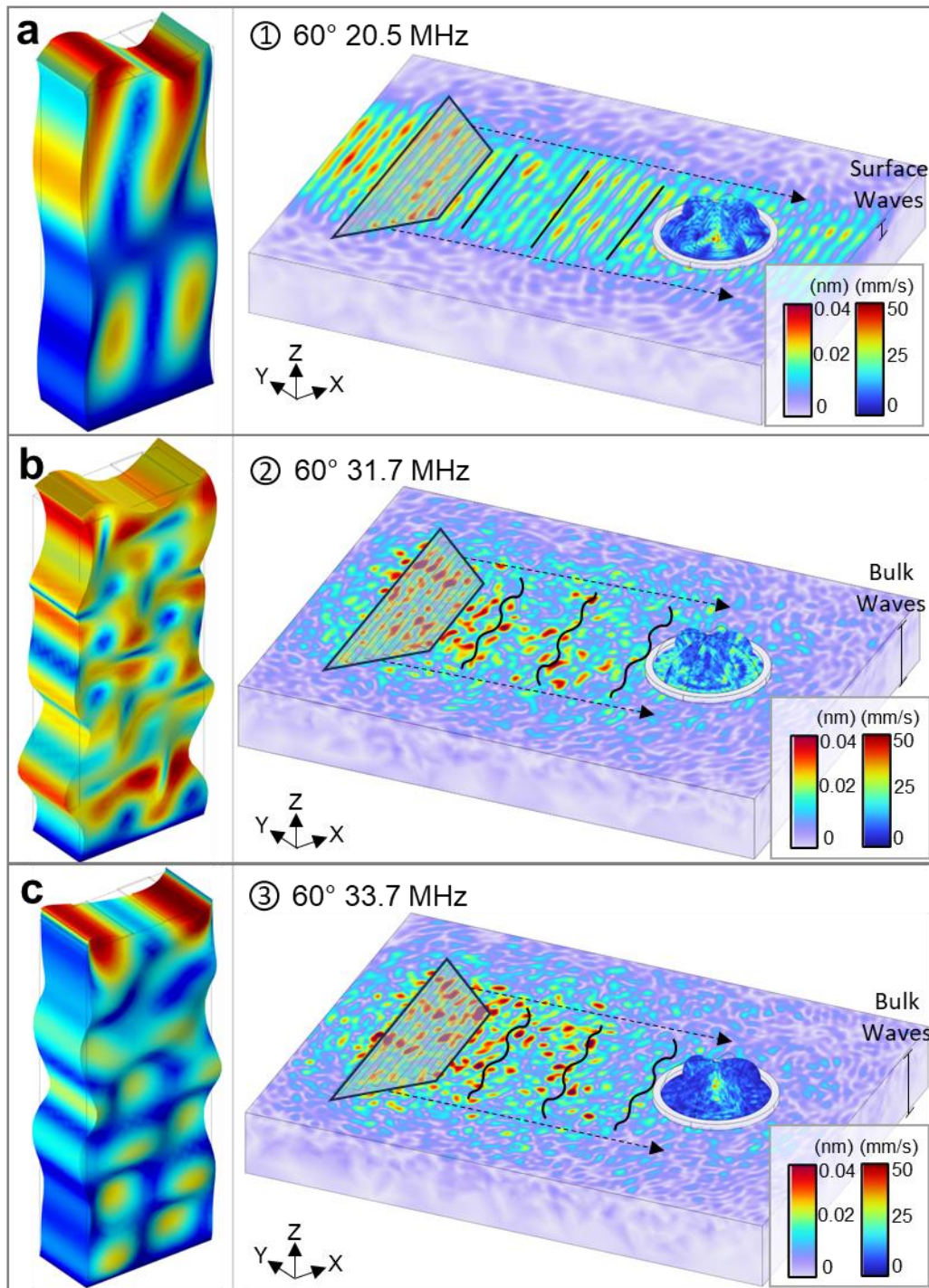


Figure 6.24. Wave mode and wavefield of top 3 simulated S_{11} results at 60° angle with respect to the X-direction where being (a) 20.5 MHz, (b) 31.7 MHz, and (c) 33.7 MHz.

6.3.5.6 75 degrees

Figure 6.25 illustrates the simulated characteristics at an orientation angle of 75° with respect to the X-rotation. Although there exists a relationship between the S_{11} minima

values and the coupling coefficient, it is noteworthy that the coupling coefficient is greatest at 35.5 MHz, while the largest S_{11} minima occurs at 33.4 MHz. It is important to acknowledge that the introduction of mechanical damping during S_{11} minima simulation may initiate alterations impacting both the S_{11} minima and coupling coefficient outcomes. The dominant three frequencies are at 30.7 MHz, 33.4 MHz, and 35.5 MHz, corresponding to mode 11, mode 14, and mode 15, respectively. In contrast to preceding angles, the 75° X-rotation angle presents favourable characteristics particularly at higher frequencies. The power flow angle demonstrates variability with frequency, where the power flow angle is -2.5° , -2.9° , and 5.2° for the largest three S_{11} minima, respectively. While Z displacement remains highest for R-SAW at 18.1 MHz (0.034 nm), higher frequencies such as 33.4 MHz display comparable Z displacement of 0.024 nm, representing only a 30% reduction. Interestingly, at 35.5 MHz, characterised by the highest coupling coefficient (4.7%) and moderate S_{11} minima (-0.01 dB), minimal Z displacement (less than ~ 0.01 nm) is observed, suggesting the presence of a distinct wave mode.

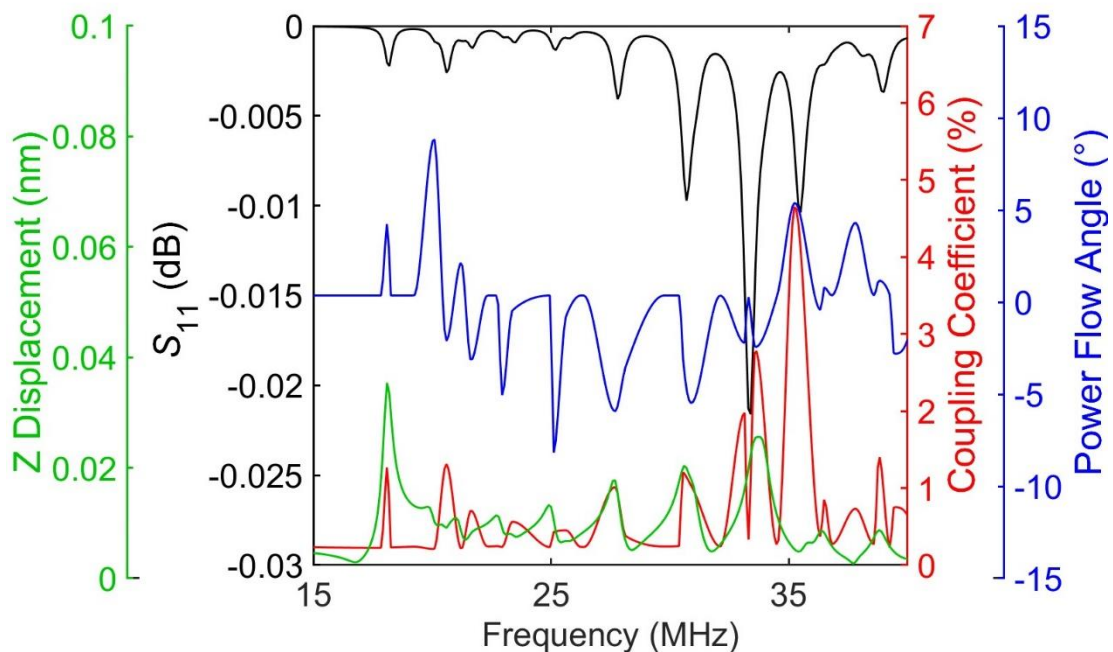


Figure 6.25. Graph of the relationship between various characteristics and frequency at 75° , illustrating the reflection coefficient (black), Z displacement (green), coupling coefficient (red), and power flow angle (blue).

The wave modes and wavefield interactions at the three dominant frequencies ((a) 30.7 MHz, (b) 33.4 MHz, and (c) 35.5 MHz) for 75° X-rotation are shown in Figure 6.26. Figure 6.26(a) and (b) both exhibit similar wave modes, akin to those observed in Figure 6.24(b) at 60° X-rotation, featuring a blend of mode components in various directions. Figure 6.26(c) also presents a combination of mode components but has closer resemblance to Figure 6.24(c), highlighting a more pronounced surface component relative to the bulk component. At these higher frequencies, all wavefields exhibit distortion in the beam profile, indicating interference between the bulk and surface waves. A beam steering can be observed due to the asymmetry, with 30.7 MHz and 33.4 MHz exhibiting similar directions, while 35.5 MHz shows the opposite direction, aligning with the calculated power flow angles. The maximum displacement amplitudes across the wavefield remain relatively consistent for each frequency. However, there is minimal Z displacement at 35.5 MHz, suggesting predominant displacement in alternative directions, as previously discussed. The wavefield droplet interaction displays minimal RMS acoustic velocity for 30.7 MHz when compared to the other frequencies, despite a larger Z displacement (~0.02 nm) and comparable S_{11} minima (-0.01 dB) to 35.5 MHz. Nevertheless, 35.5 MHz exhibits a higher coupling coefficient, and the displacement wavefield indicates that another displacement direction, other than Z displacement, could be valuable for fluid actuation. The acoustic velocity distribution remains consistent at both 33.4 and 35.5 MHz frequencies.

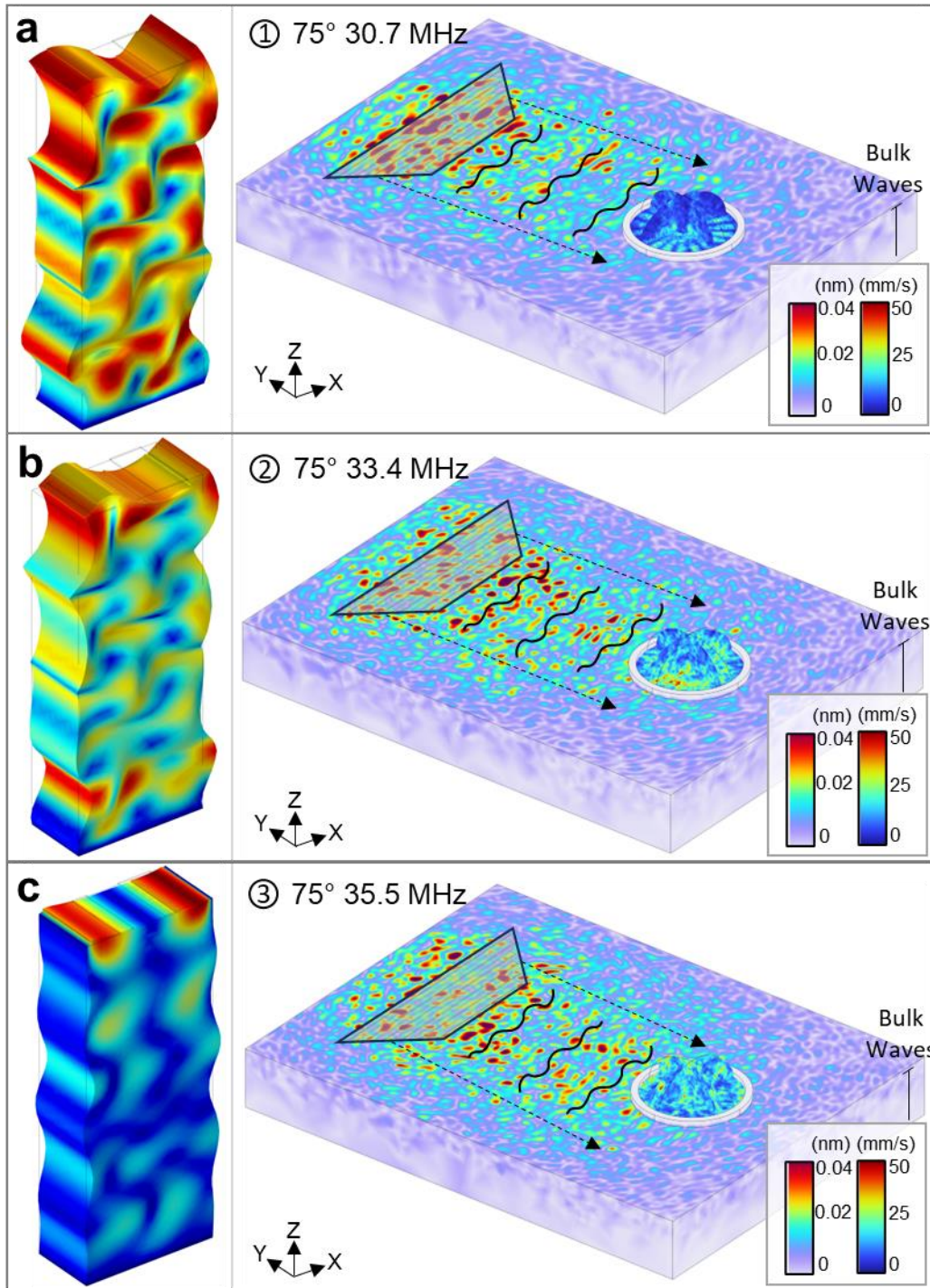


Figure 6.26. Wave mode and wavefield of top 3 simulated S_{11} results at 75° angle with respect to the X-direction where being (a) 30.7 MHz, (b) 33.4 MHz, and (c) 35.5 MHz.

6.3.5.7 90 degrees

Figure 6.27 shows the simulated characteristics at an orientation angle of 90° with respect to the X-rotation. The 90° X-rotation characteristics parallels the 75° X-rotation

observations; however, the frequencies show a slight shift and an increase in magnitude. For example, similar to the observations at 75°, a correlation exists between the S_{11} minima values and the coupling coefficient, albeit with slight variations; the coupling coefficient peaks at 35.4 MHz, while the largest S_{11} minima occurs at 33.4 MHz. The dominant frequencies, 30.3 MHz, 33.4 MHz, and 35.4 MHz, correspond to the same modes as at 75° (mode 11, mode 14, and mode 15, respectively). However, unlike at 75°, the power flow angle at 90° remains relatively constant across frequencies, close to zero, aligning well with theoretical expectations [295]. The Z displacement remains largest for R-SAW at 18.3 MHz (~0.043 nm), with higher frequencies such as 33.4 MHz displaying comparable Z displacement of ~0.034nm, a 20% reduction. Additionally, this Z displacement is only ~40% of R-SAW at 0° X-rotation. Similar to at 75° X-rotation angle, 35.4 MHz has the highest coupling coefficient (5.1%) and moderate S_{11} minima (-0.017 dB), yet minimal Z displacement (~0.01 nm) is observed.

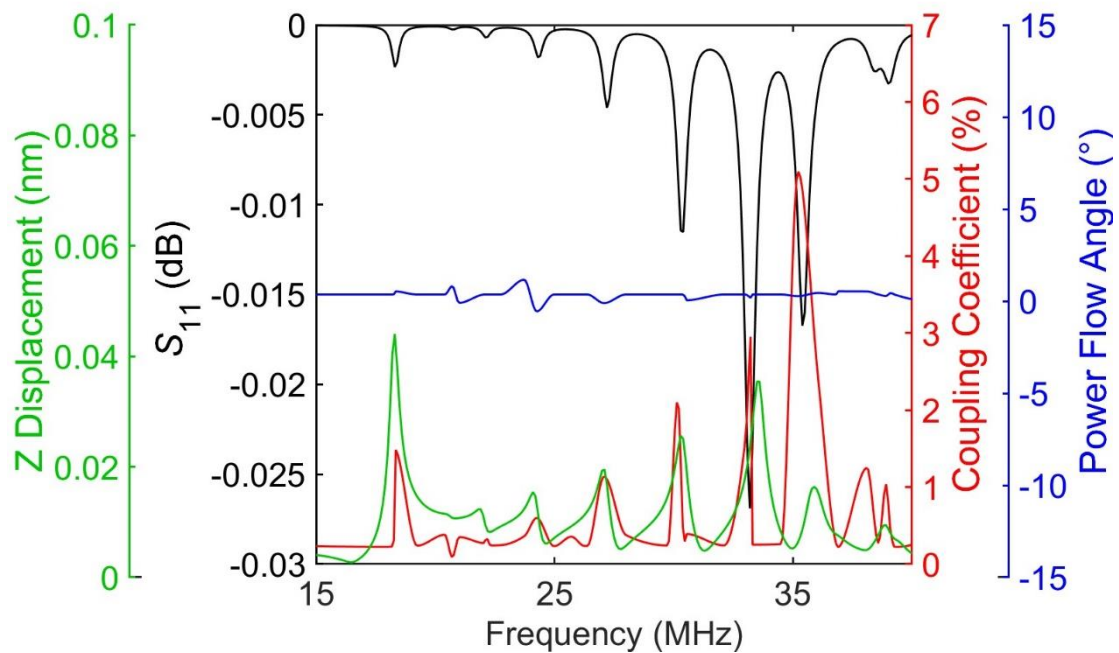


Figure 6.27. Graph of the relationship between various characteristics and frequency at 90°, illustrating the reflection coefficient (black), Z displacement (green), coupling coefficient (red), and power flow angle (blue).

The wave modes and wavefield interactions at the prominent frequencies ((a) 30.7 MHz, (b) 33.4 MHz, and (c) 35.5 MHz) for 90° X-rotation are shown in Figure 6.28.

These wave modes exhibit similarities to those observed at 75° X-rotation, characterised by a blend of mode components in various directions. Moreover, each wavefield displays distortion in the beam profile, consistent with the higher frequency wavefields in previous X-rotation angles. Quantifying the minimal beam steering is problematic due to the distorted nature, however a clear trajectory of maximum displacements is observed predominantly in the centre. The maximum displacement amplitudes across the wavefield remain relatively consistent for each frequency, similar to 75° X-rotation, albeit with larger magnitudes. In terms of the wavefield droplet interaction, a reduction in acoustic velocity is noted at 30.3 MHz compared to 33.4 MHz and 35.3 MHz, like at the 75° X-rotation.

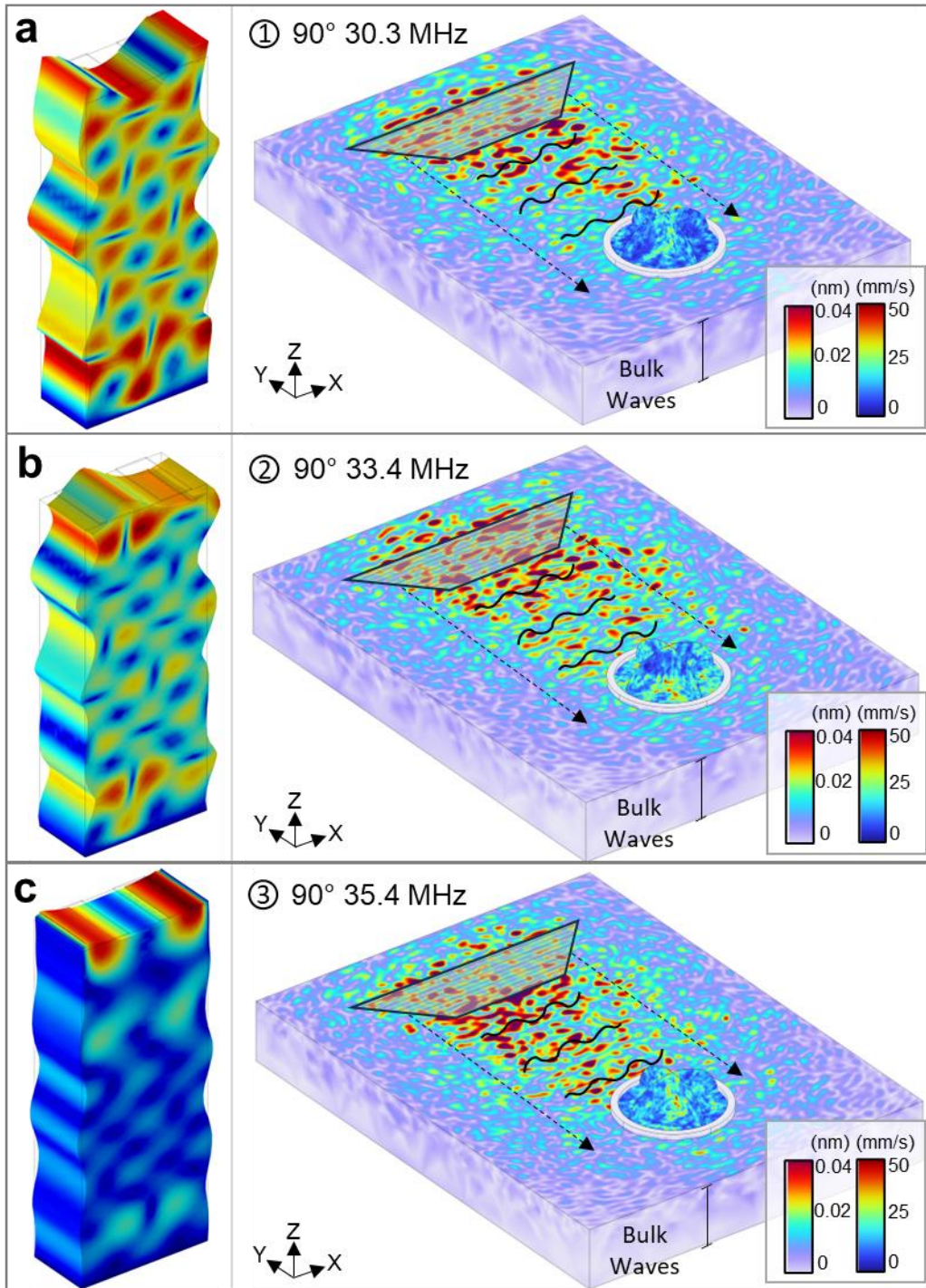


Figure 6.28. Wave mode and wavefield of top 3 simulated S_{11} results at 90° angle with respect to the X-direction where being (a) 30.3 MHz, (b) 33.4 MHz, and (c) 35.4 MHz.

6.3.6 Optimal Wave Modes

In summary, regarding R-SAW, the S_{11} minimum is lower, and the coupling coefficient is higher at 0° than at other angles. IDT arrangements at 15° and 30° still exhibit good

R-SAW performance, but beyond these angles, R-SAW quality diminishes. At 45°, were R-SAW performance alone is poor, a combination of wave modes proves effective. Nevertheless, the beam profile at these frequencies still resembles R-SAW, indicating its primary wave mode component.

At X-rotation angles of 60°, 75°, and 90°, higher frequencies demonstrate good performance. The beam profile distortion at these frequencies suggest excitation of waves interfering with the surface waves [6]. Notably, higher frequencies display more irregularities in the simulated wave modes, likely due to increased crossovers in frequency and needing a smaller mesh size. Improvement in coupling coefficient and power flow calculations could be achieved by reducing the frequency (currently 0.1 MHz) and rotation angle (currently 1 degree) incremental size, however this is at the expense of computational power. Additionally, future research utilizing a laser vibrometer could provide further validation of power flow angles. Nevertheless, at 0° and 90°, the power flow angles are mostly near zero, whereas the angles in between have a greater variation in power flow angle which corresponds well with theory [295]. Interestingly, although the highest coupling coefficient is R-SAW at 0° of ~5.5%, 90° at ~35.2 MHz shows a comparable coupling coefficient of ~5.1%.

The key wave mode shape for each angle and frequency (between 15 to 40 MHz) is shown in Figure 6.29. The black arrows indicate the direction of moment of the different wave types. Figure 6.29 illustrates the distinct surface component and vertical displacement of the R-SAW at X-rotations 0°, 15°, and 30°. However, at 15° and 30°, the vertical displacement deviates due to beam steering. At 45°, the L-SAW illustrates vertical displacement at the surface, also affected by beam steering. Additionally, in the bulk of the substrate, horizontal displacement perpendicular and parallel to the propagation direction is apparent. The optimal wave modes at X-rotations of 60°, 75°, and 90° demonstrate components in the surface and bulk of the substrate. The substrates surface displays vertical and horizontal displacements, indicative of non-pure modes of R-SAW and SH-SAW, respectively. Additionally, an elliptical-shaped displacement occurs in the substrates bulk, involving horizontal motion parallel to the surface (aligned with the propagation direction) and vertical motion perpendicular to the surface. This criss-cross pattern highlights the amalgamation of wave modes.

Typically, pure SH-SAW propagates along a substrate's surface with a displacement perpendicular to the wave's propagation and no vertical displacement [416]. However, when excited, SH-SAW often do not exhibit pure SH-wave behaviour [5]; rather, they typically manifest as a mixture of different wave modes with varying ratios. The observed wave mode resembles SH-SAW wave with horizontal displacement on both the surface and bulk of the substrate. It does not strictly adhere to the criteria for SH-SAW propagation due to the horizontal displacement aligning parallel to the propagation direction, along with the presence of vertical normal displacement. Hence, this mode is termed P-SH-SAW.

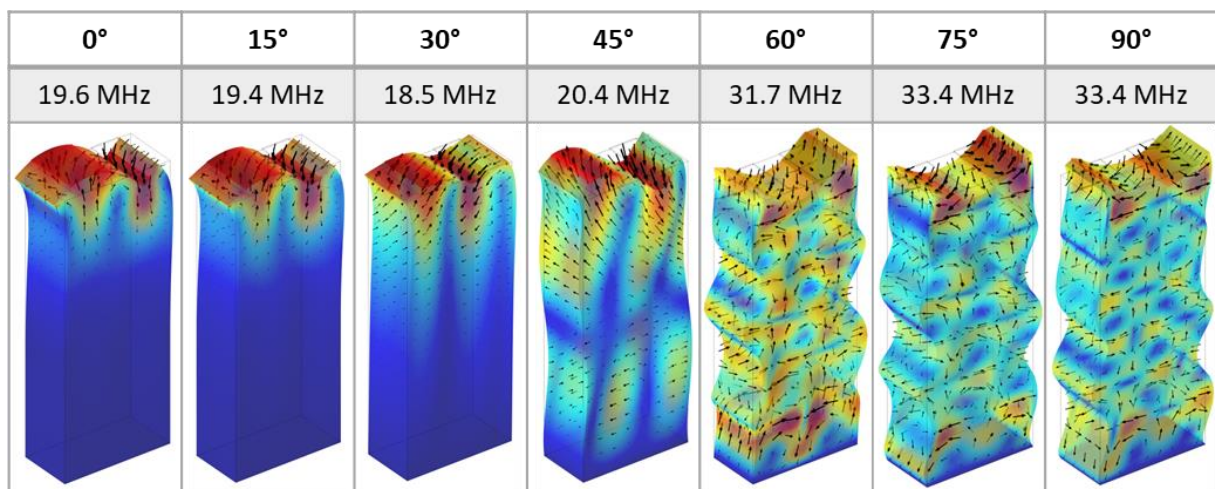


Figure 6.29. Eigenmode shape for the key frequency at each angle (0°, 15°, 30°, 45°, 60°, 75°, 90°). Black arrows demonstrating displacement direction.

To provide further insight into the wave modes, Figure 6.30 displays the (a) X and (b) Y displacement at 0° and 90° X-rotation, observed from a point on the unit models surface relative to the substrate's axis, across various frequencies. When positioned at 0° (X-orientation), the R-SAW exhibits X displacement (~0.06 nm), while at 90° X-rotation (Y-orientation), there is near zero X displacement, relative to the substrate axis. Conversely, the Y displacement is greater for 90° X-rotation at 35.4 MHz (~0.06 nm) and 33.4 MHz (~0.03 nm), compared to the wave modes at 0° (<0.01 nm). The Y displacement during 90° X-rotation at 33.4 MHz is comparable to its corresponding X displacement (~0.03 nm) and 35.4 MHz surpasses their corresponding Z displacement (0.01 nm) demonstrating the SH-SAW component.

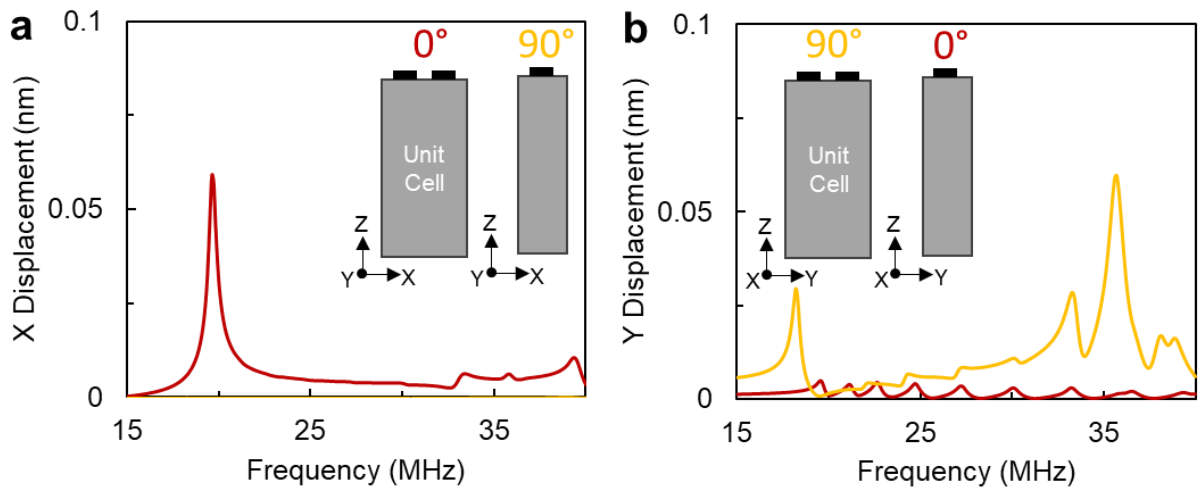


Figure 6.30. Displacement of (a) X and (b) Y at 0° (X-orientation) and 90° X-rotation (Y-orientation), observed from a specific point on the unit models surface with respect to the substrate's axis, across the frequency range of 15 – 40 MHz. The model illustrates the orientations at 0° and 90° X-rotation for clarity on axis directions.

Overall, Figure 6.31 illustrates the optimal wave modes (between 15 to 40 MHz) for the 128° YX-cut LiNbO_3 substrate, with the dominant R-SAW at 0° and P-SH-SAW at 90° . Observations indicate that the R-SAW mode is optimal at X-rotation angles near 0° , while P-SH-SAW is optimal at angles near 90° . The angles in-between is typically a combined mode. These findings present opportunities for investigations using the Hexagonal FPCB IDT at other angles. Leveraging this understanding of wavefields allows for adjustments in wave mode selection without necessitating IDT structure redesign for different applications. For example, if an IDT offset is desired, 30° X-rotation R-SAW could be utilized, offering moderate coupling coefficient ($\sim 2\%$) and a substantial power flow angle ($\sim 12.1^\circ$). Moreover, this numerical analysis technique [413] holds promise for investigating wave modes in other piezoelectric materials or a larger range of frequencies.

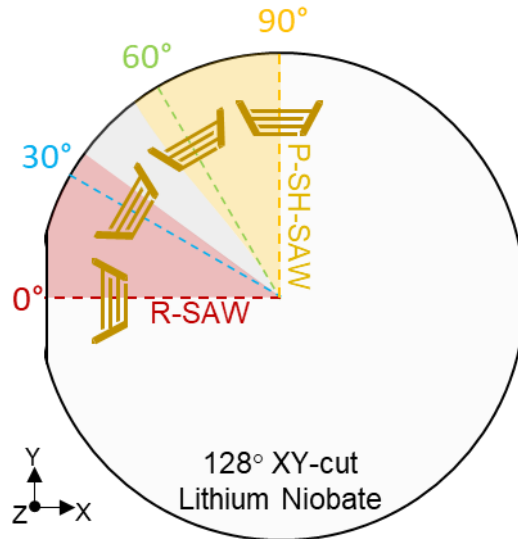


Figure 6.31. Illustration of the key wave modes around the 128° YX-cut LiNbO₃ substrate.

6.3.7 Pseudo-SH-SAW

This section provides an in-depth analysis of P-SH-SAW for fluid actuation. Utilizing the real-scale 2D model with a refined mesh, it offers a comprehensive numerical examination, aimed to elucidate the underlining mechanism governing P-SH-SAW fluidic actuation.

Brodie et al. [9] studied SH-SAW using 36° Y-X LiTaO₃ and found the flow had larger streaming velocities than those of the R-SAW, which corresponds well to the cases shown in Figure 6.28(b), validating the effects due to SH-SAW component. Figure 6.32(a) shows the R-SAW and P-SH-SAW propagating along the length of the substrate demonstrating the SH-wave component of the wave within the bulk as well as the vertical component on the surface. Additionally, it illustrates the unique criss-cross pattern that was observed in the wave mode shape in Figure 6.29. Figure 6.32(b) displays the Z displacement for each mode demonstrating that the R-SAW is almost double in magnitude which validates those shown in Figure 6.27. Furthermore, the observed phenomenon of P-SH-SAW streaming is intriguing given the minimal attenuation of the SH-wave when interacting with the fluid [9]. This unexpected behaviour can be attributed to the reduced Z displacement inherent in SH-SAW, hindering efficient momentum transfer to the fluid. Numerical modelling (Figure 6.27

and Figure 6.32)) demonstrates that the P-SH-SAW component is 40% that of R-SAW, making it unlikely to solely account for the observed streaming velocities [9].

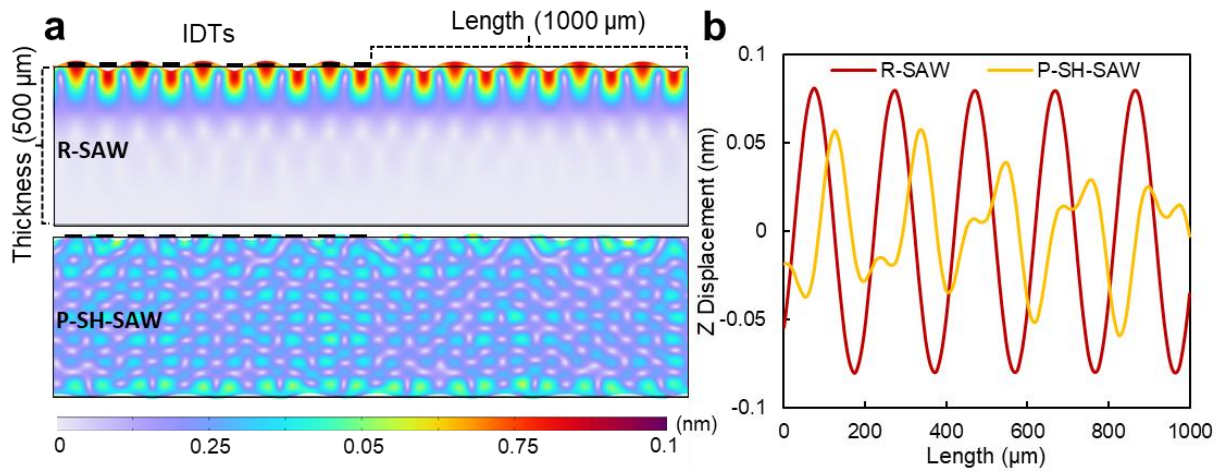


Figure 6.32. Displacement pattern for (a) 2D side view R-SAW displacement (top) and P-SH-SAW (bottom). (b) Z displacement along the length (1000 μm) for both R-SAW (red) and P-SH-SAW (orange).

Brodie et al. [9] propose a mechanism involving the entrapment of a thin visco-elastic fluid layer for shear wave polarised devices, which has a decay length of,

$$\delta = \sqrt{\frac{2\eta_f}{\omega\rho_f}} \quad (6.4)$$

where η_f is the shear viscosity of the fluid and ρ_f is the density of the fluid, and ω is the angular frequency [9,417,418]. The oscillation of this layer generates a small pressure difference relative to the surrounding liquid, attributable to the compression wave formed at the droplet boundary. The resultant oscillation of this boundary pressure generates to acoustic waves.

Figure 6.33 shows the simulated streaming mechanisms for both (a) R-SAW and (b) P-SH-SAW. The top images show the displacement and pressure distribution, and the bottom images show the laminar flow velocity. The scale values are capped for comparison purposes. Figure 6.33(a) demonstrates the R-SAW surface displacement that enters the droplet at the Rayleigh angle ($\theta_R = \sim 22^\circ$). Whereas Figure 6.33(b) confirms the pressure difference at the boundary, giving rise to large boundary laminar

flow velocities at $\theta_{SH} = 90^\circ$. However, the P-SH-SAW also shows vertical cross-section patterns which is not typical for SH-SAW. This demonstrates the vertical displacement from the R-SAW component. Both these wave modes show similar streaming patterns as shown by the white arrows. Notably, the P-SH-SAW has shown a minimal damping effect in the liquid compared to the R-SAW, as the oscillation of the boundary layer plays a pivotal role in the streaming phenomena [9].

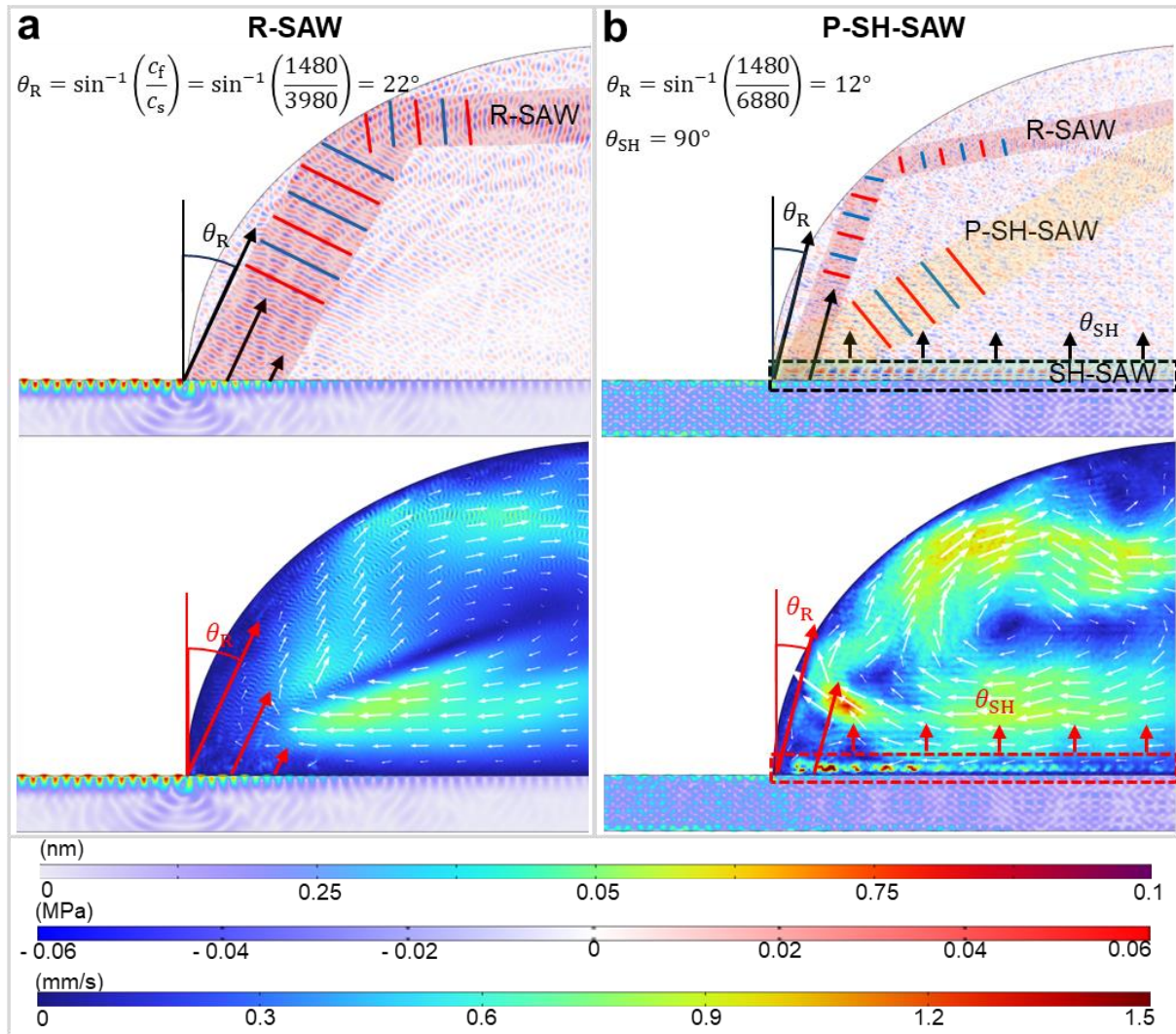


Figure 6.33. 2D side view demonstrating streaming mechanism for (a) R-SAW and (b) P-SH-SAW. The top images show the displacement and pressure distribution. The bottom images show displacement and laminar flow velocity. The white arrows indicate the streaming direction inside the droplet.

7.1 Introduction

This chapter investigates the wave fields and wave modes at various angles using the Hexagonal FPCB IDT. This study contributes to existing literature by examining diverse wave modes and angles, demonstrating their acoustofluidic effects via acoustic streaming. The highly adaptable FPCB IDT setup allows disassembly and rotation, facilitating this investigation. As a result of this thesis, alternative directions for fluid manipulation can be considered, and enhances device optimization by shifting focus from modifying IDT designs to manipulating wave mode selection, thus enhancing tailored acoustofluidic outcomes. Leveraging this knowledge, alternative methods for concentrating micro- and nano- particles are explored.

7.2 Experimental Findings

7.2.1 Device Characterisation

The S_{11} of the Hexagonal FPCB IDT device was measured at IDT-oriented angles of 0° , 15° , 30° , 45° , 60° , 75° , and 90° with respect to the X-direction (Figure 7.1(right)). This involved three configurations, Figure 7.1(a) where the trapezoidal IDT of the Hexagonal FPCB was placed parallel to the reference flat at 0° , and the other five IDTs were positioned at 60° , 120° , 180° , 240° , 300° . Note that due to the symmetry of 128° XY-cut LiNbO₃ the S-parameters for $0^\circ = 180^\circ$ and $60^\circ = 120^\circ = 240^\circ = 300^\circ$. The second configuration (Figure 7.1(b)) was rotated by 15° to realise IDT in positions 15° , 75° , 135° , 195° , 255° , 315° , where $15^\circ = 195^\circ$, $75^\circ = 255^\circ$, and $45^\circ = 135^\circ = 315^\circ$. Lastly, Figure 7.1(c) was rotated by 30° to realise IDT in positions 30° , 90° , 150° , 210° , 270° , 330° , where $90^\circ = 270^\circ$ and $30^\circ = 150^\circ = 210^\circ = 330^\circ$. This device allows further study of different wave modes in opposite directions or a combination of different wave modes simultaneously.

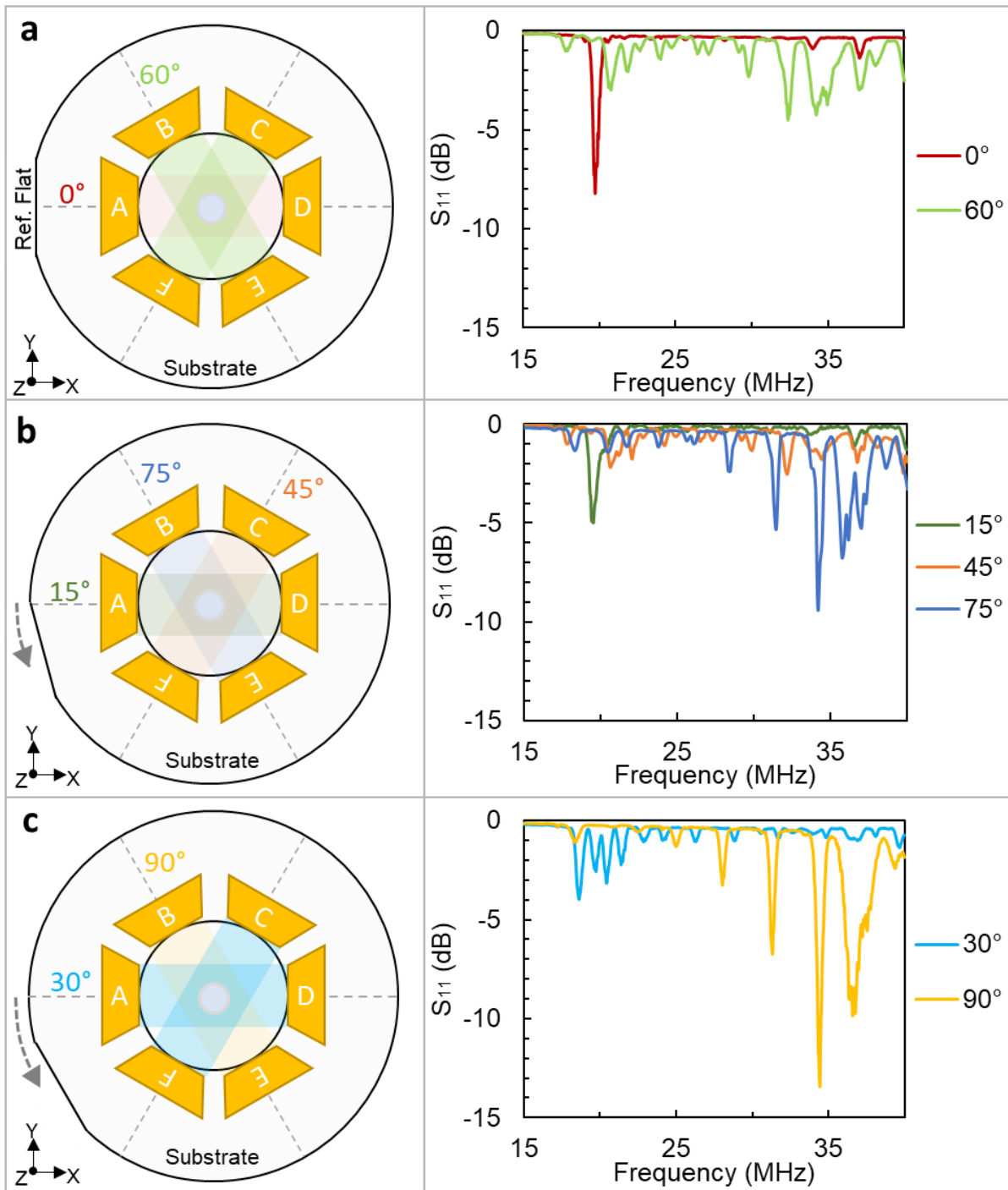


Figure 7.1. Three configurations (left) of the Hexagonal FPCB IDTs for experimental verification and the corresponding S_{11} values (right) for angles (a) 0° and 60° , (b) 15° , 45° , and 75° (c) 30° and 90° .

7.2.1.1 Simulations vs Experiments

The experimental S_{11} results were found to correlate well with the simulated values. The largest S_{11} minima were at an angle of 90° , followed by the R-SAW at 0° . Figure

7.2 illustrates the comparison between experimental and simulated results for 0° and 90° X-rotation. However, the simulated data indicate a slight frequency shift decrease. Interestingly, Mikhaylov *et al.* also observed this shift in frequency when comparing cleanroom IDT S_{11} with PCB-IDT [15]. Therefore, this difference is likely attributed to factors like unaccounted coupling effects in simulations, such as substrate surface imperfections or fabrication discrepancies in the FPCB SAW device.

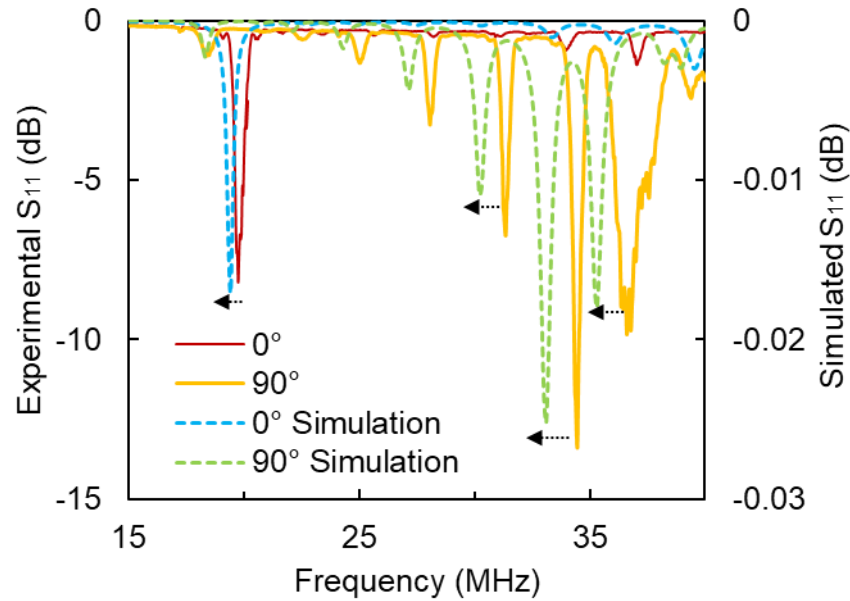


Figure 7.2. Comparison of experimental and simulated S_{11} results for 0° and 90°.

Compared to cleanroom made SAW devices, the Hexagonal FPCB IDT depends on the clamping efficiency. The clamping could be affected by the imperfections within the surface of the substrate or the IDT. To simulate and mimic these imperfections, a substantial 0.5 μm air gap was introduced in the unit cell simulation. This size was selected to maintain mesh size and minimize simulation time, although in reality, such gaps would likely be more irregular and smaller than 0.5 μm . Figure 7.3 shows the simulated S_{11} results with an air gap between the substrate and the electrode for various X-rotation angles. Interestingly, with a 0.5 μm air gap, the frequencies of the wave modes also experienced shifts, aligning closely with the experimental results. However, there was an approximate 70% decrease in S_{11} minima compared to the simulation without an air gap, suggesting that the FPCB could compromise the SAW performance.

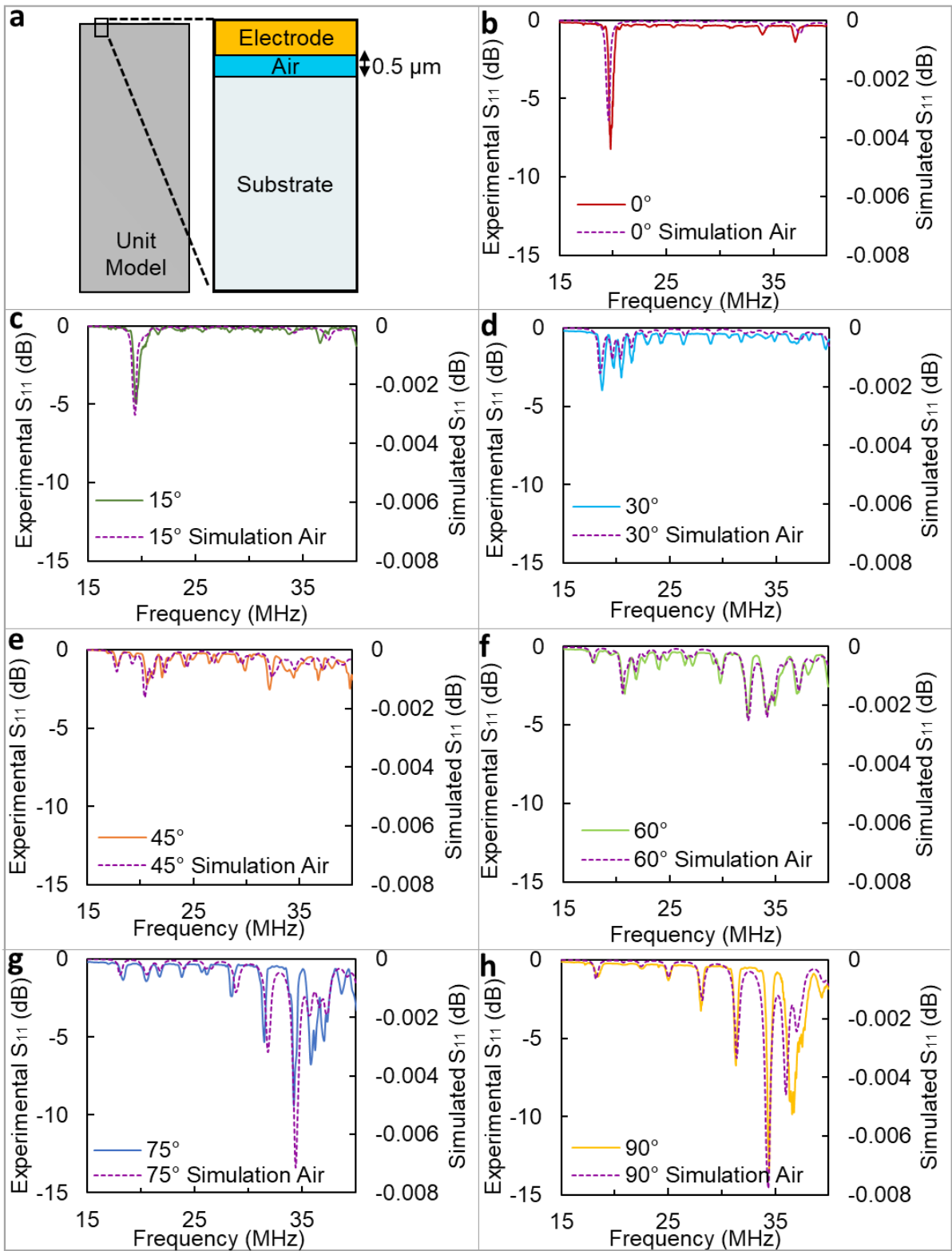


Figure 7.3. Comparison of experimental and simulated S_{11} results across different X-rotation angles with an air gap. (a) Schematic of unit cell model featuring the 0.5 μm air gap. S_{11} results at (b) 0°, (c) 15°, (d) 30°, (e) 45°, (f) 60°, (g) 75°, and (h) 90°.

7.2.1.2 FPCB Viability

Our team has conducted numerous studies to characterise the performance of the PCB and FPCB IDT device, as referenced in [14,15,419]. In Figure 7.4 Mikhaylov *et al.* concluded that increasing the clamping force on a rigid PCB-IDT resulted in higher S_{11} minima for R-SAW. However, this also led to a decrease in droplet velocity at a higher clamping, possibly due to over-compression of the device [15]. These findings underscore the significant impact of clamping efficiency on fluidic actuation.

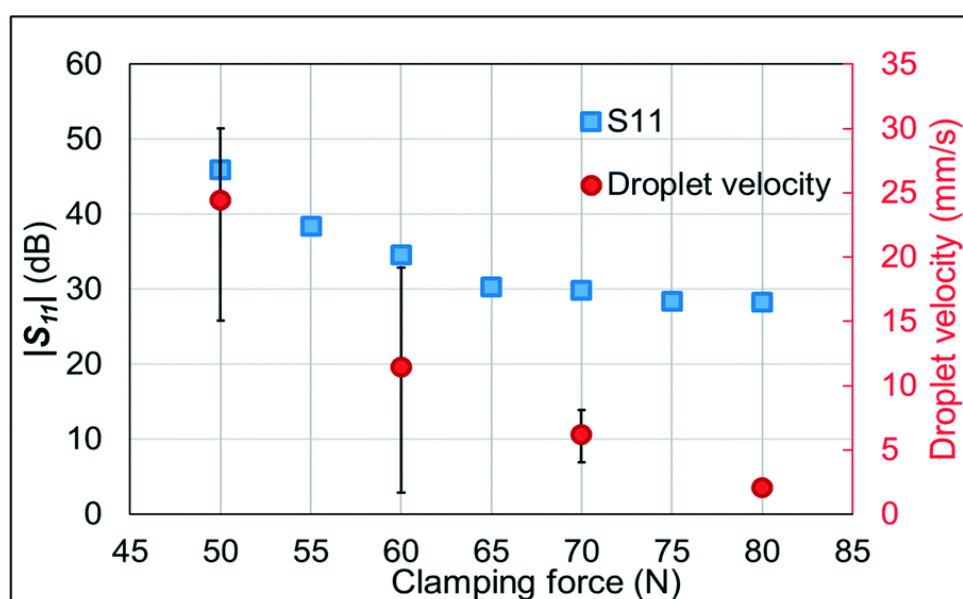


Figure 7.4. Relationship between the clamping force, S_{11} and the droplet velocity on the rigid PCB-IDT [15]. [Reprinted from ‘Development and characterisation of acoustofluidic devices using detachable electrodes made from PCB’ by Mikhaylov *et al.*, Lab on a Chip, Volume 20, Issue 10, 2021, DOI: 10.1088/1361-6439/ac0515. Copyright The Royal Society of Chemistry.]

Mikhaylov *et al.* also compared the performance of the PCB-IDT device with the cleanroom IDT (CR-IDT) by actuating droplets across different input powers [15]. These findings revealed that the PCB-IDT exhibited lower efficiency in converting input power to SAW, attributed to imperfect signal coupling due to the mechanical clamping [15]. As shown in Figure 7.5, the CR-IDT achieved a droplet velocity of 20 mm/s at 0.6 W, a performance level attained at approximately 1.2 W with the PCB-IDT device. Consequently, the observed decrease in with the air gap (Section 6.3.1.1) is justifiable.

Nevertheless, even with this decline, the device remains viable and can be effectively compensated by increasing the input power.

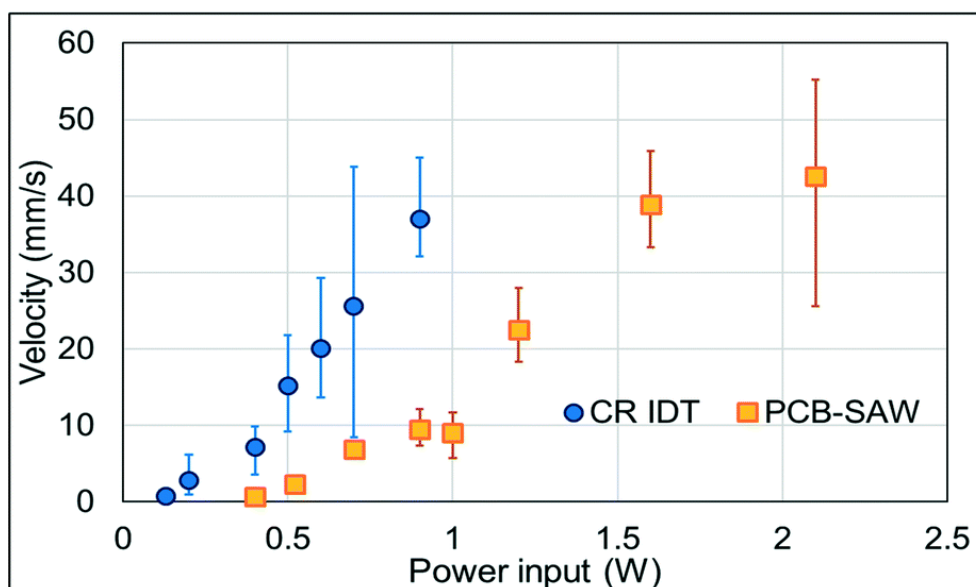


Figure 7.5. Comparison between the droplet velocities, which are driven by different input powers in the PCB-SAW device and CR-IDT [15]. [Reprinted from ‘Development and characterisation of acoustofluidic devices using detachable electrodes made from PCB’ by Mikhaylov *et al.*, Lab on a Chip, Volume 20, Issue 10, 2021, DOI: 10.1088/1361-6439/ac0515. Copyright The Royal Society of Chemistry.]

Compared to the PCB-IDT device, the FPCB-IDT, being a thin-film material, can be easily pressed by the silicone pad to compensate for any surface roughness, ensuring improved surface contact between the finger electrodes and the LiNbO₃ substrate [419]. Unlike the rigid PCB-IDT, the FPCB-IDT does not require evenly distributed pressure for effective electrical conductivity [419]. By mitigating these factors using the unique structure and dynamic flexing, Sun *et al.* found that the FPCB-IDT achieves a minimum S_{11} of -47.12 dB (with a matching network), comparable to conventional CR-IDTs [419].

Moreover, Sun *et al.* also observed that the relationship between minimum S_{11} and R-SAW frequency varies with clamping force, shown in Figure 7.6 [419]. Initially, tightening screws increases clamping force and reduces the S_{11} until around 133 N, where optimal contact is reached [419]. Further force increase deforms the FPCB, worsening the S_{11} . Hence, there is an optimal clamping force for minimal S_{11} for SAW

operation, suggesting monitoring the S_{11} on the VNWA to inform completion of screw fastening [419].

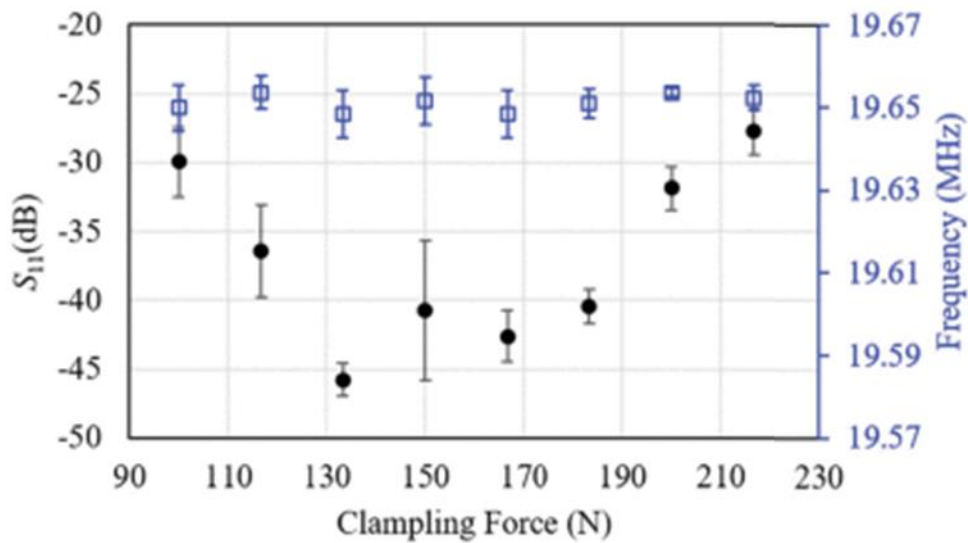


Figure 7.6. Relationship between the clamping force, S_{11} and R-SAW frequency on the FPCB-IDT [419]. [© 2021 IEEE. Reprinted, with permission, from Sun *et al.*, "Flexible Printed Circuit Board as Novel Electrodes for Acoustofluidic Devices," IEEE Transactions on Electron Devices, vol. 68, no. 1, pp. 393, January 2021.]

Additionally, Sun *et al.* demonstrated that the droplet pumping velocity using an FPCB-IDT device exceeds that of a rigid PCB-IDT (Figure 7.7) [419], likely due to superior mechanical contact between the FPCB and the substrate.

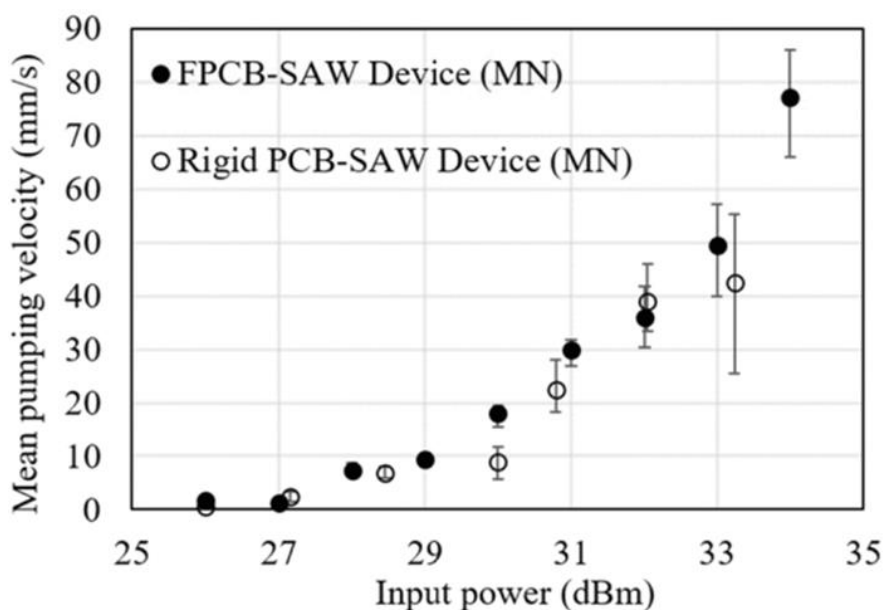


Figure 7.7. Comparison of the pumping velocity of a droplet between the FPCB-IDT and the rigid PCB-IDT device at different input powers (using matching networks) [419]. © 2021 IEEE. Reprinted with permission from Sun *et al.*, "Flexible Printed Circuit Board as Novel Electrodes for Acoustofluidic Devices,". IEEE Transactions on Electron Devices, vol. 68, no. 1, pp. 393, 2021.

7.2.1.3 Repeatability

Compared to cleanroom made SAW devices, the FPCB IDTs needs to be manually positioned and aligned when reconfiguring. Previous work has demonstrated that FPCB-IDT offers good reproducibility and small inter-device variability. For instance, Sun *et al.* show the assembly repeatability with respect to the R-SAW frequency and minimum S_{11} is shown in Figure 7.8 [419]. Each IDT was assembled at the optimal clamping force read by the S_{11} . Both variations in the R-SAW frequency with and without the matching network are within 0.03 MHz, with the average frequencies of 19.63 and 19.75 MHz, respectively. The variations in the minimum S_{11} value with and without the matching network are $-6.79 \text{ dB} \pm 1.06 \text{ dB}$ and $-45.49 \text{ dB} \pm 6.20 \text{ dB}$, respectively [419].

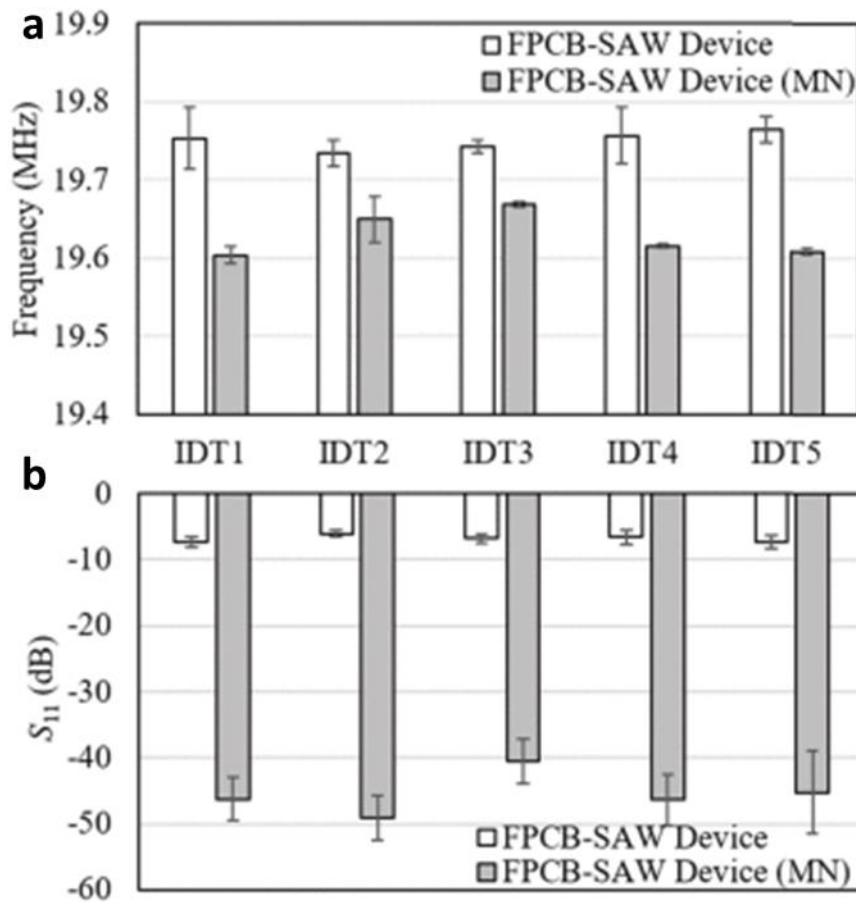


Figure 7.8. The reproducibility in the (a) R-SAW mode frequency and (b) the minimum S_{11} of the reassembly of a FPCB-IDT device with and without the matching network [419]. [© 2021 IEEE. Reprinted with permission from Sun *et al.*, "Flexible Printed Circuit Board as Novel Electrodes for Acoustofluidic Devices," IEEE Transactions on Electron Devices. vol. 68, no. 1, pp. 393, 2021.]

Moreover, our previous work with a reconfigurable FPCB IDT device has shown that the VNWA can be used to measure and monitor the positioning and alignment when reconfiguring the device [14]. This is demonstrated by connecting two FPCB IDTs to the VNWA as a two-port network, as shown in Figure 7.9 [14]. The test keeps one of the IDTs held, as the receiving IDT, while rotating the other IDT, as the transmitting IDT. The S_{11} of the transmitting IDT is measured to monitor how it changes with rotation.

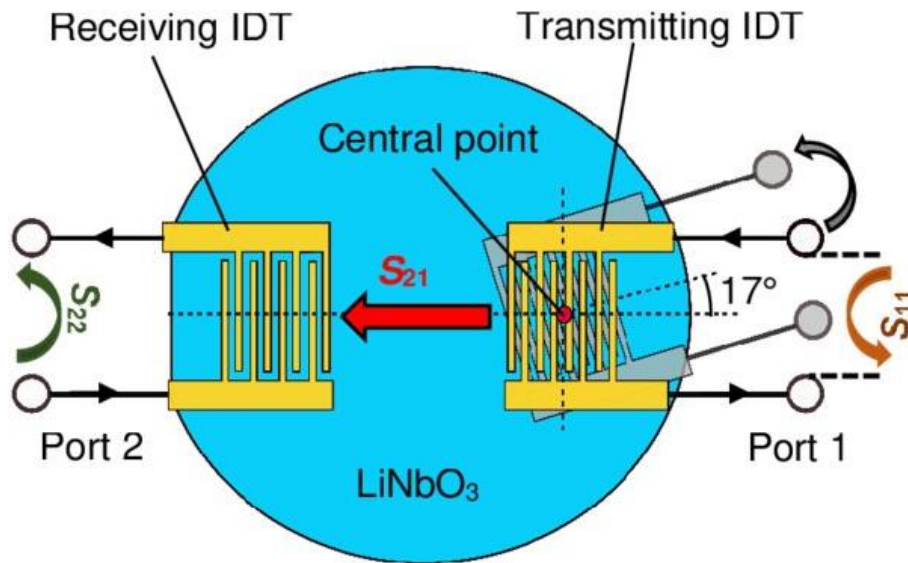


Figure 7.9. FPCB IDT rotation test for investigating the use of the VNWA to register the alignment of the IDTs. The transmitting IDT being rotated around its central point, while the receiving IDT is held fixed. [14]. [Reprinted from 'A reconfigurable and portable acoustofluidic system based on flexible printed circuit board for the manipulation of microspheres' by Mikhaylov *et al.*, Journal of Micromechanics and Microengineering, Volume 31, Number 7, 2021, DOI: 10.1088/1361-6439/ac0515. This figure is licensed under a Creative Commons Attribution 4.0 International License.]

Figure 7.10(a). shows the S_{11} minima when the FPCB is misaligned at different rotations, demonstrating the largest dip is when the FPCB is placed with 0° rotation [14]. The S_{21} peak can be used to establish the angle of the IDTs, when the IDTs are parallel (0° angle) the maximum S_{21} peak is achieved as shown in Figure 7.10(b) [14]. This demonstrates that the VNWA can be used when reconfiguring the device to achieve repeatability.

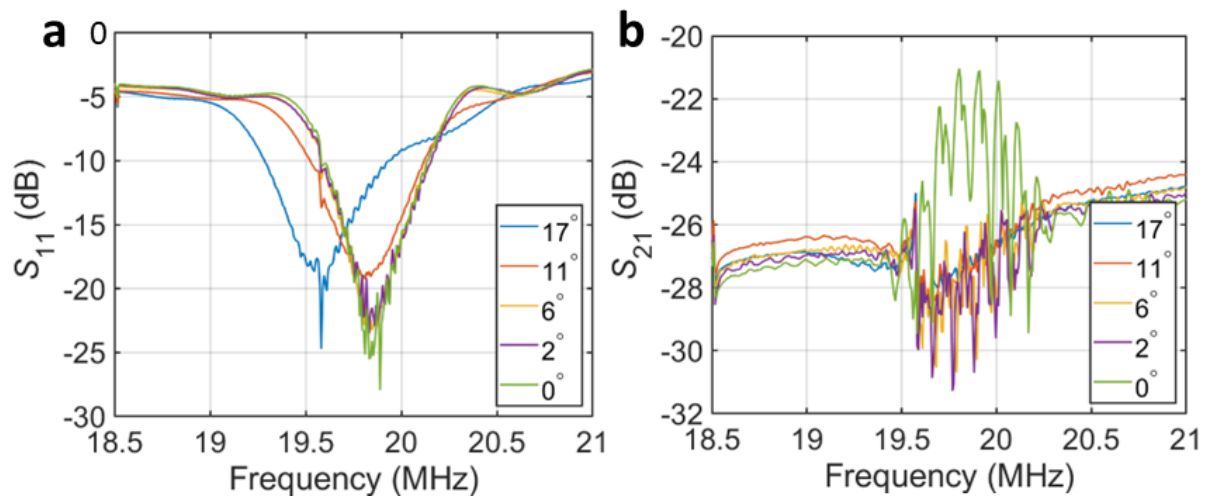


Figure 7.10. FPCB IDT device S-parameter results for different rotation angles of the IDT where (a) S_{11} (b) S_{21} [14]. [Reprinted from ‘A reconfigurable and portable acoustofluidic system based on flexible printed circuit board for the manipulation of microspheres’ by Mikhaylov *et al.*, Journal of Micromechanics and Microengineering, Volume 31, Number 7, 2021, DOI: 10.1088/1361-6439/ac0515. This figure is licensed under a Creative Commons Attribution 4.0 International License.]

The Hexagonal FPCB IDT incorporated several enhancements for improved repeatability. As described in Chapter 4, this includes an aluminium holder with a recessed circular section to securely position the substrate, a paper template for precise rotation, and a securely screwed holder to maintain stability. The VNWA was also used verify proper screw tightening and positioning. Figure 7.11 displays the S_{11} of the six IDTs for a specific configuration ((a) 0° and (b) 60°), demonstrating minimal inter-device variability, and thereby ensuring consistent performance.

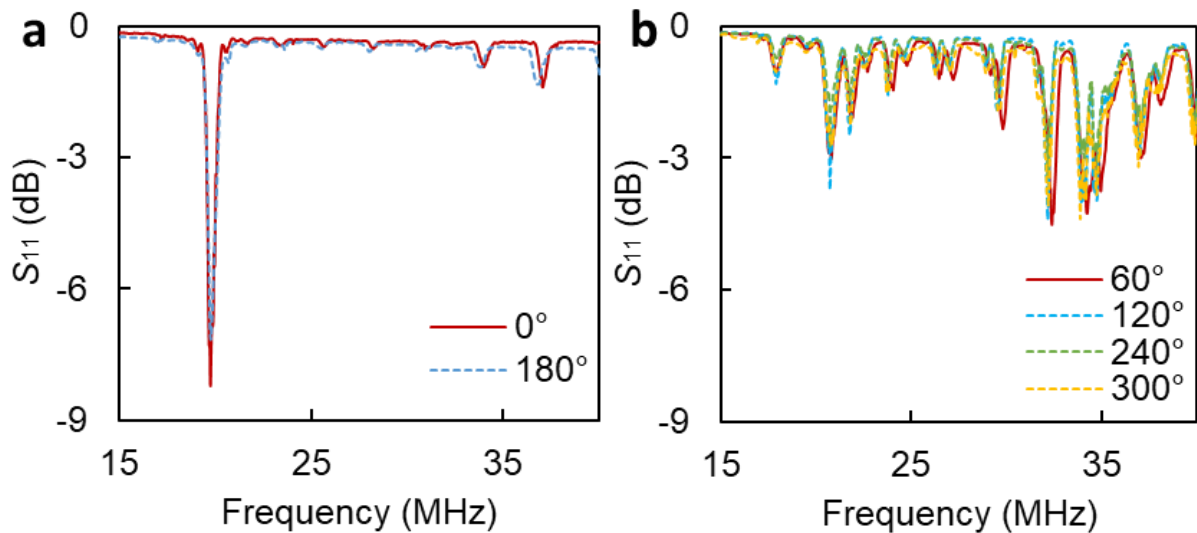


Figure 7.11. S_{11} minima for a specific configuration (0° and 60°) of the Hexagonal FPCB IDT showcasing inter-device variability where (a) $0^\circ = 180^\circ$, (b) $60^\circ = 120^\circ = 240^\circ = 300^\circ$.

7.2.2 Acoustic Streaming Velocities

The Hexagonal FPCB IDT was utilized for conducting fluid actuation tests frequencies corresponding to the three most prominent S_{11} minima, across different X-rotation angles (0° , 15° , 30° , 45° , 60° , 75° , and 90°). Figure 7.12 reveals the average area streaming velocities measured during these tests, displayed for each configuration, for clarity. Specifically, Figure 7.12(a), (b) and (c) present the velocities at 0° and 60° , 15° , 45° and 75° , as well as 30° and 90° . The absolute S_{11} values for each angle are shaded in the corresponding colour, demonstrating the significant correlation of velocities with the measured S_{11} minima.

Notably, at 90° rotation, each frequency (31.3 MHz, 34.4 MHz, and 36.6 MHz) achieved comparable average area velocities (~ 1.19 mm/s, 1.58 mm/s, and 1.33 mm/s, respectively) to that of R-SAW at 0° 19.8 MHz (~ 1.35 mm/s). It is probable that those 3 frequencies at 90° rotation have R-SAW and SH-SAW components. Among the 90° wave modes, the 34.4 MHz had the highest acoustic streaming, which correlates with its larger Z displacement of ~ 0.034 nm (compared to other Z displacements at 90°) and a lower S_{11} of -13.4 dB. At 90° 31.3 MHz, the Z displacement measured ~ 0.02 nm, higher than the 0.01 nm at 90° 36.6 MHz, yet the latter offered a higher S_{11} of -9.8 dB compared to -6.7 dB. The reflection coefficient signifies how much

of the input power reflected to the input port of the device; therefore, the 90° 36.6 MHz frequency proved more efficient than 31.3 MHz, which explained its superior average acoustic streaming velocity. At P-SH-SAW 34.4 MHz, the average area velocity magnitude was increased by ~15% compared to 0° R-SAW. Despite the lesser Z displacement (0.034 nm) of P-SH-SAW 34.4 MHz compared to 0° R-SAW (0.09 nm), the former had a larger S_{11} minima of -13.4 dB compared to -8.2 dB. Nonetheless, both R-SAW at 0° and SH-SAW at 90° demonstrated notably higher streaming velocities compared to other angles and frequencies.

The average area velocities at 30° rotation were measured at 1.04 mm/s and 1.03 mm/s for frequencies 18.6 MHz and 20.5 MHz, respectively. Notably, although slower than the velocities observed at 0° R-SAW, they outperformed other R-SAW velocities for 15° rotation at 19.5 MHz (0.57 mm/s). This finding is unexpected considering R-SAW at 15° exhibited larger S_{11} minima, coupling coefficient and Z displacement compared to 30° R-SAW. It is worth noting that the measurements did not show significant error bars, however, were based on three repeats rather than the usual six. At a 45° rotation angle, the highest average area velocity recorded was 0.62 mm/s at 20.6 MHz, slightly lower than the streaming observed for the 60° P-SH-SAW, which was ~0.72 mm/s (32.3 MHz) and 0.69 mm/s (34.2 MHz). The decline in 60° P-SH-SAW average area acoustic streaming velocity, compared to 90° P-SH-SAW at 34.4 MHz, was corresponding with the reduced Z displacement (~0.014 nm for both) and S_{11} values (4.5 dB and 4 dB). Despite equivalent Z displacement with 90° 36.6 MHz, the latter had significantly greater S_{11} minima (~40%) and ~30% greater average area acoustic streaming velocity. Similar results to those of the 90° rotation were observed at 75° rotation, where 34.2 MHz demonstrated an average area velocity of 1.54 mm/s. Notably, at 31.5 MHz and 35.8 MHz 75° rotation, the average area velocities were lower at 0.79 mm/s and 0.72 mm/s, respectively. However, the presence of large error bars indicates instability.

All angles still offer viable acoustic streaming velocities for acoustofluidic applications. However, the frequency should be adjusted to obtain optimal acoustic streaming velocities. This highlights the potential of employing alternative angles using different wave modes for acoustofluidic applications, with the measured S_{11} minima serving as useful guidelines for utilizing other harmonics. Overall, P-SH-SAW emerges as a

valuable tool for actuation in acoustofluidics, facilitating opportunities for simultaneous sensing and actuation.

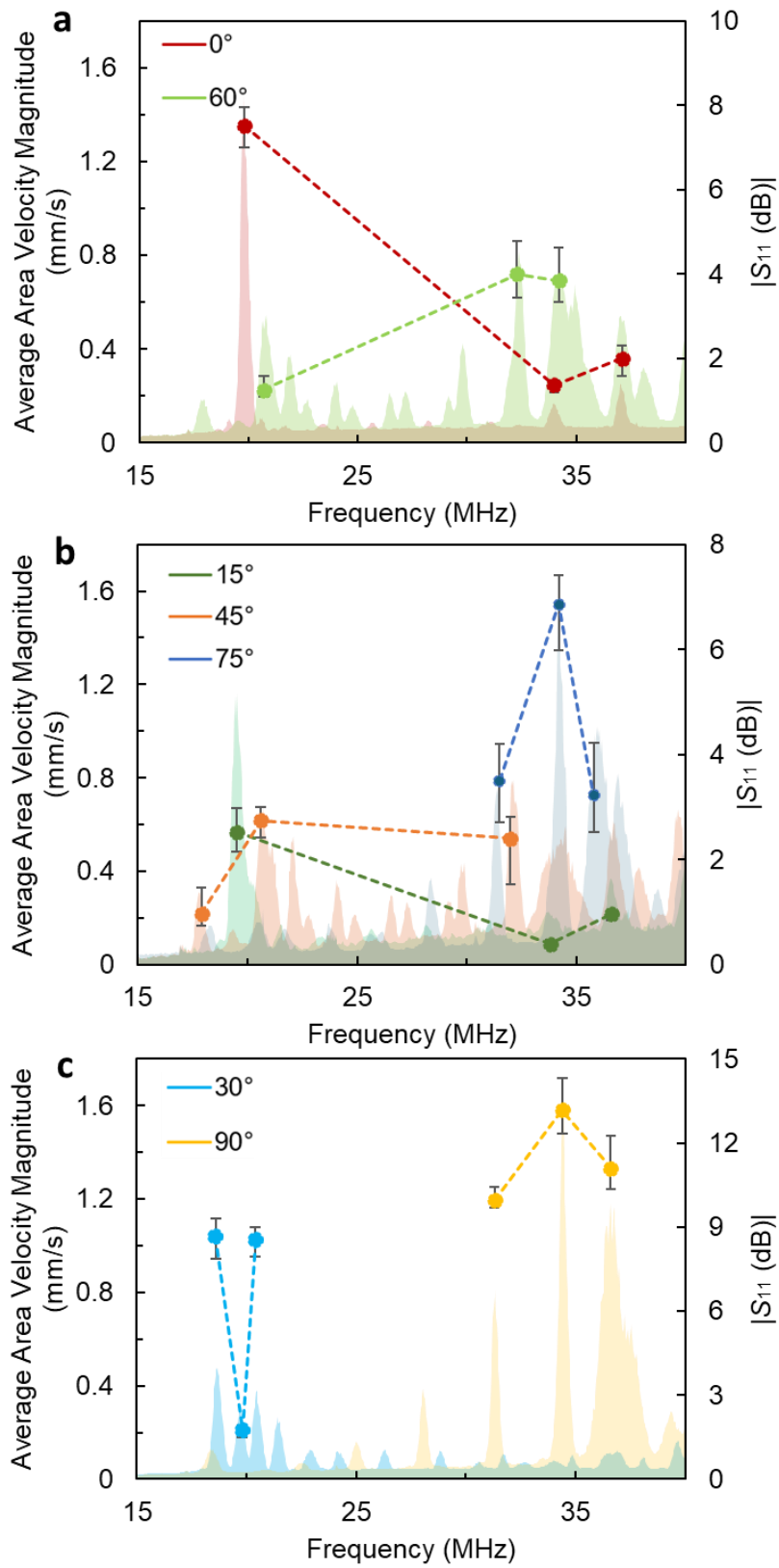


Figure 7.12. Measured average area velocity magnitude for the largest three S_{11} minima frequencies for each configuration. (a) 0° and 60° ($n = 6$), (a) 15° , 45° and 75° ($n = 3$), (c) 30° and 90° ($n = 6$). The absolute S_{11} of the corresponding angle is shown shaded in the same colour.

7.2.3 Acoustic Streaming Patterns

In Figure 7.13, distinct streaming patterns were found for each angle: 0° at 19.8 MHz, 15° at 19.5 MHz, 30° at 18.6 MHz, 45° at 20.6 MHz, 60° at 32.2 MHz, 75° at 34.2 MHz, and 90° at 34.4 MHz. Variations in these streaming patterns may be originated from differences in power flow angles. At 0° and 90° , where the power flow angle is 0° , a butterfly-shape streaming pattern occurs with the wave propagating through the centre. Notably, the R-SAW double vortex exhibits stagnant regions near the IDT actuation, with the highest acoustic streaming velocity in the centre of the droplet where the wave is propagating through. Whereas the P-SH-SAW's double vortex has stagnant regions further from the IDT, with highest acoustic streaming at the droplet's boundary, likely due to reduced damping. This pattern holds true for the 15° and 30° R-SAW as well as 60° and 90° P-SH-SAW configurations. Additionally, at R-SAW at 15° and 30° , with power flow angles of approximately -6.6° and -12.1° respectively, one vortex appears larger than the other, possibly due to an offset in the propagating wave. At 20.6 MHz 45° , the leaky SAW wave mode is employed, showcasing patterns akin to R-SAW. A double vortex pattern emerges, likely attributed to the low beam steering (-0.8°). Both 60° and 75° P-SH-SAW show a similar vortex pattern, with power flow angles of approximately -2.2° and -2.9° , respectively. Nevertheless, the P-SH-SAW angles appears to have larger vortex patterns than that for the R-SAW angles, even with smaller power flow angles. This result may arise from inconsistent or inaccurate positioning of the IDT/PDMS ring, as even a minor milli-metre scale alteration could significantly impact the result. It is important to acknowledge that various other factors might also affect the streaming patterns. Further validation of power flow angles could be achieved through future research employing a laser vibrometer.

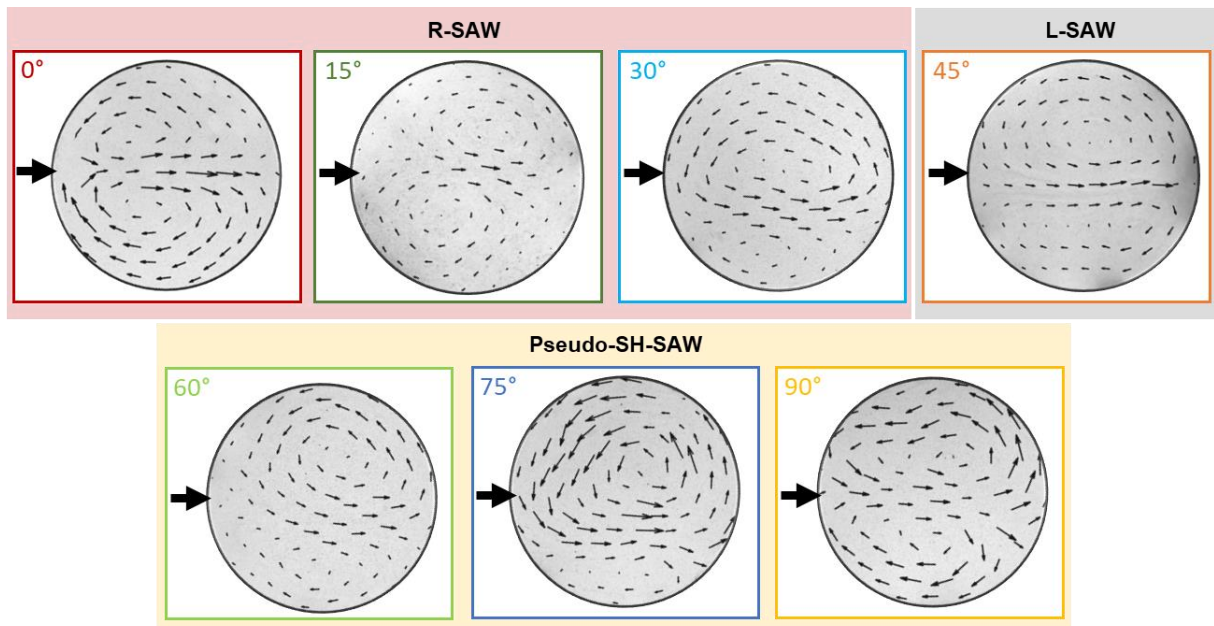


Figure 7.13. Corresponding streaming patterns for optimal frequencies / wave modes (0° at 19.8 MHz, 15° at 19.5 MHz, 30° at 18.6 MHz, 45° at 20.6 MHz, 60° at 32.2 MHz, 75° at 34.2 MHz, and 90° at 34.4 MHz.). The 100 μl fluid (50:50, water: glycerol) within a PDMS ring was actuated at 30 dBm (1 W).

7.2.4 Damping Effects

Further exploration was undertaken to delve into the damping phenomena within the fluid medium. It is well-established that SH-SAW experiences significantly less attenuation when penetrating the liquid compared to R-SAW [9]. However, there is evidence suggesting that some attenuation does occur due to both in-plane, normal and parallel to surface components [420]. In Figure 7.14(a), the average area velocity magnitude of R-SAW and P-SH-SAW fluid actuation at 20 dBm (0.1W) is shown across different viscosity ratios of water and glycerol. The results reveal that at lower viscosities, P-SH-SAW exhibits average area viscosity values exceeding those of R-SAW by over 50%. The P-SH-SAW component demonstrates a velocity magnitude reduction of 55% with increasing viscosity, while R-SAW experiences a reduction of 42%. These findings show that the damping effect exists with the P-SH-SAW component when increasing the viscosity. This phenomenon is likely attributable to the high viscosity impacting the R-SAW component (Z displacement) of the P-SH-SAW. Nevertheless, the SH-SAW component continues to contribute effective

boundary layer streaming. This underscores the potential of utilizing P-SH-SAW for applications involving highly viscous samples, such as blood.

Additionally, Figure 7.14(b) shows the average area velocity at varying powers while maintaining a viscosity ratio of 60:40 (water: glycerol). Both wave modes display a consistent linear increase in average area velocity magnitude, with P-SH-SAW consistently outperforming R-SAW by 50%. This shows that P-SH-SAW can achieve equivalent acoustic streaming with reduced power consumption, making it advantageous for low-power applications.

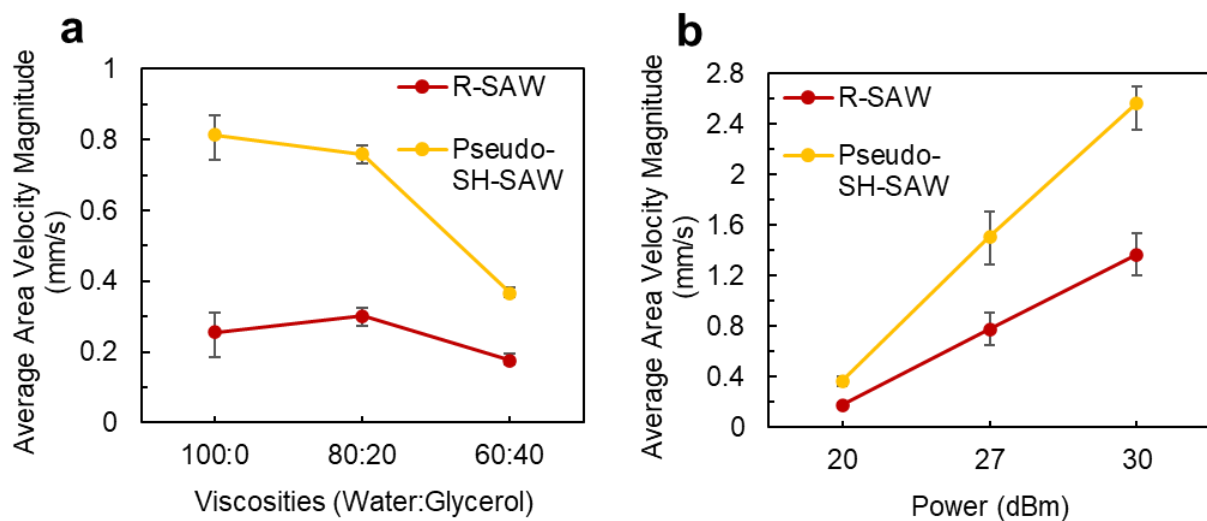


Figure 7.14. Average area velocity magnitude for 0° R-SAW and 90° P-SH-SAW for different (a) viscosity fluids (water: glycerol ratio) (b) IDT power (20 dBm (0.1W), 27 dBm (0.5W), and 30 dBm (1 W))

Despite the influence of viscosity on P-SH-SAW, macro-streaming is demonstrated within a 1 ml fluid volume PDMS ring. Figure 7.15 captures the initial frame ($t=0$), where particles are pipetted into the fluid for visualisation purposes. Within just two seconds, P-SH-SAW propagates through the entire 1 ml sample (25mm diameter), leaving a distinct clear central line. In contrast, within the same timeframe, R-SAW induces only minimal fluid movement. Since the boundary layer oscillation is also responsible for the P-SH-SAW streaming, less damping would be expected. This indicates that P-SH-SAW can generate acoustic streaming in sample sizes that are more clinically relevant.

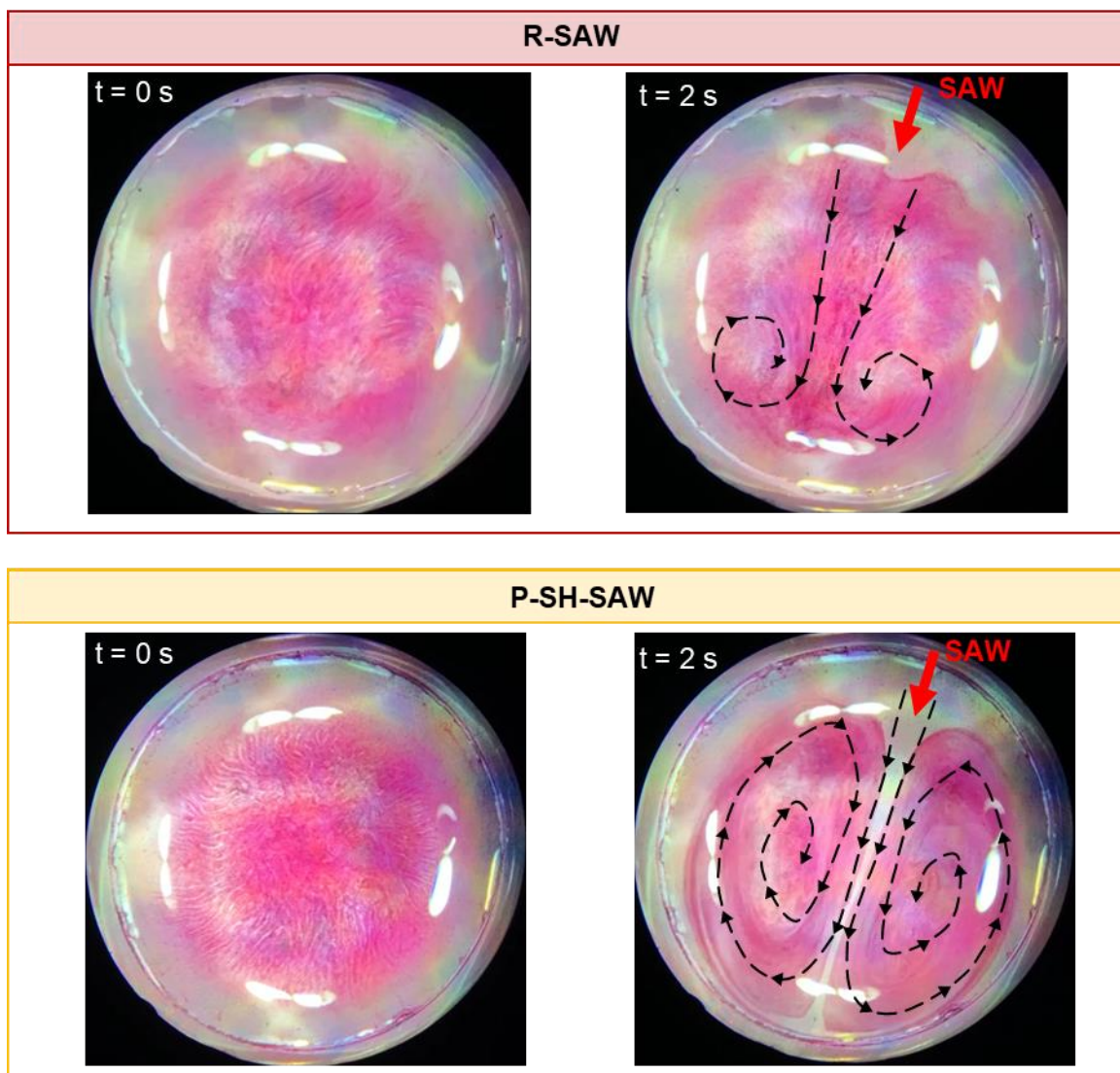


Figure 7.15. Macro-streaming using 0° R-SAW and 90° P-SH-SAW for a 1 ml fluid volume (PDMS ring diameter 25 mm) showing at $t = 0$ and $t = 2$ seconds.

The P-SH-SAW wave mode, characterized by its minimal wave damping as illustrated in Figure 7.14 and Figure 7.15, was applied to a single 96-well culture plate coupled with a droplet of glycerol (Figure 7.16(a)). The ability to use a culture plate for SAW applications offers significant advantages over direct application on the piezoelectric substrate. Culture plates provide standardization, scalability, and biocompatibility, fitting seamlessly into existing laboratory workflows and equipment [343]. They also reduce contamination risk, are cost-effective, and offer greater versatility for various assays and experimental conditions [233]. Figure 7.16(b) illustrates the average area velocity magnitude at various powers for both P-SH-SAW and R-SAW, focusing on a segment of culture plate fluid (as shown in the area and scale depicted in Figure

7.16(c)). P-SH-SAW demonstrates a significantly higher streaming velocity of ~ 1.2 mm/s, outperforming the R-SAW, which fails to generate any streaming through the culture plate at 1 W (30 dBm). Overall, these results demonstrate the effectiveness of using P-SH-SAW within culture plates, suggesting significant potential for various biological applications. For instance, it can be utilized for mixing to ensure uniform cell exposure to nutrients and factors, as well as facilitating non-enzymatic cell detachment offering a gentler method of harvesting [421–423].

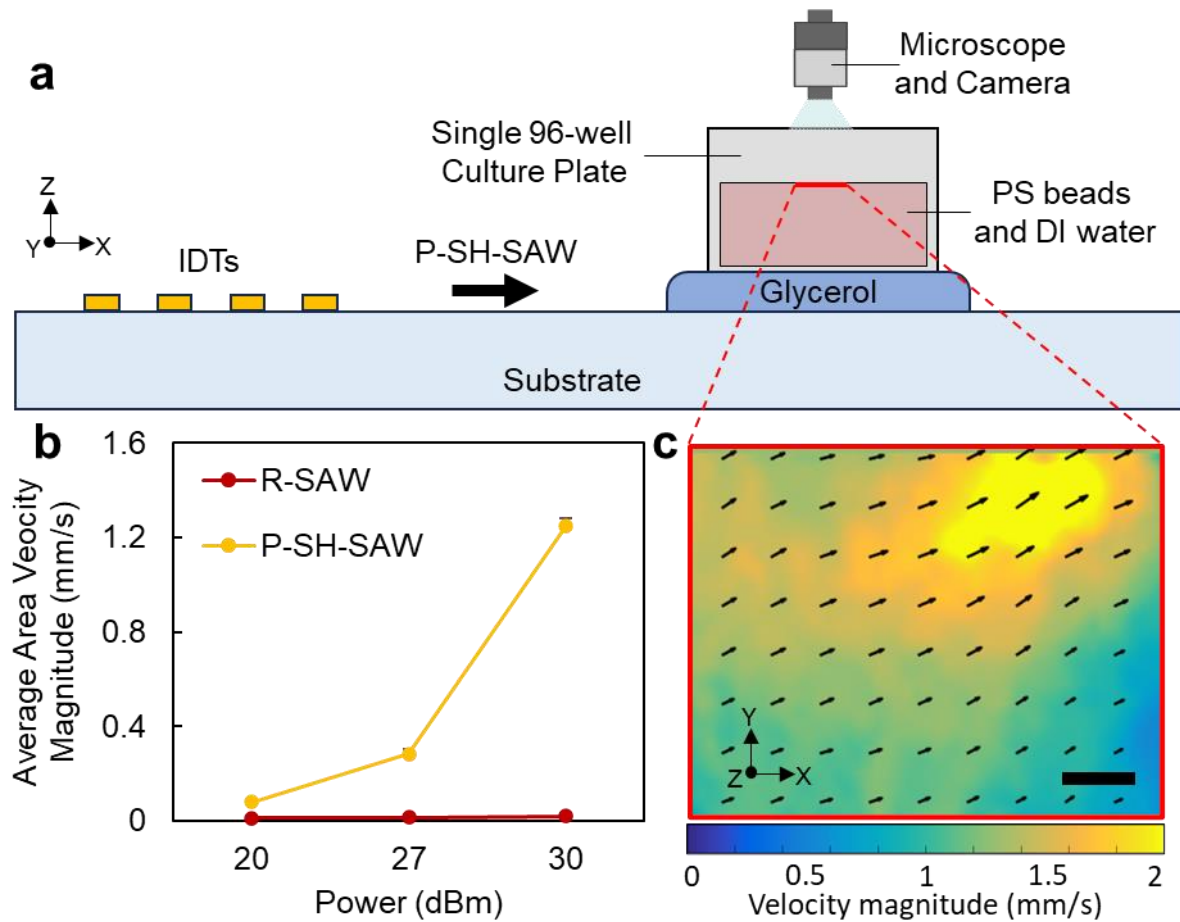


Figure 7.16. Streaming in a culture plate coupled with glycerol. (a) 2D device set-up with a glycerol layer coupling a single 96-well culture plate. (b) Average area velocity magnitude for 0° R-SAW and 90° P-SH-SAW inside a culture plate at different powers. (c) PIVLab image of the streaming velocity magnitude for 90° P-SH-SAW inside a culture plate at 30 dBm. Scale represents 0.25 mm.

7.3 Concentration of micro- and nano- particles

The investigation into wave modes and angles provides a pathway to enhance device optimization by shifting the focus from altering IDT designs to manipulating the wave mode selection. This shift facilitates tailored improvements in acoustofluidic performance. For example, our previous research demonstrated that a different X-rotation angle around the 128° YX-cut LiNbO₃ substrate enabled the utilization of a different wave mode, offering a synergistic blend of R-SAW and SH-SAW mechanisms for rapid exosome concentration [12]. This approach involved employing the 60° X-rotation Dual SAW (D-SAW) at an offset to the PDMS ring, to generate a singular vortex for concentration. Despite this, a comprehensive exploration of wave modes and angles remained unaddressed. Through COMSOL studies and utilization of the Hexagonal FPCB IDT, additional novel wave modes on the 128° YX-cut LiNbO₃ substrate have been identified, demonstrating enhanced efficacy in acoustofluidic actuation. For instance, as shown in section 7.2.2, the 90° X-rotation P-SH-SAW exhibited enhanced average area velocities compared to 60° X-rotation D-SAW. Hence, this section investigates the utilization of the 90° X-rotation P-SH-SAW for concentration.

It should be noted that in our previous studies of 60° X-rotation D-SAW concentration [12], we used 50 µl fluid volume. However, for these particle concentration experiments, we have increased the fluid volume to 100 µl. This larger volume is more clinically relevant, providing a more accurate representation of real-world sample sizes used in medical and laboratory settings [424]. This adjustment not only aligns our experiments with clinical standards but also allows for better scalability, throughput, and potential integration into existing diagnostics workflows.

7.3.1 Numerical Analysis

Three concentration configurations were evaluated: the conventional R-SAW at 0° X-rotation, 60° X-rotation D-SAW, and 90° X-rotation P-SH-SAW. An offset position was used on each setup to create a single vortex pattern for concentration. Figure 7.17 illustrates the concentration test setups (left) and corresponding numerical analysis (right) for these configurations. The numerical analysis reveals vibration amplitude and acoustic pressure distribution within the PDMS ring fluid, both of which are capped for

comparison purposes. Figure 7.17(a,right) depicts the R-SAW wavefield pattern and the low-pressure regions in both the centre and periphery of the fluid. Conversely, Figure 7.17(b,right) shows the beam distortion profile and a low-pressure region solely at the centre of the fluid. Nevertheless, Figure 7.17(c,right) demonstrates a more intensive acoustic pressure distribution than the previous two configurations.

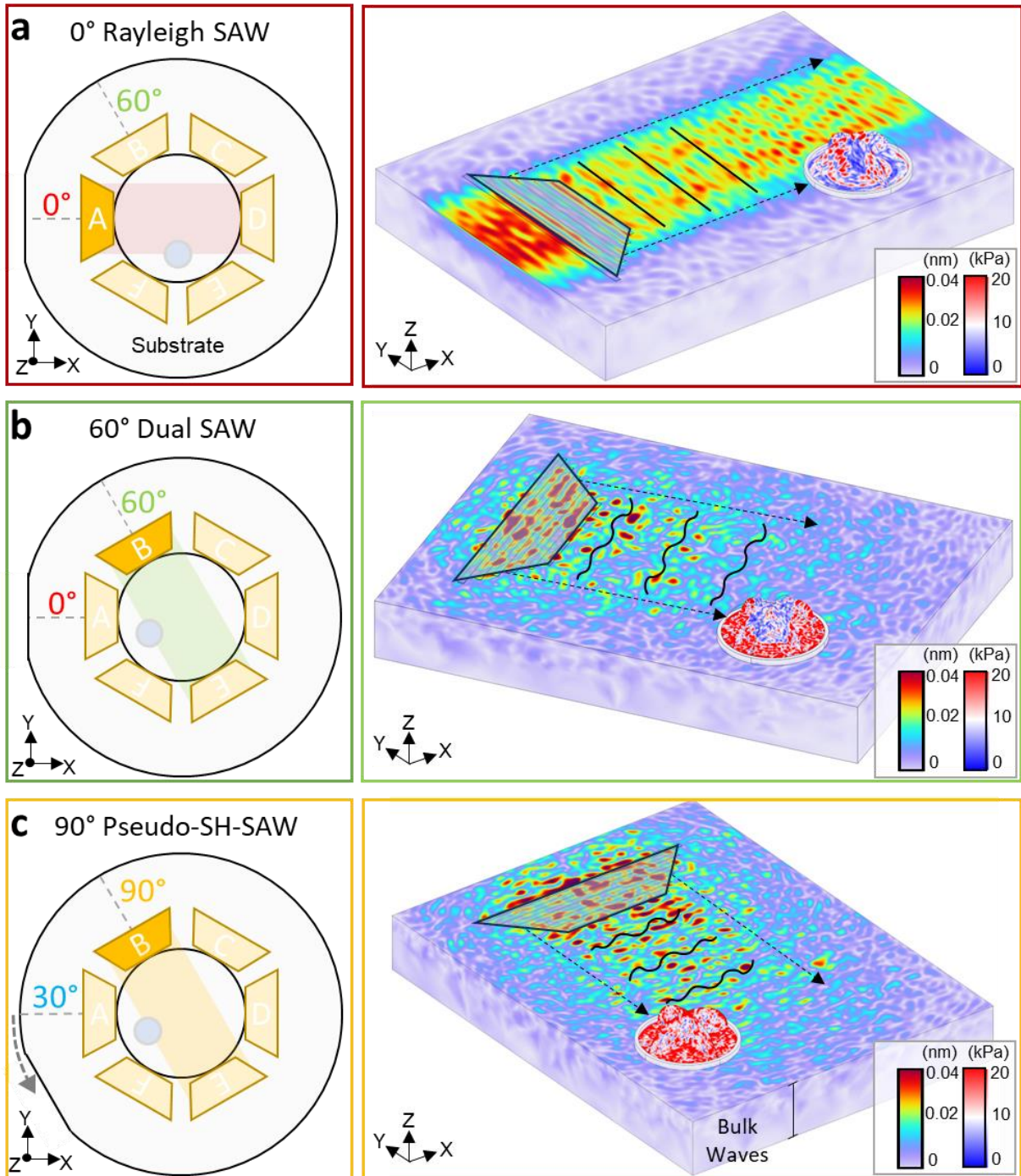


Figure 7.17. Illustration of concentration test configurations (left) and corresponding numerical analysis (right). (a) R-SAW configuration with 0° X-rotation and PDMS ring offset. (b) D-SAW configuration with 60° X-rotation and PDMS ring offset [12]. (c) P-SH-SAW configuration with 90° X-rotation and PDMS ring offset.

7.3.2 Working Mechanism

The asymmetric interaction of SAW within a fluid creates a single vortex flow field. The dynamic is driven by various forces, including the acoustic streaming-based drag force, the centrifugal force, the acoustic radiation force due to SSAW or TSAWs, leading to different particle concentration behaviours [359].

Previous studies [359,425] have shown that the trajectory and final position of particles in a sessile droplet are influenced mainly by two factors [360]: (1) the ratio of the acoustic wave attenuation length (α^{-1} , Equation 2.11) to the droplet radius; and (2) the ratio of the particle size to the acoustic wavelength in the fluid ($\kappa = k_f r_p$), where k_f is the wave number in the fluid and r_p is the radius of the particle. When $\kappa > 1$, the acoustic radiation force from TSAWs predominantly affects the particles. Whereas, when $\kappa < 1$, the acoustic radiation force from SSAWs becomes more significant [359]. When the wave attenuation length exceeds the droplet radius ($\alpha^{-1} > r_d$), and the particle size is small relative to the wavelength in the fluid ($\kappa < 1$), particles within the vortex streaming field will move and concentrate to the centre. However, even with $\kappa < 1$, smaller particles ($< 3 \mu\text{m}$) [359] are less influenced by the SSAWs acoustic radiation force and are more affected by the acoustic streaming drag force.

The PDMS ring plays a role in facilitating droplet spinning, enabling the concentration of smaller particles. A PDMS ring confines the boundary of the fluid, ensuring that a water droplet forms its equilibrium hemispherical shape when the force of gravity and surface tension are balanced [360]. At high acoustic amplitudes, the droplet deforms and achieves a stable spin with periodic boundary deformation, resulting in a “rotational capillary wave” [360]. When this occurs, particles within the droplet follow a dual-axis helical trajectory towards the centre [360].

For particles smaller than 1 μm with diameter, the drag force generated by both acoustic streaming (tangential direction) and spinning-enhanced secondary flow

(radial direction) significantly influences the movement of the particles along the fluid streamlines [360]. In the case of nanoparticles, the secondary flow induced by the spinning motion has a radial drag force component and dominates the concentration process, gradually drawing the particles inward [360].

7.3.3 Concentration Results

The concentration results for the three different configurations are presented in Figure 7.18. For the larger 10 μm PS particles, each wave mode demonstrates similar concentration times of around 8 seconds. This similarity is likely due to the formation of SSAWs from reflections, which utilize the acoustic radiation force to concentrate the particles in the centre [359].

In contrast, for the 1 μm PS particles, the concentration time and effectiveness of R-SAW significantly decreases. At this smaller particle size, the acoustic radiation force from the SSAW is less dominant, and the drag force becomes more significant, causing many particles to follow the single vortex acoustic streaming pattern rather than concentrating at the centre. Both D-SAW and P-SH-SAW maintain good and comparable concentration times of around 30 seconds. The higher velocities at these wave modes result in greater acoustic attenuation lengths, leading to the formation of SSAWs that facilitate concentration. Additionally, the concentration of these small PS particles is also due to the spinning phenomenon within the PDMS ring [360]. It is probable that R-SAW does not produce a high enough acoustic amplitude at this power due to wave damping and does not induce sufficient spinning for small particle concentration. However, when a combination of wave modes is employed at higher frequencies, these wave modes experience less damping, which allows SSAW formation and sufficient spinning for concentrating smaller particles [12]. Too high amplitude, however, can cause excessive spinning, resulting in centrifugal forces that push some PS particles of this size to the droplet periphery [426], which might explain why D-SAW performs slightly better than P-SH-SAW. Nonetheless, the differences are minimal, necessitating further testing to confirm these observations.

For the smallest 500 nm PS particles, R-SAW again shows inferior concentration ability compared to the other wave modes for the same reasons. P-SH-SAW and D-SAW exhibit comparable concentration times of 40 seconds. P-SH-SAW may achieve

slightly better results for smaller particles due to its capacity to produce higher amplitudes, as shown in Chapter 6, thus enhancing the spinning effect for nanoparticles. Future experiments using P-SH-SAW with smaller particles are recommended to validate these findings.

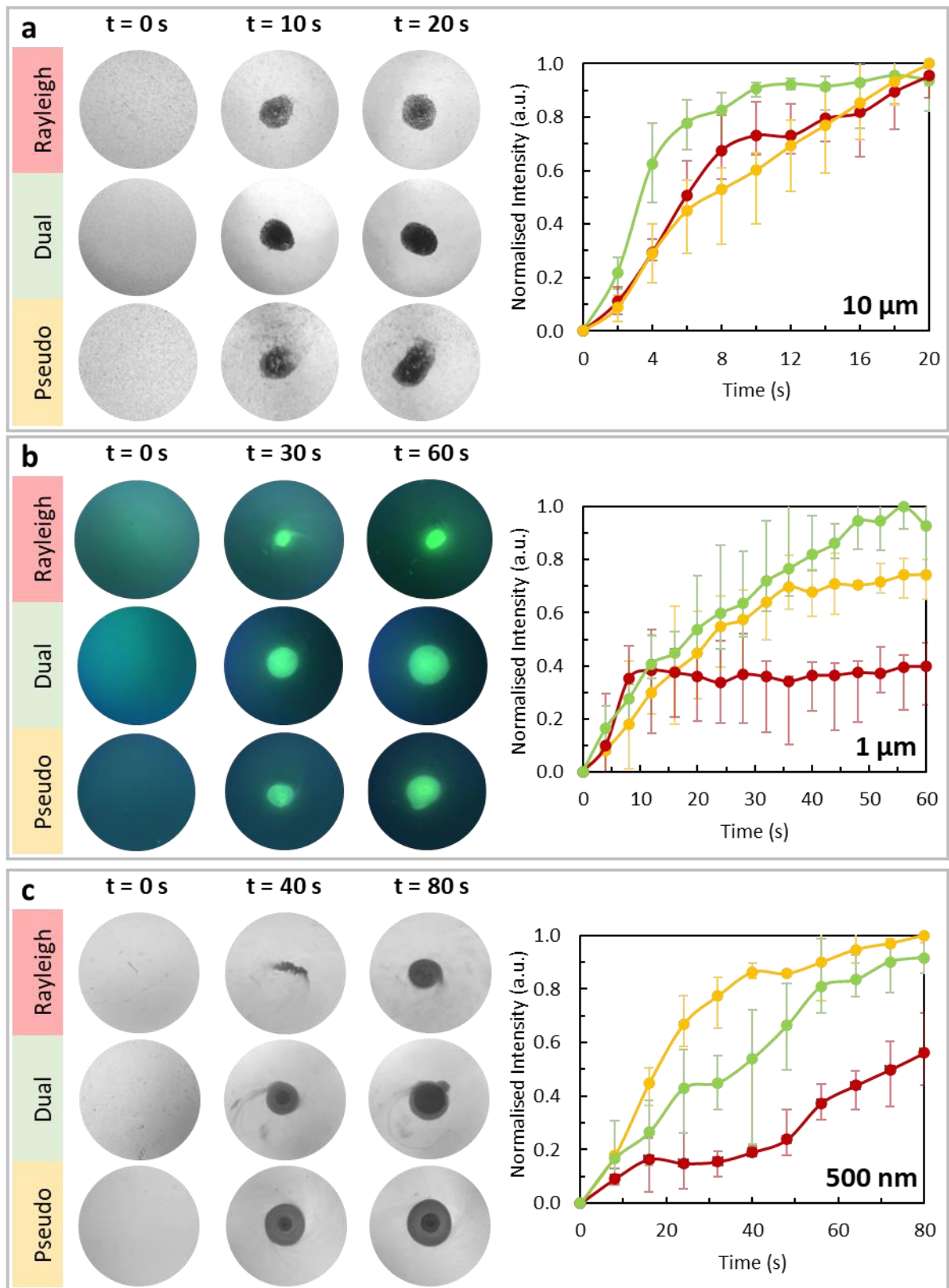


Figure 7.18. Concentration results, at 32 dBm power, for different configurations at three different size PS beads (a) 10 μm , (b) 1 μm (c) 500 nm. The three configurations are R-SAW (red), D-SAW (green), and P-SH-SAW (yellow).

7.3.4 Additional Concentration Results

Furthermore, other configurations of 60° X-rotation D-SAW were explored given it consistently yielded effective concentration results for $10\ \mu\text{m}$, $1\ \mu\text{m}$, and $500\ \text{nm}$, when compared to the other wave modes. In section 6.3.4, it was observed that at 60° X-rotation D-SAW, there was a power flow angle of approximately -4.4° . Consequently, its inherent offset was leveraged for concentration. Centralising the PDMS ring while using 60° X-rotation D-SAW enhances the Hexagonal FPCB IDT device multi-functionality as each of the surrounding IDTs can then also perform their own specific function to the fluid. This makes the device more practical and effective for achieving multiple applications with one configuration, such as 0° X-rotation R-SAW for mixing [2] and 60° X-rotation D-SAW for concentration. Figure 7.19 shows two configurations employing the 60° X-rotation D-SAW: (a) one with a single IDT positioned directly opposite the central PDMS ring fluid, and the other (b) employing a pair of opposite IDTs positioned directly opposite the central PDMS ring.

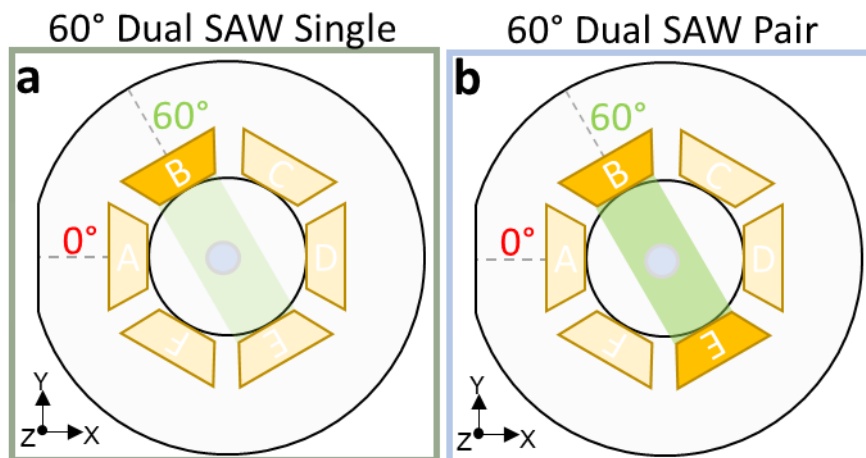


Figure 7.19. 60° X-rotation D-SAW configurations for concentration, with the PDMS ring placed centrally directly opposite the IDTs. (a) single IDT. (b) pair of opposite IDTs.

Figure 7.20 presents the concentration results using 60° X-rotation D-SAW without an offset for (a) $10\ \mu\text{m}$, (b) $1\ \mu\text{m}$, and (c) $500\ \text{nm}$ sized particles. These results are normalised with respect to the previous findings in Figure 7.18. The configuration employing a pair of IDT demonstrates superior concentration performance compared to the single IDT configuration across all three particle sizes. The single IDT did not

produce a sufficient offset to generate an adequate single vortex pattern for particle concentration. Instead, it produced a double vortex with two regions of concentration, where one vortex was larger and concentrated most of the particles, as shown in Figure 7.20. In contrast, the pair of IDTs produced the desired single vortex pattern, as any double vortex pattern formed would have one larger vortex on each side, effectively cancelling each other out. The larger error bars indicate that interference from imperfect offsetting of the opposing IDTs could influence the results. For 500 nm, both methods exhibited poor concentration compared to the previous results with D-SAW and P-SH-SAW with an offset, as shown in in Figure 7.18. This may be due to the opposing IDTs reducing the spinning mechanism by producing an interfered single vortex pattern.

Nevertheless, for micro-particle size, the concentration times are better than for R-SAW with an offset (red dashed line in Figure 7.20). This highlights the ability to utilize 60° X-rotation D-SAW without an offset to achieve improved concentration times for micro-sized particles to that of the conventional R-SAW with an offset. Therefore, this demonstrates the versatility of the Hexagonal FPCB IDT when coupled with the PDMS ring positioned at the centre, enabling multifaceted manipulation of particles. Specifically, the 60° X-rotation D-SAW can induce concentration whereby altering the activation of different IDTs around the substrate allow for adjustment of the vortex direction. Moreover, employing the conventional R-SAW at 0° in this configuration can initiate double vortex streaming, as shown in section 7.2.3, potentially offering advantages for mixing [2].

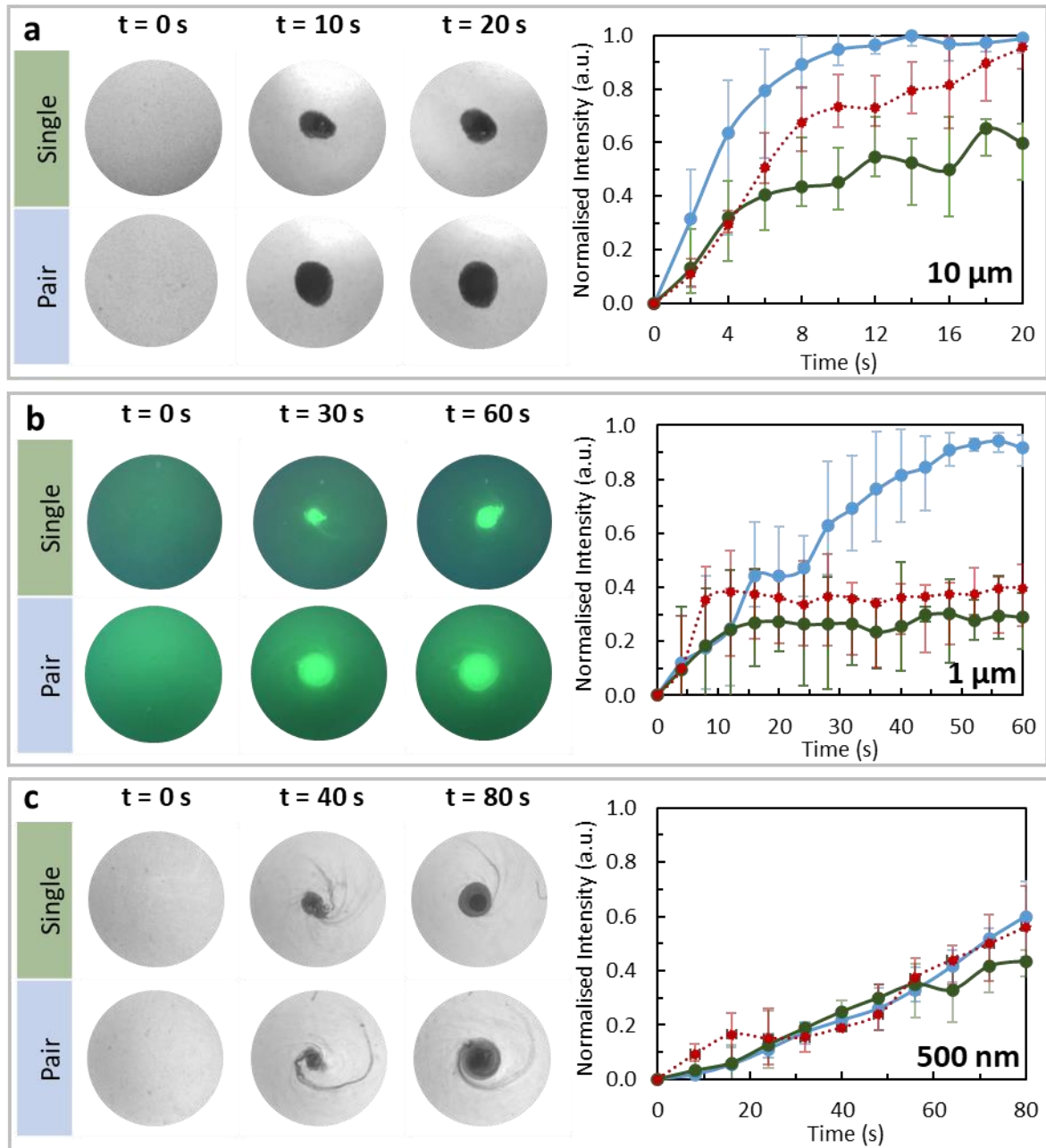


Figure 7.20. Concentration results using 60° X-rotation D-SAW single and pair configuration with no offset for (a) $10\ \mu\text{m}$, (b) $1\ \mu\text{m}$, and (c) $500\ \text{nm}$ sized particles. The red dashed line shows R-SAW concentration for comparison.

8.1 Conclusion

This research set out to investigate innovative configurations for producing acoustic streaming with SAWs to enable microparticle manipulation for versatile biomedical applications. The primary objectives included: reviewing the mechanisms and applications of acoustic streaming, developing a reconfigurable device for rapid investigation, exploring different angles and wave modes, simulating and characterizing these wave modes, and evaluating the fluid and particle manipulation capabilities of the resulting acoustic streaming. Through comprehensive analysis, several key findings emerged, demonstrating that the research successfully met its aims and objectives.

Firstly, this thesis provided both qualitative and quantitative insights into the acoustic streaming mechanism and its applications, addressing the first objective. Secondly, the reconfigurable Hexagonal FPCB IDT device was developed, enabling rapid investigation, which met the second objective. This device facilitated the exploration of different X-rotation angles and wave modes of the conventional 128° XY-cut LiNbO_3 , addressing the third objective. Through COMSOL simulations, a large range of wave modes were characterized, with their coupling coefficients and power flow angles calculated, fulfilling the fourth objective. Subsequent 2D and 3D simulations validated these findings and demonstrated interaction between the wavefield and the fluidic environment.

A P-SH-SAW based streaming mechanism on the 128° XY-cut LiNbO_3 was discovered, which effectively combines R-SAW and SH-SAW components, offering significant Z displacement and advantageous boundary layer streaming with minimal damping. This mechanism achieved comparable streaming velocities to R-SAW at 30 dBm, with a 100 μl (50:50, water: glycerol ratio) sample. Notably, damping experiments demonstrated the influence of viscous damping on P-SH-SAW performance, highlighting the considerable promise of P-SH-SAW in both macro- and micro- scale acoustic streaming compared to R-SAW. Additionally, P-SH-SAW demonstrated its utility in generating streaming flow in a culture plate, showcasing its potential for real-world applications with standardized and biocompatible equipment. This addressed

the fifth objective of evaluating fluid and particle manipulation capabilities. Lastly, different concentration mechanisms were investigated, demonstrating that a combination of wave modes at different X-rotation angles can produce superior micro- and nano- particle concentration compared to the conventional R-SAW, also meeting the final objective.

The findings of this thesis have several important implications. Theoretically, this research contributes to the understanding of alternative wave modes and their impact on acoustic streaming mechanisms. Methodologically, this thesis demonstrates the effectiveness of using COMSOL simulations to characterize wave modes. Practically, it suggests new ways to enhance acoustofluidic applications, making them more versatile and effective, particularly in biomedical research and clinical science.

Despite its contributions, this research has several limitations. One limitation is the specific focus on 128° XY-cut LiNbO₃ at wave modes between 15-40 MHz, which does not generalise to other materials or substrates. Another limitation is the scope of the COMSOL simulation, which, while extensive, may not capture all real-world fluid manipulation variabilities. Lastly, while this thesis has discovered a new wave mode with significant potential for practical applications, it has not demonstrated these applications in a biological context. However, it has laid a solid foundation for future biological projects to build upon and explore these promising wave modes.

Reflecting on this research journey, invaluable insights were gained into the complexities and potential of acoustic streaming mechanisms. Despite the challenges posed by the pandemic, which limited laboratory access and resources, adaptations were made to focus on other critical aspects such as writing a comprehensive review paper, conducting simulations, and exploring different angles and wave modes. This determination and adaptability not only enriched technical skills but also enhanced the ability to navigate uncertainty and persevere through setbacks. In conclusion, this research underscores the importance of exploring alternative wave modes and angles of substrates in acoustofluidics. This work sets the stage for future exploration in creating more versatile and effective acoustofluidic systems for biomedical applications.

8.2 Future Work

This thesis has presented initial numerical analysis and simulation of different acoustic waves as well as the development and characterization of the multidirectional Hexagonal FPCB IDT for acoustic streaming. This has provided a foundation for future work in the following areas:

Theory and modelling [1,3,17] –

- Studies need to be focused on improving computational modelling for acoustic streaming problems in three dimensions for different fluids, geometries, and frequency regimes, as well as the nonlinear interactions between the liquid and particles [1].
- The large discrepancy in time and space domains between the driving SAW and the resulting liquid streaming remains poorly understood. Hence challenges with numerical computational simulations as a very small time step and a very fine mesh are required to capture the SAW actuation of the liquid, but the resulting streaming occurs over a relatively large time scale and large spatial dimensions [3].

Device applications –

The development and thorough characterization of the Hexagonal FPCB IDT has opened opportunities for various applications. By utilizing different IDTs, the Hexagonal FPCB IDT supports multiple applications. A few hypotheses for future applications are outlined below:

Application 1: Enzyme-free release of adhered cells from standard culture plates [421–423].

This method enables the release of adhered cells from standard culture plates without compromising cellular viability, providing an efficient and safer alternative for cell culture in biomedical applications. Traditionally, trypsin is used to detach cells, but it can damage cell membranes and is toxic. P-SH-SAWs, due to their efficient propagation through culture plates at relatively low powers, can be actuated to induce sufficient shear stress via the vibration of the culture plate and fluid motion, thereby

acousto-mechanically detaching adhered cells from the culture plate surface. Previous studies with SAW for cell detachment on culture plates demonstrated its capability to perform cell detachment difficult adherent cell types, however, much higher powers were needed ~200 W [421] and 200 V [422]. This P-SH-SAW approach eliminates the need for trypsin and high power, thus avoiding harmful effects on cells.

Preliminary results shown in Figure 8.1 demonstrate the detachment of green fluorescent protein (GFP) cells that had settled on the single 96-well plate overnight. Figure 8.1(a) illustrates the GFP cells adhered to the bottom of the culture plate using an inverted fluorescent microscope (SOPTTOP ICV41) before the application of SAW. When P-SH-SAW was applied for 1 min at only 4 W (36 dBm), the majority of GFP cells detached from the bottom, as observed in Figure 8.1(b). The percentage of green fluorescent in Figure 8.1(c) shows a significant change (72%) before and after SAW application, indicating successful cell detachment. Cell viability (Figure 8.1(d)) decreased by only 18%, suggesting feasible results for practical use.

Future experiments should focus on optimizing parameters such as power levels, actuation times, and cell adhesion/settling times to maximize cell detachment while minimizing the drop in cell viability. Additionally, different dyes should be used to quantify the data in both control (no SAW applied) and experimental (SAW applied) samples. For example, DAPI/Hoechst dyes could be used to confirm cell presence by indicating nuclei, F-actin to visualize cell shape and size, and WGA to observe the extracellular environment. A live/dead discrimination dye like PI would also be beneficial.

To enhance visualization for better quantification, the Hexagonal FPCB IDT device requires adjustment and optimization. The current device is too large to fit properly under the microscope with clear visualization. A new Hexagonal FPCB IDT device should be constructed with a thinner and smaller bottom aluminium plate, as well as a reduced size and thickness for aluminium holder.

This technique could also be applied to difficult-to-detach cells types that cannot be treated with trypsin such as mesenchymal stem cells [421], thus opening a whole new PhD research project.

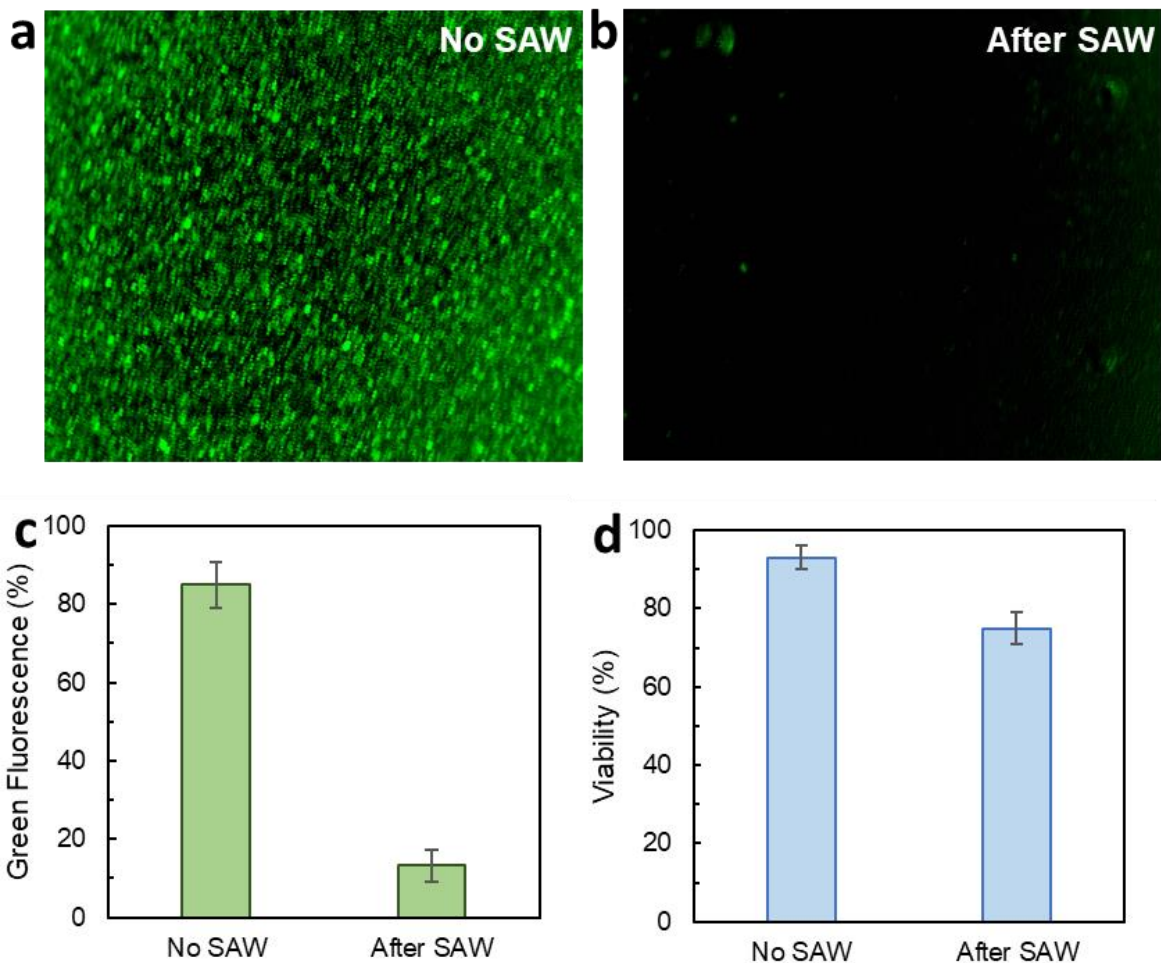


Figure 8.1. Preliminary cell detachment results. (a) GFP cells with no SAW. (b) GFP cells after SAW has been applied for 1 minute at 4 W (36 dBm). (c) Percentage of green fluorescence and (d) percentage viability with no SAW applied, and after SAW applied (n = 2).

Application 2: Nanoparticle enrichment [12] and separation [360].

Currently, nanoparticle concentration and separation can currently be achieved by only a handful of methods [360,427]. Utilizing multiple IDTs with different wave modes may enable improved separation across various fluid volumes. Further investigation into the combined use of R-SAW, D-SAW, and P-SH-SAW is needed to determine their nanoparticle concentration limits at specific power levels, aiming to achieve size-selective nanoparticle concentration and separation in different fluid volumes. For example, previous concentration results in our team demonstrated that D-SAW can achieve 100 nm and 20 nm concentration in 50 s and 105 s, respectively [12]. The

significant time difference facilitates effective size-selective separation. However, as shown in Figure 8.2, preliminary separation results were difficult to quantify due to colour crossover issues with our microscope, even with different wavelength emission/excitation particles and the correct filters. For example, green light and filter were needed to visualize the 100 nm red fluorescent particles (Sigma Aldrich, USA), and ultraviolet light and filter were needed to visualize the 20 nm blue (Invitrogen, USA) fluorescent particles. Nevertheless, red fluorescence was visible even without any 100 nm particles in water, and the 100 nm particles were still visible under ultraviolet light. This means quantifying the separation based on colours was not feasible, and the nanoparticle tracking analysis device cannot detect particles as small as 20 nm. This problem could be mitigated by designing and constructing a smaller device that can fit inside a higher quality fluorescent microscope from other laboratories (e.g. Cardiff Tissue Microenvironment Group; TMEG) to prevent colour crossover.

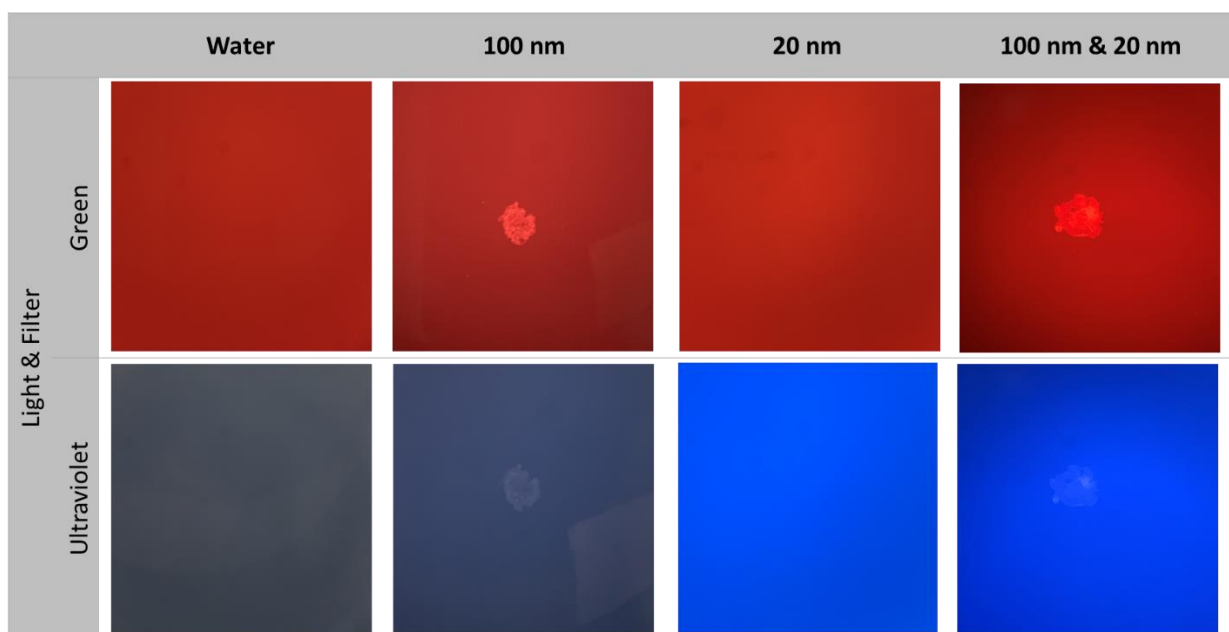


Figure 8.2. Preliminary concentration and separation results demonstrating colour cross-over using the microscope (GX Vision Ltd, GXM-L2800).

Application 3: Transfection for cell therapy [428,429].

This application hypothesis explores transfection for cell therapy, with increased transfection efficiency and cell viability compared to traditional viral-based methods

and other ultrasound bubble-based techniques [428]. It should be noted that the original design and application for this device (pre-COVID) was using multidirectional SAW to enable acoustic streaming for cell therapy transfection. Nevertheless, due to the pandemic, resource limitation meant this project was not achievable. This prompted the exploration of different angles and wave modes with the Hexagonal FPCB IDT device post- COVID, leading to the discovery of P-SH-SAW. P-SH-SAW could likely generate greater acoustic streaming-induced shear forces when compared to R-SAW. Such forces could enhance the cell membrane and nuclear envelope permeability [428]. This method could be particularly advantageous if performed in standard culture plates [430] rather than PDMS chambers [428,431,432]. Experimentation to assess the temperature variability of P-SH-SAW may elucidate whether thermal pulses could contribute to this enhancement [428]. Moreover, the simultaneous use of multiple IDTs could ensure sufficient shear stress even at low powers, mitigating the risk of damage. Consequently, this approach could enable safe, efficient, and high-throughput transfection.

Standardisation and commercialisation –

- Applications should be thoroughly investigated and standardised. Once achieved, the optimized hexagonal FPCB IDT can offer an all-in-one acoustofluidic prototype suitable for a range of uses. This versatility would be highly advantageous for biomedical research laboratories.
- Cost is a critical factor in the commercialisation of acoustofluidics devices. The hexagonal FPCB IDT already offers cost benefits due to its flexible PCB design. The next step is achieving on-chip functionality that eliminates the need for costly external equipment and requires minimal user training [433]. Simplifying adjustments and SAW actuation can be accomplished by integrating modern technologies such as mobile phones, touch screens, Bluetooth, and the Internet [282]. Automation through simple interfaces, like buttons or apps, will further reduce the need for user input.

Bibliography

- [1] Rufo J, Cai F, Friend J, et al. Acoustofluidics for biomedical applications. *Nat Rev Methods Primer* 2022;2:1–21. <https://doi.org/10.1038/s43586-022-00109-7>.
- [2] Stringer M, Zeng Z, Zhang X, et al. Methodologies, technologies, and strategies for acoustic streaming-based acoustofluidics. *Appl Phys Rev* 2023;10:011315. <https://doi.org/10.1063/5.0134646>.
- [3] Ding X, Li P, Lin S-CS, et al. Surface acoustic wave microfluidics. *Lab Chip* 2013;13:3626. <https://doi.org/10.1039/c3lc50361e>.
- [4] Pang H-F, Tao R, Luo J, et al. Rayleigh and shear-horizontal surface acoustic waves simultaneously generated in inclined ZnO films for acoustofluidic lab-on-a-chip. *Surf Coat Technol* 2022;442:128336. <https://doi.org/10.1016/j.surfcoat.2022.128336>.
- [5] Fu YQ, Luo JK, Nguyen NT, et al. Advances in piezoelectric thin films for acoustic biosensors, acoustofluidics and lab-on-chip applications. *Prog Mater Sci* 2017;89:31–91. <https://doi.org/10.1016/j.pmatsci.2017.04.006>.
- [6] R.Weser Aw, M.Weihnacht Sm. The complexity of surface acoustic wave fields used for microfluidic applications. *Ultrasonics* 2020;106:106160.
- [7] Boluriaan S, Morris PJ. Acoustic Streaming: From Rayleigh to Today. *Int J Aeroacoustics* 2003;2:255–92. <https://doi.org/10.1260/147547203322986142>.
- [8] Wiklund M, Green R, Ohlin M. Acoustofluidics 14: Applications of acoustic streaming in microfluidic devices. *Lab Chip* 2012;12:2438–51. <https://doi.org/10.1039/C2LC40203C>.
- [9] Brodie DS, Fu YQ, Li Y, et al. Shear horizontal surface acoustic wave induced microfluidic flow. *Appl Phys Lett* 2011;99:153704. <https://doi.org/10.1063/1.3651487>.
- [10] Mandal D, Banerjee S. Surface Acoustic Wave (SAW) Sensors: Physics, Materials, and Applications. *Sensors* 2022;22:820. <https://doi.org/10.3390/s22030820>.
- [11] Ostachowicz W, Kudela P, Krawczuk M, et al. *Guided Waves in Structures for SHM: The Time - Domain Spectral Element Method*. New York, UNITED KINGDOM: John Wiley & Sons, Incorporated; 2012.
- [12] Dumčius P, Mikhaylov R, Zhang X, et al. Dual-Wave Acoustofluidic Centrifuge for Ultrafast Concentration of Nanoparticles and Extracellular Vesicles. *Small* n.d.;n/a:2300390. <https://doi.org/10.1002/smll.202300390>.
- [13] Akthakul A. Study of waveguide and anisotropy effects upon surface acoustic wave velocities in thin films. Thesis. Massachusetts Institute of Technology, 1998.

- [14] Mikhaylov R, Martin MS, Dumcius P, et al. A reconfigurable and portable acoustofluidic system based on flexible printed circuit board for the manipulation of microspheres. *J Micromechanics Microengineering* 2021;31:074003. <https://doi.org/10.1088/1361-6439/ac0515>.
- [15] Mikhaylov R, Wu F, Wang H, et al. Development and characterisation of acoustofluidic devices using detachable electrodes made from PCB. *Lab Chip* 2020;20:1807–14. <https://doi.org/10.1039/C9LC01192G>.
- [16] Resonance Bowl (Chinese Spouting Bowl). *Am Sci* n.d. <https://www.americanscientific.com/product/resonance-bowl-chinese-spouting-bowl-2/> (accessed October 12, 2021).
- [17] Friend J, Yeo LY. Microscale acoustofluidics: Microfluidics driven via acoustics and ultrasonics. *Rev Mod Phys* 2011;83:647–704. <https://doi.org/10.1103/RevModPhys.83.647>.
- [18] Kundt A. Ueber eine neue Art akustischer Staubfiguren und über die Anwendung derselben zur Bestimmung der Schallgeschwindigkeit in festen Körpern und Gasen. *Ann Phys Chem* 1866;203:497–523. <https://doi.org/10.1002/andp.18662030402>.
- [19] Pavlic A, Dual J. On the streaming in a microfluidic Kundt's tube. *J Fluid Mech* 2021;911:A28. <https://doi.org/10.1017/jfm.2020.1046>.
- [20] Rayleigh, Lord. On the Circulation of Air Observed in Kundt's Tubes, and on Some Allied Acoustical Problems. *Philos Trans R Soc Lond* 1884;175:1–21.
- [21] "Berechnung ebener periodischer Grenzschichtströmungen (Calculation of Plane Periodic Boundary Layer Streaming)," *Phys Z* 1932;Vol. 33.
- [22] Westervelt PJ. The Theory of Steady Rotational Flow Generated by a Sound Field. *J Acoust Soc Am* 1953;25:60–7. <https://doi.org/10.1121/1.1907009>.
- [23] Nyborg WL. Acoustic Streaming due to Attenuated Plane Waves. *J Acoust Soc Am* 1953;25:68–75. <https://doi.org/10.1121/1.1907010>.
- [24] Gu Y, Chen C, Rufo J, et al. Acoustofluidic Holography for Micro- to Nanoscale Particle Manipulation. *ACS Nano* 2020;14:14635–45. <https://doi.org/10.1021/acsnano.0c03754>.
- [25] Collins DJ, Ma Z, Han J, et al. Continuous micro-vortex-based nanoparticle manipulation via focused surface acoustic waves. *Lab Chip* 2016;17:91–103. <https://doi.org/10.1039/C6LC01142J>.
- [26] Destgeer G, Cho H, Ha BH, et al. Acoustofluidic particle manipulation inside a sessile droplet: four distinct regimes of particle concentration. *Lab Chip* 2016;16:660–7. <https://doi.org/10.1039/c5lc01104c>.
- [27] Zhang N, Zuniga-Hertz JP, Zhang EY, et al. Microliter ultrafast centrifuge platform for size-based particle and cell separation and extraction using novel

- omnidirectional spiral surface acoustic waves. *Lab Chip* 2021;21:904–15. <https://doi.org/10.1039/D0LC01012J>.
- [28] Gu Y, Chen C, Mao Z, et al. Acoustofluidic centrifuge for nanoparticle enrichment and separation. *Sci Adv* 2021;7. <https://doi.org/10.1126/sciadv.abc0467>.
- [29] Zhou J, Mukherjee P, Gao H, et al. Label-free microfluidic sorting of microparticles. *APL Bioeng* 2019;3:041504. <https://doi.org/10.1063/1.5120501>.
- [30] Kumar C, Hejazian M, From C, et al. Modeling of mass transfer enhancement in a magnetofluidic micromixer. *Phys Fluids* 2019;31:063603. <https://doi.org/10.1063/1.5093498>.
- [31] Zhao C, Yang C. Electrokinetics of non-Newtonian fluids: a review. *Adv Colloid Interface Sci* 2013;201–202:94–108. <https://doi.org/10.1016/j.cis.2013.09.001>.
- [32] Lapizco-Encinas BH. On the recent developments of insulator-based dielectrophoresis: A review. *ELECTROPHORESIS* 2019;40:358–75. <https://doi.org/10.1002/elps.201800285>.
- [33] Johnson AC, Bowser MT. Micro free flow electrophoresis. *Lab Chip* 2017;18:27–40. <https://doi.org/10.1039/c7lc01105a>.
- [34] Paiè P, Zandrini T, Vázquez RM, et al. Particle Manipulation by Optical Forces in Microfluidic Devices. *Micromachines* 2018;9:E200. <https://doi.org/10.3390/mi9050200>.
- [35] Wang Y, Zhang Q, Zhu Z, et al. Laser streaming: Turning a laser beam into a flow of liquid. *Sci Adv* 2017;3:e1700555. <https://doi.org/10.1126/sciadv.1700555>.
- [36] Ozcelik A, Rufo J, Guo F, et al. Acoustic tweezers for the life sciences. *Nat Methods* 2018;15:1021–8. <https://doi.org/10.1038/s41592-018-0222-9>.
- [37] Le M-CN, Fan ZH. Exosome isolation using nanostructures and microfluidic devices. *Biomed Mater Bristol Engl* 2021;16:022005. <https://doi.org/10.1088/1748-605X/abde70>.
- [38] Novotny J, Lenshof A, Laurell T. Acoustofluidic platforms for particle manipulation. *Electrophoresis* 2022;43:804–18. <https://doi.org/10.1002/elps.202100291>.
- [39] Mazalan MB, Noor AM, Wahab Y, et al. Current Development in Interdigital Transducer (IDT) Surface Acoustic Wave Devices for Live Cell In Vitro Studies: A Review. *Micromachines* 2021;13:30. <https://doi.org/10.3390/mi13010030>.
- [40] Mohanty S, Khalil ISM, Misra S. Contactless acoustic micro/nano manipulation: a paradigm for next generation applications in life sciences. *Proc Math Phys Eng Sci* 2020;476:20200621. <https://doi.org/10.1098/rspa.2020.0621>.

- [41] Inui T, Mei J, Imashiro C, et al. Focused surface acoustic wave locally removes cells from culture surface. *Lab Chip* 2021. <https://doi.org/10.1039/D0LC01293A>.
- [42] Jung JH, Destgeer G, Park J, et al. Microfluidic flow switching *via* localized acoustic streaming controlled by surface acoustic waves. *RSC Adv* 2018;8:3206–12. <https://doi.org/10.1039/C7RA11194K>.
- [43] Nam J, Jang WS, Kim J, et al. Lamb wave-based molecular diagnosis using DNA hydrogel formation by rolling circle amplification (RCA) process. *Biosens Bioelectron* 2019;142:111496. <https://doi.org/10.1016/j.bios.2019.111496>.
- [44] Zhang P. Acoustic streaming vortices enable contactless, digital control of droplets'. *Sci Adv* 2020;6:0606,. <https://doi.org/10.1126/sciadv.aba0606>.
- [45] Tan MK, Friend JR, Yeo LY. Interfacial Jetting Phenomena Induced by Focused Surface Vibrations. *Phys Rev Lett* 2009;103:024501. <https://doi.org/10.1103/PhysRevLett.103.024501>.
- [46] Jangi M, Luo JT, Tao R, et al. Concentrated vertical jetting mechanism for isotropically focused ZnO/Si surface acoustic waves. *Int J Multiph Flow* 2019;114:1–8. <https://doi.org/10.1016/j.ijmultiphaseflow.2019.02.002>.
- [47] Collins DJ, Manor O, Winkler A, et al. Atomization off thin water films generated by high-frequency substrate wave vibrations. *Phys Rev E Stat Nonlin Soft Matter Phys* 2012;86:056312. <https://doi.org/10.1103/PhysRevE.86.056312>.
- [48] Cortez-Jugo C, Qi A, Rajapaksa A, et al. Pulmonary monoclonal antibody delivery via a portable microfluidic nebulization platform. *Biomicrofluidics* 2015;9. <https://doi.org/10.1063/1.4917181>.
- [49] Wang J, Hu H, Ye A, et al. Experimental investigation of surface acoustic wave atomization. *Sens Actuators Phys* 2016;238:1–7. <https://doi.org/10.1016/j.sna.2015.11.027>.
- [50] Zhou J, Tao X, Luo J, et al. Nebulization using ZnO/Si surface acoustic wave devices with focused interdigitated transducers. *Surf Coat Technol* 2019;367:127–34. <https://doi.org/10.1016/j.surfcoat.2019.03.078>.
- [51] Galopin E, Beaugeois M, Pinchemel B, et al. SPR biosensing coupled to a digital microfluidic microstreaming system. *Biosens Bioelectron* 2007;23:746–50. <https://doi.org/10.1016/j.bios.2007.08.009>.
- [52] Chen C, Gu Y, Philippe J, et al. Acoustofluidic rotational tweezing enables high-speed contactless morphological phenotyping of zebrafish larvae. *Nat Commun* 2021;12:1118. <https://doi.org/10.1038/s41467-021-21373-3>.
- [53] Zhang J, Yang S, Chen C, et al. Surface acoustic waves enable rotational manipulation of *Caenorhabditis elegans*. *Lab Chip* 2019;19:984–92. <https://doi.org/10.1039/c8lc01012a>.

- [54] Marqus S, Lee L, Istivan T, et al. High frequency acoustic nebulization for pulmonary delivery of antibiotic alternatives against *Staphylococcus aureus*. *Eur J Pharm Biopharm* 2020;151:181–8. <https://doi.org/10.1016/j.ejpb.2020.04.003>.
- [55] Gong Z, Huang L, Tang X, et al. Acoustic Droplet Printing Tumor Organoids for Modeling Bladder Tumor Immune Microenvironment within a Week. *Adv Healthc Mater* 2021;10:2101312. <https://doi.org/10.1002/adhm.202101312>.
- [56] Wang Y, Zhang Q, Tao R, et al. Flexible/Bendable Acoustofluidics Based on Thin-Film Surface Acoustic Waves on Thin Aluminum Sheets. *ACS Appl Mater Interfaces* 2021;13:16978–86. <https://doi.org/10.1021/acsami.0c22576>.
- [57] Lim H, Back SM, Choi H, et al. Acoustic mixing in a dome-shaped chamber-based SAW (DC-SAW) device. *Lab Chip* 2019;20:120–5. <https://doi.org/10.1039/C9LC00820A>.
- [58] Yang Y, Dejous C, Hallil H. Trends and Applications of Surface and Bulk Acoustic Wave Devices: A Review. *Micromachines* 2023;14:43. <https://doi.org/10.3390/mi14010043>.
- [59] Campbell CK. Applications of surface acoustic and shallow bulk acoustic wave devices. *Proc IEEE* 1989;77:1453–84. <https://doi.org/10.1109/5.40664>.
- [60] Mamishev AV, Sundara-Rajan K, Yang F, et al. Interdigital sensors and transducers. *Proc IEEE* 2004;92:808–45.
- [61] Datta S. *Surface Acoustic Wave Devices*. Prentice-Hall; 1986.
- [62] Campbell CK. *Surface Acoustic Wave Devices for Mobile and Communication Applications*. Academic Press; 1998.
- [63] Plessky V, Reindl L. Review on SAW RFID tags. *IEEE Trans Ultrason Ferroelectr Fre Control* 2010;57:654–68.
- [64] Fu YQ, Luo JK, Nguyen NT, et al. Advances in piezoelectric thin films for acoustic biosensors, acoustofluidics and lab-on-chip applications. *Prog Mater Sci* 2017;89:31–91. <https://doi.org/10.1016/j.pmatsci.2017.04.006>.
- [65] Wu M, Chen K, Yang S, et al. High-throughput cell focusing and separation via acoustofluidic tweezers. *Lab Chip* 2018;18:3003–10. <https://doi.org/10.1039/C8LC00434J>.
- [66] Wu M, Huang P-H, Zhang R, et al. Circulating Tumor Cell Phenotyping via High-Throughput Acoustic Separation. *Small* 2018;14:1801131. <https://doi.org/10.1002/smll.201801131>.
- [67] Zhang G. *Bulk and Surface Acoustic Waves: Fundamentals, Devices, and Applications*. New York: Jenny Stanford Publishing; 2022. <https://doi.org/10.1201/9781003256625>.

- [68] Fu Y-Q, Pang H-F, Torun H, et al. Engineering inclined orientations of piezoelectric films for integrated acoustofluidics and lab-on-a-chip operated in liquid environments. *Lab Chip* 2021;21:254–71. <https://doi.org/10.1039/D0LC00887G>.
- [69] Nam J, Lim H, Shin S. Manipulation of microparticles using surface acoustic wave in microfluidic systems: a brief review. *Korea-Aust Rheol J* 2011;23:255–67. <https://doi.org/10.1007/s13367-011-0031-5>.
- [70] Song S, Wang Q, Zhou J, et al. Design of interdigitated transducers for acoustofluidic applications. *Nanotechnol Precis Eng* 2022;5:035001. <https://doi.org/10.1063/10.0013405>.
- [71] Nair MP, Teo AJT, Li KHH. Acoustic Biosensors and Microfluidic Devices in the Decennium: Principles and Applications. *Micromachines* 2021;13:24. <https://doi.org/10.3390/mi13010024>.
- [72] Biroun MH, Rahmati MT, Jangi M, et al. Computational and experimental analysis of droplet transportation/jetting behaviours driven by thin film surface acoustic waves. *Sens Actuators Phys* 2019;299:111624. <https://doi.org/10.1016/j.sna.2019.111624>.
- [73] Lei J, Glynne-Jones P, Hill M. Comparing methods for the modelling of boundary-driven streaming in acoustofluidic devices. *Microfluid Nanofluidics* 2017;21:23. <https://doi.org/10.1007/s10404-017-1865-z>.
- [74] Bruus H. Acoustofluidics 2: Perturbation theory and ultrasound resonance modes. *Lab Chip* 2012;12:20–8. <https://doi.org/10.1039/C1LC20770A>.
- [75] Sadhal SS. Acoustofluidics 13: Analysis of acoustic streaming by perturbation methods. *Lab Chip* 2012;12:2292–300. <https://doi.org/10.1039/C2LC40202E>.
- [76] Rapp BE. Chapter 9 - Fluids. In: Rapp BE, editor. *Microfluid. Model. Mech. Math.*, Oxford: Elsevier; 2017, p. 243–63. <https://doi.org/10.1016/B978-1-4557-3141-1.50009-5>.
- [77] Zarembo LK. Acoustic Streaming. In: Rozenberg LD, editor. *High-Intensity Ultrason. Fields*, Boston, MA: Springer US; 1971, p. 135–99. https://doi.org/10.1007/978-1-4757-5408-7_3.
- [78] Liu S, Yang Y, Ni Z, et al. Investigation into the Effect of Acoustic Radiation Force and Acoustic Streaming on Particle Patterning in Acoustic Standing Wave Fields. *Sensors* 2017;17:1664. <https://doi.org/10.3390/s17071664>.
- [79] Barnkob R, Augustsson P, Laurell T, et al. Acoustic radiation- and streaming-induced microparticle velocities determined by microparticle image velocimetry in an ultrasound symmetry plane. *Phys Rev E Stat Nonlin Soft Matter Phys* 2012;86:056307. <https://doi.org/10.1103/PhysRevE.86.056307>.
- [80] Evander M, Nilsson J. Acoustofluidics 20: Applications in acoustic trapping. *Lab Chip* 2012;12:4667–76. <https://doi.org/10.1039/C2LC40999B>.

- [81] Settnes M, Bruus H. Forces acting on a small particle in an acoustical field in a viscous fluid. *Phys Rev E* 2012;85:016327. <https://doi.org/10.1103/PhysRevE.85.016327>.
- [82] Bruus H. Acoustofluidics 7: The acoustic radiation force on small particles. *Lab Chip* 2012;12:1014–21. <https://doi.org/10.1039/C2LC21068A>.
- [83] Glynne-Jones P, Hill M. Acoustofluidics 23: acoustic manipulation combined with other force fields. *Lab Chip* 2013;13:1003–10. <https://doi.org/10.1039/C3LC41369A>.
- [84] Shi J, Huang H, Stratton Z, et al. Continuous particle separation in a microfluidic channel via standing surface acoustic waves (SSAW). *Lab Chip* 2009;9:3354–9. <https://doi.org/10.1039/B915113C>.
- [85] Bach JS, Bruus H. Suppression of Acoustic Streaming in Shape-Optimized Channels. *Phys Rev Lett* 2020;124:214501. <https://doi.org/10.1103/PhysRevLett.124.214501>.
- [86] Lighthill SJ. Acoustic streaming. *J Sound Vib* 1978;61:391–418. [https://doi.org/10.1016/0022-460X\(78\)90388-7](https://doi.org/10.1016/0022-460X(78)90388-7).
- [87] Laurell T, Lenshof A. *Microscale Acoustofluidics*. Royal Society of Chemistry; 2014.
- [88] Luo X, Cao J, Gong H, et al. Phase separation technology based on ultrasonic standing waves: A review. *Ultrason Sonochem* 2018;48:287–98. <https://doi.org/10.1016/j.ultsonch.2018.06.006>.
- [89] Devendran C, Albrecht T, Brenker J, et al. The importance of travelling wave components in standing surface acoustic wave (SSAW) systems. *Lab Chip* 2016;16:3756–66. <https://doi.org/10.1039/c6lc00798h>.
- [90] Tan MK, Yeo LY, Friend JR. Rapid fluid flow and mixing induced in microchannels using surface acoustic waves. *EPL Europhys Lett* 2009;87:47003. <https://doi.org/10.1209/0295-5075/87/47003>.
- [91] Riley N. Steady Streaming. *Annu Rev Fluid Mech* 2001;33:43–65. <https://doi.org/10.1146/annurev.fluid.33.1.43>.
- [92] Nama N, Barnkob R, Mao Z, et al. Numerical study of acoustophoretic motion of particles in a PDMS microchannel driven by surface acoustic waves. *Lab Chip* 2015;15:2700–9. <https://doi.org/10.1039/C5LC00231A>.
- [93] Riaud A, Baudoin M, Bou Matar O, et al. On the influence of viscosity and caustics on acoustic streaming in sessile droplets: an experimental and a numerical study with a cost-effective method. *J Fluid Mech* 2017;821:384–420. <https://doi.org/10.1017/jfm.2017.178>.
- [94] Sritharan K, Strobl CJ, Schneider MF, et al. Acoustic mixing at low Reynold's numbers. *Appl Phys Lett* 2006;88:054102. <https://doi.org/10.1063/1.2171482>.

- [95] Luo JK, Fu YQ, Milne WI. Acoustic Wave Based Microfluidics and Lab-on-a-Chip. *Model Meas Methods Acoust Waves Acoust Microdevices* 2013. <https://doi.org/10.5772/56387>.
- [96] Li J, Biroun MH, Tao R, et al. Wide range of droplet jetting angles by thin-film based surface acoustic waves. *J Phys Appl Phys* 2020;53:355402. <https://doi.org/10.1088/1361-6463/ab8f50>.
- [97] Guttenberg Z, Rathgeber A, Keller S, et al. Flow profiling of a surface-acoustic-wave nanopump. *Phys Rev E* 2004;70:056311. <https://doi.org/10.1103/PhysRevE.70.056311>.
- [98] Arzt RM, Salzmann E, Dransfeld K. Elastic surface waves in quartz at 316 MHz. *Appl Phys Lett* 1967;10:165–7. <https://doi.org/10.1063/1.1754894>.
- [99] Wu M, Ozcelik A, Rufo J, et al. Acoustofluidic separation of cells and particles. *Microsyst Nanoeng* 2019;5. <https://doi.org/10.1038/s41378-019-0064-3>.
- [100] Bui T, Nguyen V, Vollebregt S, et al. Effect of droplet shrinking on surface acoustic wave response in microfluidic applications. *Appl Surf Sci* 2017;426:253–61. <https://doi.org/10.1016/j.apsusc.2017.07.140>.
- [101] Destgeer G, Jung JH, Park J, et al. Particle Separation inside a Sessile Droplet with Variable Contact Angle Using Surface Acoustic Waves. *Anal Chem* 2017;89:736–44. <https://doi.org/10.1021/acs.analchem.6b03314>.
- [102] Sachs S, Baloochi M, Cierpka C, et al. On the acoustically induced fluid flow in particle separation systems employing standing surface acoustic waves – Part I. *Lab Chip* 2022;22:2011–27. <https://doi.org/10.1039/D1LC01113H>.
- [103] Zhang AL, Wu ZQ, Xia XH. Transportation and mixing of droplets by surface acoustic wave. *Talanta* 2011;84:293–7. <https://doi.org/10.1016/j.talanta.2011.01.017>.
- [104] Shilton RJ, Travagliati M, Beltram F, et al. Nanoliter-droplet acoustic streaming via ultra high frequency surface acoustic waves. *Adv Mater* 2014;26:4941–6. <https://doi.org/10.1002/adma.201400091>.
- [105] Darinskii AN, Weihnacht M, Schmidt H. Surface acoustic wave electric field effect on acoustic streaming: Numerical analysis. *J Appl Phys* 2018;123:014902. <https://doi.org/10.1063/1.5005849>.
- [106] Shilton R, Tan MK, Yeo LY, et al. Particle concentration and mixing in microdrops driven by focused surface acoustic waves. *J Appl Phys* 2008;104. <https://doi.org/10.1063/1.2951467>.
- [107] Singh R, Sankaranarayanan SKRS, Bhethanabotla VR. Enhancement of acoustic streaming induced flow on a focused surface acoustic wave device: Implications for biosensing and microfluidics. *J Appl Phys* 2010;107:024503. <https://doi.org/10.1063/1.3279687>.

- [108] Liu J, Li S, Bhethanabotla VR. Integrating Metal-Enhanced Fluorescence and Surface Acoustic Waves for Sensitive and Rapid Quantification of Cancer Biomarkers from Real Matrices. *ACS Sens* 2018;3:222–9. <https://doi.org/10.1021/acssensors.7b00876>.
- [109] Li Y, Fu YQ, Brodie SD, et al. Integrated microfluidics system using surface acoustic wave and electrowetting on dielectrics technology. *Biomicrofluidics* 2012;6:12812–128129. <https://doi.org/10.1063/1.3660198>.
- [110] Sankaranarayanan SKRS, Cular S, Bhethanabotla VR, et al. Flow induced by acoustic streaming on surface-acoustic-wave devices and its application in biofouling removal: A computational study and comparisons to experiment. *Phys Rev E* 2008;77:066308. <https://doi.org/10.1103/PhysRevE.77.066308>.
- [111] Wang Q, Ding Z, Wong G, et al. Skipping the Boundary Layer: High-Speed Droplet-Based Immunoassay Using Rayleigh Acoustic Streaming. *Anal Chem* 2023;95:6253–60. <https://doi.org/10.1021/acs.analchem.2c03877>.
- [112] Djukelic M, Wixforth A, Westerhausen C. Influence of neighboring adherent cells on laminar flow induced shear stress in vitro—A systematic study. *Biomicrofluidics* 2017;11:024115. <https://doi.org/10.1063/1.4979295>.
- [113] Peng D, Tong W, Collins DJ, et al. Mechanisms and Applications of Neuromodulation Using Surface Acoustic Waves—A Mini-Review. *Front Neurosci* 2021;15:37. <https://doi.org/10.3389/fnins.2021.629056>.
- [114] Kugler EM, Michel K, Kirchenbüchler D, et al. Sensitivity to Strain and Shear Stress of Isolated Mechanosensitive Enteric Neurons. *Neuroscience* 2018;372:213–24. <https://doi.org/10.1016/j.neuroscience.2017.12.052>.
- [115] Ravin R, Blank PS, Steinkamp A, et al. Shear forces during blast, not abrupt changes in pressure alone, generate calcium activity in human brain cells. *PLoS One* 2012;7:e39421. <https://doi.org/10.1371/journal.pone.0039421>.
- [116] Sivanantha N, Ma C, Collins DJ, et al. Characterization of adhesive properties of red blood cells using surface acoustic wave induced flows for rapid diagnostics. *Appl Phys Lett* 2014;105:103704. <https://doi.org/10.1063/1.4895472>.
- [117] Jötten AM, Angermann S, Stamp MEM, et al. Correlation of in vitro cell adhesion, local shear flow and cell density. *RSC Adv* 2018;9:543–51. <https://doi.org/10.1039/C8RA07416J>.
- [118] Bussonnière A, Miron Y, Baudoin M, et al. Cell detachment and label-free cell sorting using modulated surface acoustic waves (SAWs) in droplet-based microfluidics. *Lab Chip* 2014;14:3556. <https://doi.org/10.1039/C4LC00625A>.
- [119] Farooq U, Liu X, Zhou W, et al. Cell lysis induced by nanowire collision based on acoustic streaming using surface acoustic waves. *Sens Actuators B Chem* 2021;345:130335. <https://doi.org/10.1016/j.snb.2021.130335>.

- [120] Tan MK, Friend JR, Yeo LY. Microparticle collection and concentration via a miniature surface acoustic wave device. *Lab Chip* 2007;7:618–25. <https://doi.org/10.1039/B618044B>.
- [121] Schnitzler LG, Junger S, Loy DM, et al. Size tunable nanoparticle formation employing droplet fusion by acoustic streaming applied to polyplexes. *J Phys Appl Phys* 2019;52:244002. <https://doi.org/10.1088/1361-6463/ab131f>.
- [122] Li H, Friend JR, Yeo LY. Surface acoustic wave concentration of particle and bioparticle suspensions. *Biomed Microdevices* 2007;9:647–56. <https://doi.org/10.1007/s10544-007-9058-2>.
- [123] Destgeer G, Jung JH, Park J, et al. Particle Separation inside a Sessile Droplet with Variable Contact Angle Using Surface Acoustic Waves'. *Anal Chem* 2017;89:736-744,. <https://doi.org/10.1021/acs.analchem.6b03314>.
- [124] Nam H, Sung HJ, Park J, et al. Manipulation of cancer cells in a sessile droplet via travelling surface acoustic waves. *Lab Chip* 2021;22:47–56. <https://doi.org/10.1039/D1LC00801C>.
- [125] Ang KM, Yeo LY, Hung YM, et al. Amplitude modulation schemes for enhancing acoustically-driven microcentrifugation and micromixing. *Biomicrofluidics* 2016;10:054106. <https://doi.org/10.1063/1.4963103>.
- [126] Gelin P, Sardan Sukas Ö, Hellemans K, et al. Study on the mixing and migration behavior of micron-size particles in acoustofluidics. *Chem Eng J* 2019;369:370–5. <https://doi.org/10.1016/j.cej.2019.03.004>.
- [127] Rogers PR, Friend JR, Yeo LY. Exploitation of surface acoustic waves to drive size-dependent microparticle concentration within a droplet. *Lab Chip* 2010;10:2979–85. <https://doi.org/10.1039/c004822d>.
- [128] Bourquin Y, Syed A, Reboud J, et al. Rare-cell enrichment by a rapid, label-free, ultrasonic isopycnic technique for medical diagnostics. *Angew Chem Int Ed Engl* 2014;53:5587–90. <https://doi.org/10.1002/anie.201310401>.
- [129] Wang Z, Rich J, Hao N, et al. Acoustofluidics for simultaneous nanoparticle-based drug loading and exosome encapsulation. *Microsyst Nanoeng* 2022;8:1–11. <https://doi.org/10.1038/s41378-022-00374-2>.
- [130] Collignon S, Friend J, Yeo L. Planar microfluidic drop splitting and merging. *Lab Chip* 2015;15:1942–51. <https://doi.org/10.1039/c4lc01453g>.
- [131] Jung JH, Destgeer G, Ha B, et al. On-demand droplet splitting using surface acoustic waves. *Lab Chip* 2016;16:3235–43. <https://doi.org/10.1039/C6LC00648E>.
- [132] Liang W, Zhang F, Yang G, et al. Separation of water from a microliter oil/water mixed drop using Lamb waves on an inclined glass plate. *Microfluid Nanofluidics* 2017;21:2–5. <https://doi.org/10.1007/s10404-017-2002-8>.

- [133] Beyssen D, Le Brizoual L, Elmazria O, et al. Microfluidic device based on surface acoustic wave. *Sens Actuators B Chem* 2006;118:380–5. <https://doi.org/10.1016/j.snb.2006.04.084>.
- [134] Baudoin M, Brunet P, Matar OB, et al. Low power sessile droplets actuation via modulated surface acoustic waves. *Appl Phys Lett* 2012;100:154102. <https://doi.org/10.1063/1.3701725>.
- [135] Guttenberg Z, Müller H, Habermüller H, et al. Planar chip device for PCR and hybridization with surface acoustic wave pump. *Lab Chip* 2005;5:308–17. <https://doi.org/10.1039/b412712a>.
- [136] Chen C, Zhang SP, Mao Z, et al. Three-dimensional numerical simulation and experimental investigation of boundary-driven streaming in surface acoustic wave microfluidics. *Lab Chip* 2018;18:3645–54. <https://doi.org/10.1039/C8LC00589C>.
- [137] Bao J-Y, Zhang A-L. Transporting droplets by help of a medium on a piezoelectric substrate. *Ferroelectrics* 2020;558:199–206. <https://doi.org/10.1080/00150193.2020.1735903>.
- [138] Zhang A, Zha Y, Zhang J. A surface acoustic wave micropump to pump fluids from a droplet into a closed microchannel using evaporation and capillary effects. *AIP Adv* 2014;4:127144. <https://doi.org/10.1063/1.4905062>.
- [139] Ai Y, Marrone BL. Droplet translocation by focused surface acoustic waves. *Microfluid Nanofluidics* 2012;13:715–22. <https://doi.org/10.1007/s10404-012-0990-y>.
- [140] Du XY, Swanwick ME, Fu YQ, et al. Surface acoustic wave induced streaming and pumping in 128° Y-cut LiNbO₃ for microfluidic applications. *J Micromechanics Microengineering* 2009;19:035016. <https://doi.org/10.1088/0960-1317/19/3/035016>.
- [141] Luo JT, Gherardi NR, Guan JH, et al. Slippery Liquid-Infused Porous Surfaces and Droplet Transportation by Surface Acoustic Waves. *Phys Rev Appl* 2017;7:014017. <https://doi.org/10.1103/PhysRevApplied.7.014017>.
- [142] Wu L, Guo Z, Liu W. Surface behaviors of droplet manipulation in microfluidics devices. *Adv Colloid Interface Sci* 2022;308:102770. <https://doi.org/10.1016/j.cis.2022.102770>.
- [143] Tao R, Mchale G, Reboud J, et al. Hierarchical nanotexturing enables acoustofluidics on slippery yet sticky, flexible surfaces. *Nano Lett* 2020;20:3263–70. <https://doi.org/10.1021/acs.nanolett.0c00005>.
- [144] Wang Y, Tao X, Tao R, et al. Acoustofluidics along inclined surfaces based on AlN/Si Rayleigh surface acoustic waves. *Sens Actuators Phys* 2020;306:111967. <https://doi.org/10.1016/j.sna.2020.111967>.

- [145] Wixforth A, Strobl C, Gauer Ch, et al. Acoustic manipulation of small droplets. *Anal Bioanal Chem* 2004;379:982–91. <https://doi.org/10.1007/s00216-004-2693-z>.
- [146] Zhang SP, Lata J, Chen C, et al. Digital acoustofluidics enables contactless and programmable liquid handling. *Nat Commun* 2018;9:2928. <https://doi.org/10.1038/s41467-018-05297-z>.
- [147] Phan D-T, Chung G-S. The effect of geometry and post-annealing on surface acoustic wave characteristics of AlN thin films prepared by magnetron sputtering. *Appl Surf Sci* 2011;257:8696–701. <https://doi.org/10.1016/j.apsusc.2011.05.050>.
- [148] Darmawan M, Byun D. Focused surface acoustic wave induced jet formation on superhydrophobic surfaces. *Microfluid Nanofluidics* 2015;18:1107–14. <https://doi.org/10.1007/s10404-014-1503-y>.
- [149] Lee D, Lee N, Choi G, et al. Heat transfer characteristics of a focused surface acoustic wave (F-SAW) device for interfacial droplet jetting. *Inventions* 2018;3:38. <https://doi.org/10.3390/inventions3020038>.
- [150] Fu C, Quan AJ, Luo JT, et al. Vertical jetting induced by shear horizontal leaky surface acoustic wave on 36° Y-X LiTaO₃. *Appl Phys Lett* 2017;110:173501. <https://doi.org/10.1063/1.4982073>.
- [151] Rezk AR, Tan JK, Yeo LY. HYbriD Resonant Acoustics (HYDRA). *Adv Mater* 2016;28:1970–5. <https://doi.org/10.1002/adma.201504861>.
- [152] Rezk AR, Ramesan S, Yeo LY. Plug-and-actuate on demand: multimodal individual addressability of microarray plates using modular hybrid acoustic wave technology. *Lab Chip* 2018;18:406–11. <https://doi.org/10.1039/C7LC01099K>.
- [153] Laude V, Gérard D, Khelifaoui N, et al. Subwavelength focusing of surface acoustic waves generated by an annular interdigital transducer. *Appl Phys Lett* 2008;92:094104. <https://doi.org/10.1063/1.2891055>.
- [154] Zhou J, Pang HF, Garcia-Gancedo L, et al. Discrete microfluidics based on aluminum nitride surface acoustic wave devices. *Microfluid Nanofluidics* 2015;18:537–48. <https://doi.org/10.1007/s10404-014-1456-1>.
- [155] Guo YJ, Lv HB, Li YF, et al. High frequency microfluidic performance of LiNbO₃ and ZnO surface acoustic wave devices. *J Appl Phys* 2014;116. <https://doi.org/10.1063/1.4885038>.
- [156] Pang HF, Fu YQ, Garcia-Gancedo L, et al. Enhancement of microfluidic efficiency with nanocrystalline diamond interlayer in the ZnO-based surface acoustic wave device. *Microfluid Nanofluidics* 2013;15:377–86. <https://doi.org/10.1007/s10404-013-1155-3>.

- [157] Bhattacharjee PK, McDonnell AG, Prabhakar R, et al. Extensional flow of low-viscosity fluids in capillary bridges formed by pulsed surface acoustic wave jetting. *New J Phys* 2011;13. <https://doi.org/10.1088/1367-2630/13/2/023005>.
- [158] Castro JO, Ramesan S, Rezk AR, et al. Continuous tuneable droplet ejection via pulsed surface acoustic wave jetting. *Soft Matter* 2018;14:5721–7. <https://doi.org/10.1039/C7SM02534C>.
- [159] Chen K, Sui C, Wu Y, et al. A digital acoustofluidic device for on-demand and oil-free droplet generation. *Nanotechnology* 2018;30:084001. <https://doi.org/10.1088/1361-6528/aaf3fd>.
- [160] Demirci U. Acoustic picoliter droplets for emerging applications in semiconductor industry and biotechnology. *J Microelectromechanical Syst* 2006;15:957–66. <https://doi.org/10.1109/JMEMS.2006.878879>.
- [161] Li R, Gong Z, Wu Z, et al. Nozzle-free droplet generation with focused acoustic beams for encapsulation of single circulating tumor cells. *Nano Futur* 2020;4:045001. <https://doi.org/10.1088/2399-1984/abbf02>.
- [162] Li R, Gong Z, Yi K, et al. Efficient Detection and Single-Cell Extraction of Circulating Tumor Cells in Peripheral Blood. *ACS Appl Bio Mater* 2020;3:6521–8. <https://doi.org/10.1021/acsabm.0c00957>.
- [163] Wei X, Chen K, Cai B, et al. An Acoustic Droplet-Induced Enzyme Responsive Platform for the Capture and On-Demand Release of Single Circulating Tumor Cells. *ACS Appl Mater Interfaces* 2019;11:41118–26. <https://doi.org/10.1021/acsami.9b16566>.
- [164] Xia Y, Huang L-X, Chen H, et al. Acoustic Droplet Vitrification Method for High-Efficiency Preservation of Rare Cells. *ACS Appl Mater Interfaces* 2021;13:12950–9. <https://doi.org/10.1021/acsami.1c01452>.
- [165] Chen K, Jiang E, Wei X, et al. The acoustic droplet printing of functional tumor microenvironments. *Lab Chip* 2021;21:1604–12. <https://doi.org/10.1039/D1LC00003A>.
- [166] Qi A, Yeo LY, Friend JR. Interfacial destabilization and atomization driven by surface acoustic waves. *Phys Fluids* 2008;20:074103. <https://doi.org/10.1063/1.2953537>.
- [167] Ang KM, Yeo LY, Hung YM, et al. Graphene-mediated microfluidic transport and nebulization via high frequency Rayleigh wave substrate excitation. *Lab Chip* 2016;16:3503–14. <https://doi.org/10.1039/C6LC00780E>.
- [168] Rajapaksa A, Qi A, Yeo LY, et al. Enabling practical surface acoustic wave nebulizer drug delivery via amplitude modulation. *Lab Chip* 2014;14:1858–65. <https://doi.org/10.1039/C4LC00232F>.

- [169] Ang KM, Yeo LY, Friend JR, et al. Nozzleless spray cooling using surface acoustic waves. *J Aerosol Sci* 2015;79:48–60. <https://doi.org/10.1016/j.jaerosci.2014.10.004>.
- [170] Qi A, Friend JR, Yeo LY, et al. Miniature inhalation therapy platform using surface acoustic wave microfluidic atomization. *Lab Chip* 2009;9:2184–93. <https://doi.org/10.1039/B903575C>.
- [171] Ho J, Tan MK, Go DB, et al. Paper-Based Microfluidic Surface Acoustic Wave Sample Delivery and Ionization Source for Rapid and Sensitive Ambient Mass Spectrometry. *Anal Chem* 2011;83:3260–6. <https://doi.org/10.1021/ac200380q>.
- [172] Kwok PCL, McDonnell A, Tang P, et al. In vivo deposition study of a new generation nebuliser utilising hybrid resonant acoustic (HYDRA) technology. *Int J Pharm* 2020;580:119196. <https://doi.org/10.1016/j.ijpharm.2020.119196>.
- [173] Gracioso Martins AM, Glass NR, Harrison S, et al. Toward complete miniaturisation of flow injection analysis systems: microfluidic enhancement of chemiluminescent detection. *Anal Chem* 2014;86:10812–9. <https://doi.org/10.1021/ac502878p>.
- [174] Westerhausen C, Schnitzler LG, Wendel D, et al. Controllable Acoustic Mixing of Fluids in Microchannels for the Fabrication of Therapeutic Nanoparticles. *Micromachines* 2016;7. <https://doi.org/10.3390/mi7090150>.
- [175] Greco G, Agostini M, Shilton R, et al. Surface Acoustic Wave (SAW)-Enhanced Chemical Functionalization of Gold Films. *Sensors* 2017;17. <https://doi.org/10.3390/s17112452>.
- [176] Shilton RJ, Yeo LY, Friend JR. Quantification of surface acoustic wave induced chaotic mixing-flows in microfluidic wells. *Sens Actuators B Chem* 2011;160:1565–72. <https://doi.org/10.1016/j.snb.2011.09.007>.
- [177] Zeng Q, Guo F, Yao L, et al. Milliseconds mixing in microfluidic channel using focused surface acoustic wave. *Sens Actuators B Chem* 2011;160:1552–6. <https://doi.org/10.1016/j.snb.2011.08.075>.
- [178] Frommelt T, Kostur M, Wenzel-Schäfer M, et al. Microfluidic mixing via acoustically driven chaotic advection. *Phys Rev Lett* 2008;100:034502. <https://doi.org/10.1103/PhysRevLett.100.034502>.
- [179] Ahmed H, Park J, Destgeer G, et al. Surface acoustic wave-based micromixing enhancement using a single interdigital transducer. *Appl Phys Lett* 2019;114:043702. <https://doi.org/10.1063/1.5079815>.
- [180] Nam J, Lim CS. Micromixing using swirling induced by three-dimensional dual surface acoustic waves (3D-dSAW). *Sens Actuators B Chem* 2018;255:3434–40. <https://doi.org/10.1016/j.snb.2017.09.173>.

- [181] Nam J, Jang WS, Lim CS. Micromixing using a conductive liquid-based focused surface acoustic wave (CL-FSAW). *Sens Actuators B Chem* 2018;258:991–7. <https://doi.org/10.1016/j.snb.2017.11.188>.
- [182] Ahmed D, Mao X, Shi J, et al. A millisecond micromixer via single-bubble-based acoustic streaming. *Lab Chip* 2009;9:2738–41. <https://doi.org/10.1039/B903687C>.
- [183] Ahmed D, Chan CY, Lin S-CS, et al. Tunable, pulsatile chemical gradient generation via acoustically driven oscillating bubbles. *Lab Chip* 2013;13:328–31. <https://doi.org/10.1039/C2LC40923B>.
- [184] Orbay S, Ozcelik A, Lata J, et al. Mixing high-viscosity fluids via acoustically driven bubbles. *J Micromechanics Microengineering Struct Devices Syst* 2017;27:015008.
- [185] Ozcelik A, Ahmed D, Xie Y, et al. An Acoustofluidic Micromixer via Bubble Inception and Cavitation from Microchannel Sidewalls. *Anal Chem* 2014;86:5083–8. <https://doi.org/10.1021/ac5007798>.
- [186] Läubli NF, Gerlt MS, Wüthrich A, et al. Embedded Microbubbles for Acoustic Manipulation of Single Cells and Microfluidic Applications. *Anal Chem* 2021;93:9760–70. <https://doi.org/10.1021/acs.analchem.1c01209>.
- [187] Ovchinnikov M, Zhou J, Yalamanchili S. Acoustic streaming of a sharp edge. *J Acoust Soc Am* 2014;136:22–9. <https://doi.org/10.1121/1.4881919>.
- [188] Endaylalu SA, Tien W-H. Mixing enhancement in T-junction microchannel with acoustic streaming induced by triangular structure. *Biomicrofluidics* 2021;15:034102. <https://doi.org/10.1063/5.0042541>.
- [189] Doinikov A, Gerlt M, Pavlic A, et al. Acoustic streaming produced by sharp-edge structures in microfluidic devices. *Microfluid Nanofluidics* 2020;24:32. <https://doi.org/10.1007/s10404-020-02335-5>.
- [190] Nama N, Huang P-H, Huang TJ, et al. Investigation of micromixing by acoustically oscillated sharp-edges. *Biomicrofluidics* 2016;10:024124. <https://doi.org/10.1063/1.4946875>.
- [191] Nama N, Huang P-H, Huang TJ, et al. Investigation of acoustic streaming patterns around oscillating sharp edges. *Lab Chip* 2014;14:2824–36. <https://doi.org/10.1039/C4LC00191E>.
- [192] Zhang C, Guo X, Brunet P, et al. Acoustic streaming near a sharp structure and its mixing performance characterization. *Microfluid Nanofluidics* 2019;23:104. <https://doi.org/10.1007/s10404-019-2271-5>.
- [193] Boss J, Poland W. Evaluation of the homogeneity degree of a mixture. *Bulk Solids Handl* 1986;6:1207–15.

- [194] Huang P-H, Xie Y, Ahmed D, et al. An acoustofluidic micromixer based on oscillating sidewall sharp-edges. *Lab Chip* 2013;13:3847–52. <https://doi.org/10.1039/C3LC50568E>.
- [195] Zhang C, Guo X, Royon L, et al. Unveiling of the mechanisms of acoustic streaming induced by sharp edges. *Phys Rev E* 2020;102:043110. <https://doi.org/10.1103/PhysRevE.102.043110>.
- [196] Zhao S, He W, Ma Z, et al. On-chip stool liquefaction via acoustofluidics. *Lab Chip* 2019;19:941–7. <https://doi.org/10.1039/c8lc01310a>.
- [197] Wang Z, Huang P-H, Chen C, et al. Cell lysis via acoustically oscillating sharp edges. *Lab Chip* 2019;19:4021–32. <https://doi.org/10.1039/c9lc00498j>.
- [198] Huang P-H, Nama N, Mao Z, et al. A reliable and programmable acoustofluidic pump powered by oscillating sharp-edge structures. *Lab Chip* 2014;14:4319–23. <https://doi.org/10.1039/C4LC00806E>.
- [199] Ozcelik A, Nama N, Huang P-H, et al. Acoustofluidic Rotational Manipulation of Cells and Organisms Using Oscillating Solid Structures. *Small Weinh Bergstr Ger* 2016;12:5120–5. <https://doi.org/10.1002/sml.201601760>.
- [200] Feng L, Song B, Zhang D, et al. On-Chip Tunable Cell Rotation Using Acoustically Oscillating Asymmetrical Microstructures. *Micromachines* 2018;9:596. <https://doi.org/10.3390/mi9110596>.
- [201] Sun L, Lehnert T, Gijs MAM, et al. Polydimethylsiloxane microstructure-induced acoustic streaming for enhanced ultrasonic DNA fragmentation on a microfluidic chip. *Lab Chip* 2022;22:4224–37. <https://doi.org/10.1039/D2LC00366J>.
- [202] Lin L, Dang H, Zhu R, et al. Effects of Side Profile on Acoustic Streaming by Oscillating Microstructures in Channel. *Micromachines* 2022;13:1439. <https://doi.org/10.3390/mi13091439>.
- [203] Zhou M, Gao D, Yang Z, et al. Streaming-enhanced, chip-based biosensor with acoustically active, biomarker-functionalized micropillars: A case study of thrombin detection. *Talanta* 2021;222:121480. <https://doi.org/10.1016/j.talanta.2020.121480>.
- [204] Hayakawa T, Sakuma S, Arai F. On-chip 3D rotation of oocyte based on a vibration-induced local whirling flow. *Microsyst Nanoeng* 2015;1:1–9. <https://doi.org/10.1038/micronano.2015.1>.
- [205] Hayakawa T, Sakuma S, Fukuhara T, et al. A Single Cell Extraction Chip Using Vibration-Induced Whirling Flow and a Thermo-Responsive Gel Pattern. *Micromachines* 2014;5:681–96. <https://doi.org/10.3390/mi5030681>.
- [206] Lu X, Martin A, Soto F, et al. Parallel Label-Free Isolation of Cancer Cells Using Arrays of Acoustic Microstreaming Traps. *Adv Mater Technol* 2019;4:1800374. <https://doi.org/10.1002/admt.201800374>.

- [207] Shen H, Zhao K, Wang Z, et al. Local Acoustic Fields Powered Assembly of Microparticles and Applications. *Micromachines* 2019;10:882. <https://doi.org/10.3390/mi10120882>.
- [208] Brugger MS, Baumgartner K, Mauritz SCF, et al. Vibration enhanced cell growth induced by surface acoustic waves as in vitro wound-healing model. *Proc Natl Acad Sci* 2020;117:31603–13. <https://doi.org/10.1073/pnas.2005203117>.
- [209] Liao D, Li F, Lu D, et al. Activation of Piezo1 mechanosensitive ion channel in HEK293T cells by 30 MHz vertically deployed surface acoustic waves. *Biochem Biophys Res Commun* 2019;518:541–7. <https://doi.org/10.1016/j.bbrc.2019.08.078>.
- [210] Sun C, Dong Y, Wei J, et al. Acoustically accelerated neural differentiation of human embryonic stem cells. *Acta Biomater* 2022. <https://doi.org/10.1016/j.actbio.2022.07.041>.
- [211] Ramesan S, Rezk AR, Cevaal PM, et al. Acoustofection: High-Frequency Vibrational Membrane Permeabilization for Intracellular siRNA Delivery into Nonadherent Cells. *ACS Appl Bio Mater* 2021;4:2781–9. <https://doi.org/10.1021/acsbam.1c00003>.
- [212] Wu M, Chen C, Wang Z, et al. Separating extracellular vesicles and lipoproteins via acoustofluidics. *Lab Chip* 2019;19:1174–82. <https://doi.org/10.1039/C8LC01134F>.
- [213] Wang Z, Wang H, Becker R, et al. Acoustofluidic separation enables early diagnosis of traumatic brain injury based on circulating exosomes. *Microsyst Nanoeng* 2021;7:1–11. <https://doi.org/10.1038/s41378-021-00244-3>.
- [214] Li P, Mao Z, Peng Z, et al. Acoustic separation of circulating tumor cells. *Proc Natl Acad Sci U S A* 2015;112:4970–5. <https://doi.org/10.1073/pnas.1504484112>.
- [215] Altay R, Yapici MK, Koşar A. A Hybrid Spiral Microfluidic Platform Coupled with Surface Acoustic Waves for Circulating Tumor Cell Sorting and Separation: A Numerical Study. *Biosensors* 2022;12:171. <https://doi.org/10.3390/bios12030171>.
- [216] Wang K, Zhou W, Lin Z, et al. Sorting of tumour cells in a microfluidic device by multi-stage surface acoustic waves. *Sens Actuators B Chem* 2018;258:1174–83. <https://doi.org/10.1016/j.snb.2017.12.013>.
- [217] Ma Z, Collins DJ, Ai Y. Detachable Acoustofluidic System for Particle Separation via a Traveling Surface Acoustic Wave. *Anal Chem* 2016;88:5316–23. <https://doi.org/10.1021/acs.analchem.6b00605>.
- [218] Ng JW, Devendran C, Neild A. Acoustic tweezing of particles using decaying opposing travelling surface acoustic waves (DOTSAW). *Lab Chip* 2017;17. <https://doi.org/10.1039/C7LC00862G>.

- [219] Collins DJ, Khoo BL, Ma Z, et al. Selective particle and cell capture in a continuous flow using micro-vortex acoustic streaming. *Lab Chip* 2017;17:1769–77. <https://doi.org/10.1039/C7LC00215G>.
- [220] Collins DJ, Ma Z, Ai Y. Highly Localized Acoustic Streaming and Size-Selective Submicrometer Particle Concentration Using High Frequency Microscale Focused Acoustic Fields. *Anal Chem* 2016;88:5513–22. <https://doi.org/10.1021/acs.analchem.6b01069>.
- [221] Zhou Y, Ma Z, Ai Y. Hybrid microfluidic sorting of rare cells based on high throughput inertial focusing and high accuracy acoustic manipulation. *RSC Adv* 2019;9:31186–95. <https://doi.org/10.1039/C9RA01792E>.
- [222] Wang Y, Pan H, Mei D, et al. Programmable motion control and trajectory manipulation of microparticles through tri-directional symmetrical acoustic tweezers. *Lab Chip* 2022;22:1149–61. <https://doi.org/10.1039/D2LC00046F>.
- [223] Riaud A, Thomas J-L, Charron E, et al. Anisotropic Swirling Surface Acoustic Waves from Inverse Filtering for On-Chip Generation of Acoustic Vortices. *Phys Rev Appl* 2015;4:034004. <https://doi.org/10.1103/PhysRevApplied.4.034004>.
- [224] Li J, Crivoi A, Peng X, et al. Three dimensional acoustic tweezers with vortex streaming. *Commun Phys* 2021;4:1–8. <https://doi.org/10.1038/s42005-021-00617-0>.
- [225] Glass NR, Shilton RJ, Chan PPY, et al. Miniaturized Lab-on-a-Disc (miniLOAD). *Small* 2012;8:1881–8. <https://doi.org/10.1002/smll.201102282>.
- [226] Tan MK, Siddiqi A, Yeo LY. A Facile and Flexible Method for On-Demand Directional Speed Tunability in the Miniaturised Lab-on-a-Disc. *Sci Rep* 2017;7. <https://doi.org/10.1038/s41598-017-07025-x>.
- [227] Park J, Destgeer G, Afzal M, et al. Acoustofluidic generation of droplets with tunable chemical concentrations. *Lab Chip* 2020;20:3922–9. <https://doi.org/10.1039/D0LC00803F>.
- [228] Bussiere V, Vigne A, Link A, et al. High-Throughput Triggered Merging of Surfactant-Stabilized Droplet Pairs Using Traveling Surface Acoustic Waves. *Anal Chem* 2019;91:13978–85. <https://doi.org/10.1021/acs.analchem.9b03521>.
- [229] Link A, McGrath JS, Zaimagaoglu M, et al. Active single cell encapsulation using SAW overcoming the limitations of Poisson distribution. *Lab Chip* 2022;22:193–200. <https://doi.org/10.1039/D1LC00880C>.
- [230] Zhang P, Wang W, Fu H, et al. Deterministic droplet coding via acoustofluidics. *Lab Chip* 2020;20:4466–73. <https://doi.org/10.1039/D0LC00538J>.
- [231] Zhang N, Horesh A, Friend J. Manipulation and Mixing of 200 Femtoliter Droplets in Nanofluidic Channels Using MHz-Order Surface Acoustic Waves. *Adv Sci* 2021;8:2100408. <https://doi.org/10.1002/advs.202100408>.

- [232] Miansari M, Friend JR. Acoustic Nanofluidics via Room-Temperature Lithium Niobate Bonding: A Platform for Actuation and Manipulation of Nanoconfined Fluids and Particles. *Adv Funct Mater* 2016;26:7861–72. <https://doi.org/10.1002/adfm.201602425>.
- [233] Greco G, Agostini M, Tonazzini I, et al. Surface-Acoustic-Wave (SAW)-Driven Device for Dynamic Cell Cultures. *Anal Chem* 2018;90:7450–7. <https://doi.org/10.1021/acs.analchem.8b00972>.
- [234] Sreejith S, Kishor R, Abbas A, et al. Nanomechanical Microfluidic Mixing and Rapid Labeling of Silica Nanoparticles using Allenamide-Thiol Covalent Linkage for Bioimaging. *ACS Appl Mater Interfaces* 2019. <https://doi.org/10.1021/acsami.8b20315>.
- [235] Celik Cogal G, Das PK, Yurdabak Karaca G, et al. Fluorescence Detection of miRNA-21 Using Au/Pt Bimetallic Tubular Micromotors Driven by Chemical and Surface Acoustic Wave Forces. *ACS Appl Bio Mater* 2021;4:7932–41. <https://doi.org/10.1021/acsabm.1c00854>.
- [236] Xu C, Wang C, Zheng T, et al. Surface acoustic wave (SAW)-induced synthesis of HKUST-1 with different morphologies and sizes. *CrystEngComm* 2018;20:7275–80. <https://doi.org/10.1039/C8CE01144C>.
- [237] Bai C, Wang C, Zheng T, et al. Growth of β -glycine crystals promoted by standing surface acoustic waves (SSAWs). *CrystEngComm* 2018;20:1245–51. <https://doi.org/10.1039/C7CE02038D>.
- [238] Tengfei Z, Chaohui W, Baogang M, et al. Isolation of sodium chloride crystals induced by standing surface acoustic waves (SSAWs) in a drying droplet. *CrystEngComm* 2016;18:6784–8. <https://doi.org/10.1039/C6CE01151A>.
- [239] Hsu J-C, Lin Y-D. Microparticle concentration and separation inside a droplet using phononic-crystal scattered standing surface acoustic waves. *Sens Actuators Phys* 2019;300:111651. <https://doi.org/10.1016/j.sna.2019.111651>.
- [240] Han JL, Hu H, Huang QY, et al. Particle separation by standing surface acoustic waves inside a sessile droplet. *Sens Actuators Phys* 2021;326:112731. <https://doi.org/10.1016/j.sna.2021.112731>.
- [241] Sun D, F. Böhringer K, Sorensen M, et al. Droplet delivery and nebulization system using surface acoustic wave for mass spectrometry. *Lab Chip* 2020;20:3269–77. <https://doi.org/10.1039/D0LC00495B>.
- [242] Sui M, Dong H, Mu G, et al. Droplet transportation by adjusting the temporal phase shift of surface acoustic waves in the exciter–exciter mode. *Lab Chip* 2022;22:3402–11. <https://doi.org/10.1039/D2LC00402J>.
- [243] Lei Y, Hu H, Chen J, et al. Microfluidic jetting deformation and pinching-off mechanism in capillary tubes by using traveling surface acoustic waves. *Actuators* 2020;9:5. <https://doi.org/10.3390/act9010005>.

- [244] Jo MC, Guldiken R. Dual surface acoustic wave-based active mixing in a microfluidic channel. *Sens Actuators Phys* 2013;196:1–7. <https://doi.org/10.1016/j.sna.2013.03.028>.
- [245] Sriphutkiat Y, Zhou Y. Particle Accumulation in a Microchannel and Its Reduction by a Standing Surface Acoustic Wave (SSAW). *Sensors* 2017;17:106. <https://doi.org/10.3390/s17010106>.
- [246] Zhang A, Zha Y. Single-drop liquid phase microextraction accelerated by surface acoustic wave. *J Sep Sci* 2013;36:1085–9. <https://doi.org/10.1002/jssc.201200973>.
- [247] Zhang A-L, Zha Y. Rapid drop-to-drop liquid–liquid microextraction by help of surface acoustic wave. *Chem Eng Process Process Intensif* 2012;62:145–9. <https://doi.org/10.1016/j.cep.2012.07.014>.
- [248] Fakhfour A, Devendran C, Ahmed A, et al. The size dependant behaviour of particles driven by a travelling surface acoustic wave (TSAW). *Lab Chip* 2018;18:3926–38. <https://doi.org/10.1039/C8LC01155A>.
- [249] Wu F, Shen MH, Yang J, et al. An Enhanced Tilted-Angle Acoustofluidic Chip for Cancer Cell Manipulation. *IEEE Electron Device Lett* 2021;PP:1–1. <https://doi.org/10.1109/LED.2021.3062292>.
- [250] Li S, Ma F, Bachman H, et al. Acoustofluidic bacteria separation. *J Micromechanics Microengineering* 2016;27:015031. <https://doi.org/10.1088/1361-6439/27/1/015031>.
- [251] Mu C, Zhang Z, Lin M, et al. Development of a highly effective multi-stage surface acoustic wave SU-8 microfluidic concentrator. *Sens Actuators B Chem* 2015;215:77–85.
- [252] Jo MC, Guldiken R. A label-free cell separation using surface acoustic waves. 2011 Annu. Int. Conf. IEEE Eng. Med. Biol. Soc., 2011, p. 7691–4. <https://doi.org/10.1109/IEMBS.2011.6091895>.
- [253] Jo MC, Guldiken R. Active density-based separation using standing surface acoustic waves. *Sens Actuators Phys* 2012;187:22–8. <https://doi.org/10.1016/j.sna.2012.08.020>.
- [254] Hsu J-C, Hsu C-H, Huang Y-W. Acoustophoretic control of microparticle transport using dual-wavelength surface acoustic wave devices. *Micromachines* 2019;10:52.
- [255] Ren L, Yang S, Zhang P, et al. Standing Surface Acoustic Wave (SSAW)-Based Fluorescence-Activated Cell Sorter. *Small* 2018;14:1801996. <https://doi.org/10.1002/smll.201801996>.
- [256] Jo MC, Guldiken R. Particle manipulation by phase-shifting of surface acoustic waves. *Sens Actuators Phys* 2014;207:39–42. <https://doi.org/10.1016/j.sna.2013.12.020>.

- [257] Simon G, Andrade MAB, Reboud J, et al. Particle separation by phase modulated surface acoustic waves. *Biomicrofluidics* 2017;11:054115. <https://doi.org/10.1063/1.5001998>.
- [258] Lee J, Rhyou C, Kang B, et al. Continuously phase-modulated standing surface acoustic waves for separation of particles and cells in microfluidic channels containing multiple pressure nodes. *J Phys Appl Phys* 2017;50:165401. <https://doi.org/10.1088/1361-6463/aa62d5>.
- [259] Collins DJ, Devendran C, Ma Z, et al. Acoustic tweezers via sub-time-of-flight regime surface acoustic waves. *Sci Adv* 2016;2:e1600089. <https://doi.org/10.1126/sciadv.1600089>.
- [260] Nam J, Lim H, Kim C, et al. Density-dependent separation of encapsulated cells in a microfluidic channel by using a standing surface acoustic wave. *Biomicrofluidics* 2012;6:024120. <https://doi.org/10.1063/1.4718719>.
- [261] Ding X, Lin S-CS, Lapsley MI, et al. Standing surface acoustic wave (SSAW) based multichannel cell sorting. *Lab Chip* 2012;12:4228–31. <https://doi.org/10.1039/C2LC40751E>.
- [262] Shamloo A, Boodaghi M. Design and simulation of a microfluidic device for acoustic cell separation. *Ultrasonics* 2018;84:234–43. <https://doi.org/10.1016/j.ultras.2017.11.009>.
- [263] Li S, Ding X, Mao Z, et al. Standing surface acoustic wave (SSAW)-based cell washing. *Lab Chip* 2015;15:331–8. <https://doi.org/10.1039/c4lc00903g>.
- [264] Wu M, Ouyang Y, Wang Z, et al. Isolation of exosomes from whole blood by integrating acoustics and microfluidics. *Proc Natl Acad Sci U S A* 2017;114:10584–9. <https://doi.org/10.1073/pnas.1709210114>.
- [265] Feng G, Peng L, Jarrod BF, et al. Controlling cell–cell interactions using surface acoustic waves. *Proc Natl Acad Sci* 2015;112:43. <https://doi.org/10.1073/pnas.1422068112>.
- [266] Collins DJ, Morahan B, Garcia-Bustos J, et al. Two-dimensional single-cell patterning with one cell per well driven by surface acoustic waves. *Nat Commun* 2015;6:8686. <https://doi.org/10.1038/ncomms9686>.
- [267] Devendran C, Gunasekara NR, Collins DJ, et al. Batch process particle separation using surface acoustic waves (SAW): integration of travelling and standing SAW. *RSC Adv* 2016;6:5856–64. <https://doi.org/10.1039/C5RA26965B>.
- [268] Zheng T, Wang C, Xu C, et al. Patterning microparticles into a two-dimensional pattern using one column standing surface acoustic waves. *Sens Actuators Phys* 2018;284:168–71. <https://doi.org/10.1016/j.sna.2018.10.001>.

- [269] Guo F, Mao Z, Chen Y, et al. Three-dimensional manipulation of single cells using surface acoustic waves. *Proc Natl Acad Sci* 2016;113:1522–7. <https://doi.org/10.1073/pnas.1524813113>.
- [270] Yang S, Tian Z, Wang Z, et al. Harmonic acoustics for dynamic and selective particle manipulation. *Nat Mater* 2022;21:540–6. <https://doi.org/10.1038/s41563-022-01210-8>.
- [271] Tian Z, Yang S, Huang P-H, et al. Wave number–spiral acoustic tweezers for dynamic and reconfigurable manipulation of particles and cells. *Sci Adv* 2019;5:eaau6062. <https://doi.org/10.1126/sciadv.aau6062>.
- [272] Bernard I, Doinikov AA, Marmottant P, et al. Controlled rotation and translation of spherical particles or living cells by surface acoustic waves. *Lab Chip* 2017;17:2470–80. <https://doi.org/10.1039/C7LC00084G>.
- [273] Naseer SM, Manbachi A, Samandari M, et al. Surface acoustic waves induced micropatterning of cells in gelatin methacryloyl (GelMA) hydrogels. *Biofabrication* 2017;9:015020. <https://doi.org/10.1088/1758-5090/aa585e>.
- [274] Tao X, Nguyen TD, Jin H, et al. 3D patterning/manipulating microparticles and yeast cells using ZnO/Si thin film surface acoustic waves. *Sens Actuators B Chem* 2019;299. <https://doi.org/10.1016/j.snb.2019.126991>.
- [275] Nguyen TD, Tran VT, Fu YQ, et al. Patterning and manipulating microparticles into a three-dimensional matrix using standing surface acoustic waves. *Appl Phys Lett* 2018;112:213507. <https://doi.org/10.1063/1.5024888>.
- [276] Ding X, Lin S-CS, Kiraly B, et al. On-chip manipulation of single microparticles, cells, and organisms using surface acoustic waves. *Proc Natl Acad Sci* 2012;109:11105–9.
- [277] Chen B, Wu Y, Ao Z, et al. High-throughput acoustofluidic fabrication of tumor spheroids. *Lab Chip* 2019;19:1755–63. <https://doi.org/10.1039/C9LC00135B>.
- [278] Chen K, Wu M, Guo F, et al. Rapid formation of size-controllable multicellular spheroids via 3D acoustic tweezers. *Lab Chip* 2016;16:2636–43. <https://doi.org/10.1039/C6LC00444J>.
- [279] Destgeer G, Sung HJ. Recent advances in microfluidic actuation and micro-object manipulation via surface acoustic waves. *Lab Chip* 2015;15:2722–38. <https://doi.org/10.1039/C5LC00265F>.
- [280] Guex AG, Di Marzio N, Eglin D, et al. The waves that make the pattern: a review on acoustic manipulation in biomedical research. *Mater Today Bio* 2021;10:100110. <https://doi.org/10.1016/j.mtbio.2021.100110>.
- [281] Li Y, Cai S, Shen H, et al. Recent advances in acoustic microfluidics and its exemplary applications. *Biomicrofluidics* 2022;16:031502. <https://doi.org/10.1063/5.0089051>.

- [282] Zhang P, Bachman H, Ozcelik A, et al. Acoustic Microfluidics. *Annu Rev Anal Chem Palo Alto Calif* 2020;13:17–43. <https://doi.org/10.1146/annurev-anchem-090919-102205>.
- [283] Zhang AL, Wu ZQ, Xia XH. Transportation and mixing of droplets by surface acoustic wave. *Talanta* 2011;84:293–7. <https://doi.org/10.1016/j.talanta.2011.01.017>.
- [284] Fogel R, Limson J, Seshia AA. Acoustic biosensors. *Essays Biochem* 2016;60:101–10. <https://doi.org/10.1042/EBC20150011>.
- [285] Länge K. Bulk and Surface Acoustic Wave Sensor Arrays for Multi-Analyte Detection: A Review. *Sensors* 2019;19:E5382. <https://doi.org/10.3390/s19245382>.
- [286] Mujahid A, Dickert FL. Surface Acoustic Wave (SAW) for Chemical Sensing Applications of Recognition Layers. *Sensors* 2017;17:E2716. <https://doi.org/10.3390/s17122716>.
- [287] Destgeer G, Ha BH, Jung JH, et al. Submicron separation of microspheres via travelling surface acoustic waves. *Lab Chip* 2014;14:4665–72. <https://doi.org/10.1039/C4LC00868E>.
- [288] Malocha D. *The Electrical Engineering Handbook* Ed. Richard C. Dorf Boca Raton: CRC Press LLC, 2000 2000.
- [289] Morgans DP. *Surface Acoustic Wave Devices for Signal processing*. Elsevier; 1991.
- [290] Feldmann M, Henaff J. *Surface Acoustic Waves for Signal Processing* 1989.
- [291] Winkler A, Brünig R, Faust C, et al. Towards efficient surface acoustic wave (SAW)-based microfluidic actuators. *Sens Actuators Phys* 2016;247:259–68. <https://doi.org/10.1016/j.sna.2016.06.006>.
- [292] Kirschner J. *Surface Acoustic Wave Sensors (SAWS) : Design for Application*, 2010.
- [293] Rocha-Gaso M-I, Jimenez Y, Francis LA, et al. Love Wave Biosensors: A Review, 2013. <https://doi.org/10.5772/53077>.
- [294] Zhang N, Mei J, Gopesh T, et al. Optimized, Omnidirectional Surface Acoustic Wave Source: 152° Y-Rotated Cut of Lithium Niobate for Acoustofluidics. *IEEE Trans Ultrason Ferroelectr Freq Control* 2020;67:2176–86. <https://doi.org/10.1109/TUFFC.2020.2993766>.
- [295] Anisimkin VI. Anisotropy of the acoustic plate modes in ST-quartz and 128°Y-LiNbO₃. *IEEE Trans Ultrason Ferroelectr Freq Control* 2014;61:120–32. <https://doi.org/10.1109/tuffc.2014.6689780>.

- [296] Smirnov A, Anisimkin V, Voronova N, et al. Multimode Design and Piezoelectric Substrate Anisotropy Use to Improve Performance of Acoustic Liquid Sensors. *Sensors* 2022;22:7231. <https://doi.org/10.3390/s22197231>.
- [297] Weser R, Winkler A, Weihnacht M, et al. The complexity of surface acoustic wave fields used for microfluidic applications. *Ultrasonics* 2020;106:106160. <https://doi.org/10.1016/j.ultras.2020.106160>.
- [298] Ntagwirumugara E, Gryba T, Zhang VY, et al. Analysis of frequency response of IDT/ZnO/Si SAW filter using the coupling of modes model. *IEEE Trans Ultrason Ferroelectr Freq Control* 2007;54:2011–5.
- [299] Akiyama M, Nagao K, Ueno N, et al. Influence of metal electrodes on crystal orientation of aluminum nitride thin films. *Vacuum* 2004;74:699–703.
- [300] Vorobiev A, Gevorgian S. Impact of the electrode material and shape on performance of intrinsically tunable ferroelectric FBARs. *IEEE Trans Ultrason Ferroelectr Freq Control* 2014;61:840–8. <https://doi.org/10.1109/TUFFC.2014.2975>.
- [301] Soluch W, Brzozowski E. Effect of metal electrodes on surface acoustic wave properties in bulk Z-cut GaN crystal. *IEEE Trans Electron Devices* 2014;61:3395–8.
- [302] Chen J, He X, Wang W, et al. Bendable transparent ZnO thin film surface acoustic wave strain sensors on ultra-thin flexible glass substrates. *J Mater Chem C* 2014;2:9109–14.
- [303] Zhou J, Wu XZ, Xiao DB, et al. Deposition of aluminum doped ZnO as electrode for transparent ZnO/glass surface acoustic wave devices. *Surf Coat Technol* 2017;320:39–46. <https://doi.org/10.1016/j.surfcoat.2017.02.013>.
- [304] Mišeikis V, Shilton RJ, Travagliati M, et al. Acoustic streaming of microparticles using graphene-based interdigital transducers. *Nanotechnology* 2021;32:375503. <https://doi.org/10.1088/1361-6528/ac0473>.
- [305] Zhou J, Zheng J, Shi X, et al. Graphene-Based Fully Transparent Thin Film Surface Acoustic Wave Devices for Sensing and Lab-on-Chip Applications. *J Electrochem Soc* 2019;166:B432. <https://doi.org/10.1149/2.0981906jes>.
- [306] Yao Y, Xue Y. Influence of the oxygen content on the humidity sensing properties of functionalized graphene films based on bulk acoustic wave humidity sensors. *Sens Actuators B Chem* 2016;222:755–62.
- [307] Mayorov AS, Hunter N, Muchenje W, et al. Surface acoustic wave generation and detection using graphene interdigitated transducers on lithium niobate. *Appl Phys Lett* 2014;104:083509.
- [308] Roshchupkin D, Ortega L, Zizak I, et al. Surface acoustic wave propagation in graphene film. *J Appl Phys* 2015;118:104901.

- [309] Zhou J, Shi X, Xiao D, et al. Surface acoustic wave devices with graphene interdigitated transducers. *J Micromechanics Microengineering* 2019;29:015006. <https://doi.org/10.1088/1361-6439/aeee61>.
- [310] Fu YQ, Garcia-Gancedo L, Pang HF, et al. Microfluidics based on ZnO/nanocrystalline diamond surface acoustic wave devices. *Biomicrofluidics* 2012;6:24105–2410511. <https://doi.org/10.1063/1.3699974>.
- [311] Jin H, Zhou J, He X, et al. Flexible surface acoustic wave resonators built on disposable plastic film for electronics and lab-on-a-chip applications. *Sci Rep* 2013;3:2140. <https://doi.org/10.1038/srep02140>.
- [312] Lee D-S, Luo J, Fu Y, et al. Nanocrystalline ZnO film layer on silicon and its application to surface acoustic wave-based streaming. *J Nanosci Nanotechnol* 2008;8:4626–9. <https://doi.org/10.1166/jnn.2008.ic44>.
- [313] Sun C, Wu F, Fu Y, et al. Thin film Gallium nitride (GaN) based acoustofluidic Tweezer: Modelling and microparticle manipulation. *Ultrasonics* 2020;108:106202. <https://doi.org/10.1016/j.ultras.2020.106202>.
- [314] Sun C, Wu F, Wallis DJ, et al. Gallium Nitride: A Versatile Compound Semiconductor as Novel Piezoelectric Film for Acoustic Tweezer in Manipulation of Cancer Cells. *IEEE Trans Electron Devices* 2020;67:3355–61. <https://doi.org/10.1109/TED.2020.3002498>.
- [315] Büyükköse S, Vratzov B, van der Veen J, et al. Ultrahigh-frequency surface acoustic wave generation for acoustic charge transport in silicon. *Appl Phys Lett* 2013;102:013112. <https://doi.org/10.1063/1.4774388>.
- [316] Büyükköse S, Vratzov B, Ataç D, et al. Ultrahigh-frequency surface acoustic wave transducers on ZnO/SiO₂/Si using nanoimprint lithography. *Nanotechnology* 2012;23:315303.
- [317] Zhou J, Zhang D, Liu Y, et al. Record-breaking frequency of 44 GHz based on the higher order mode of surface acoustic waves with LiNbO₃/SiO₂/SiC heterostructures. *Engineering* 2022:S2095809922003575. <https://doi.org/10.1016/j.eng.2022.05.003>.
- [318] Zahertar S, Torun H, Sun C, et al. Flexible Platform of Acoustofluidics and Metamaterials with Decoupled Resonant Frequencies. *Sensors* 2022;22:4344. <https://doi.org/10.3390/s22124344>.
- [319] Ma Z, Teo AJT, Tan SH, et al. Self-Aligned Interdigitated Transducers for Acoustofluidics. *Micromachines* 2016;7. <https://doi.org/10.3390/mi7120216>.
- [320] Rezk AR, Friend JR, Yeo LY. Simple, low cost MHz-order acoustofluidics using aluminium foil electrodes. *Lab Chip* 2014;14:1802–5. <https://doi.org/10.1039/C4LC00182F>.

- [321] Hodgson RP, Tan M, Yeo L, et al. Transmitting high power rf acoustic radiation via fluid couplants into superstrates for microfluidics. *Appl Phys Lett* 2009;94:024102. <https://doi.org/10.1063/1.3049128>.
- [322] Fu C, Lee K, Lee K, et al. A stable and highly sensitive strain sensor based on a surface acoustic wave oscillator. *Sens Actuators Phys* 2014;218:80–7.
- [323] Lehtonen S, Plessky VP, Hartmann CS, et al. SPUDT filters for the 2.45 GHz ISM band. *IEEE Trans Ultrason Ferroelectr Freq Control* 2004;51:1697–703. <https://doi.org/10.1109/TUFFFC.2004.1386687>.
- [324] Nakamura H, Yamada T, Ishizaki T, et al. A new design concept for low-loss SAW filters based on different-width split-finger SPUDT. *IEEE Trans Microw Theory Tech* 2001;49:761–8. <https://doi.org/10.1109/22.915461>.
- [325] Kodama T, Kawabata H, Sato H, et al. Design of low-loss saw filters employing distributed acoustic reflection transducers. *Electron Commun Jpn Part II Electron* 1987;70:32–44. <https://doi.org/10.1002/ecjb.4420700904>.
- [326] Morgan DP. Quasi-static analysis of floating-electrode unidirectional SAW transducers (FEUDT's). 1999 IEEE Ultrason. Symp. Proc. Int. Symp. Cat No99CH37027, vol. 1, 1999, p. 107–11 vol.1. <https://doi.org/10.1109/ULTSYM.1999.849366>.
- [327] de Lima Jr MM, Alsina F, Seidel W, et al. Focusing of surface-acoustic-wave fields on (100) GaAs surfaces. *J Appl Phys* 2003;94:7848–55.
- [328] Wu T-T, Tang H-T, Chen Y-Y, et al. Analysis and design of focused interdigital transducers. *IEEE Trans Ultrason Ferroelectr Freq Control* 2005;52:1384–92. <https://doi.org/10.1109/TUFFFC.2005.1509798>.
- [329] Lamothe M, Plessky V, Friedt J-M, et al. Ultra-wideband SAW sensors and tags. *Electron Lett* 2013;49:1576–7. <https://doi.org/10.1049/el.2013.3333>.
- [330] Plessky V, Lamothe M. Hyperbolically frequency modulated transducer in SAW sensors and tags. *Electron Lett* 2013;49:1503–4.
- [331] Ding X, Shi J, Steven Lin S-C, et al. Tunable patterning of microparticles and cells using standing surface acoustic waves. *Lab Chip* 2012;12:2491–7. <https://doi.org/10.1039/C2LC21021E>.
- [332] Chen Y, Ding X, Steven Lin S-C, et al. Tunable Nanowire Patterning Using Standing Surface Acoustic Waves. *ACS Nano* 2013;7:3306–14. <https://doi.org/10.1021/nn4000034>.
- [333] Mansoorzare H, Abdolvand R. Ultra-Wideband Non-Reciprocal Micro-Acoustic Delay Lines with Slanted-Finger Interdigital Transducers. 2022 IEEE 35th Int. Conf. Micro Electro Mech. Syst. Conf. MEMS, 2022, p. 1014–7. <https://doi.org/10.1109/MEMS51670.2022.9699654>.

- [334] Laude V, Gérard D, Khelifaoui N, et al. P4L-3 Anisotropic Wave-Surface Shaped Annular Interdigital Transducer, 2007, p. 2115–8. <https://doi.org/10.1109/ULTSYM.2007.532>.
- [335] Zaehringer S, Schwesinger N. What happens turning a 250- μm -thin piezo-stack sideways? *Microsyst Technol* 2010;16:871–7.
- [336] O'Rorke R, Winkler A, Collins D, et al. Slowness curve surface acoustic wave transducers for optimized acoustic streaming. *RSC Adv* 2020;10:11582–9. <https://doi.org/10.1039/C9RA10452F>.
- [337] Pan C, Xiao G, Feng Z, et al. Electromechanical characteristics of discal piezoelectric transducers with spiral interdigitated electrodes. *Smart Mater Struct* 2014;23:125029. <https://doi.org/10.1088/0964-1726/23/12/125029>.
- [338] Xiao GJ, Pan CL, Liu YB, et al. In-plane torsion of discal piezoelectric actuators with spiral interdigitated electrodes. *Sens Actuators Phys* 2015;227:1–10.
- [339] Pan CL, Ma YT, Liu YB, et al. Torsional displacement of piezoelectric fiber actuators with helical electrodes. *Sens Actuators Phys* 2008;148:250–8.
- [340] Biryukov SV, Martin G, Weihnacht M. Ring waveguide resonator on surface acoustic waves. *Appl Phys Lett* 2007;90:173503. <https://doi.org/10.1063/1.2731683>.
- [341] Kang P, Tian Z, Yang S, et al. Acoustic tweezers based on circular, slanted-finger interdigital transducers for dynamic manipulation of micro-objects. *Lab Chip* 2020;20:987–94. <https://doi.org/10.1039/C9LC01124B>.
- [342] Riaud A, Baudoin M, Thomas J-L, et al. SAW Synthesis With IDTs Array and the Inverse Filter: Toward a Versatile SAW Toolbox for Microfluidics and Biological Applications. *IEEE Trans Ultrason Ferroelectr Freq Control* 2016;63:1601–7. <https://doi.org/10.1109/TUFFFC.2016.2558583>.
- [343] Tian Z. Generating multifunctional acoustic tweezers in Petri dishes for contactless, precise manipulation of bioparticles'. *Sci Adv* 2020;6:0494,. <https://doi.org/10.1126/sciadv.abb0494>.
- [344] Baudoin M, Gerbedoen J-C, Riaud A, et al. Folding a focalized acoustical vortex on a flat holographic transducer: Miniaturized selective acoustical tweezers. *Sci Adv* 2019;5:eaav1967. <https://doi.org/10.1126/sciadv.aav1967>.
- [345] Tsuji T, Mihara R, Saito T, et al. Highly Sensitive Ball Surface Acoustic Wave Hydrogen Sensor with Porous Pd-Alloy Film. *Mater Trans* 2014;55:1040–4. <https://doi.org/10.2320/matertrans.l-M2014816>.
- [346] Lin C-M, Wu T-T, Chen Y-Y, et al. Improved Frequency Responses of Saw Filters with Interdigitated Interdigital Transducers on ZnO/Diamond/Si Layered Structure. *J Mech* 2007;23:253–60. <https://doi.org/10.1017/S1727719100001295>.

- [347] Mańka M, Rosiek M, Martowicz A, et al. PZT based tunable Interdigital Transducer for Lamb waves based NDT and SHM. *Mech Syst Signal Process* 2016;78:71–83. <https://doi.org/10.1016/j.ymssp.2015.12.013>.
- [348] Zhu J, Emanetoglu NW, Lu Y, et al. A multi-IDT input tunable surface acoustic wave filter. *IEEE Trans Ultrason Ferroelectr Freq Control* 2001;48:1383–8. <https://doi.org/10.1109/58.949747>.
- [349] Lima MM de, Santos PV. Modulation of photonic structures by surface acoustic waves. *Rep Prog Phys* 2005;68:1639–701. <https://doi.org/10.1088/0034-4885/68/7/R02>.
- [350] de Lima Jr MM, Seidel W, Kostial H, et al. Embedded interdigital transducers for high-frequency surface acoustic waves on GaAs. *J Appl Phys* 2004;96:3494–500.
- [351] Zhang Q, Han T, Tang G, et al. SAW characteristics of AlN/SiO₂/3C-SiC layered structure with embedded electrodes. 2015 IEEE Int. Ultrason. Symp. IUS, 2015, p. 1–4. <https://doi.org/10.1109/ULTSYM.2015.0116>.
- [352] Zhang Q, Han T, Chen J, et al. Enhanced coupling factor of surface acoustic wave devices employing ScAlN/diamond layered structure with embedded electrodes. *Diam Relat Mater* 2015;58:31–4. <https://doi.org/10.1016/j.diamond.2015.06.001>.
- [353] Hon SF, Kwok KW, Li HL, et al. Self-focused acoustic ejectors for viscous liquids. *Rev Sci Instrum* 2010;81:065102. <https://doi.org/10.1063/1.3442526>.
- [354] Kwok KW, Hon SF, Lin D. Lead-free self-focused piezoelectric transducers for viscous liquid ejection. *Sens Actuators Phys* 2011;168:168–71. <https://doi.org/10.1016/j.sna.2011.04.011>.
- [355] Lee C-Y, Pang W, Yu H, et al. Subpicoliter droplet generation based on a nozzle-free acoustic transducer. *Appl Phys Lett* 2008;93:034104. <https://doi.org/10.1063/1.2958342>.
- [356] Kalantar-Zadeh K, Powell DA, Wlodarski W, et al. Comparison of layered based SAW sensors. *Sens Actuators B Chem* 2003;91:303–8.
- [357] Shih W-C, Su H-Y, Wu M-S. Deposition of ZnO thin films on SiO₂/Si substrate with Al₂O₃ buffer layer by radio frequency magnetron sputtering for high frequency surface acoustic wave devices. *Thin Solid Films* 2009;517:3378–81.
- [358] Legrani O, Elmazria O, Zhgoon S, et al. Packageless AlN/ZnO/Si Structure for SAW Devices Applications. *IEEE Sens J* 2013;13:487–91. <https://doi.org/10.1109/JSEN.2012.2219692>.
- [359] Destgeer G, Cho H, Ha BH, et al. Acoustofluidic particle manipulation inside a sessile droplet: four distinct regimes of particle concentration. *Lab Chip* 2016;16:660–7. <https://doi.org/10.1039/c5lc01104c>.

- [360] Gu Y, Chen C, Mao Z, et al. Acoustofluidic centrifuge for nanoparticle enrichment and separation. *Sci Adv* 2021;7. <https://doi.org/10.1126/sciadv.abc0467>.
- [361] Doinikov A, Gerlt M, Pavlic A, et al. Acoustic streaming produced by sharp-edge structures in microfluidic devices'. *Microfluid Nanofluidics* 2020;24:32. <https://doi.org/10.1007/s10404-020-02335-5>.
- [362] Hou X, Zhang YS, Santiago GT, et al. Interplay between materials and microfluidics. *Nat Rev Mater* 2017;2:1–15. <https://doi.org/10.1038/natrevmats.2017.16>.
- [363] Iranmanesh I, Barnkob R, Bruus H, et al. Tunable-angle wedge transducer for improved acoustophoretic control in a microfluidic chip. *J Micromechanics Microengineering* 2013;23:105002. <https://doi.org/10.1088/0960-1317/23/10/105002>.
- [364] Chen Y, Wu M, Ren L, et al. High-throughput acoustic separation of platelets from whole blood. *Lab Chip* 2016;16:3466–72. <https://doi.org/10.1039/C6LC00682E>.
- [365] Lenshof A, Evander M, Laurell T, et al. Acoustofluidics 5: Building microfluidic acoustic resonators. *Lab Chip* 2012;12:684–95. <https://doi.org/10.1039/C1LC20996E>.
- [366] Ren K, Zhou J, Wu H. Materials for Microfluidic Chip Fabrication. *Acc Chem Res* 2013;46:2396–406. <https://doi.org/10.1021/ar300314s>.
- [367] Johnston ID, McCluskey DK, Tan CKL, et al. Mechanical characterization of bulk Sylgard 184 for microfluidics and microengineering. *J Micromechanics Microengineering* 2014;24:035017. <https://doi.org/10.1088/0960-1317/24/3/035017>.
- [368] McDonald JC, Duffy DC, Anderson JR, et al. Fabrication of microfluidic systems in poly(dimethylsiloxane). *ELECTROPHORESIS* 2000;21:27–40. [https://doi.org/10.1002/\(SICI\)1522-2683\(20000101\)21:1<27::AID-ELPS27>3.0.CO;2-C](https://doi.org/10.1002/(SICI)1522-2683(20000101)21:1<27::AID-ELPS27>3.0.CO;2-C).
- [369] Xu K, Clark CP, Poe BL, et al. Isolation of a Low Number of Sperm Cells from Female DNA in a Glass–PDMS–Glass Microchip via Bead-Assisted Acoustic Differential Extraction. *Anal Chem* 2019;91:2186–91. <https://doi.org/10.1021/acs.analchem.8b04752>.
- [370] Wu M, Huang P-H, Zhang R, et al. Circulating Tumor Cell Phenotyping via High-Throughput Acoustic Separation. *Small* 2018;14:1801131. <https://doi.org/10.1002/smll.201801131>.
- [371] Zhao S, Wu M, Yang S, et al. A disposable acoustofluidic chip for nano/microparticle separation using unidirectional acoustic transducers. *Lab Chip* 2020;20:1298–308.

- [372] Barani A, Mosaddegh P, Haghjooy Javanmard S, et al. Numerical and experimental analysis of a hybrid material acoustophoretic device for manipulation of microparticles. *Sci Rep* 2021;11:22048. <https://doi.org/10.1038/s41598-021-01459-0>.
- [373] Barnkob R, Augustsson P, Laurell T, et al. Acoustic radiation- and streaming-induced microparticle velocities determined by microparticle image velocimetry in an ultrasound symmetry plane. *Phys Rev E* 2012;86:056307. <https://doi.org/10.1103/PhysRevE.86.056307>.
- [374] Niculescu A-G, Chircov C, Bîrcă AC, et al. Fabrication and Applications of Microfluidic Devices: A Review. *Int J Mol Sci* 2021;22:2011. <https://doi.org/10.3390/ijms22042011>.
- [375] Faustino V, Catarino SO, Lima R, et al. Biomedical microfluidic devices by using low-cost fabrication techniques: A review. *J Biomech* 2016;49:2280–92. <https://doi.org/10.1016/j.jbiomech.2015.11.031>.
- [376] Gale BK, Jafek AR, Lambert CJ, et al. A Review of Current Methods in Microfluidic Device Fabrication and Future Commercialization Prospects. *Inventions* 2018;3. <https://doi.org/10.3390/inventions3030060>.
- [377] Rodríguez CF, Andrade-Pérez V, Vargas MC, et al. Breaking the clean room barrier: exploring low-cost alternatives for microfluidic devices. *Front Bioeng Biotechnol* 2023;11.
- [378] Laermer F. Dry Etching. *Ref. Module Mater. Sci. Mater. Eng.*, Elsevier; 2016. <https://doi.org/10.1016/B978-0-12-803581-8.00526-9>.
- [379] Xia Y, Whitesides GM. SOFT LITHOGRAPHY. *Annu Rev Mater Sci* 1998;28:153–84. <https://doi.org/10.1146/annurev.matsci.28.1.153>.
- [380] Nge PN, Rogers CI, Woolley AT. Advances in Microfluidic Materials, Functions, Integration, and Applications. *Chem Rev* 2013;113:2550–83. <https://doi.org/10.1021/cr300337x>.
- [381] Mikhaylov R, Martin MS, Dumcius P, et al. A reconfigurable and portable acoustofluidic system based on flexible printed circuit board for the manipulation of microspheres. *J Micromechanics Microengineering* 2021;31:074003. <https://doi.org/10.1088/1361-6439/ac0515>.
- [382] Scott SM, Ali Z. Fabrication Methods for Microfluidic Devices: An Overview. *Micromachines* 2021;12:319. <https://doi.org/10.3390/mi12030319>.
- [383] Schulmeyer P, Weihnacht M, Schmidt H. A Dual-Mode Surface Acoustic Wave Delay Line for the Detection of Ice on 64°-Rotated Y-Cut Lithium Niobate. *Sensors* 2024;24:2292. <https://doi.org/10.3390/s24072292>.
- [384] Huang W, Yang Q, Liao J, et al. Integrated Rayleigh wave streaming-enhanced sensitivity of shear horizontal surface acoustic wave biosensors. *Biosens Bioelectron* 2024;247:115944. <https://doi.org/10.1016/j.bios.2023.115944>.

- [385] Agostini M, Lunardelli F, Gagliardi M, et al. Surface-Acoustic-Wave (SAW) Induced Mixing Enhances the Detection of Viruses: Application to Measles Sensing in Whole Human Saliva with a SAW Lab-On-a-Chip. *Adv Funct Mater* 2022;32:2201958. <https://doi.org/10.1002/adfm.202201958>.
- [386] Hur Y, Han J, Seon J, et al. Development of an SH-SAW sensor for the detection of DNA hybridization. *Sens Actuators Phys* 2005;120:462–7. <https://doi.org/10.1016/j.sna.2005.01.027>.
- [387] Li S, Wan Y, Su Y, et al. Gold nanoparticle-based low limit of detection Love wave biosensor for carcinoembryonic antigens. *Biosens Bioelectron* 2017;95:48–54. <https://doi.org/10.1016/j.bios.2017.04.012>.
- [388] Fu C. Vertical jetting induced by shear horizontal leaky surface acoustic wave on 36° Y-X LiTaO₃. *Appl Phys Lett* 2017;110. <https://doi.org/10.1063/1.4982073>.
- [389] Alghane M, Chen BX, Fu YQ, et al. Experimental and numerical investigation of acoustic streaming excited by using a surface acoustic wave device on a 128° YX-LiNbO₃ substrate. *J Micromechanics Microengineering* 2010;21:015005. <https://doi.org/10.1088/0960-1317/21/1/015005>.
- [390] David Morgan. *Surface Acoustic Wave Filters: With Applications to Electronic Communications and Signal Processing*. vol. 2nd ed. Amsterdam: Academic Press; 2007.
- [391] Sankaranarayanan SKRS, Cular S, Bhethanabotla VR. Finite Element modeling of hexagonal surface acoustic wave biosensor based on LiTaO₃. 2008 IEEE Sens., 2008, p. 514–7. <https://doi.org/10.1109/ICSENS.2008.4716490>.
- [392] Cular S, Bhethanabotla V, Branch D. Simultaneous Surface Manipulation and Sensing in a Biosensor Using a Hexagonal SAW Device. *AIChE Annu Meet Conf Proc* 2006.
- [393] Sankaranarayanan SKRS, Bhethanabotla VR. Finite-Element Modeling of a Hexagonal Surface Acoustic Wave Device Based on LiNbO_3 Substrate. *IEEE Sens J* 2009;9:329–39. <https://doi.org/10.1109/JSEN.2009.2013505>.
- [394] Setter N, Damjanovic D, Eng L, et al. Ferroelectric thin films: Review of materials, properties, and applications. *J Appl Phys* 2006;100:051606. <https://doi.org/10.1063/1.2336999>.
- [395] Kawamata A, Hosaka H, Morita T. Non-hysteresis and perfect linear piezoelectric performance of a multilayered lithium niobate actuator. *Sens Actuators Phys* 2007;135:782–6. <https://doi.org/10.1016/j.sna.2006.08.025>.
- [396] Shibayama K, Yamanouchi K, Sato H, et al. Optimum cut for rotated Y-cut LiNbO₃ crystal used as the substrate of acoustic-surface-wave filters. *Proc IEEE* 1976;64:595–7. <https://doi.org/10.1109/PROC.1976.10181>.

- [397] Slobodnik AJ, Szabo T. New high-coupling low-diffraction cut for acoustic surface waves on LiNbO₃. *Electron Lett* 1971;7:257–8. <https://doi.org/10.1049/el:19710175>.
- [398] Kurosawa M, Takahashi M, Higuchi T. Ultrasonic linear motor using surface acoustic waves. *IEEE Trans Ultrason Ferroelectr Freq Control* 1996;43:901–6. <https://doi.org/10.1109/58.535493>.
- [399] Sun C, Mikhaylov R, Fu Y, et al. Flexible Printed Circuit Board as Novel Electrodes for Acoustofluidic Devices. *IEEE Trans Electron Devices* 2021;68:393–8. <https://doi.org/10.1109/TED.2020.3039760>.
- [400] Mikhaylov R, Wu F, Wang H, et al. Development and characterisation of acoustofluidic devices using detachable electrodes made from PCB. *Lab Chip* 2020;20:1807–14. <https://doi.org/10.1039/C9LC01192G>.
- [401] Kim S, Prasad B, Kim J. Alignment of Microbeads Using Spinning Helical Minichannel Cartridge. *J Korean Soc Vis* 2016;14:38–45. <https://doi.org/10.5407/JKSV.2016.14.3.038>.
- [402] Adrian RJ. Particle-Imaging Techniques for Experimental Fluid Mechanics. *Annu Rev Fluid Mech* 1991;23:261–304. <https://doi.org/10.1146/annurev.fl.23.010191.001401>.
- [403] Thielicke W, Sonntag R. Particle Image Velocimetry for MATLAB: Accuracy and enhanced algorithms in PIVlab 2021;9:12. <https://doi.org/10.5334/jors.334>.
- [404] Surface Acoustic Wave Gas Sensor. COMSOL n.d. <https://www.comsol.com/model/surface-acoustic-wave-gas-sensor-2129> (accessed November 1, 2023).
- [405] Ledbetter H, Ogi H, Nakamura N. Elastic, anelastic, piezoelectric coefficients of monocrystal lithium niobate. *Mech Mater* 2004;36:941–7. <https://doi.org/10.1016/j.mechmat.2003.08.013>.
- [406] Namnabat MS, Moghimi Zand M, Houshfar E. 3D numerical simulation of acoustophoretic motion induced by boundary-driven acoustic streaming in standing surface acoustic wave microfluidics. *Sci Rep* 2021;11:13326. <https://doi.org/10.1038/s41598-021-90825-z>.
- [407] Eigenfrequency Analysis n.d. <https://www.comsol.com/multiphysics/eigenfrequency-analysis> (accessed November 1, 2023).
- [408] Structural Mechanics Module User Guide 2008.
- [409] Yang R-Y, Su Y-K, Weng M-H, et al. Characteristics of coplanar waveguide on lithium niobate crystals as a microwave substrate. *J Appl Phys* 2007;101:014101. <https://doi.org/10.1063/1.2402978>.

- [410] Liu X, Zheng T, Wang C. Three-dimensional modeling and experimentation of microfluidic devices driven by surface acoustic wave. *Ultrasonics* 2023;129:106914. <https://doi.org/10.1016/j.ultras.2022.106914>.
- [411] Chen C. Three-dimensional numerical simulation and experimental investigation of boundary-driven streaming in surface acoustic wave microfluidics'. *Lab Chip* 2018;18:3645-3654,. <https://doi.org/10.1039/C8LC00589C>.
- [412] Ye R. Acoustic forces and microparticles manipulation using CMUT arrays. University of British Columbia, 2022. <https://doi.org/10.14288/1.0416181>.
- [413] Koigerov AS, Korlyakov AV. Finite Element Modeling of Surface Acoustic Wave Devices Using COMSOL. *Russ Microelectron* 2022;51:226–35. <https://doi.org/10.1134/S1063739722040072>.
- [414] Lustig S, Elata D. Ambiguous definitions of the piezoelectric coupling factor. *J Intell Mater Syst Struct* 2020;31:1689–96. <https://doi.org/10.1177/1045389X20930104>.
- [415] Kuznetsova IE, Zaitsev BD, Teplykh AA, et al. The Power Flow Angle of Acoustic Waves in Thin Piezoelectric Plates. *Inst Electr Electron Eng* 2008;55.
- [416] Mandal D, Banerjee S. Surface Acoustic Wave (SAW) Sensors: Physics, Materials, and Applications. *Sensors* 2022;22:820. <https://doi.org/10.3390/s22030820>.
- [417] Martin SJ, Ricco AJ, Niemczyk TM, et al. Characterization of SH acoustic plate mode liquid sensors. *Sens Actuators* 1989;20:253–68. [https://doi.org/10.1016/0250-6874\(89\)80124-6](https://doi.org/10.1016/0250-6874(89)80124-6).
- [418] McHale G, Newton MI, Banerjee MK, et al. Acoustic wave–liquid interactions. *Mater Sci Eng C* 2000;12:17–22. [https://doi.org/10.1016/S0928-4931\(00\)00151-X](https://doi.org/10.1016/S0928-4931(00)00151-X).
- [419] Sun C, Mikhaylov R, Fu Y, et al. Flexible Printed Circuit Board as Novel Electrodes for Acoustofluidic Devices. *IEEE Trans Electron Devices* 2021;68:393–8. <https://doi.org/10.1109/TED.2020.3039760>.
- [420] Ballandras S, Reinhardt A, Khelif A, et al. Theoretical analysis of damping effects of guided elastic waves at solid/fluid interfaces. *J Appl Phys* 2006;99:054907. <https://doi.org/10.1063/1.2168242>.
- [421] Salari A, Appak-Baskoy S, Coe IR, et al. An ultrafast enzyme-free acoustic technique for detaching adhered cells in microchannels. *RSC Adv* n.d.;11:32824–9. <https://doi.org/10.1039/d1ra04875a>.
- [422] Kurashina Y, Imashiro C, Hirano M, et al. Enzyme-free release of adhered cells from standard culture dishes using intermittent ultrasonic traveling waves. *Commun Biol* 2019;2:1–11. <https://doi.org/10.1038/s42003-019-0638-5>.

- [423] Imashiro C, Hirano M, Morikura T, et al. Detachment of cell sheets from clinically ubiquitous cell culture vessels by ultrasonic vibration. *Sci Rep* 2020;10:9468. <https://doi.org/10.1038/s41598-020-66375-1>.
- [424] Exosomes Frequently Asked Questions (FAQs) - UK n.d. <https://www.thermofisher.com/uk/en/home/life-science/cell-analysis/exosomes/exosomes-webinar-q-and-a.html> (accessed May 24, 2024).
- [425] Shilton R, Tan MK, Yeo LY, et al. Particle concentration and mixing in microdrops driven by focused surface acoustic waves'. *J Appl Phys* 2008;104. <https://doi.org/10.1063/1.2951467>.
- [426] Liu Y, Ji M, Yu N, et al. Enhanced Detection in Droplet Microfluidics by Acoustic Vortex Modulation of Particle Rings and Particle Clusters via Asymmetric Propagation of Surface Acoustic Waves. *Biosensors* 2022;12:399. <https://doi.org/10.3390/bios12060399>.
- [427] Salafi T, Kwek Zeming K, Zhang Y. Advancements in microfluidics for nanoparticle separation. *Lab Chip* 2017;17:11–33. <https://doi.org/10.1039/C6LC01045H>.
- [428] Liu X, Rong N, Tian Z, et al. Acoustothermal transfection for cell therapy. *Sci Adv* 2024;10:eadk1855. <https://doi.org/10.1126/sciadv.adk1855>.
- [429] Lentacker I, De Cock I, Deckers R, et al. Understanding ultrasound induced sonoporation: Definitions and underlying mechanisms. *Adv Drug Deliv Rev* 2014;72:49–64. <https://doi.org/10.1016/j.addr.2013.11.008>.
- [430] Rasouli R, Paun RA, Tabrizian M. Sonoprinting nanoparticles on cellular spheroids via surface acoustic waves for enhanced nanotherapeutics delivery. *Lab Chip* 2023;23:2091–105. <https://doi.org/10.1039/D2LC00854H>.
- [431] Ramesan S, Rezk AR, Dekiwadia C, et al. Acoustically-mediated intracellular delivery. *Nanoscale* 2018;10:13165–78. <https://doi.org/10.1039/C8NR02898B>.
- [432] Fan Z, Kumon RE, Deng CX. Mechanisms of microbubble-facilitated sonoporation for drug and gene delivery. *Ther Deliv* 2014;5:467–86. <https://doi.org/10.4155/tde.14.10>.
- [433] Yeo LY, Chang H-C, Chan PPY, et al. Microfluidic devices for bioapplications. *Small* Weinheim Bergstr Ger 2011;7:12–48. <https://doi.org/10.1002/smll.201000946>.